AD-A098 189 SCIENCE APPLICATIONS INC MCLEAN VA F/G 8/3
A REVIEW OF OCEAN MODELS.(U)
JAN 81 W J GRABOWSKI, G T HEBENSTREIT N00014-78-C-0849
UNCLASSIFIED SAI-81-346-WA NL

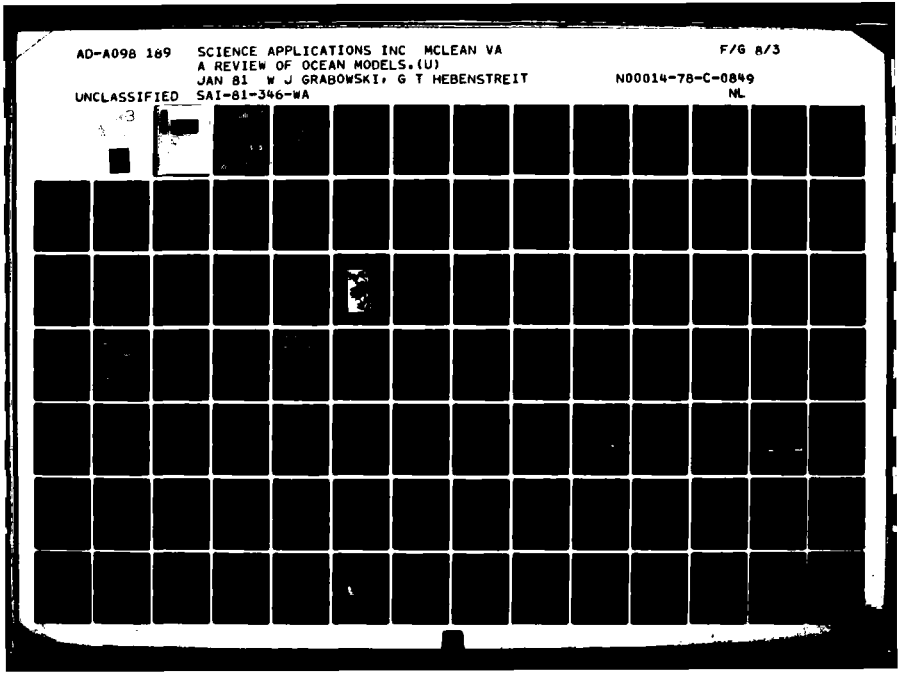

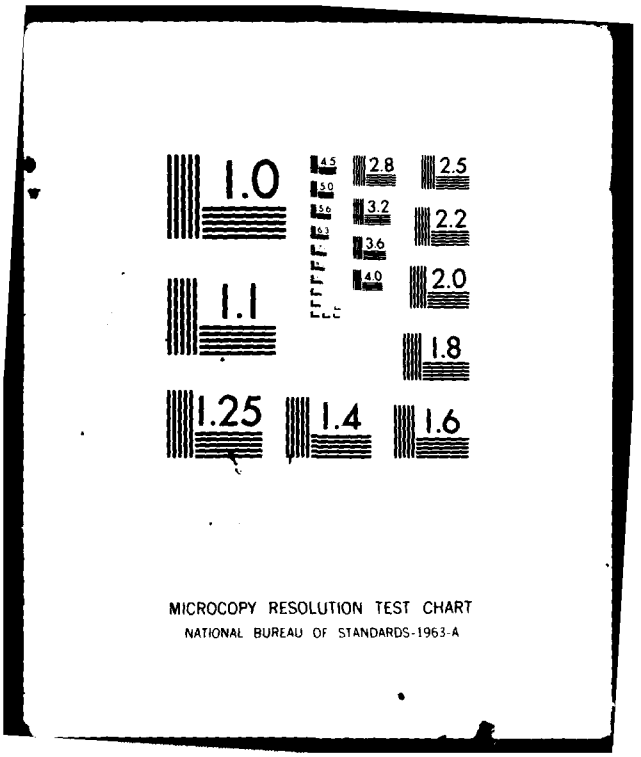
1.0
1.1
1.25
1.4
1.6
1.8
2.0
2.2
2.5
2.8
3.2
3.6
4.0
4.5
5.0
5.6
6.3
MICROCOPY RESOLUTION TEST CHART
NATIONAL BUREAU OF STANDARDS-1963-A

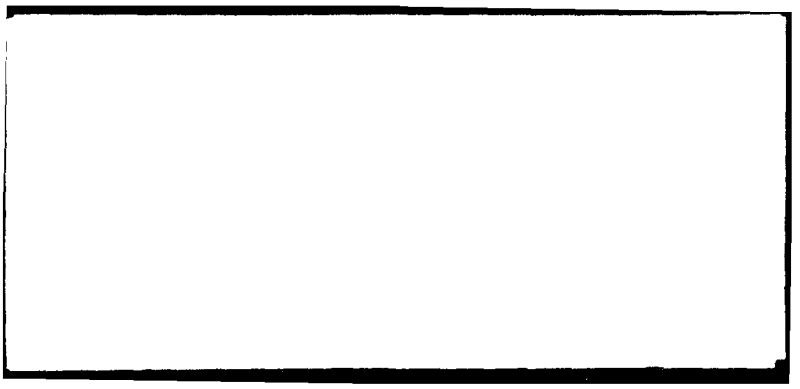

12

LEVEL II

A Review of Ocean Models

SAI-81-346-WA

SAI
ATLANTA • ANN ARBOR • BOSTON • CHICAGO • CLEVELAND • DENVER • HUNTSVILLE • LA JOLLA
LITTLE ROCK • LOS ANGELES • SAN FRANCISCO • SANTA BARBARA • TUCSON • WASHINGTON

(6) A Review of Ocean Models.

(14) SAI-81-346-WA

Accession For	
NTIS GRA&I	X
DTIC TAB	☐
Unannounced	☐
Justification	Per Letter on File
By	
Distribution/	
Availability Codes	
Dist	Avail and/or Special
A	

(11) 23 Jan [redacted] 81

(10) Walter J. [redacted] Grabowski
Gerald T. Hebenstreit

(12) 274

(15) for:
Contract No. N00014-78-C-0849
Naval Ocean Research and Development Activity
NSTL Station, Mississippi 39529

(9) Final rept. 25 Sep 78-30 Jan 82.

SCIENCE APPLICATIONS, INC.
1710 Goodridge Drive, P.O. Box 1303
McLean, Virginia 22102
(703) 821-4300

UNCLASSIFIED

SECURITY CLASSIFICATION OF THIS PAGE (When Data Entered)

REPORT DOCUMENTATION PAGE	READ INSTRUCTIONS BEFORE COMPLETING FORM
1. REPORT NUMBER: SAI-81-346-WA	2. GOVT ACCESSION NO.: AD-A098 189
	3. RECIPIENT'S CATALOG NUMBER:
4. TITLE (and Subtitle): A Review of Ocean Models	5. TYPE OF REPORT & PERIOD COVERED: Final 9/15/78 - 1/30/81
	6. PERFORMING ORG. REPORT NUMBER: SAI-81-346-WA
7. AUTHOR(s): Walter J. Grabowski, Gerald T. Hebenstreit	8. CONTRACT OR GRANT NUMBER(s): N00014-78-0849
9. PERFORMING ORGANIZATION NAME AND ADDRESS: Science Applications, Inc. 1710 Goodridge Dr. McLean, Virginia 22102	10. PROGRAM ELEMENT, PROJECT, TASK AREA & WORK UNIT NUMBERS:
11. CONTROLLING OFFICE NAME AND ADDRESS: Office of Naval Research 800 N. Quincy Street Arlington, Virginia 22217	12. REPORT DATE: 1/30/81
	13. NUMBER OF PAGES: 270
14. MONITORING AGENCY NAME & ADDRESS (if different from Controlling Office): Scientific Officer Ocean Exploratory Development Office Naval Ocean Research & Development Activity NSTL Station, Bay St. Louis, MS 39529 ATTN: Dr. E. M. Stanley, NORDA, Code 500	15. SECURITY CLASS. (of this report): Unclassified
	15a. DECLASSIFICATION/DOWNGRADING SCHEDULE: N/A
16. DISTRIBUTION STATEMENT (of this Report):	
17. DISTRIBUTION STATEMENT (of the abstract entered in Block 20, if different from Report):	
18. SUPPLEMENTARY NOTES:	

19. KEY WORDS (Continue on reverse side if necessary and identify by block number)

Ocean Models
Circulation Models
Fronts
Eddies
Upper Ocean Models
Internal Waves
Fine Structure
Mixed Layer Dynamics

20. ABSTRACT (Continue on reverse side if necessary and identify by block number)

This report is a review of current trends and approaches to modeling various ocean phenomena. We begin with a brief discussion of large scale circulation models. This leads to a summary of models of large (i.e., tens of kilometers) fronts and attempts to model them. The next section is a detailed discussion of upper ocean dynamics and the models used for simulations. The final section discusses Garrett-Munk type internal wave models and models of the effects of finestructure.

DD FORM 1 JAN 73 1473 EDITION OF 1 NOV 65 IS OBSOLETE
S/N 0102-LF-014-6601

UNCLASSIFIED
SECURITY CLASSIFICATION OF THIS PAGE (When Data Entered)

TABLE OF CONTENTS

Section 1
REVIEW OF OCEAN MODELS

The ocean is continuously in motion. The internal and external forces which cause oceanic motions are bound together in an incredibly complex network of actions and interactions. One approach oceanographers have used to sort out and study these motions is the development of analytical and, with the advent of computers, increasingly sophisticated numerical models which represent, in a sense, best estimates of the nature of the driving forces and interaction processes which keep the ocean moving. This document is intended to serve as a review of the types of modeling currently underway in the physical oceanographic community and as an indicator of future directions in research. Researchers are continually developing and refining models as our understanding of the physics of oceanic motions evolves. For this reason no review of this type can be totally complete and up-to-date. We do feel that it represents a reasonably thorough "snapshot" of several phases of ocean modeling as they were in late 1979 or early 1980.

We have chosen to view the ocean as a descending hierarchy of scales of motion. At the high end are the large scale motions which act as sources and sinks for energy at smaller scales. At the low end are the internal waves and fine scale motions. In between are the frontal and upper ocean models, which somehow seem to act as "middlemen" in the distribution of energy throughout the oceans.

Each section is written as a nearly self-contained unit, with its own internal numbering system and references. We do, however, attempt to smooth the transition from one chapter to the next by addressing the interconnections between the scales of motion.

Section 2 describes numerical models of large-scale ocean circulation features. These are motions with length scales from many tens to thousands of kilometers and time scales from months to centuries. These motions set the background pattern upon which smaller scale motions are superimposed. They also act as sources and sinks for energy in the smaller scales.

This section is intended to provide the reader with a sense of the power and complexity of models of large-scale models without providing a blueprint for actually implementing the models. We have consciously avoided detailed description of some important aspects of this type of modeling. Thus the knowledgeable reader will not find discussions of the various numerical schemes used to implement the models on digital computers; and such other topics as the variety of forcing functions and boundary conditions have only been touched on lightly. All of these aspects, while crucial for successful implementation of any specific model, could, we fear, deter the reader from an appreciation of the wide range of situations to which large-scale models have been and are constantly being applied. We hope that this section, while somewhat brief, achieves its designed purpose.*

* Since Section 2 was completed, a review emphasizing the use of coupled atmosphere-ocean circulation models has appeared (Haney, R.L. Reviews of Geophysics and Space Physics, 17, 1979, pp 1494-1507).

Section 3 discusses the existing models of oceanic fronts. Little is known about the role of fronts in the overall dynamics of the ocean system, although they do seem to provide sinks for some energy from larger scales and may contribute to the development of smaller-scale motions. Few numerical models of fronts exist, but this state will no doubt change as more attention and interest is focused on them. We have attempted to provide the reader with a sense of both the extent and nature of fronts and of the modeling approaches currently being taken to understand them.

Section 4 discusses models of the dynamics of the upper ocean. This region, consisting of the mixing layer and the seasonal thermocline, is marked by short-term (scales of hours to days) variations in thermohaline and velocity structure. It forms the oceanic portion of the air-sea boundary layer and, as such, the entry point through which atmospheric energy is passed to the ocean. The fact that many of man's important oceanic activities take place within this region makes an understanding of the processes affecting it vital. The emphasis in this section is on one-dimensional models (i.e., models which vary only in depth and time). The ocean is, of course, three-dimensional, but, provided certain assumptions are met, one-dimensional models can prove quite useful in examining the dynamic processes which shape the upper ocean. Three-dimensional upper-ocean models are being developed by a number of research groups and reports should soon begin to appear in the literature.

Section 5 discusses internal-wave models. This section marks the end of our descent from very large to small scale motions. The information presented in this section relies heavily on empirical knowledge of

internal waves. We know a great deal about the manifestations of internal-wave activity, but relatively little about their relation to other scales of motion. Internal waves can be enhanced by fronts (both atmospheric and oceanic) and by perturbations in the mean flow due to topography. Internal-wave energy may help to feed smaller scale (turbulent) motions. The modeling of internal waves, in the sense of simulating the processes which lead to generation and propagation, is still in its early stages.

Several topics which are related to internal wave models have not been included in this section. One, alluded to above, is the question of modeling the generation and dissipation of internal waves at all frequencies in the free wave band. Another is the generation and propagation of waves at near-inertial and sub-inertial frequencies. The underlying question which has not been addressed pertains to the nature of the forces and interactions which determine the form of the energy spectrum across the entire range of frequencies and wavenumbers at which internal motions are observed. The reason for the omission of topics such as these is the fact that only recently has the oceanographic community attempted to come to grips with them.

The reader will no doubt notice a bias in the structure of this review. As the scales of motion and time get smaller the treatment of the subject gets more detailed. This is a reflection of our view of the direction of the NORDA program, which currently tends to concentrate on the smaller scales. In this view the large-scale motions are primarily important in their role of providing the mean

motions. Fronts play a somewhat more important, although still unclear, role in feeding the smaller scales. The state of the upper ocean directly influences these motions and thus must be understood in greater detail.

We should reiterate to the reader that this review can only serve as an instantaneous summary of the state of our ability to model oceanic motions. New perceptions, new methods, new applications are continually evolving. Thus, we recognize that this document, while we have tried to make it as thorough as time would allow, can only serve as a basis for continued study by the interested reader.

Section 2

NUMERICAL MODELS OF LARGE-SCALE OCEAN CIRCULATION

Section 2

NUMERICAL MODELS OF LARGE-SCALE OCEAN CIRCULATION

2.1 INTRODUCTION

Large-scale ocean circulation models attempt to describe ocean movements which occur over long distances and long periods of time. These motions typically have time scales from months (seasonal variations) to hundreds of years (basin overturning) and length scales from tens of kilometers (boundary currents, eddies) to thousands of kilometers (basin-sized gyres). The resolution of the numerical models is geared to accommodating these scales. Although simulations explicitly aimed at resolving eddy-sized (a hundred kilometers, say) motions have recently appeared in the literature, the majority of circulation models to date have attempted to describe the dynamics of basin-scale mean (time scales of 100 years or more) flows.

The following discussion is intended to provide the reader with an overview of the bases for large-scale circulation models. We will first discuss the equations which go into circulation models, and then describe the development of numerical circulation models. The early efforts involved geometrically simplified basins and simplified form of forcing functions. Once the ability of numerical models to successfully describe circulation

dynamics was established, applications to realistic cases involving close approximations to actual basin geometry and realistic forcing functions followed. These are discussed in the sections covering global models, regional models, and diagnostic models.

Current trends in circulation research are addressing two very important problems: (1) the response of the mean flow to time-varying forcing functions on the scale of months to years, and (2) the generation and dynamics of eddy-scale motions. Progress in these areas and potential benfits are discussed in Sections 2.7 and 2.8. The final section will directly address the usefulness of the large-scale models to programs which are interested in smaller scales of motion.

Two approaches to large-scale numerical modeling exist: predictive and diagnostic. Predictive models start with the ocean in some initial state (i.e., some specified density and current structure) and allow the models to "spin up" to equilibrium or quasi-equilibrium under the influence of specified forcing. The time-varying progress of the density and current fields toward equilibrium is predicted by these models. Diagnostic models also start with some initial state (usually based on observed density structure in the ocean) and allow the ocean to spin up. But the initial density field is held fixed and only the currents are predicted. The majority of diagnostic model research has been carried out in the Soviet Union. We will restrict our discussion largely to the more readily accessible predictive models.

A discussion of the numerical schemes used to implement the mathematical forms of the models on digital computers is beyond the scope of this review. All of the models discussed employ finite-difference approximations of the partial differential equations of motion and some type of three-dimensional grid lattice to represent the horizontal and vertical locations of the coordinates at which variables are defined.

2.2 MODEL FORMULATION

2.2.1 Basic Equations

All large-scale circulation models are based on some combination of conservation equations for mass, momentum, heat, and salt, depending on the processes and variables required for a specific study. The basic set of equations used to represent large-scale circulation can be expressed as follows:

$$\partial_t \underline{\upsilon} + \underline{\upsilon}\cdot\nabla\underline{\upsilon} + k \times f\underline{\upsilon} + w\,\partial_z\underline{\upsilon} = -\rho_r^{-1}\nabla p + K_m\partial_{zz}\underline{\upsilon} + A_m\nabla^2\underline{\upsilon} \qquad (2.1)$$

$$\partial_t(T,S) + \underline{\upsilon}\cdot\nabla(T,S) + w\partial_z(T,S) = K_h\partial_{zz}(T,S) + A_h\nabla^2(T,S) \qquad (2.2)$$

$$\nabla\cdot\underline{\upsilon} + \partial_z w = 0 \qquad (2.3)$$

$$\partial_z p = -\rho g \qquad (2.4)$$

$$\rho = \rho(T,S,p) \qquad (2.5)$$

The variables and parameters in these equations, as well as others which will be encountered in this review, are described in Table 2-1.

Equation (2.1) represents the conservation of momentum, (2.2) the conservation of heat and salt, and (2.3) the continuity of mass. Equation (2.4) expresses the assumption that pressure below the sea surface is strictly due to hydrostatic forces. This approximation is generally valid in the ocean since mean vertical velocities tend to be quite small. The use of ρ_r in (2.1) and ρ in (2.4) indicates the use of the Boussinesq approximation, which assumes that variations in density are negligible unless they appear in conjunction with g. The hydrostatic and Boussinesq approximations appear in all large-scale models. Equation (2.5) expresses the dependence of density on temperature, salinity, and pressure. The form of the expression varies widely, although most models which require an equation of state generally assume a linear dependence of density on temperature (and salinity when calculated).

2.2.2 Initial and Boundary Conditions

A time-varying model requires initial and boundary conditions to define a unique solution. Initial conditions for most predictive models tend to consist of a relatively simple density structure (homogeneous, linearly stratified, etc.) and velocity components which are set to zero. The ocean is then spun up from this simplified state.

Table 2-1

NOMENCLATURE

t, z	-	time and vertical space coordinates
υ	-	horizontal velocity vector: $\upsilon = (u, v)$
$\underline{\Lambda}$	-	horizontal transport vector: $\underline{\Lambda} = (uh, vh)$
w	-	vertical velocity component
T	-	ocean temperature
S	-	salinity
ρ	-	<u>in situ</u> density
ρ_r	-	reference density
p	-	ocean pressure
g	-	local acceleration due to gravity
f	-	Coriolis parameter
Q_s	-	surface net heat flux
h	-	depth below some reference level (usually mean sea level
∇	-	horizontal gradient operator whose form depends on the model coordinate system
∂_x	-	partial derivative with respect to subscripted variable
K_h, K_m	-	vertical eddy exchange coefficient due to conductivity (h) and viscosity (m)
A_h, A_m	-	corresponding horizontal exchange coefficients
B_h, B_m	-	higher order analogs to $A_{h,m}$
$\underline{k}$	-	vertical unit vector
$\underline{n}$	-	unit vector perpendicular to a boundary
s	-	subscript indicating quantity defined at the surface of the ocean

Boundary conditions play a vital role in simulations, since they drive the interior to a solution. Conditions for velocity components along closed (impermeable) lateral boundaries and bottom boundaries usually assume combinations of no-slip (i.e., $[\underline{\upsilon}, w] = 0$) for the component tangential to the boundary and no-flux (i.e., $[\underline{\upsilon} \cdot n, \partial_z w] = 0$) through the boundaries. Fluxes of heat and salt are usually not permitted through closed boundaries. If a lateral boundary is open rather than closed, the usual procedure is to specify values of currents, heat, and salt (or their fluxes) along the open portion of the boundary at each point.

Surface boundary conditions provide the atmospheric energy input which drives circulation models. Most employ formulations of mean* surface wind stress (τ_s) and heat flux (Q_s) which vary in space. Little work has been done with time-varying surface boundary conditions in large scale models, with the exception of the long-term anomaly models. A rigid ocean surface is usually specified ($w = 0$), which acts to filter out externally generated high frequency surface gravity waves and allow larger time step sizes than would otherwise be possible.

---

* In most cases, mean implies averages over many years, rather than seasonal or yearly averages.

2.2.3 Sub-Grid Scale Influences

The terms in (2.1) and (2.2) contain eddy exchange coefficients which serve to parameterize the horizontal and vertical fluxes of momentum, heat, and salt which exert an important influence on the mean flow but which occur on length scales smaller than the grid spacing of the model. These terms allow the numerical scheme to include these motions without requiring grid spacing so small as to make calculations prohibitively expensive.

Values of the A's and K's are generally dictated by vague notions of what oceanic values should be and by the computational requirement to preserve numerical stability while retaining relatively coarse grid spacing. As Table 2-2 illustrates, no general agreement exists on values of the coefficients, although the orders of magnitude are similar. The magnitudes of these coefficients should be a function of the resolution of the model since it determines the scales of motion which are parameterized.

2.3 MODELS OF SIMPLIFIED BASINS

The earliest numerical circulation studies were of the behavior of bodies of water in geometrically simple basins under restricted conditions. These studies were attempts to elucidate and extend earlier analytic work. Studies by Bryan (1963), Veronis (1966a,b), and Blandford (1971) established the varying influences of lateral friction and bottom friction in the formation and behavior of boundary currents in a homogeneous ocean in a flat-bottomed, rotating rectangular basin being acted on by a steady wind stress.

Table 2-2

Multi-Level Ocean Circulation Models

Model Feature	Bryan and Cox (1968)	Cox (1970)	Friedrick (1970)	Holland (1973)	Haney (1974)
Domain	Simplified Basin	Indian Ocean	North Atlantic	Simplified Basin	Simplified Basin
Vertical levels	6	7	14	?	6
Grid size (long x lat)	$3^{o}x3^{o}$	$1^{o}x1^{o}$	$3^{o}x3^{o}$	?	$3.0^{o}x2.5^{o}$
Horizontal viscosity cm^2s^{-1}	$8.5x10^6$	$5x10^7$	10^8-$2x10^9$	$5x10^8$	$2.x10^8$
Horizontal diffusivity cm^2s^{-1}	$8.5x10^6$	$5x10^7$	10^8	$5x10^7$	$2.x10^8$
Vertical viscosity cm^2s^{-1}	5	1	10	10	1.5
Vertical diffusivity cm^2s^{-1}	5	1	1	1	1.5
Lateral boundary condition	No slip	No Slip	No Slip	?	No Slip
Bottom boundary condition	Free slip	Free Slip	No slip	?	Free Slip
Bottom topography	No	No	Yes	Yes	No
Salinity	No	Yes	Yes	Yes	Yes
Equation of state	Linear (T)	Linear (T, S)	Nonlinear (T, S, z)	?	Linear (T)
Forcing frequency (cy yr^{-1})	0	2	1	0	0
Mixed layer	No	No	Wind stirring and Convection	No	No

Table 2-2 (Continued)
Multi-Level Ocean Circulation Models

Model Feature	Cox (1975)	Bryan et. al (1975)	Holland and Lin (1975)	Semtner (1976)	Semtner and Wintz (1977)
Domain	World	Coupled Atm-Ocean	Simplified Eddy resolving	Arctic Ocean	Gulf Stream Eddy Resolving
Vertical Levels	9	12	2	14	5
Grid size (long x lat)	2.0^{o}x2.0^{o}	5.6^{o}x4.7^{o}	20x20km	1^{o}x1^{o}	37x37 km
Horizontal viscosity cm^2s^{-1}	$8x10^8$	$8x10^9$	$1\text{-}26x10^6$	$4x10^8$	10^7
Horizontal diffusivity cm^2s^{-1}	10^7	$2.5x10^7$	—	10^7	10^7
Vertical viscosity cm^2s^{-1}	10^2	0.3	—	0.3	1.5
Vertical diffusivity cm^2s^{-1}	10^2	0.3	—	0.3	1.5
Lateral boundary condition	No slip	No slip	Free and no slip	No slip	Free slip
Bottom boundary condition	Free slip	Free slip	Free and no slip	?	Quadratic stress
Bottom topography	Yes	Yes	No	Yes	Some
Salinity	Yes	Yes	No	Yes	No
Equation of state	Nonlinear (T, S, p)	Linear (T, S,p)	—	Linear (T,S)	Linear (T)
Forcing frequency ($cy\ yr^{-1}$)	0	0	0	0	0
Mixed layer	No	Wind-Stirring and connection	No	No	No

Table 2-2 (Continued)
Multi-Level Ocean Circulation Models

Model Feature	Mintz (1978)	Kim and Gates (1978)	Bryan and Lewis (1979)	Huang (1979)
Domain	World	World	World	North Pacific
Vertical levels	5	4	12	10
Grid size (long x lat)	2.5^{o}x4.0^{o}	5.0^{o}x4.0^{o}	2.8^{o}x2.4^{o}	2.5^{o}x2.5^{o}
Horizontal viscosity $cm^2 s^{-1}$	10^9	$4x10^9$	10^9	$2.5x10^8$
Horizontal diffusivity $cm^2 s^{-1}$	$2.5x10^7$	$5x10^7$	vrbl ~ 10	10^7
Vertical viscosity $cm^2 s^{-1}$	1	[illegible]	10^2	1.5
Vertical diffusivity $cm^2 s^{-1}$	1	1	vbrl ~ 1	1
Lateral boundary condition	No Slip	No Slip	No slip	No Slip
Bottom boundary condition	Free Slip	Free Slip	Free Slip	Free Slip
Bottom topography	No	Yes	Yes	No
Salinity	No	No	Yes	Yes
Equation of state	Linear (T)	Linear (T)	Nonlinear (T, S, p)	Linear (T, S)
Forcing frequency (cy yr^{-1})	0 and 1	0,1,...6	0 and 1	0, 1 and 2
Mixed Layer	No	Yes	Wind stirring	No

The real ocean is not homogeneous, however, but baroclinic (i.e., density and pressure surfaces are not necessarily parallel). Thus, the next step was to study the effects of density stratification in simplified basins. The studies which included baroclinicity provided the catalyst for present day circulation studies.

2.3.1 Wind-driven, Baroclinic Models

Bryan and Cox (1968a,b) described results of an investigation of the role of stratification on the circulation of a wind-driven ocean in a simplified basin. While no explicit attempt was made to apply the model to a specific ocean, the model basin (65°S to 65°N, 0° to 45°E) had roughly the dimensions of the Atlantic basin. Mirror symmetry across the equator was assumed so that only the northern hemisphere was treated. Salinity variations were not included in the model.

The model comprised six layers in the vertical -- three above the main thermicline and three below. The horizontal grid spacing in the ocean interior was 3° and the time step was roughly three hours. One non-dimensional time unit corresponded to 8.7 years and thus each time unit comprised approximately 20,000 time steps. The lateral boundary conditions specified no-slip and complete insulation. The surface was a rigid lid.

The surface boundary conditions specified were

$$T_s = T^* G_1(\phi) \tag{2.6}$$

$$\tau_s^x = \tau^* G_2(\phi) \tag{2.7}$$

where T* and τ* are maximum and heat flux wind stress values and $G_1(\phi)$ and $G_2(\phi)$ were defined with the latitude dependence shown in Figure (2.1). The wind stress form defined three atmospheric gyres: a small counterclockwise gyre near the equator, a large clockwise gyre between roughly 20°N and 50°N, and an intermediate counterclockwise subarctic gyre.

The simulation was run for over 200 years beginning from a horizontally uniform stratified density field at rest. The first phase of the simulation, which spun the model up to near-equilibrium, lasted for 190 model years on a grid with uniform 3° grid spacing. The second, shorter phase continued the simulation on a variable grid with spacing as fine as 0.3° along the lateral boundaries to resolve motions due to frictional, mixing, and inertial forces. Figure 2.2 shows the vertically integrated (a) and meridionally integrated (b) transports at the end of the first phase. The intensified western boundary flow and the eastward flow along the equator agree with observations and theoretical analyses of Atlantic circulation.

Figure 2.3 shows the time-dependent mass transport stream function in the region of the western boundary. The sequence shows the generation, growth, and decay of gyres separating from the boundary in the vicinity of the latitude which marks the change from the cyclonic subarctic wind gyre to the anticyclonic, subtropical gyre. This transient behavior is similar to the behavior of the Gulf Stream as it separates from the continental shelf. These transients only appear when resolution is improved along the boundary.

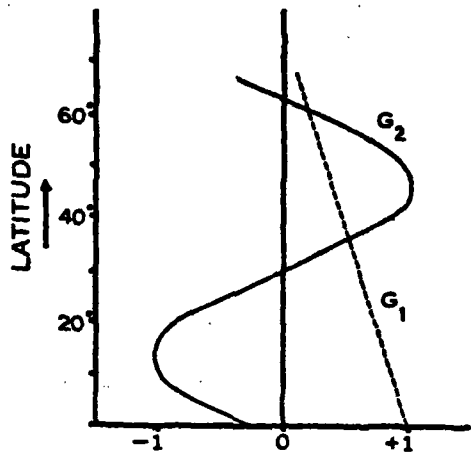

Figure 2-1. Temperature distribution and the X-directed component of the wind stress specified for surface boundary conditions by Bryan and Cox (1968)

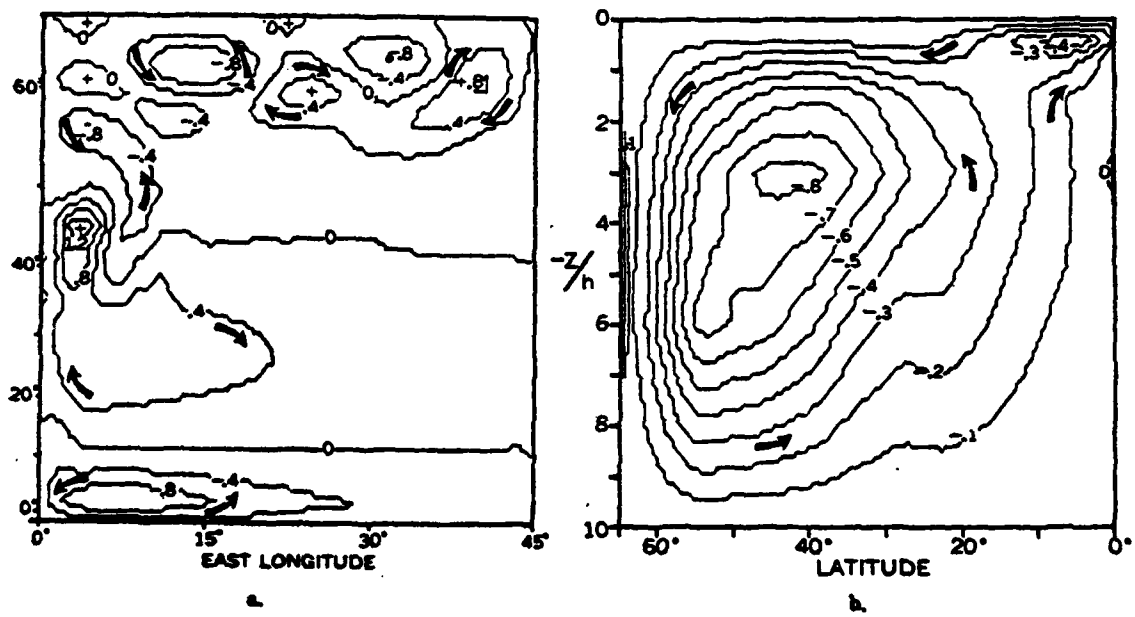

Figure 2.2. Total mass transport integrated in the vertical (a) and longitudinal (b) directions by Bryan and Cox (1968)

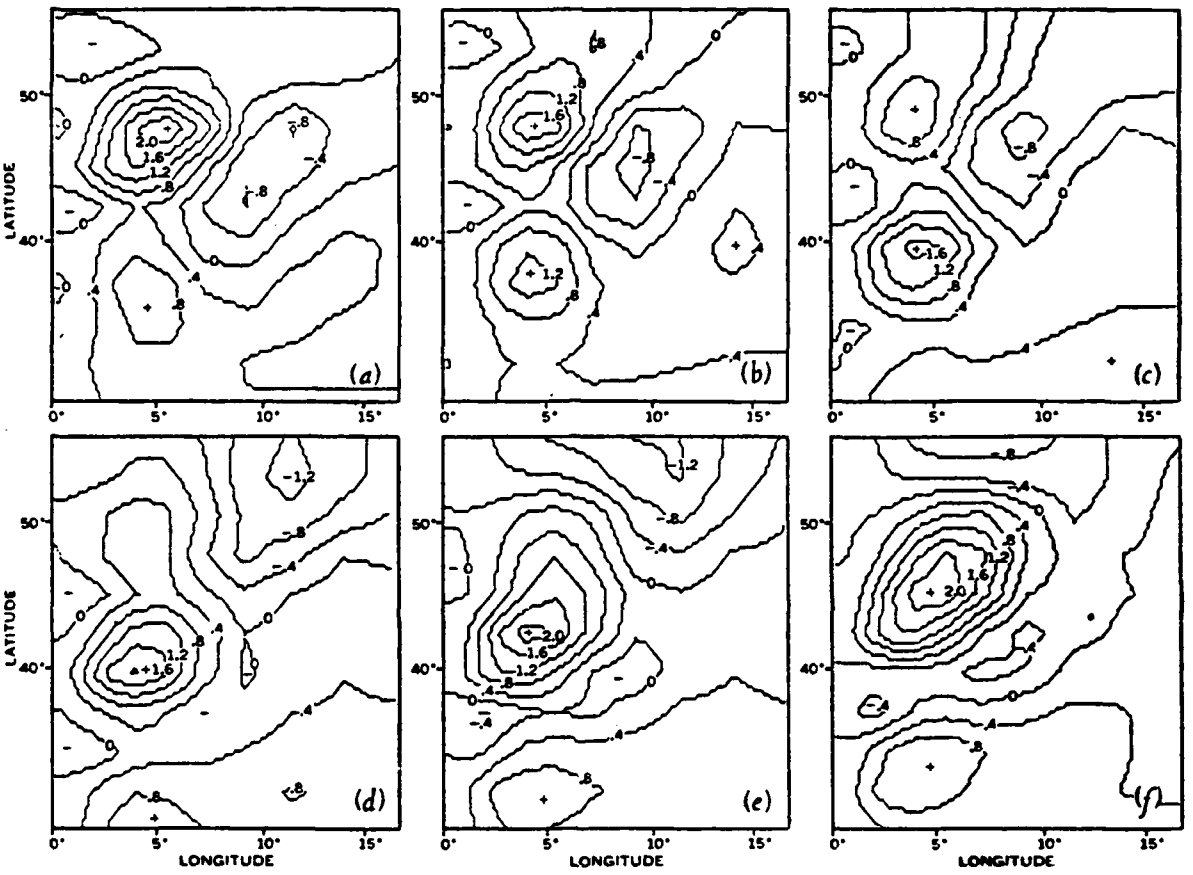

Figure 2.3. Mass transport as a function of time showing the growth and movement of disturbances in the western boundary current region. Plots are roughly two model months apart (Bryan and Cox, 1968)

Haney (1974) developed a similar model for a basin stretching from 51°S to 49°N. Table 2-2 shows the increased exchange coefficient values used in this model. Wind stress was asymmetrical about the equator; surface heat flux was expressed as

$$Q_S = Q_2 (T_A^* - T_S)$$

where T_S is the temperature of the uppermost ocean level, T_A^* is an atmospheric equilibrium temperature (defined by Haney), and Q_2 is a coupling coefficient. Forms of and Q_2 appear in Fig. 2-4.

Haney's results are similar to those of Bryan and Cox. His vertically integrated mass transport streamfunction field is reproduced in Fig. 2-5. Both hemispheres showed strong westward intensification and the strong equatorial transport was once again present. The failure of the model to produce transient motions separating from the western boundary flow is important, because it shows that the grid spacing (2.5° in latitude, 3° in longitude) and exchange coefficient values were not small enough to allow generation of the eddies, even though the size of the eddies seen in the Bryan and Cox results (roughly 5°) could have been resolved once they were produced.

2.3.2 Bottom Topography Effects

The two models referred to above dealt only with the effects of wind stress and density stratification in flat-bottom basins. Several additional model studies addressed the influence of variable bottom topography.

(a)

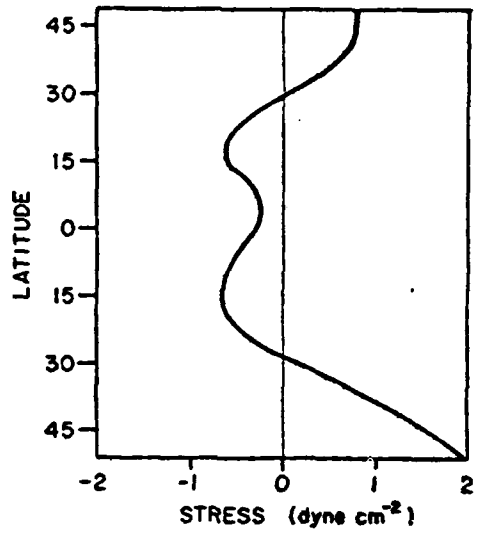

(b)

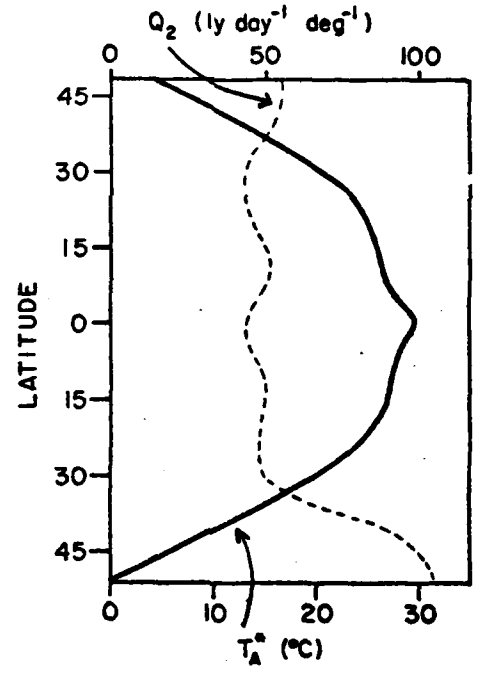

Figure 2.4. Mean zonal wind stress (a) and heat flux parameters (b) specified as surface boundary conditions by Haney (1974)

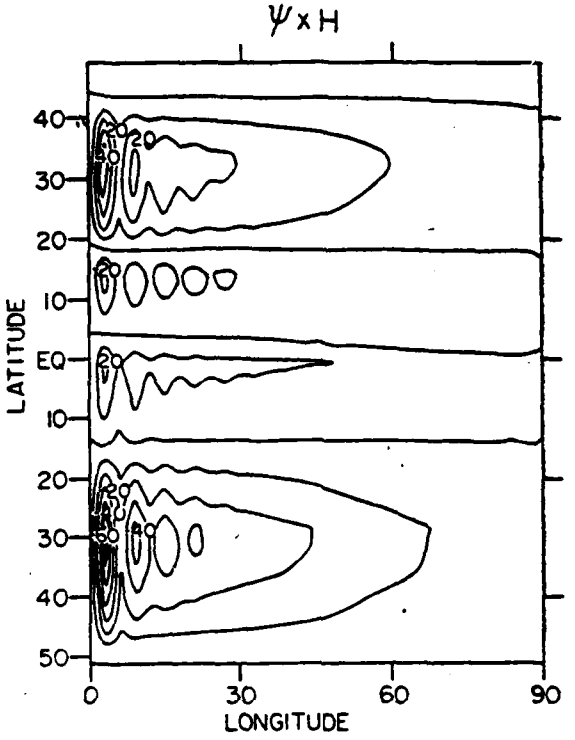

Figure 2.5. Vertically integrated transport streamfunctions predicted at the end of the second integration phase by Haney (1974)

Holland (1973) modeled a rectangular basin with a continental shelf/slope structure along the western boundary. His results indicated that bottom torques associated with the slope played a major factor in steering the resulting flow. Vertically integrated mass transport for three different simulations are shown in Fig. 2-6. The intensification brought on by the combination of baroclinicity and variable depth is quite striking.

The success with which idealized models such as those mentioned above reproduce many of the known features of large-scale ocean circulation (westward intensification, eastward equatorial flow, separation of eddies, etc.) lends credibility to studies which seek to apply these models to the circulation of realistic basins.

2.4 GLOBAL MODELS

The ultimate utility of large-scale circulation models is to describe the entire world ocean system and, even further, the coupled world atmosphere-ocean system. The development of increasingly larger and faster computers has made modeling on a global scale feasible.

2.4.1 World Ocean Models

Cox (1975) reported preliminary results obtained with a model of the world ocean system utilizing the Bryan and Cox model. The grid, which is characterized by 2° spacing, extended to 69° north and south. The grid system actually consisted of three grids: a large grid covering

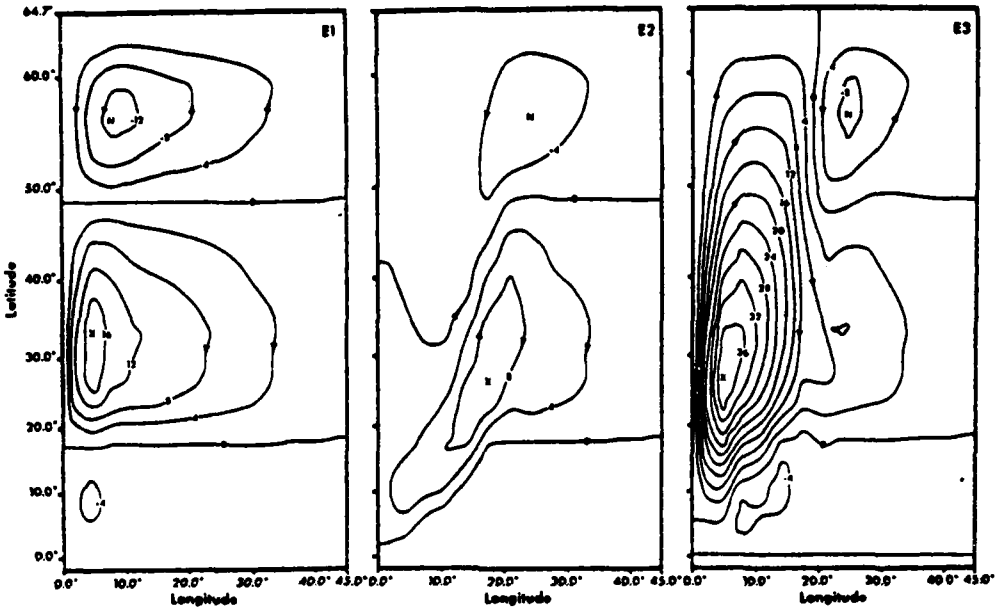

Figure 2.6 Vertically integrated mass transport streamfunctions predicted by Holland (1973) for three cases: (a) baroclinic, constant depth ocean; (b) homogeneous, variable depth ocean; and (c) baroclinic, variable depth ocean

the region from 62°S to 62°N with origin at the equator, and two smaller spherical grids, one for each polar region, with axes running through the appropriate pole. All three grids overlapped considerably to simplify splicing them together. Realistic bottom topography was employed.

The lateral boundary conditions called for no-slip and no-flux at closed walls. At the surface, temperature, salinity, and wind stress were specified.

Cox ran three experiments. In all three, the ocean was initially at rest. In the first case, the ocean was specified as isothermal and isohaline and maintained that way throughout the run. In the second, the ocean took on mean temperature and salinity fields as determined from NODC records and were held constant. In the third, the mean temperature and salinity fields were once again imposed as initial conditions, but this time were allowed to vary with the current field. The horizontal mass transport stream functions predicted for Case III are shown in Fig. 2-7. Because of the long time period required to obtain equilibrium between the vertical advection and diffusion of heat, this experiment could not be run to steady state. The flows produced by the model agreed well with observations, although the transport magnitudes were not necessarily realistic.

In the barotropic case, Case I, flow tended to follow isobaths, and circulation gyres were relatively weak. Addition of baroclinicity (Case II) reduced the steering effect due to bottom topography, but intensified the circulation gyres, as well as the Antarctic Circumpolar Current.

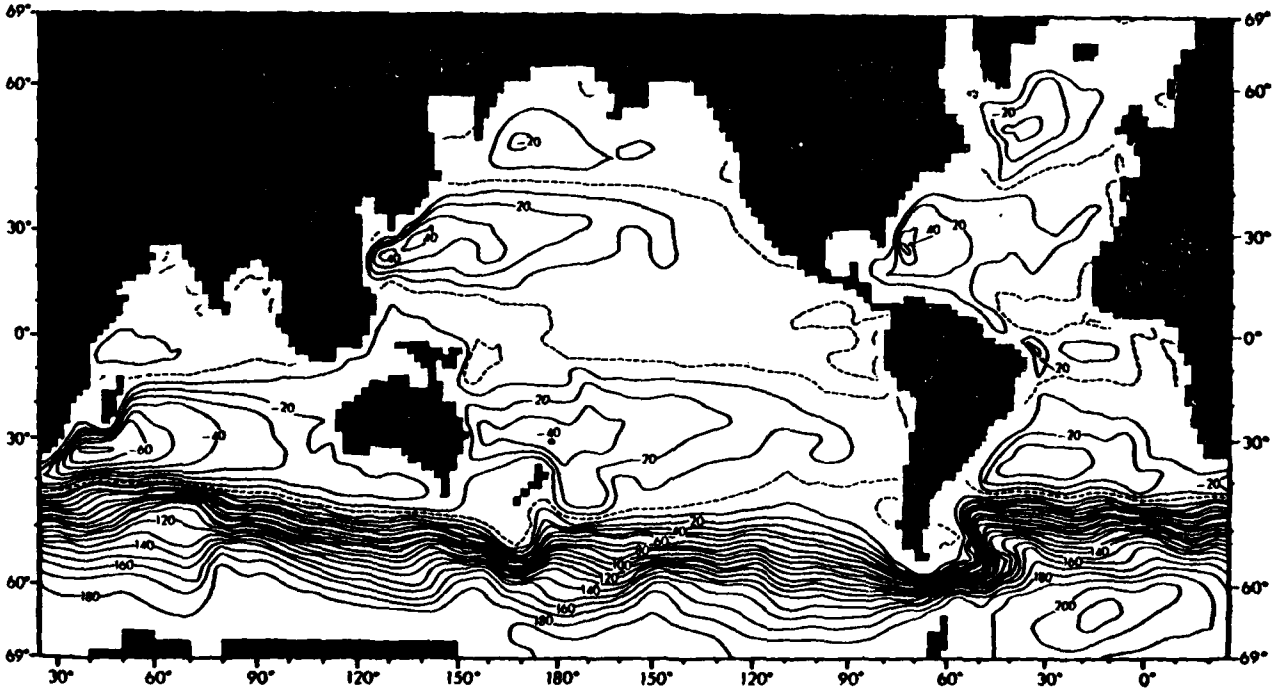

Figure 2.7. Vertically integrated transport streamfunctions predicted for Case III of the world ocean model (Cox, 1975)

The increased organization and coherence in the Northern Hemisphere gyres for Case III, in which the density field was allowed to adjust along with the flow field, could be due to the inability of the model to resolve eddy motion effects which should be present in the real data field.

2.4.2 Coupled Ocean-Atmosphere Models

Coupling of large-scale ocean and atmosphere models is a logical application for ocean circulation models since the two fluids are so inextricably dependent upon one another. One such coupled model is being developed at GFDL. Manabe et. al. (1975) describe the atmospheric circulation, while Bryan et. al. (1975) discuss the oceanic circulation. The oceanic model takes the approach used by Bryan and Cox in previous studies. The main difference lies in the fact that the surface momentum, heat, and salt fluxes are supplied by the atmospheric portion of the model, rather than imposed externally.

Results obtained with this model have been encouraging, although only general agreement with prevailing ideas on ocean circulation has been obtained thus far. Continued research using higher resolution models should improve results for both the atmosphere and the ocean.

2.5 REGIONAL CIRCULATION MODELS

2.5.1 Arctic Ocean

The Arctic Ocean and the Greenland Sea strongly influence the rest of the world ocean. The Greenland Sea is the source of much of the cold bottom water which plays a

strong role in the North Atlantic thermohaline circulation. The sea ice formed in the Arctic Ocean is a major factor in the Northern Hemisphere atmospheric heat budget. Semtner (1976) used the Bryan and Cox model, with salinity included, to study the circulation in these basins. Approximations to the realistic basin configurations and bottom topography were specified.

Because of the sparseness of data, initial and boundary conditions had to be pieced together from various sources. Conditions of no-slip and no-flux were specified at closed boundaries (side walls and bottom). Fixed temperature and salinity fields along open boundaries were taken from observed data, and velocities were calculated from observed densities and mass transports.

Surface wind stresses were derived from long-term mean atmospheric pressure fields over the area using two assumptions: (a) the long-term wind field is essentially geostrophic, and (b) the long-term wind stress on the sea ice is transmitted directly to the underlying water.

The surface heat flux was also taken from long-term averages. A constant loss of 64 kcal/cm^2 yr was assumed, except in areas where surface temperature dropped below -2^{o}C and, presumably, sea ice covered the region. Then the heat flux was reduced to roughly 2% of its ice-free value.

The surface flux of salt was specified over most of the area to reflect an excess of precipitation over evaporation equal to 20 cm/yr rain. Fresh water runoff from the eight major rivers feeding the Arctic basin was included in the appropriate locations.

Three tests were run, corresponding to high (Case I), medium (Case II), and low (Case III) wind stress magnitudes. Simulation periods for the cases varied from 107 years to 36 years. Only Case I (107 years) included the Greenland Sea. Verification of the model predictions was necessarily limited because of the sparse data base available. Qualitative agreement with observations seemed good, however. The integrated transport stream functions in Fig. 2-8 show the two-gyre system observed in this area.

Fine tuning of the exchange coefficients presented a major problem with this model. The A_M and A_H values had to be high to suppress numerical instabilities. But this led to a situation where, depending on the wind stress magnitude, either the current fields were reasonable and the density fields weren't, or the current fields were underestimated and the density fields were realistic. Semtner indicated that higher resolution (already at 1^o spacing) in the horizontal would alleviate this problem, but such a modification would greatly increase computer costs.

2.5.2 Indian Ocean

The Indian Ocean presents an interesting problem for study because of the seasonal variability of the Somali Current in response to the monsoon cycle. Cox (1970) applied the Bryan-Cox forumlation (with salinity added) to this region.

The model started with horizontally uniform temperature and salinity fields. Temperature, salinity, and wind stress were specified at the surface as functions of

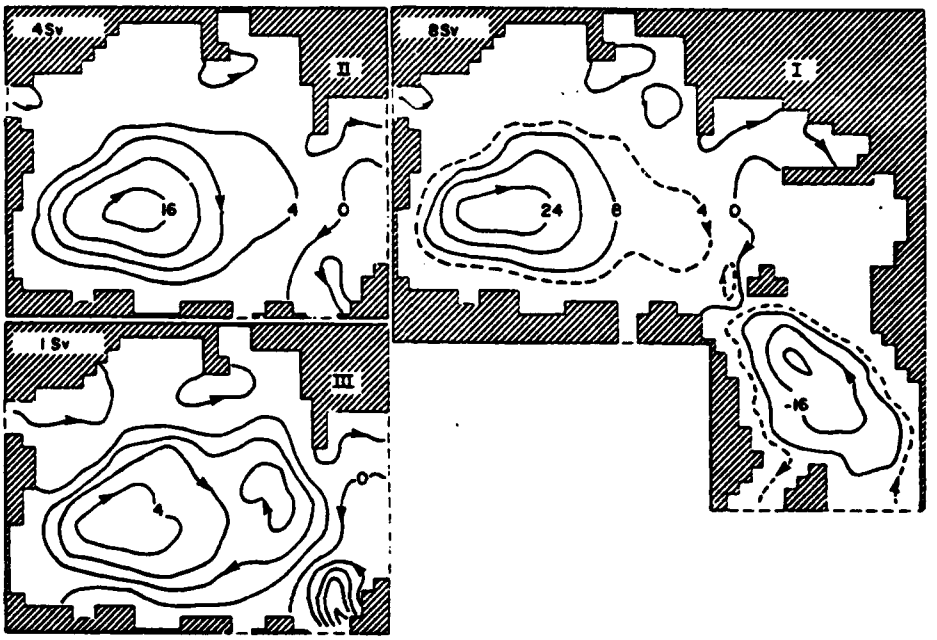

Figure 2.8. Vertically integrated transport streamfunctions predicted for the Arctic Ocean by Semtner (1976) Case numbers are explained in the text.

position and time using seasonal mean data. Temperature and salinity at open boundaries were derived from observations and total transport across the boundaries was set to zero. The simulation spanned 192 years in three stages, with grid spacing being successively reduced from 4° to 2° to 1°.

Once again, the results agreed well qualitatively with limited observations. As Figure 2-9 illustrates, the Somali current oscillated between a strong northerly flow during the southwest monsoon and a weak southerly flow during the northwest monsoon. The phase lag between wind reversal and current reversal agreed well with observations also. This success shows the ability of this type of model to deal with forcing functions with time scales of months rather than years. However, certain discrepancies, such as uniformly overestimated thermocline depths and underestimated Somali Current transport show the need for fine tuning of mixing coefficients if operationally useful large-scale models are to be developed.

2.5.3 North Atlantic Ocean

Friedrich (1970) described a model of the North Atlantic based on the Bryan and Cox approach. His formulation of the equations predicted vorticity, temperture, salinity, and velocity variations from mean values

Conditions of no-slip and no-flux were specified at closed boundaries, while temperature, salinity, vorticity flux and momentum flux were specified at open boundaries. Temperature, salinity, vorticity, and velocities were held fixed in the vertical at the grid point corresponding to the Straits of Gibraltar to simulate the influx of Mediterranean

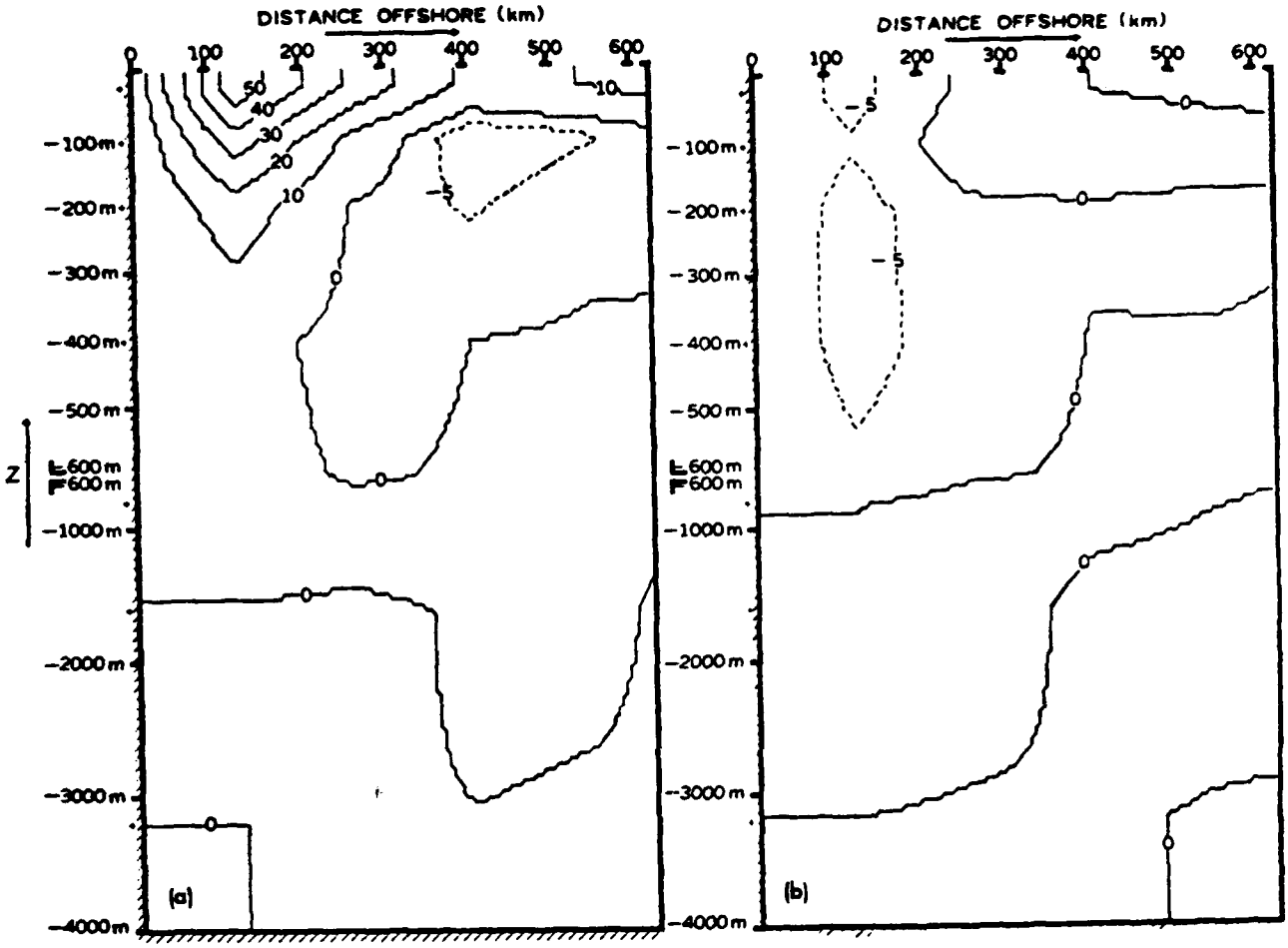

Figure 2.9. Longshore velocity component predicted by Cox (1971) for the Indian Ocean for (a) southwest monsoon and (b) northwest monsoon

water into the Atlantic. Surface wind stresses were those prescribed by Haney (1974). The surface temperature and salinity fields were prescribed by determining mean winter and summer values at each point and allowing for a sinusoidal oscillation between these extremes through the course of the year.

The model was applied in three phases:

An 80-year spinup using 5^{o} grid spacing, a 70-year continuation using 3^{o} grid spacing, to take the model to near-equilibrium and a second continuation using 1^{o} grid spacing. Results from this last phase were not reported, and only some portions of the results from the second phase were discussed.

The predicted time-varying temperature and salinity fields agreed reasonably well with observations, and the transport stream functions reproduced many of the large-scale features of the Atlantic circulation. The combination of course grid spacing and high horizontal mixing coefficients probably prevented more accurate simulations.

2.6 DIAGNOSTIC MODELS

All of the studies we have looked at up to now have employed fully predictive models. This type of model has been used almost exclusively for large- and mesoscale studies, in preference to diagnostic models. Two of the reasons for this preference are: (1) diagnostic models require comprehensive data sets from which to build the density field to drive the models, and (2) predictive models

provide information about the variability of potential energy, which is essential for an understanding of the energetics of ocean circulation.

Soviet modelers have devoted a considerable amount of effort to developing diagnostic models. Sarkisyan and Keonjiyan (1975) and Sarkisyan (1977) present detailed summaries of this approach. The fundamental question addressed by diagnostic models is: given a specific three-dimensional density structure in the ocean and specified wind stress or sea-level pressure fields at the surface, what can be said about the flow velocity? Numerous studies using this technique have arrived at the same conclusions about the relative importance of wind stress, bottom topography, baroclinicity, etc., as have resulted from predictive models. Diagnostic models are able to predict believable mean flow regimes as long as the prescribed density field is free from serious errors. This last factor, of course, represents a major stumbling block in application of these models.

2.7 LARGE-SCALE ANOMALY MODELS

Another intriguing application of circulation models is the study of large-scale (> 1000 km) and long period (> months) variations in the mean flow of basins. Considerable work in the North Pacific has been done by Huang (1978, 1979). He is using a model based on Haney's (1974) work to study the role of seasonally varying atmospheric forcing in the transient behavior of the ocean. The model was first spun up over 60 years using mean atmospheric fields of air temperature, vapor pressure, sea level pressure, cloud cover, and wind speed. The resulting heat fluxes and wind stresses derive from bulk aerodynamic and

climatological formulas. Once a quasi-equilibrium flow was attained, the model, using a finer horizontal grid mesh, was driven by seasonally varying atmospheric fields.

Results to date have been preliminary, but encouraging. Despite the lack of varying bottom topography, the major time-dependent features of the North Pacific circulation have been reproduced; predicted transports fall within the ranges of observations (see Figure 2-10), as do sea surface temperatures below the subarctic region (see Figure 2-11). The lack of adequate treatment of mixed layer dynamics leads to poorly predicted subsurface thermal structure. But, in general, results predicted by this model show great potential for examining long-term variability in the mean flow.

This study is important because it is one of the first attempts to model the large-scale response to time varying forcing. Research in this area should begin to bridge the gap between the large-sale and small-scale motions of the ocean.

2.8 EDDY-RESOLVING MODELS

Eddy resolving models address explicitly the influence of factors such as eddies and fronts which usually have length scales below the resolution of large-scale models and are normally treated parametrically. Recently, efforts have been taken to study the generation of eddies and their relationship to the mean flow.

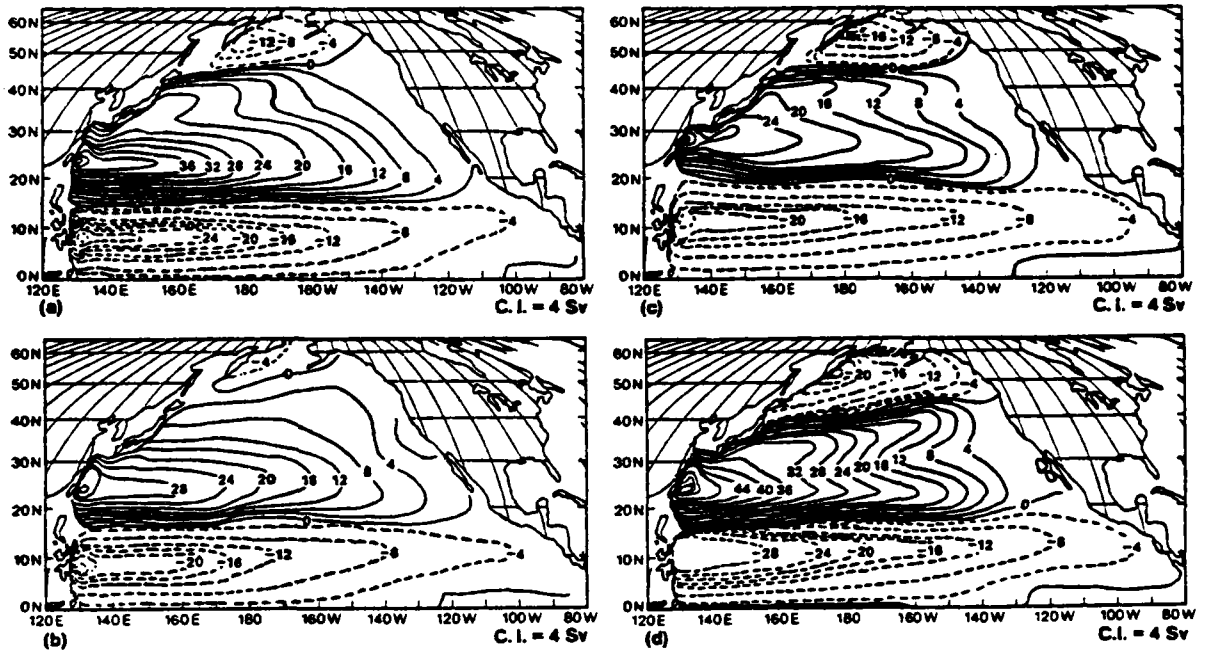

Figure 2-10. Seasonal variation of vertically integrated transport predicted by Huang (1979) for (a) spring, (b) summer, (c) fall, and (d) winter

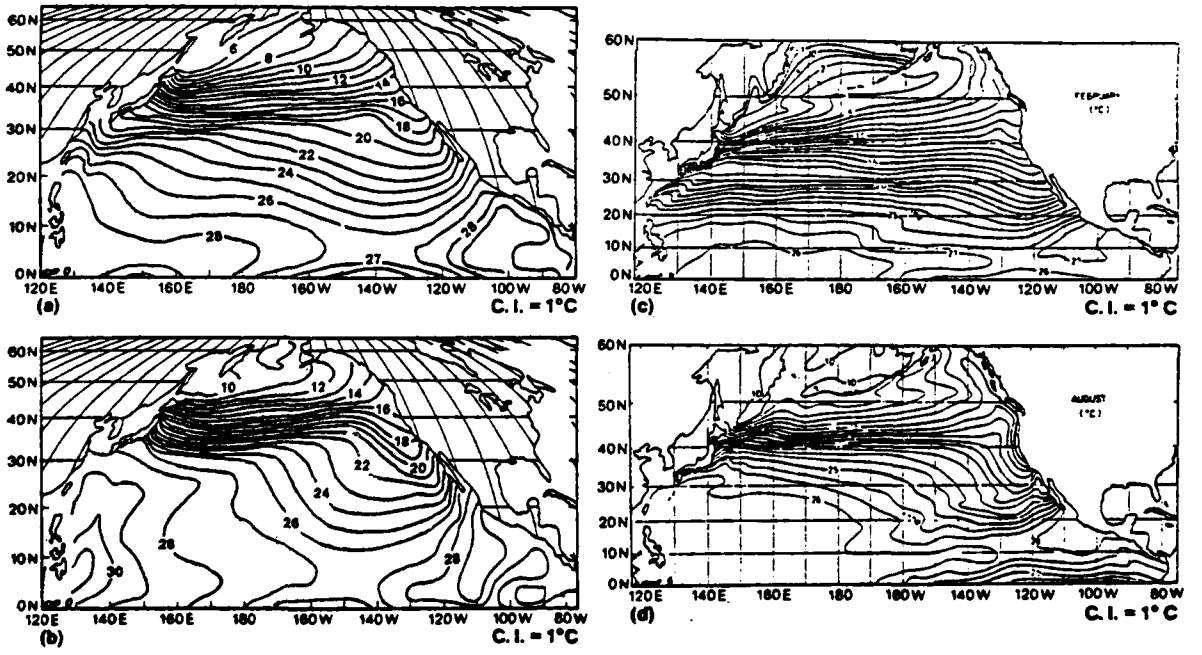

Figure 2-11. Comparison of simulated and observed sea surface temperatures for (a) simulated February, (b) simulated August, (c) observed February, and (d) observed August (Huang, 1979)

Holland and Lin (1975a, b) described a two-layer, rectangular, flat-bottomed basin study with fine enough grid spacing to resolve eddies. The model treats only the momentum and continuity equations of the form

$$\partial_t \underline{\Lambda}_i + \underline{\upsilon}_i \cdot \nabla \underline{\Lambda}_i + \underline{k} \times f \underline{\Lambda}_i = -h_i \nabla P_i + A h_i \nabla^2 \underline{\upsilon}_i + \underline{\tau}_i \quad (i = 1,2) \tag{2.6}$$

$$\underline{\Lambda}_i = \underline{\upsilon}_i h_i \tag{2.7}$$

$$\underline{\tau}_1 = (\tau_s^x, 0) \tag{2.8}$$

$$\underline{\tau}_2 = (0, 0) \tag{2.9}$$

$$h_1 + h_2 = H_o \tag{2.10}$$

$$\nabla p_2 = \nabla p_1 + g' \nabla h_2 \tag{2.11}$$

where H_o is the total basin depth, g' is the reduced gravity $g \Delta \rho / \rho_o$, $\Delta \rho$ is the density difference between the two layers, and the subscript i refers to the layer (i = 1 for upper, i = 2 for lower). The x-directed stress component, τ_s^x, varied only with latitude. The horizontal exchange coefficient, A, did not attempt to parameterize eddy-induced mixing because of the fine model resolution (20 km grid spacing) and thus took on values one or two orders of magnitude smaller than those used in earlier models.

The results of a large number of parametric studies indicated several conclusions:

- the model produces eddies with diameters of 220 km and periods of 64 days when the resolution is fine and viscosity is small enough. Figure 2-12 illustrates the eddy motions produced;

- the eddies are generated by baroclinic instabilities;

- once the eddies have reached a statistically steady state, Reynolds stresses act to slow the motion of the upper layer mean flow and drive the lower layer mean flow;

- the eddies are important to the mean flow because they produce regions of both positive viscosity, in which energy from the mean flow is transferred to the eddies, and negative viscosity, in which energy is transferred from the eddies to the mean flow. This fact opens up speculation on a strong role played by eddies in maintaining mean circulation.

Semtner and Mintz (1977) performed a study of Gulf Stream eddies using (2.1) - (2.5), without salinity. Their model, which used a grid spacing of 37 km, employed a bottom topography which roughly approximates that of the Gulf Stream area. The basin started at rest with a simple, horizontally uniform temperature stratification. A steady wind stess distribution and heat flux parameter distribution as formulated by Haney (1974) were imposed at the surface.

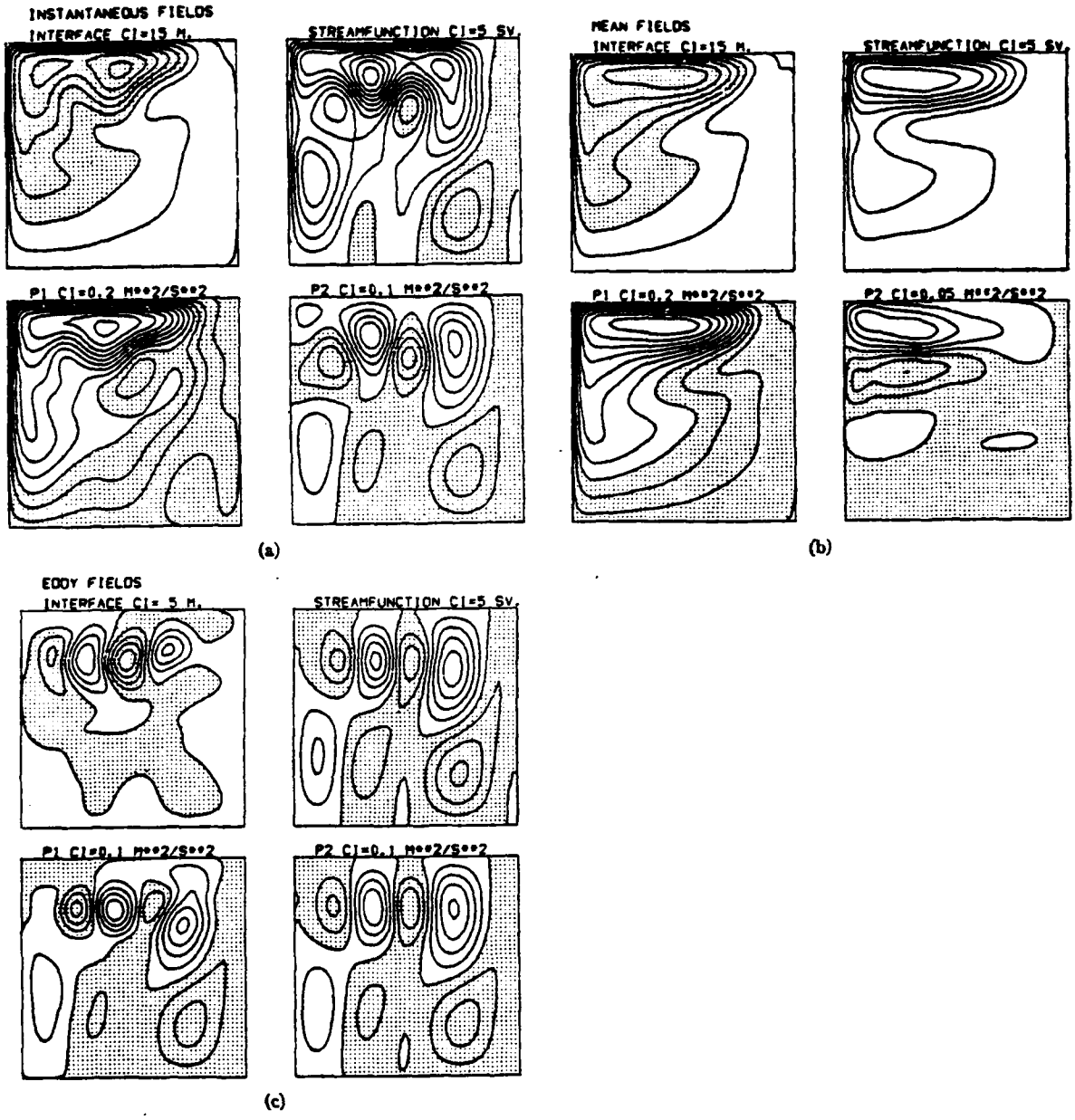

Figure 2.12. Predictions from eddy-resolving model of Holland and Lin (1975a). CI = contour interval. (a) Instantaneous fields at day 2160 of interface depth (shaded area indicates depth below static position), streamfunction, upper layer pressure (P1), and lower layer pressure (P2); (b) mean fields averaged over 320 days once model has reached steady state; (c) eddy fields on day 2160

A rigid surface, no flow or heat flux through the bottom boundary, quadratic bottom stress ($\tau_b \propto [u^2 + v^2]$), free-slip on the lateral boundaries, and no heat flux through lateral boundaries were specified.

After a 15-year spin-up, with a 75 km spacing grid, two experiments were performed on a 34 km grid. The first used reduced values of A_M and A_H. The second called for replacing the lateral mixing terms so that

$$A_m \nabla^2 \underline{v} \text{ becomes } - B_m \nabla^4 \underline{v}$$

and

$$A_h \nabla^2 T \text{ becomes } - B_h \nabla^4 T.$$

The first experiment, which started where the spin-up run left off, showed weak mesoscale eddies developing south of the Gulf Stream. The second experiment, which used the final state of the first experiment as its initial condition, produced strong mesoscale eddies. The Gulf Stream jet, which corresponds to the dashed line of zero height, is strong and quasi-steady. To the south of the jet, weak eddies form and move westward. Figure 2-13 shows surface heights in the late stages of the second experiment. The Gulf Stream jet now contains noticeable meanders and eddy activity is more prevalent than in the Laplacian experiment.

The two forms of the horizontal eddy exchange terms produce the same levels of damping of short length scale effects (two grid spaces and less), but the first form also damps longer scale factors somewhat, while the second form does so to a much lesser extent. The result is that

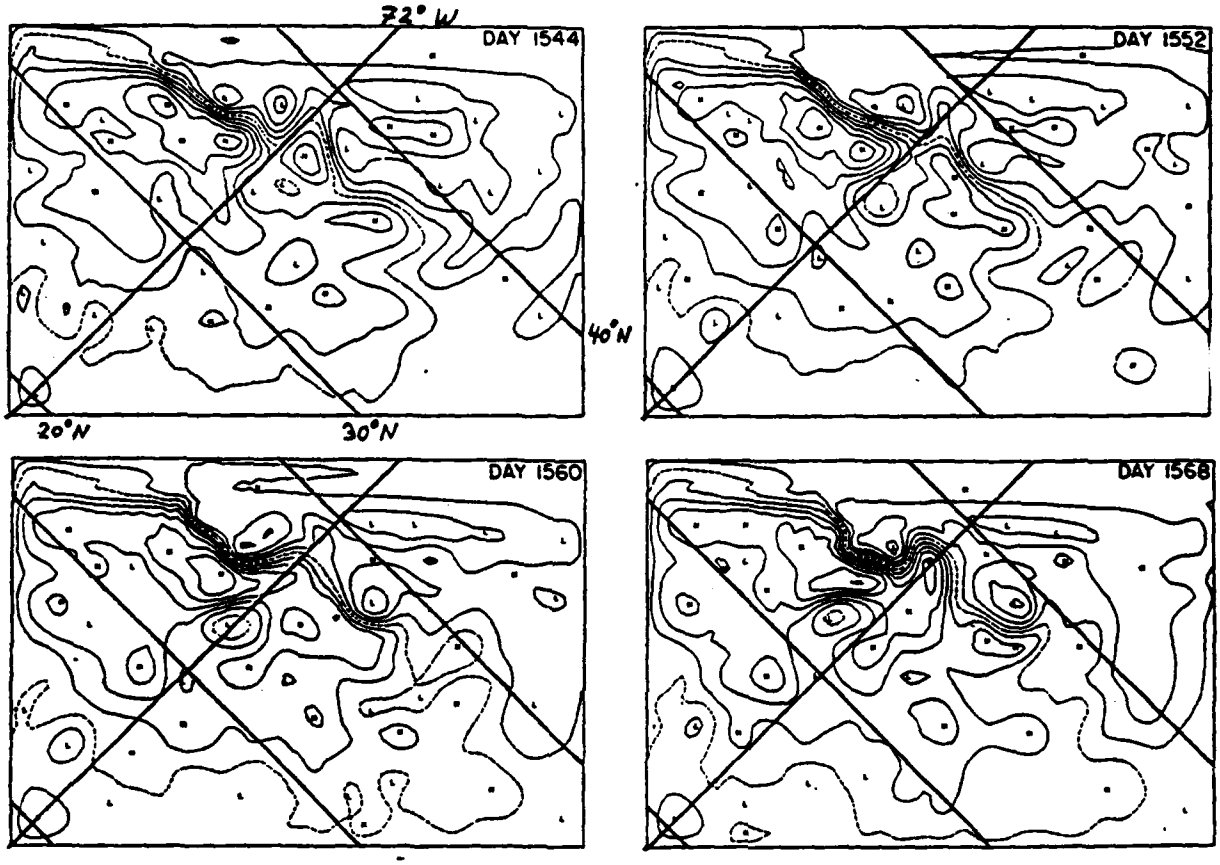

Figure 2.13. Surface elevations predicted by Semtner and Mintz (1977) at 8-day intervals in the second experiment. Dashed lines indicated rough direction of flow

the second experiment produced results which conform more closely to observations than do those predicted by the first experiment.

2.9 APPLICATION OF LARGE-SCALE MODELS TO SMALL-SCALE PROBLEMS

The models discussed in this review have been applied to problems with long length and time scales. Problems of operational interest, however, depend on processes with much shorter characterizing scales. Are these models of any use in addressing smaller scale problems? The answer seems to be "yes, but..."

The large scale circulation models could, in theory, be refined to simulate processes with scale lengths down to centimeters. The equations have no minimum scale length (at least not above the molecular scale). But such refinement would require prohibitively large amounts of computer storage. In addition, the amount of data needed to specify the surface boundary conditions would be equally prohibitive. A third consideration is that the scales of motion which drive the mean circulation are not necessarily the same scales which directly drive small scale effects such as mixed layers, seasonal thermocline, internal waves, etc. Since more suitable models exist for the smaller scale phenomena, direct application of the large models would be unnecessarily complicated and cumbersome.

The applicability of these models can be expressed in terms of the influence of the quasi-steady circulation on small scale problems. The influences are twofold: active and passive.

The mean flows exert an active influence in that in some sense they provide the conditions under which smaller scale phenomena (eddies, seasonal thermoclines, internal waves, etc.) are generated. Even if such features are directly generated by anomalies from the mean flow, the anomalies must derive their energy at least in part from the steady flow.

The mean flows exert a passive influence in that they provide the environment within which the small scale features, once generated, either propagate or dissipate.

Large-scale models, then, can be useful in two ways. They can be used to characterize the background environment against which processes that effect operational requirements evolve. They can also be used to study the transfer of energy from oceanic scales to mesoscales and, in conjunction with other modelling efforts, down to the small scales. If we define the background environment as the mean flow with long term (order of months and years) variations superimposed, then circulation modellers such as Huang (1978, 1979) are beginning to address this problem. This direction of study could lead to greatly improved descriptions and possibly predictions of ocean behaviour in areas of interest. The hemispheric mixed-layer model system under development by NORDA for FNWC (Clancy, 1979) is an example of such an attempt to combine large-scale atmospheric information to predict ocean behavior at localized areas.

The second aspect of applications is being addressed at the present time. The eddy resolving models are providing tremendous amounts of new information about the

role of eddies in the overall circulation. Related studies (Harrison, 1978) are pointing to deficiencies in the ways sub-grid scale motions are parameterized and suggesting more accurate approaches.

General circulation models cannot, by themselves, address small scale processes efficiently. They can, however, act as an interface to mesoscale and finer scale models which could eventually lead to greater understanding of the processes which shape the state of the ocean.

References

Blandford, R., 1971: Boundary Conditions in Homogeneous Ocean Models, Deep-Sea Research, 18, 738-751.

Bryan, K., 1963: A Numerical Investigation of a Nonlinear Model of a Wind-Driven Ocean, J. Atmos. Sci., 20, 594-606.

_____ and Cox, M.D., 1968a: A Nonlinear Model of an Ocean Driven by Wind and Differential Heating: Part I. Description of the Three-Dimensional Velocity and Density Fields, J. Atmos. Sci., 25, 945-967.

_____ and _____, 1968a: A Nonlinear Model of an Ocean Driven by Wind and Differential Heating: Part II. An Analysis of the Heat, Vorticity, and Energy Balance, J. Atmos. Sci., 25, 968-978.

_____, Manabe, S., and Pacanowski, R.C., 1975: A Global Ocean-Atmosphere Climate Model: Part II. The Oceanic Circulation, J. Atmos. Sci., 5, 30-46.

Clancy, R.M., 1979: The NORDA Hemispheric Mixed-Layer Model System (HMLMS): A Functional Description, NORDA Tech. Note 45, April 1979.

Cox, M.D., 1970: A Mathematical Model of the Indian Ocean, Deep-Sea Research, 17, 45-75.

_____, 1975: A Baroclinic Numerical Model of the World Ocean: Preliminary Results, in Numerical Models of Ocean Circulation, National Academy of Sciences, Washington, D.C., 107-120.

Friedrich, H.J., 1970: Preliminary Results from a Numerical Multilayer Model for the Circulation in the North Atlantic, Deutsche Hydrographische Zeitschrift,23, 145-164.

Haney, R.L., 1974: A Numerical Model of the Response of an Idealized Ocean to a Large Surface Heat and Momentum Flux, J. Atmos. Sci., 4, 145-167.

Harrison, D.E., 1978: On the Diffusion Parameterization of Mesoscale Eddy Effects from a Numerical Ocean Experiment, J. Atmos. Sci., 8, 913-918.

Holland, W.R., 1973: Baroclinic and Topographic Influences on the Transport in Western Boundary Currents, Geophys. Fluid Dyn., 4, 187-210.

_____ and Lin, L.B., 1975a: On the Generation of Mesoscale Eddies and Their Contribution to the Oceanic General Circulation: I. A Preliminary Numerical Experiment, J. Phys. Oceanogr., 5, 642-657.

_____ and _____, 1975b: On the Generation of Mesoscale Eddies and Their Contribution to the Oceanic General Circulation: II. A Parameter Study, J. Phys. Oceanogr., 5, 658-669.

Huang, J.C.K., 1978: Numerical Simulation Studies of Oceanic Anomalies in the North Pacific Basin: I. The Ocean Model and the Long-Term Mean State, J. Phys. Oceanogr., 8, 755-778.

_____, 1979: Numerical Simulation Studies of Oceanic Anom-Alies in the North Pacific Basin: II. Seasonally Varying Motions and Structures, J. Phys. Oceanogr., 9, 37-56.

Manabe, S., Bryan, K., and Spelman, M.J., 1975: A Global Ocean-Atmosphere Climate Model. Part I. The Atmospheric Circulation, J. Phys. Oceanogr., 5, 3-29.

Sarkisyan, A.S., 1977: The Diagnostic Calculations of a Large-Scale Oceanic Circulation, in The Sea, Vol. 6, Goldberg, McCave, O'Brien, and Steele, ed., Wiley Interscience, 363-458.

_____ and Keonjiyan, 1975: Review of Numerical Ocean Circulation Models Using the Observed Density Field, in Numerical Models of Ocean Circulation, National Academy of Science, Washington, D.C., 76-93.

Semtner, A.J., Jr., 1976: Numerical Simulation of the Arctic Ocean Circulation, J. Phys. Oceanogr., 6, 409-425.

_____ and Mintz, Y., 1977: Numerical Simulation of the Gulf Stream and Mid-Ocean Eddies, J. Phys. Oceanogr., 7, 208-230.

References (Continued)

Veronis, G., 1966a: Wind-Driven Ocean Circulation: Part I. Linear Theory and Perturbation Analysis, Deep-Sea Research, 13, 17-29.

_____, 1966b: Wind-Driven Ocean Circulation: Part II. Numerical Solutions of the Nonlinear Problem, Deep-Sea Research, 13, 31-55.

Section 3
MODELS OF OCEANIC FRONTS

Section 3
MODELS OF OCEANIC FRONTS

3.1 INTRODUCTION

The term "Oceanic Front," in analogy to atmospheric fronts, describes regions containing horizontal variations of temperature, salinity, density, and sound speed which are large compared to the horizontal distance over which they occur. The horizontal extents of the gradient zones range from tens of meters in the case of estuarine and river plume fronts to tens of kilometers in the case of the large frontal systems in the open ocean; lateral extents vary from a few hundred meters to nearly basin-scale (thousands of kilometers); and time duration scales vary from hours to permanent. Fronts do not usually result from two distinct water masses butting up against one another and forming a vertical interface, but rather from two masses intruding into each other and forming a sloping interface as the lighter spreads out above the heavier. The expression of a front at depth may be offset a considerable horizontal distance from the surface expression.

The large open-ocean fronts are probably generated by the combined effects of differential heating and wind stress convergence due to long term (i.e., seasonal and longer) atmospheric conditions. Fronts on slightly smaller scales (such as those found along the boundaries of the Gulf Stream and the Kuroshio current) are less directly influenced by atmospheric forcing than by variations in the mean

flow. At a still smaller scale, fronts can be found along the perimeter of warm and cold rings and in regions of strong upwelling (or downwelling). Fronts can also be related to tidal mixing in shallow water have relatively short scales, although these effects are of limited importance in the open ocean. Some of the smallest scale fronts occur in areas where strong river outflow impinges on ocean water with markedly different characteristics. Considerable observational effort has been expended on these flows.

An exhaustive study of all types of fronts is beyond the intent and scope of this report. Many types of fronts have little open-ocean importance. We will restrict our attention to large and mesoscale fronts, with passing reference to river plume fronts. These latter are useful for study because much of the frontal modelling effort has centered on these scales, and because many of the techniques applied to river plume models are now being used to address large scale frontal activity.

The best way to convey a sense of the variety of situations to which the name "oceanic front" applies is to describe specific fronts. The next section (3.2) will discuss in some detail frontal structures in the North Pacific and the North Atlantic. The following section (3.3) will describe several analytical and numerical models of fronts and their applications.

3.2 SPECIFIC EXAMPLES OF OCEANIC FRONTS

3.2.1 North Pacific Ocean Fronts

Five large-scale semi-permanent frontal zones occur in the North Pacific. These are outlined in Figure 3-1, taken from a paper by Roden (1975). A sixth feature - an equatorial front in the eastern Pacific (Pak and Zaneveld, 1974) - will not be included in this discussion.

The Kuroshio front (see Figure 3.2) exhibits strong gradients of temperature (T), salinity (S), density (σ_t) and sound speed (C_s). These fronts occur along the interface between the warm, saline water of the Kuroshio and the cold, fresh water to the northeast of the current. The position of the frontal zone varies as the Kuroshio meanders.

The Oyashio frontal zone, formed by fingers of cold, fresh water carried southward into the Kuroshio water, contains multiple small-scale fronts (see Figure 3.3). Once again, gradients of T, S, and C_s are strong, but density gradients are roughly 25% as strong as those seen in the Kuroshio. Apparently the density increase from east to west due to decreasing temperature is offset by a decrease due to decreasing salinity. The result is a front in which baroclinic flows are quite weak (Roden, 1975).

The subarctic front (Figure 3.4) is strongly influenced by wind-driven convergence (Roden, 1975 and 1977). The upper 100 m of the front reveals relatively small (compared to the Kuroshio front) σ_t gradients, but moderate gradients sloping to the south below 100 m. The

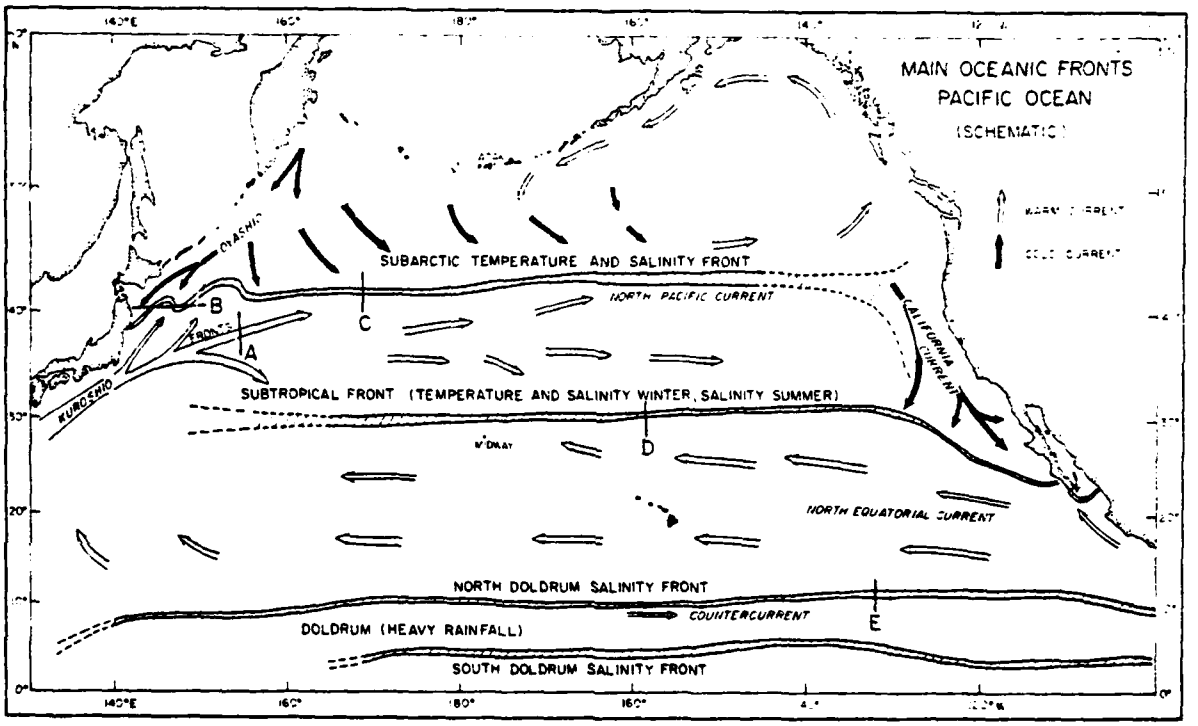

Figure 3.1. Schematic map of main north Pacific fronts. (Roden, 1975). Arrows indicate prevailing current directions.

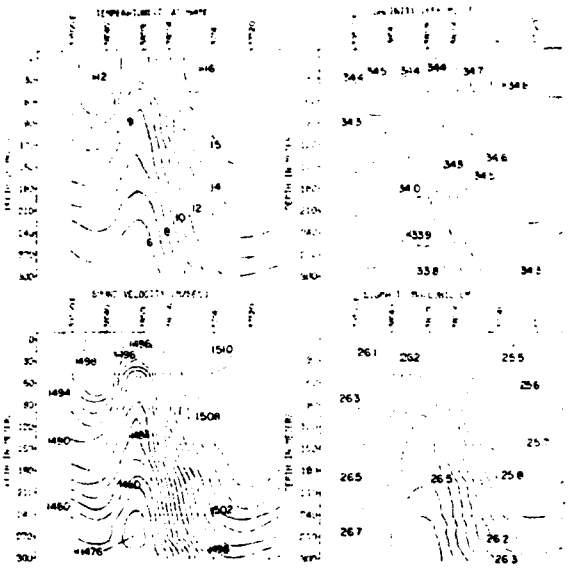

Figure 3.2. T, S, C_s and σ_t sections across the Kuroshio Front at Longitude 154°E. The sections correspond to Line A in Figure 3-1. The stations were occupied on 24 April 1971 (Roden, 1975).

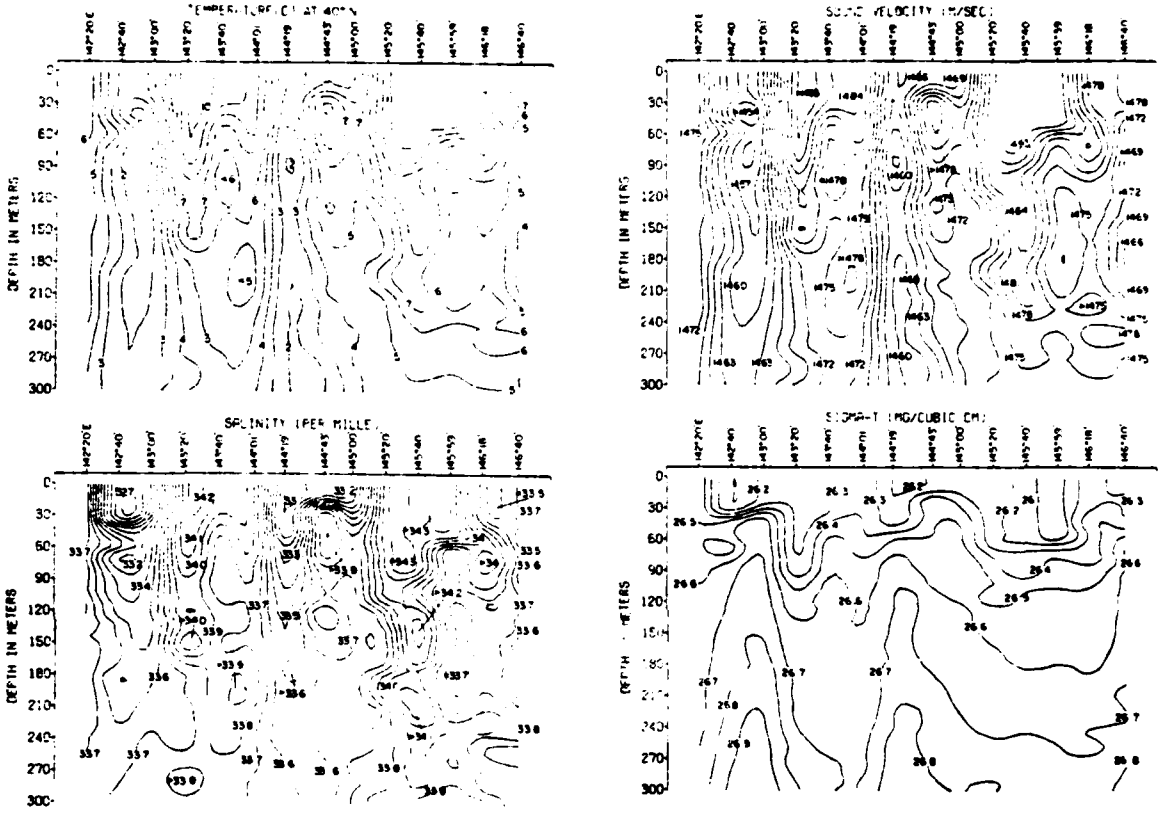

Figure 3.3. T, S, C_S and σ_t sections across the Oyashio Fronts at Latitude 40°N. The sections correspond to Line B in Figure 3-1. The stations were occupied on 28-29 April 1971 (Roden, 1975).

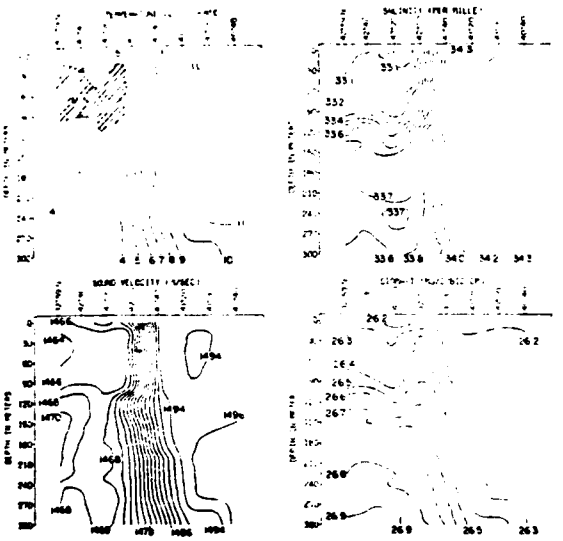

Figure 3.4. T, S, C_S and σ_t sections across the subarctic front at Longitude 168°E. The sections correspond to Line C in Figure 3-1. The stations were occupied on 3-4 April 1971 (Roden, 1975).

result is that the strongest surface baroclinic flows occur roughly 50 km south of the thermohaline front.

The subtropical frontal zone (Figure 3.5) is strongly effected by meteorological forcing, and occurs in regions of net convergence of surface wind stress and heat flux. The intensity of the frontal zone is seasonal (Roden, 1974; White et. al., 1978). During periods of strong winds (winter and spring) the frontal zone can separate into shallow and deep zones as Ekman transport causes the upper layer to drift northward. Roden (1974) points out that this zone is essentially a salinity front in summer and fall (due to radiative heating) and a thermohaline front in winter and spring.

The doldrum fronts (Figure 3.6) are influenced by wind stress and surface heat flux convergence, are marked by shallow S and σ_t gradients, but small T and C_s gradients. The strongest baroclinic flows occur roughly 180 km southward of the surface density front.

Table 3-1 (Roden, 1975) summarizes the characteristics of the five frontal zones. Note that the gradients are taken over a horizontal scale of 60 km.

3.2.2 North Atlantic Ocean Fronts

The frontal zones in the North Atlantic have not been studied in as systematic a fashion as those of the North Pacific. Little information is available to indicate the presence of fronts with the extreme length scales of some of the North Pacific fronts. The fronts discussed here occur mostly in the western boundary flows of the basin, and

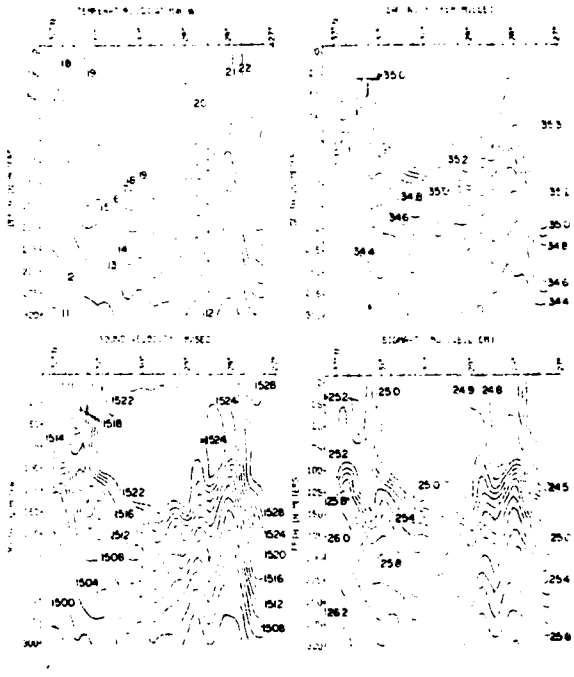

Figure 3.5. T, S, C_S and σ_t sections across the subtropical front at Longitude 158°W. The sections correspond to Line D in Figure 3-1. The stations were occupied on 25-27 January 1975 (Roden, 1975).

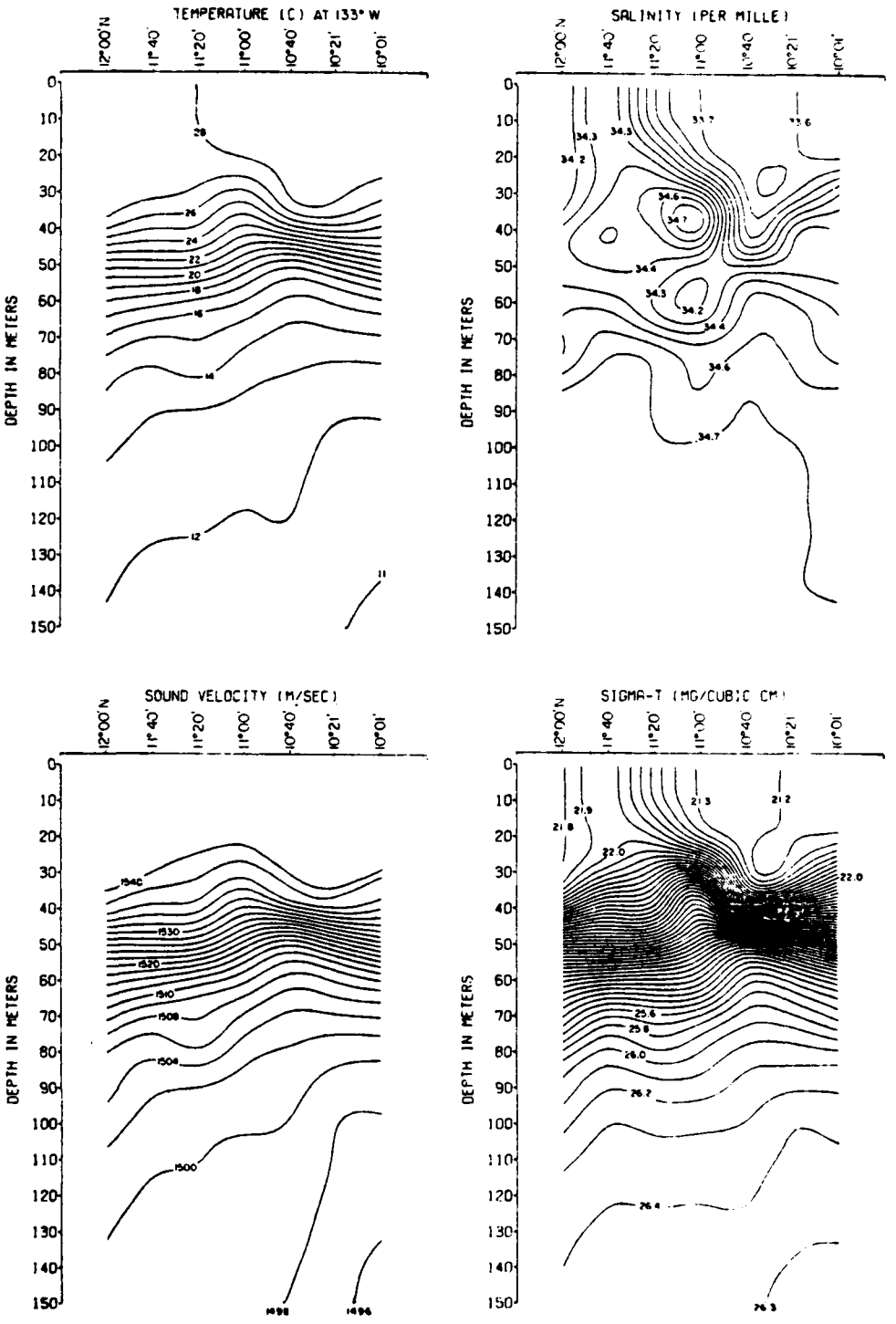

Figure 3-6. T, S, C_s and σ_t sections across the doldrum front at Longitude 133°W. The sections correspond to Line E in Figure 3-1. The stations were occupied on 18-19 October 1972 (Roden, 1975).

Table 3-1

Characteristics of North-Pacific Fronts, based on horizontal sampling at 30 km intervals. (Roden, 1975)

Characteristic*	Kuroshio	Oyashio	Subarctic	Subtropical	Doldrum
∇T(°C/60 km)	6	9	8	4	1
∇S(‰/60 km)	0.6	1.5	1.2	0.5	1.0
∇C_s(m/s/60 km)	24	39	28	12	1
$\nabla \sigma_t$(Kg/m^3/60 km)	0.8	0.2	0.2	0.8	0.7
Baroclinic Current (M/S)	0.6	0.2	0.4	0.5	0.5
Baroclinic Shear (S^{-1})	2×10^{-5}	8×10^{-6}	7×10^{-6}	10^{-5}	2×10^{-5}

* maximum observed values

in the Northeast Atlantic, where much of the data is concentrated, Figure 3.7 shows the approximate locations of major North Atlantic fronts.

The best known frontal zones in the North Atlantic occur in conjunction with the Gulf Stream. The slope front indicated in Figure 3.7 arises along the interface between the warm water in the Gulf Stream and the colder water on the continental slopes of the United States and Canada. Figures 3.8 and 3.9 show the marked temperature and salinity gradients in a cross-section through the slope front on a north-south line along a meridian which passes through Georges Bank.

Another type of Gulf Stream-related front is formed by the gradients across the perimeters of warm and cold rings which break off from Gulf Stream meanders. Figure 3.10 (Fenner, 1978) shows contours of sound speed along a line from the interior of a warm ring (position M) lying northwest of the Gulf Stream, through the surrounding slope water, and into the North wall of the Gulf Stream (position CH26). The front at the edge of the ring is indicated by the rising isopleths at a distance of 60 - 80 km from position M.

A thermal frontal zone to the southeast of the Gulf Stream has been observed (Voorhis and Hersey, 1964). This area is usually referred to as the Sargasso front or subtropical convergence zone. Legeckis (1978) presented satellite IR images showing the meandering nature of the front. Beckerle (1972) suggested that the motion of the front could be influenced by westward propagating Rossby waves.

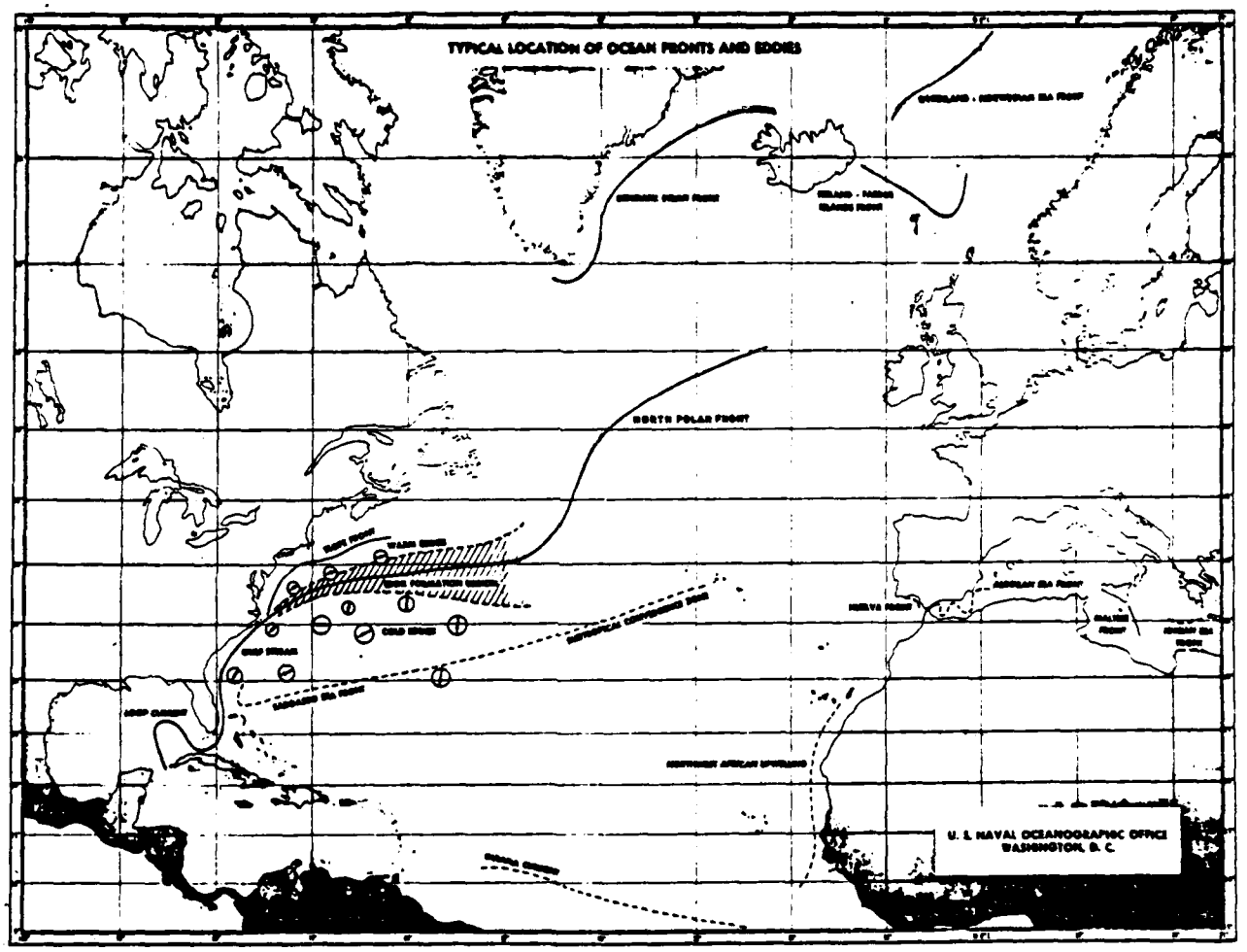

Figure 3.7. Schematic map of major ocean fronts in the North Atlantic

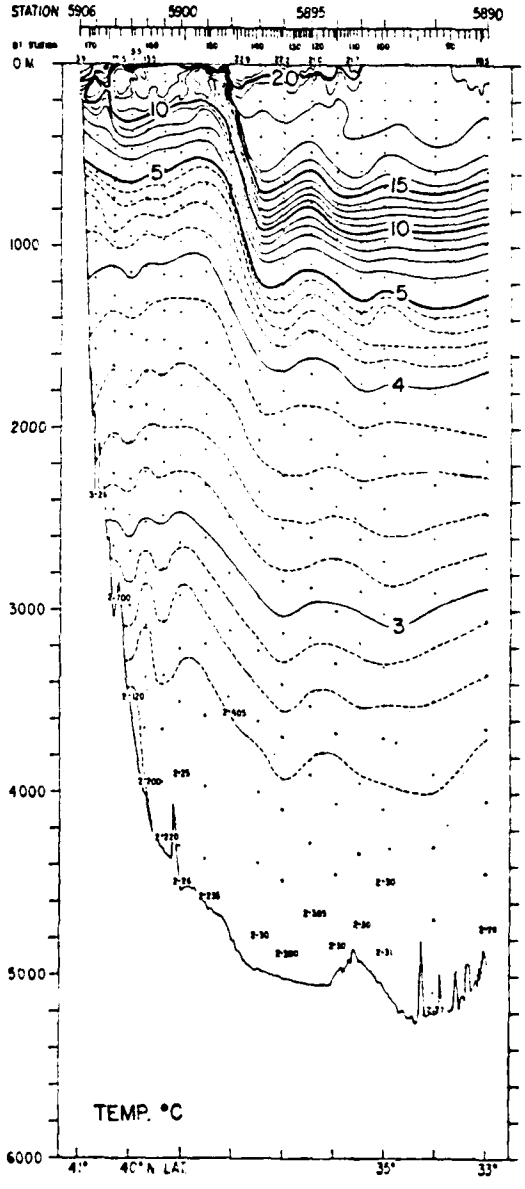

SECTION II, 66° 30′ W. Long.

Figure 3.8. Temperature section across the Gulf Stream along Longitude 66°30'W (Fuglister, 1963).

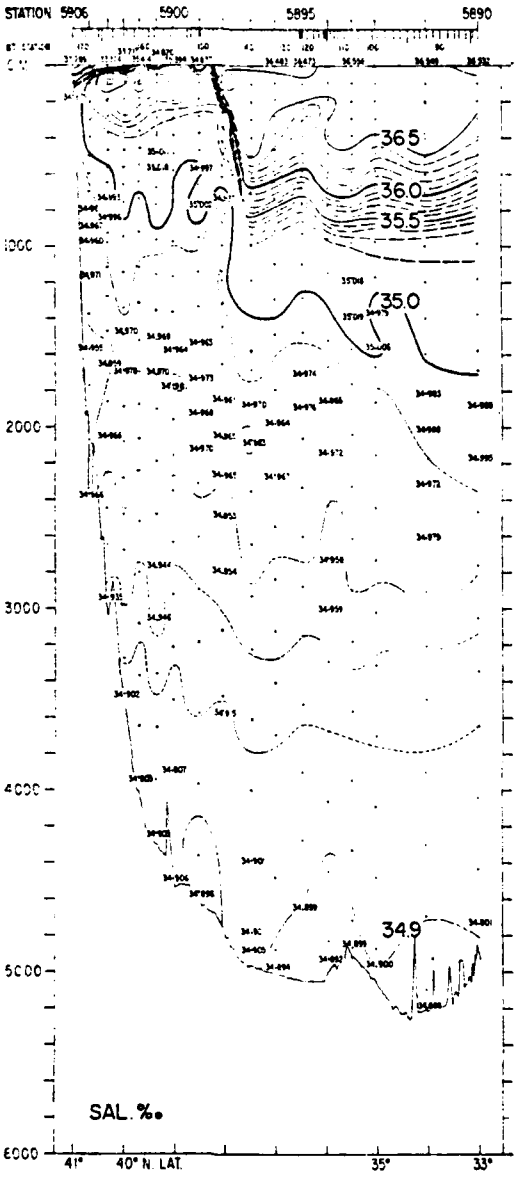

Figure 3.9. Salinity sectiion corresponding to T-section in Figure 3.8 (Fuglister, 1963).

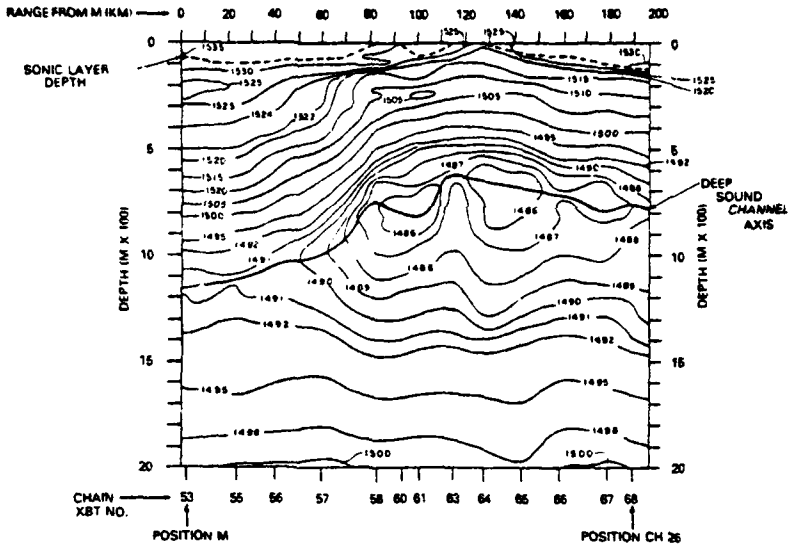

Figure 3.10. C_S section extending from warm ring north of Gulf Stream (position M) through slope water and into north wall of Stream (position CH26). Stations were occupied 9-10 November 1975 (Fenner, 1978).

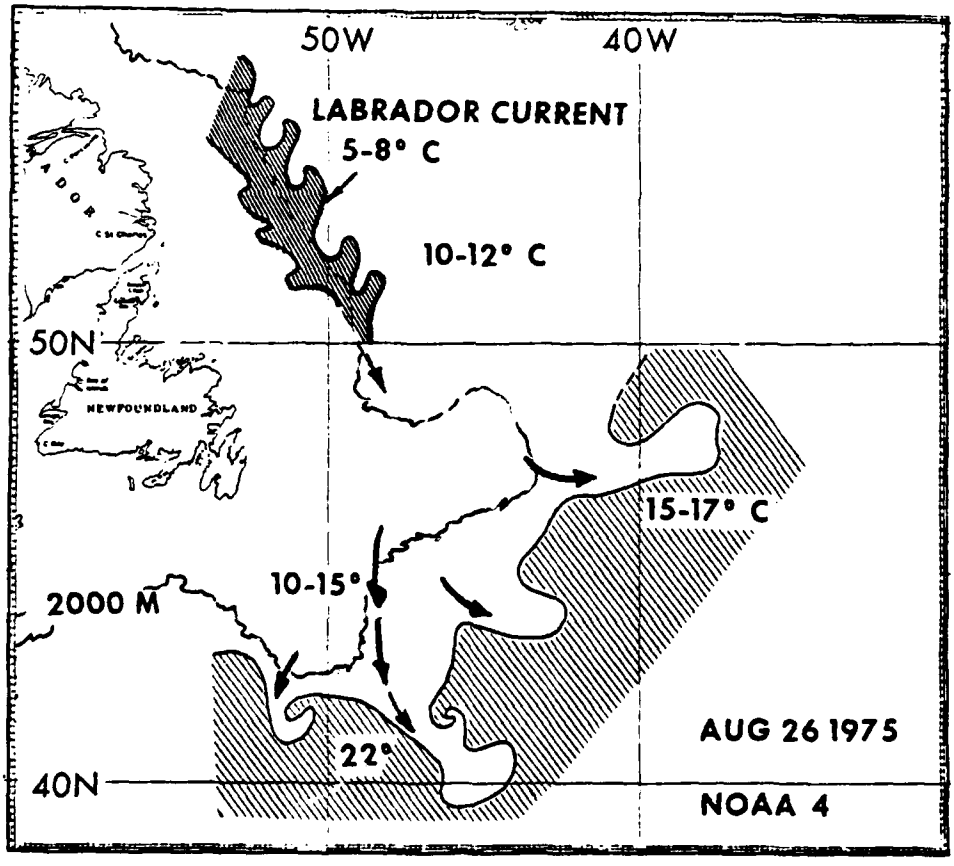

Figure 3.11. Sea surface temperature boundaries of the Labrador current and the North Atlantic Polar Front on 26 August 1975 as interpreted from VHRR images. Arrows indicate cold water filaments entrained in eddies at the front. SST values have not been corrected for atmospheric effects (Legeckis, 1978).

Legeckis (1978) in his satellite-based survey of thermal fronts described several fronts which have been observed in the Atlantic north of the Gulf Stream. Figure 3·11 shows the position and shape of the front formed by the confluence of cold Labrador Current water with the Gulf Stream. Smaller fronts occur to the north off the south coast of Greenland and the east coast of Newfoundland. These fronts, marked by sea surface temperature gradients of roughly 3°C/10 km, may be related to the extent of ice coverage in winter and spring. Legeckis also referred to a thermal front southeast of Iceland.

In general, oceanic fronts in the North Atlantic, with the exception of fronts associated with the Gulf Stream, have not been studied as systematically as those of the North Pacific. Satellite Very High Resolution Radiometer (VHRR) sea surface temperature measurements have revealed the presence of several thermal fronts, but persistent cloud cover in many areas, variable temperature gradient intensities, and lack of continuous coverage in some areas have precluded acquisition of reliable information about the positions, variability and persistence of most of them.

3.3 MODELS OF FRONTS

The purpose of the preceeding descriptions of frontal zones has not been to provide an exhaustive survey of frontal zones, but to provide examples of the variety of open-ocean structures to which the term front is applied. This diversity is perhaps a good indicator of the difficulties involved in developing generalized front models. As we shall see in Section 3.3, the existing numerical front models are hydrodynamic models which address only density fronts. Fronts which exhibit only temperature and/or salinity gradients have not yet been modelled numerically.

Garvine (1979a) separates frontal dynamics into four categories:

- frontogenesis (formation) and frontolysis (dissipation)
- hydrography and circulation of established fronts
- interaction with wave fields
- high-frequency turbulence generated in the frontal zones.

To date, the little modelling that has been reported has focussed on the first two categories.

3.3.1 A Frontogenesis Model

In the course of his study of North Pacific fronts, Roden (1977) suggested a set of equations which might describe the balance of thermohaline forces which lead to the formation and variability of oceanic fronts. The equations* for the local time change of the horizontal mean temperature and salinity gradients are expressed as

$$\partial_t|\nabla\bar{\theta}| = -(\partial_n\bar{V}_{n\theta})|\nabla\bar{\theta}| - \bar{V}_{n\theta}\partial_n|\nabla\bar{\theta}| - \partial_n\left(\frac{1}{\rho C_{vs}}\partial_z\bar{q}_z\right)$$

$$-\partial_n\left(\frac{1}{\bar{\rho}\,\overline{C_{vs}}}\partial_z\overline{\rho C_{vs}}\langle w'\theta'\rangle\right) - \partial_n\left(\bar{w}\partial_z\bar{\theta}\right) \qquad (3.1)$$

and

$$\partial_t|\nabla S| = -\left(\partial_n\bar{V}_{ns}\right)|\nabla\bar{S}| - \bar{V}_{ns}\partial_n|\nabla\bar{S}| - \partial_n\left(\frac{10^{-3}}{\rho}\partial_z\bar{r}_z\right)$$

$$-\partial_n\left(\frac{1}{\bar{\rho}}\partial_z\,\rho\,\langle w's'\rangle\right) - \partial_n\left(\bar{w}\partial_z\bar{S}\right) \qquad (3.2)$$

---

* Notation for this model is explained in Table 3-2

TABLE 3-2

Notation for Roden (1975) Front Equations:

θ	-	potential temperature (^{o}K)
S	-	salinity
$V_{n,\theta}$ and $V_{n,s}$	-	velocity components normal (in the direction of increasing values) to the temperature (θ) and salinity (s) fronts
ρ	-	density
C_{vs}	-	specific heat of sea water at constant volume and salinity
w	-	vertical velocity (positive upward)
q_z	-	vertical component of radiative heat flux (positive upward)
r_z	-	vertical components of nonturbulent salt flux (positive upward)

where the overbars indicate mean values and the primes indicate instantaneous fluctuations. The terms on the right hand sides of (3.1) and (3.2) describe, in sequence. the following effects:

- the velocity convergence in an established frontal zone,
- the advection of gradients into a zone,
- non-turbulent fluxes of heat and salt,
- turbulent fluxes of heat and salt, and
- the vertical advection of temperature and salinity.

Roden (1975) examined the frontal systems of the North Pacific in light of (3.1) and (3.2) to determine the relative magnitudes of the forces leading to frontal generation and maintenance. Vertical advection was not considered His data are presented in Table 3-3. These data indicate the dominance of the velocity convergence (and, by implication, the wind stress curl) in frontal formation in most areas. The subtropical frontal zone, and to a lesser extent the doldrum front zone, relies on a balance between wind stress and radiative heating/salinity flux.

TABLE 3-3

Estimated magnitudes of terms in (3.1) and (3.2) from Roden (1975). The second terms on the right hand sides of the equations vanish because the gradients at the front are assumed to have maximum values. Magnitudes are normalized by 1×10^{-12} units.

Terms	Kuroshio	Subarctic	Subtropical	Doldrum
Temperature Fronts				
$-\partial_n \bar{V}_{n\theta} \lvert \nabla \bar{\theta} \rvert$	120	60	30	10
$-\partial_n \left(\frac{1}{\bar{\rho} \bar{C}_{vs}} \partial_z \bar{q}_z \right)$	6	6	10	-10
$-\partial_n \left(\frac{1}{\bar{\rho} \bar{C}_{vs}} \partial_z \bar{\rho} C_{vs} \langle w' \theta' \rangle \right)$	-2	-2	-5	7
$\partial_t \lvert \nabla \theta \rvert$*	124	64	35	7
Salinity Fronts				
$-\partial_n \bar{V}_{ns} \lvert \nabla \bar{S} \rvert$	2	1	0.5	1
$-\partial_n \left(\frac{10^{-3}}{c} \partial_z \bar{r}_z \right)$	0.1	0.1	0.1	0.2
$-\partial_n \left(\frac{1}{\bar{\rho}} \partial_z \rho \langle w' s' \rangle \right)$	0.1	0.1	0.2	0.3
$\partial_t \lvert \nabla \bar{S} \rvert$*	2.2	1.2	0.8	1.5

*Sum of terms above.

Although his work has provided much information about frontal regions, Roden has not tried to actually model frontal behavior, but instead has used his equations as a predictive tool.

3.3.2 A Steady State Model

Garvine (1974, 1979a, 1979b) reported on a series of studies of small-scale, steady state oceanic fronts. His early work (1974) consisted of a two-dimensional hydrodynamic model of a shallow, small-scale front developed in a non-rotating ocean by the advection of a shallow pool of light water into a heavier water mass at rest. This situation is similar to the river plume front reported by Garvine and Monk (1974).

Garvine's later studies (1979a,b) extended the model to include two-dimensional velocities and basin rotation. Thus the extended model is more suitable for discussion in this review.

The configuration of this model is shown in Figure 3.12. Terms in the figure are defined in the caption. The model is cast in a coordinate system which moves with the front, so that the +x direction is normal to the front and into the light water pool and the +y direction is parallel to the front. The basic model assumptions are:

- the motion and density distributions near the front are quasi-steady in time;

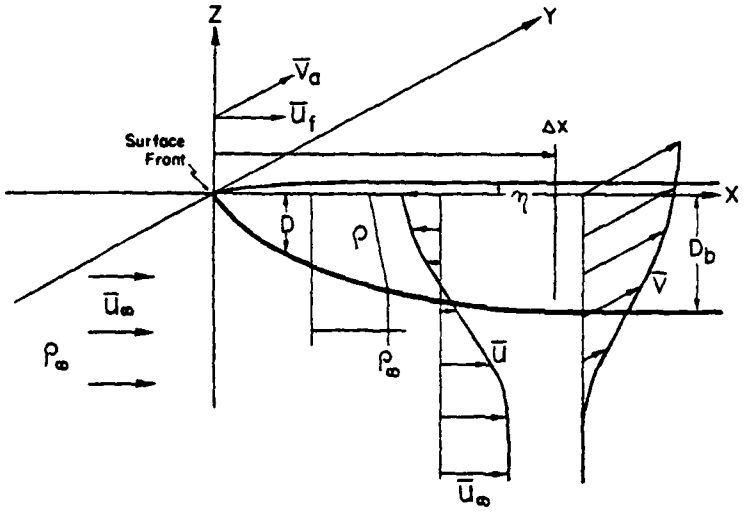

Figure 3.12. Schematic Diagram of Garvine (1979a, b) model parameters are:

ρ_∞ - density of ambient pool

$\bar{u}_\infty$ - horizontal velocity of ambient pool

D_b - depth of light water pool upstream

$D(x)$ - depth of light pool near front

$\rho(z)$ - density of light pool near front

η - surface height anomaly of light pool

Δx - length scale of front

$\bar{v}$ - along-front velocity in light pool

V_A - along-front velocity

U_F - horizontal velocity at surface front

- the velocity field is locally two-dimensional in that the length scale for variations along the front is much larger than that normal to the front. The velocity components U_F and V_A are not functions of y;

- the ambient water density is uniform, and $|\rho_\infty - \rho|$ is small;

- the vertical momentum balance is hydrostatic;

- the Coriolis parameter, f, can be held constant over the length scale of the model;

- surface wind stress and atmospheric pressure are uniform;

- D_b is much smaller than the total water depth;

- a balance exists between Coriolis acceleration, pressure gradient, and wind stresses; and

- the Boussinesq approximation applies.

If u, v, and w represent the velocity components in the model coordinate system, and we define

$$U = \int_{-D}^{0} u\,dz$$

$$V = \int_{-D}^{0} v\,dz$$

$$M_{xx} = \int_{-D}^{0} u^2\,dz$$

$$M_{xy} = \int_{-D}^{0} uv\,dz,$$

then the vertically integrated model equations can be expressed as

$$d_x U = w_i + u_i \partial_x D = q_e \tag{3.3}$$

$$d_x M_{xx} - q_e u_i - fV = -\gamma g k^{-1} \partial_x (rD^2) + \rho_\infty^{-1}(\tau_{wx} + \tau_{ix}) + \nu_h d_{xx} U \tag{3.4}$$

$$d_x M_{xy} - q_e v_i + fU - f u_\alpha D = -\gamma g k^{-1} \partial_y (rD^2) + \rho_\infty^{-1}(\tau_{wy} + \tau iy) + \nu_h d_{xx} V \quad . \tag{3.5}$$

In these equations, $r=\Delta\rho_s/\Delta\rho_m$ (where $\Delta\rho_s$ is the surface density anomaly ($\rho_\infty-\rho_s$) and $\Delta\rho_m$ is the maximum density anomaly ($\rho_\infty-\rho_m$ in parent pool)) and $\gamma = \Delta\rho_m/2\rho_\infty$, k is a constant characterizing the specified vertical density profile, the subscript i denotes values at the density interface between the parent pool and the ambient pool, τ_w is the surface wind stress, τ_i is the interfacial shear stress, and q_e is the entrainment velocity across the density interface. We denote

$$q_e = E\, q_\tau \tag{3.6}$$

and

$$\tau_i = \rho_\infty\, q_\tau\, C_f\, \underline{q}_\tau \tag{3.7}$$

where E is the interfacial entrainment coefficient (>0 for entrainment into ambient pool, <0 for outward), C_f is the interfacial friction coefficient, $\underline{q}_\tau$ is the local bulk horizontal shear velocity between the water at the interface and that below, and $q_\tau = |\underline{q}_\tau|$.

Nondimensional analysis of the model equations produced several important scale factors. Two length scales emerged. The dissipative length scale, $L_t = D_b/a$ (a is the maximum value of E), characterizes the weakening of the front due to entrainment across the interface. The second length scale is the baroclinic Rossby deformation radius. $\lambda = (2\,\lambda\, gD_b)^{1/2}/f$, which characterizes the dependence of frontal structure on rotation. The nondimensional Prandtl number, $Pr = 2^{\frac{1}{2}}\ L_t/\lambda$, indicates the relative

importance of the two terms. Dependent variables in the model change most rapidly at the scale of the smaller of the two parameters. Thus $P_r >> 1$ implies dominance by intrusive forces, while $P_r << 1$ implies dominance by rotational forces.

A third important scaling parameter, Ri_c-the cross-stream Richardson number - is expressed as

$$Ri_c = \gamma g D_b / u_\infty^2 = C^2 / u_\infty^2 \qquad (3.8)$$

The quantity, C, is the phase speed of internal waves beneath the parent pool. Thus Ri_c characterizes the velocity of the ambient pool.

A final immportant scale parameter is the normalized *Ekman volume transport*,

$$V_E = |\tau_w| \, (\rho_\infty f)^{-1} / c D_b . \qquad (3.9)$$

Application of the model requires specification of vertical profiles of ρ, r, u, and v. This indicates that mixing is not accomplished by the model itself, but is imposed upon it.

Garvine shows that, by making a number of assumptions concerning the relationship between parameters in the

frontal zone and parameters at $x=\infty$, the model equations can be greatly simplified. Equations (3.3), (3.4), and (3.5), can ultimately be reduced to two ordinary differential equations which are solved for V_i and D. The velocity components u_i is calculated from these.

Garvine applied the model to six cases: A standard test case, a river plume front, the Pacific Equatorial front, a coastal upwelling front, the subtropical Atlantic Front, and the Gulf Stream Front. The scaling parameters for each front are listed in Table 3-4.

- Garvine first applied this model to a case with the following parameters: $P_r = 1.0$, $Ri_2 = 1.0$, $V_E = 0.1$. The density profile was linear from the surface to the interface. Both rotation and dissipation are important in this instance.

  The resulting frontal zone showed surface convergence on either side of the interface and sinking along the interface at depth. The density anomaly field is shown in Figure 3.13. An intense jet formed along the front, but with a speed roughly 30% that expected from geostrophy.

- The comparison between model predictions and observations (Garvine and Monk, 1974) for a river plume front was quite good (Figure 3.14).

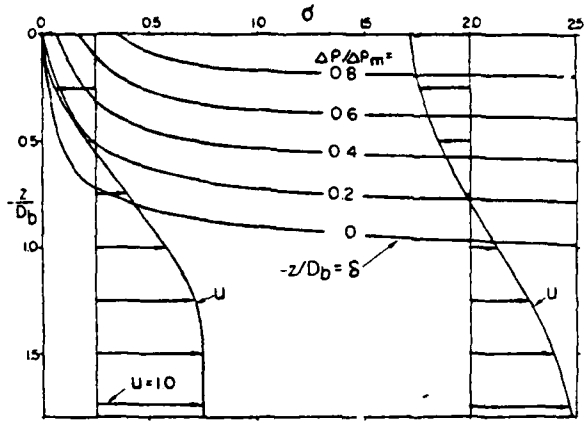

Figure 3.13. The field of density anomaly $\Delta\sigma$ normalized by its maximum and two vertical profiles of cross stream velocity for the standard case (Garvine, 1979b).

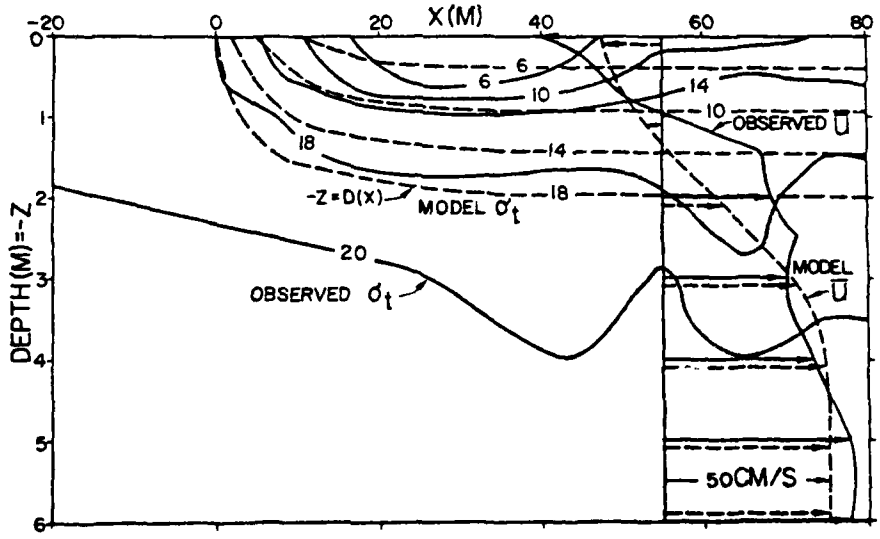

Figure 3.14. Comparison of model density (σ_t) and u profile with observational data of Garvine and Monk (1974) for Connecticut River plume front

Table 3-4
Scaling Parameters Used by Garvine (1979b)

Frontal Type	P_r	Ri_c	V_E
Standard Test	1.0	1.0	0.1
River Plume	0.029	0.6	N/A*
Pacific Equatorial	0.05	1.0	N/A*
Coastal Upwelling	2.8	3.2	0.0
Atlantic Subtropical	3.9	8.0	0.0
Gulf Stream	9.0	100.0	7.0×10^{-4}

* at very low P_r values, Ekman transports play a relatively unimportant role in model dynamics.

- The model density field for the Pacific Equatorial Front simulation is shown in Figure 3.15. No comparison with observation is possible until higher spatial resolution data becomes available, although the predicted interfacial slope is of the order of magnitude of the few observations that exist.

- Comparison of the model density field with observations in an upwelling zone by Stevenson et. al. (1974) is shown in Figure 3.16, while comparison of model streamlines and observed isotherms is shown in Figure 3.17. The model results agree reasonably well with observations, except in the region $x<0$, where bottom topography rises rapidly and the assumption $D_b << h$ is less tenable.

- The Atlantic subtropical front is almost entirely a thermal front, so that, as shown in Figure 3.18, model isopycnals and observed isotherms are directly comparable. The model pycnocline is thicker than the observed (as denoted by the 21.5^{o} isotherm), but the horizontal extent of the fronts compares well.

- Comparison with observed Gulf Stream frontal data (see Figure 3.19) is also good. The along-front transport values predicted (30 Sverdrups = 30×10^6 m^3/s) are reasonable, and the sea surface height anomaly across the front (90 cm) agrees well with surface slope measurements.

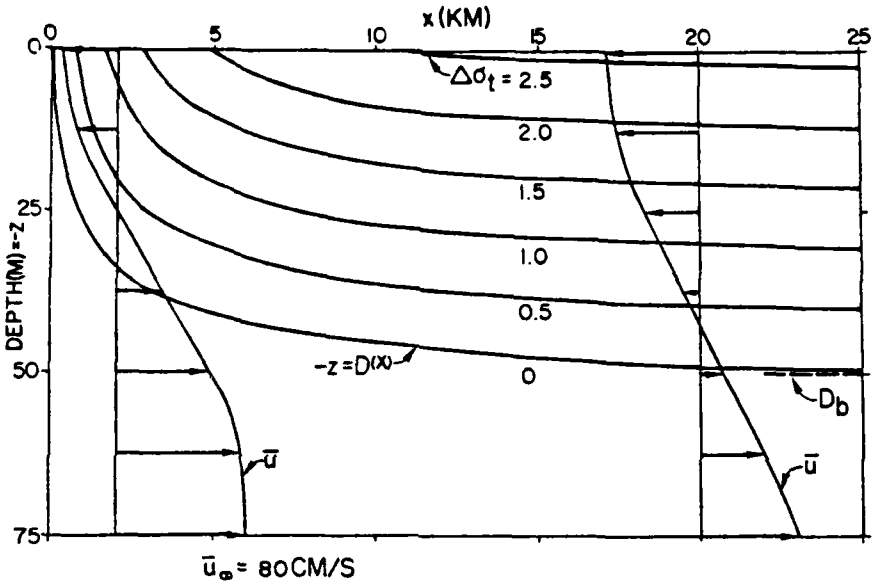

Figure 3.15. Model density anomaly (σ_t) field and two u profiles for conditions representative of the Pacific equatorial front (Garvine, 1976).

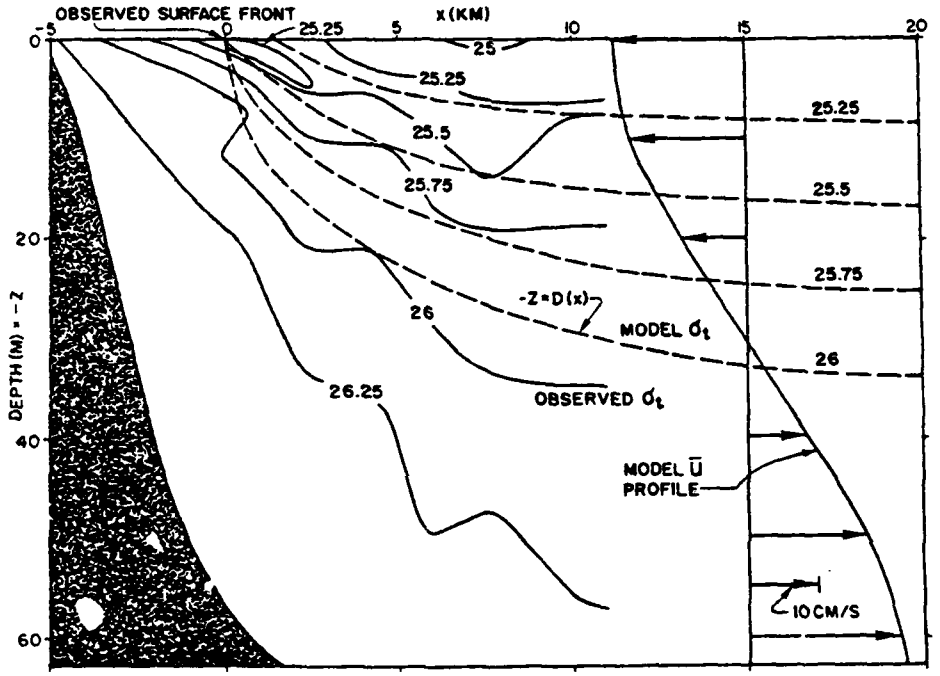

Figure 3.16. Comparison of model σ_t field with observed transect of Stevenson et. al (1974) for Oregon coastal upwelling. A model u profile is shown as well as the bottom profile (Garvine, 1979b).

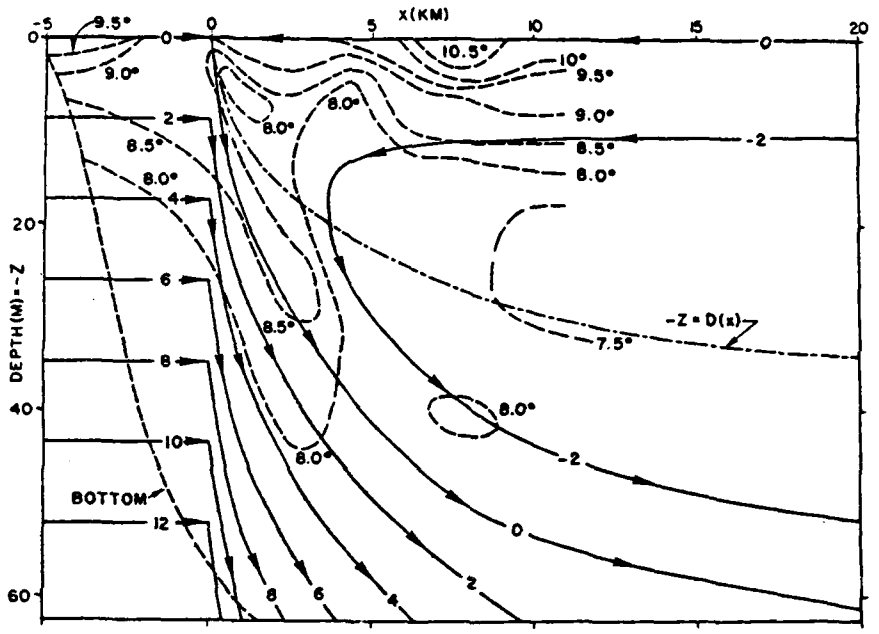

Figure 3.17. Model steamlines and observed isotherms for the coastal upwelling case (Garvine, 1979b).

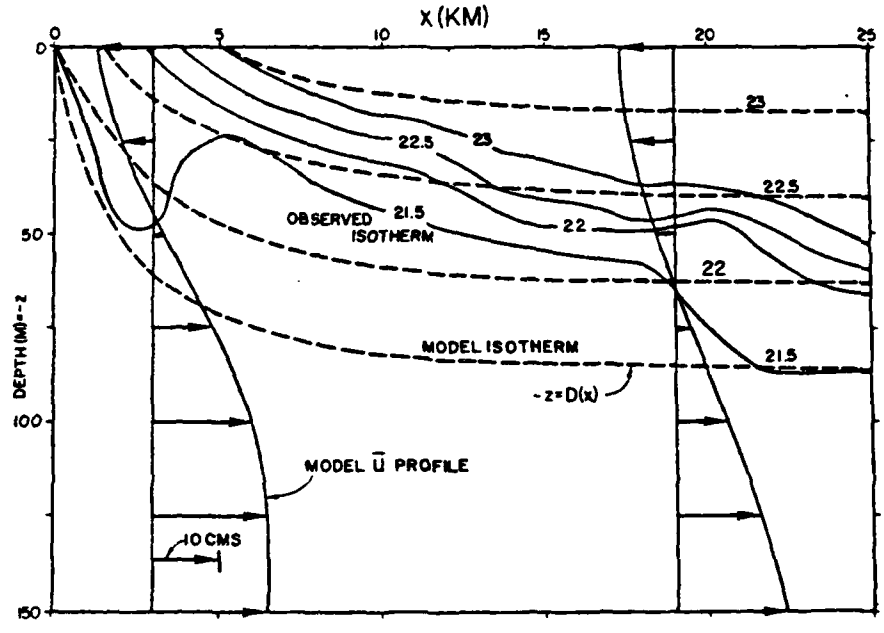

Figure 3.18 Model isotherms (dashed lines) for the Sargasso Sea case and the observed isotherms of Voorhis (1969) (solid lines) (Garvine, 1979b).

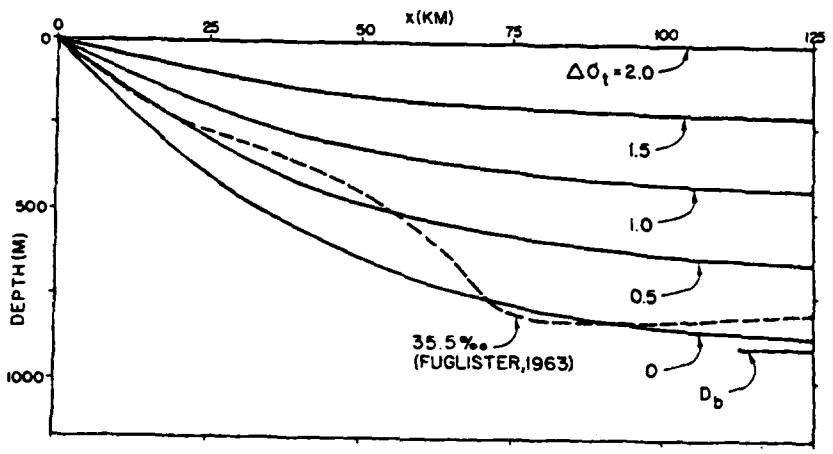

Figure 3.19. Model density field in terms of σ_t for the Gulf Stream front case. Dashed line indicates the 35.5% isohaline from the section shown in Figure 3-9.

The wide variety of cases to which this model has been applied indicates its usefulness in studying the dynamics of established density front systems. It cannot, however, be used to describe the processes involved in frontogenesis. That type of study requires a time-dependent model.

3.3.3 A Time-Dependent Frontal Model

Kao, et al. (1977) developed a time-marching model to study the frontal system formed when a body of water flows into an ambient pool of higher density. This is essentially the case studied by Garvine also. They treated the situation as an initial boundary value problem and obtained solutions to their equations by numerical integration. Their initial study did not include rotation, while their later work (Kao, et al., 1978) did. We will concern ourselves with the rotational model.

Consider the flow of a mass of water with density ρ and depth D_b at a rate Q_e into an ambient pool, of water with density ρ_o at the bottom (z=0). The ambient pool is at rest with total depth h. We can use h as a length scale, $U = Q_e/h$ as a velocity scale, and $t = d^2/Q_e$ as a time scale. The model coordinate system does not move with the front. The +x direction is into the ambient zone, and z is positive upwards from the bottom.

Define the y-directed (along-front) vorticity, density difference, and stream function respectively as

$$\zeta = \partial_z u - \partial_x w \qquad (3.10a)$$

$$\delta = (\rho-\rho_o)/\rho_o \qquad (3.10b)$$

$$u = \partial_z \Psi \ , \ w = -\partial_x \Psi. \qquad (3.10c)$$

Then, in nondimensional form, the equations for an incompressible viscous diffusive flow can be written as

$$\partial_t \delta + \partial_x(u\delta) + \partial_z(w\delta) = S_c^{-1} R_e^{-1} \nabla^2 \delta \tag{3.11}$$

$$\partial_t \zeta + \partial_x(u\zeta) + \partial_z(w\zeta) - R_o^{-1}\partial_z v = F^{-2}\partial_x \delta + R_e^{-1}\nabla^2 \zeta \tag{3.12}$$

$$\nabla^2 \psi = \zeta \tag{3.13}$$

$$\partial_t v + \partial_x(uv) + \partial_z(wv) + R_o^{-1} u = R_e^{-1}\nabla^2 v \tag{3.14}$$

where $\nabla^2 = \partial_{xx} + \partial_{zz}$, Re (Reynolds number)=Uh/ν, F(Froude number) = $U(gh)^{-1/2}$, Sc (Schmidt number) = ν/D, and R_o (Rossby number) = $U(fh)^{-1}$. The parameters ν and D represent the kinematic viscosity and diffusivity.

The boundary and surface constraints placed on the model are as follows:

- No shear or vorticity at the free surface,
- No mass transfer through the side boundaries at x=0,
- No-slip conditions at the side and bottom,
- u=v=0 at the bottom and at the side when x=0, and
- u=1 and w=0 for downstream.

The initial conditions for the inflow specify a potential flow which satisfies $\nabla^2\psi = 0$ and v = 0 and a density field such that $\bar{\delta}(z)=(\bar{\rho}(z)-\rho_o)/\rho_o$, where $\bar{\rho}(z)$ is the mean density of the ambient fluid.

The first test case reported was the intrusion of a flow into a homogeneous ambient fluid. The front accelerated into the ambient fluid and then slowed as the Coriolis force deflected it parallel to the front. Eventually (after a time period of roughly $10f^{-1}$) a quasi-geostrophic balance was established, and the front became stationary with respect to the ambient fluid. Cross sections of various front parameters at equilibrium are shown in Figure 3.20. The convergence and downwelling at the front noted by Garvine were present in this simulation.

This form of the model was then applied to Gulf Stream front data (Fuglister, 1963) with considerable success. Plots of density deficit (σ_t (light inflow) - σ_t (upstream)) at various depths in the front are shown in Figure 3.21. The isopycnal slopes at the front and the along-front flow predicted by the model agreed well with observations also.

A third test depicted flow into an ambient pool with a thermocline-type density structure. The primary difference between results of this test and those of the first test was the generation of internal waves at the thermocline. An example of this is shown in Figure 3.22. Calculations based on model results showed that the internal waves were indeed forced by the front and travelled with the front. This test was conducted with an unrealistically large Rossby number. Tests with a lower value of Ro also produced internal waves during the evolution of the front.

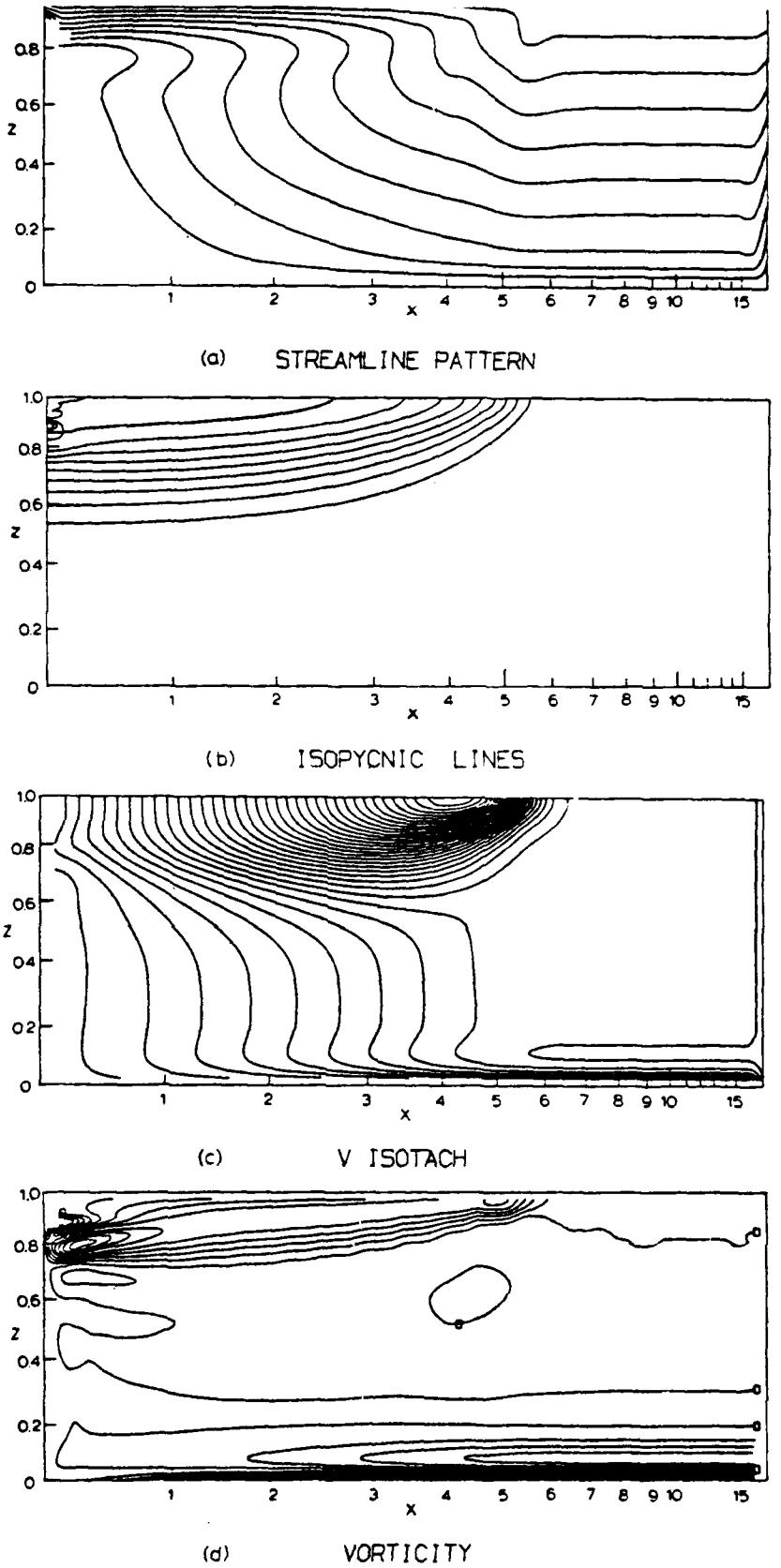

Figure 3·20. Patterns of streamlines, isopycnals, v isotachs, and voricity for flow into homogeneous ambient fluid. Variable spacing in x-direction denotes "stretched" coordinates (Kao, et. al., 1978).

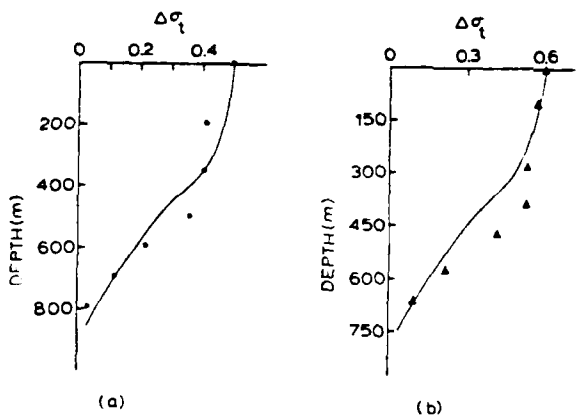

Figure 3·21. Density deficit ($\Delta\sigma_t$) as function of depth for two Gulf Stream cross-sections (dots) compared with steady state model predictions (Kao et. al., 1978).

AD-A098 189 SCIENCE APPLICATIONS INC MCLEAN VA F/G 8/3
A REVIEW OF OCEAN MODELS.(U)
JAN 81 W J GRABOWSKI, G T HEBENSTREIT N00014-78-C-0849
UNCLASSIFIED SAI-81-346-WA NL

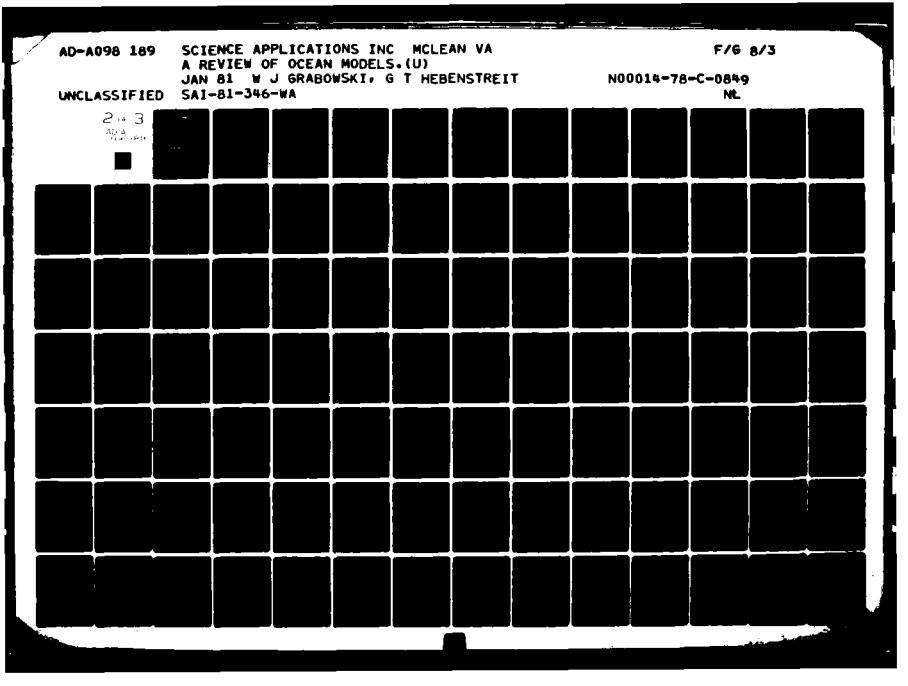

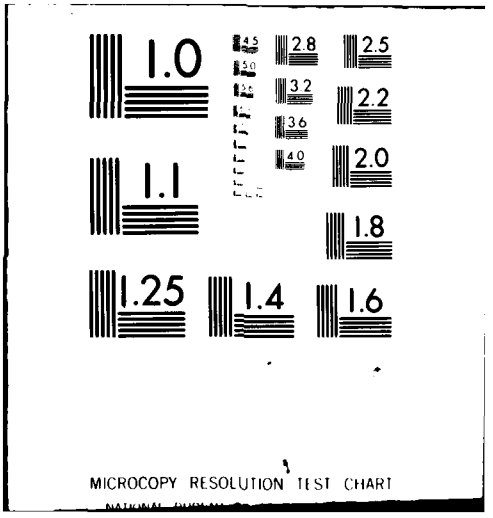
1.0
1.1
1.25
1.4
1.6
1.8
2.0
2.2
2.5
2.8
3.2
3.6
4.0
4.5
5.0
MICROCOPY RESOLUTION TEST CHART

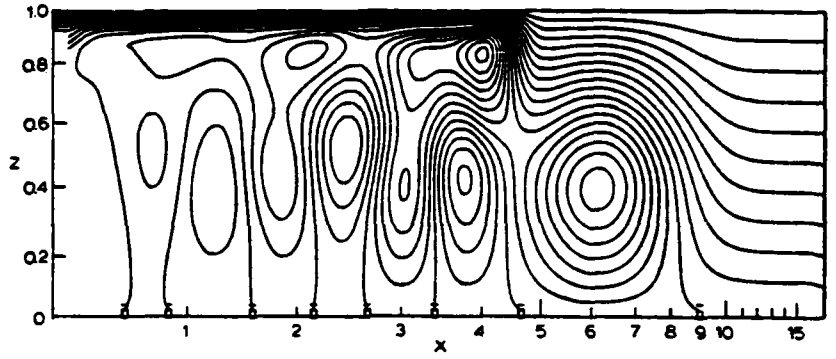

(a) STREAMLINE PATTERN

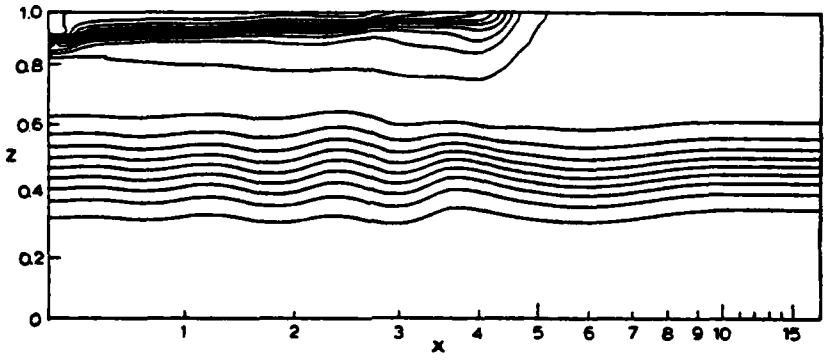

(b) ISOPYCNIC LINES

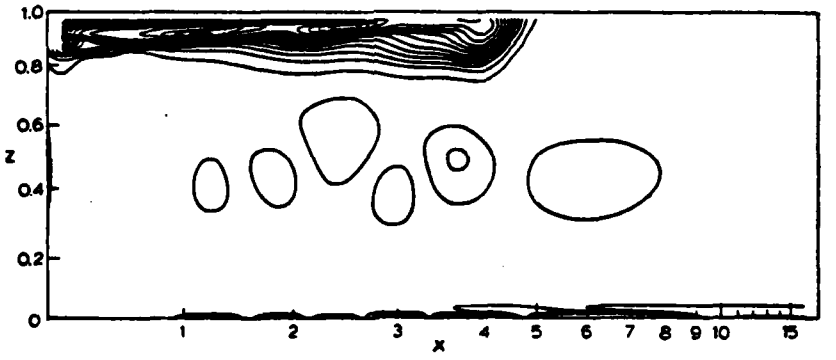

(c) VORTICITY

Figure 3.22. Parameters for flow into ambient pool with thermocline-type density structure $R_o = \infty$ (Kao, et. al., 1978).

This time-dependent model also shows great potential for studying the evolution and maintenance of oceanic density fronts. The reader should be aware that neither this model nor Garvine's can presently be used to model fronts which do not display density gradients (i.e., temperature and salinity gradients are such that density remains relatively constant across the zone). The majority of fronts reported in the literature exhibit density gradients, however, and the severity of this restriction on model usage may not be great.

3.4 RELATION OF FRONT MODELS TO OTHER SCALES

Oceanic fronts have not yet received the attention that large scale circulation patterns and eddies have received. Thus little speculation has appeared as to the role of fronts in the wide range of ocean dynamics. We know that many frontal zones come about as a result of the mean circulation of both the ocean and the atmosphere.

The relationship of fronts to smaller scales of motion is also vague. The results of Kao et al. (1978), which indicate that moving fronts could generate internal waves, may provide the link if they are borne out by observations.

From a modelling perspective, frontal models form a separate category. The large-scale models cannot resolve fronts because of the small scales over which horizontal gradients are strong. Eddy resolving models could produce fronts, although little mention of this has been made in the literature.

REFERENCES

Beckerle, J.C., 1972: Prediction of Mid-Oceanic Frontal Passage Confirmed in Near-Surface Current Measurements. Jour. Geophys. Res., 77, 1637-1646.

Fenner, D., 1978: Sound Speed Structure Across an Anti-Cyclonic Eddy and the Gulf Stream North Wall. Jour. Geophys. Res., 83, 4599-4605.

Fuglister, F., 1963: Gulf Stream '60. Progress in Oceanography, Vol. I, M. Sears, ed. McMillan, 265-273.

Garvine, R.W., 1974: Dynamics of Small-Scale Oceanic Fronts, Jour. Phys. Oceanog. 4, 557-569.

_____, 1979a: An Integral Hydrodynamic Model of Upper Ocean Frontal Dynamics: Part I. Development and Analysis. Jour. Phys. Oceanog., 9, 1-18.

_____, 1979b: An Integral Hydrodynamic Model of Upper Ocean Frontal Dynamics: Part II. Physical Characteristics and COmparison with Observations. Jour. Phys. Oceanog., 9, 19-36.

_____, and J.D. Monk, 1974: Frontal Structure of a River Plume. Jour. Geophys. Res., 79, 2251-2259.

Kao, T.W., C. Park, and H.-P. Pao, 1977: Buoyant Surface Discharge and Small-Scale Oceanic Fronts: A Numerical Study. Jour. Geophys. Res., 82, 1747-1752.

_____, H.-P. Pao, and C. Park, 1978: Surface Intrusions, Fronts, and Internal Waves. Jour. Geophys. Res., 83, 4641-4650.

Legeckis, R., 1978: A Survey of Worldwide Sea Surface Temperature Fronts Detected by Environmental Satellites. Jour. Geophys. Res., 83, 4501-4522.

Paki H. and J.R.V. Zaneveld, 1974: Equatorial Front in the Eastern Pacific Ocean. Jour. Phys. Oceanog. 4, 570-578.

Roden, G.I., 1974: Thermohaline Structure, Fronts, and Sea-Air Energy Exchange in the Trade Wind Region East of Hawaii. Jour. Phys. Oceanog., 4, 168-182.

_____, 1975: On North Pacific Temperature, Salinity, Sound, Velocity, and Density Fronts and Their Relation to the Wind and Energy Flux Fields. Jour. Phys. Oceanog., 5, 557-571.

_____, 1977: Oceanic Subarctic Fronts of the Central Pacific: Structure of and Response to Atmospheric Forcing. Jour. Phys. Oceanog., 7, 761-778.

Stevenson , M.R., R.W. Garvine, and B. Wyatt, 1974: Lagrangian Measurements in a Coastal Upwelling Zone Off Oregon. Jour. Phys. Oceanog., 4, 321-336.

Voorhis, A.D., 1969: The Horizontal Extent and Persistence of Thermal Fronts in the Sargasso Sea. Deep-Sea Res., 16, (Supplement), 331-337.

_____ and J.B. Hersey, 1964: Oceanic Thermal Fronts in the Sargasso Sea. Jour. Geophys. Res., 69, 3809-3814.

White, W.B., K. Hasunuma, and H. Solomon, 1978: Large-scale Seasonal and Secular Variability of the Subtropical Front in the Western North Pacific from 1954 to 1974. Jour. Geophys. Res., 83, 4531-4544.

Section 4

UPPER-OCEAN MODELS

Section 4
UPPER-OCEAN MODELS

4.1 INTRODUCTION

The momentum and energy fluxes which drive motion in the ocean, from the largest current systems to small-scale internal waves and turbulence, and which maintain the ocean's thermal characteristics arise, fundamentally, from fluxes across the air-sea interface. The fluxes result directly from solar irradiance at the sea surface or from differences between the air and ocean mechanical and thermal states. Momentum and kinetic energy are transferred by wind stress at the sea surface, solar radiation passes through the interface and is absorbed very near the surface; infrared radiation is emitted by the water at the surface; the occurrence of air-sea temperature differences give rise to sensible heat transfer in or out of the ocean and evaporative transfer. These are the essential momentum and energy transfer processes. They most strongly and directly affect the upper 1-2% of the ocean, and this layer has in turn a pronounced effect on them. A sound understanding of the physics of the upper ocean is therefore fundamental to the study and analysis of nearly all ocean phenomena. In this section we will describe one-dimensional upper-ocean models.

We can define the upper ocean as the depth interval from the surface which exhibits strong seasonal variations. These variations are usually most notable in the local temperature profile of the water column. Typically the upper-ocean water column consists of a very

strongly surface-flux-influenced vertical mixing layer atop a seasonal thermocline (see Figure 4-1). The depth of the mixing layer can vary from a few meters in summer up to several hundred meters in winter. Except for a very thin "constant flux" layer about a meter deep at the surface, conditions in the mixing layer often approach uniformity in the mean and this layer is usually referred to as the "mixed layer" (ML), it will be so referred to here.* Thermal and mechanical energy are transferred vertically in the mixed layer by wind-induced turbulent motion, and by convective motions which arise in cases where the surface water cools, becomes heavy, and sinks. Large values of vertical shear are often observed at the mixed-layer base, and there is evidence (for example, Halpern 1974) that when strong wind-forced vertical mixing is occurring the mixed layer responds somewhat like a rigid slab at inertial frequencies to wind forcing

The seasonal thermocline (ST) is the scene of significant internal-wave activity. The vertical fluxes of heat and salt are usually far smaller than their mixed-layer values, but momentum fluxes in the form of internal waves (which do not transport heat or salt) need not be. The ST internal-wave field may thus provide an important sink for mixed-layer momentum (Bell, 1978). Patchy turbulent regions

---

* Some experimentalists prefer the terms "mixing layer" or "wind-mixing layer" since they view the existence of truly mixed layers as rare, although there is some controversy about this. Modelers generally make the practical assumption that mixed layers exist.

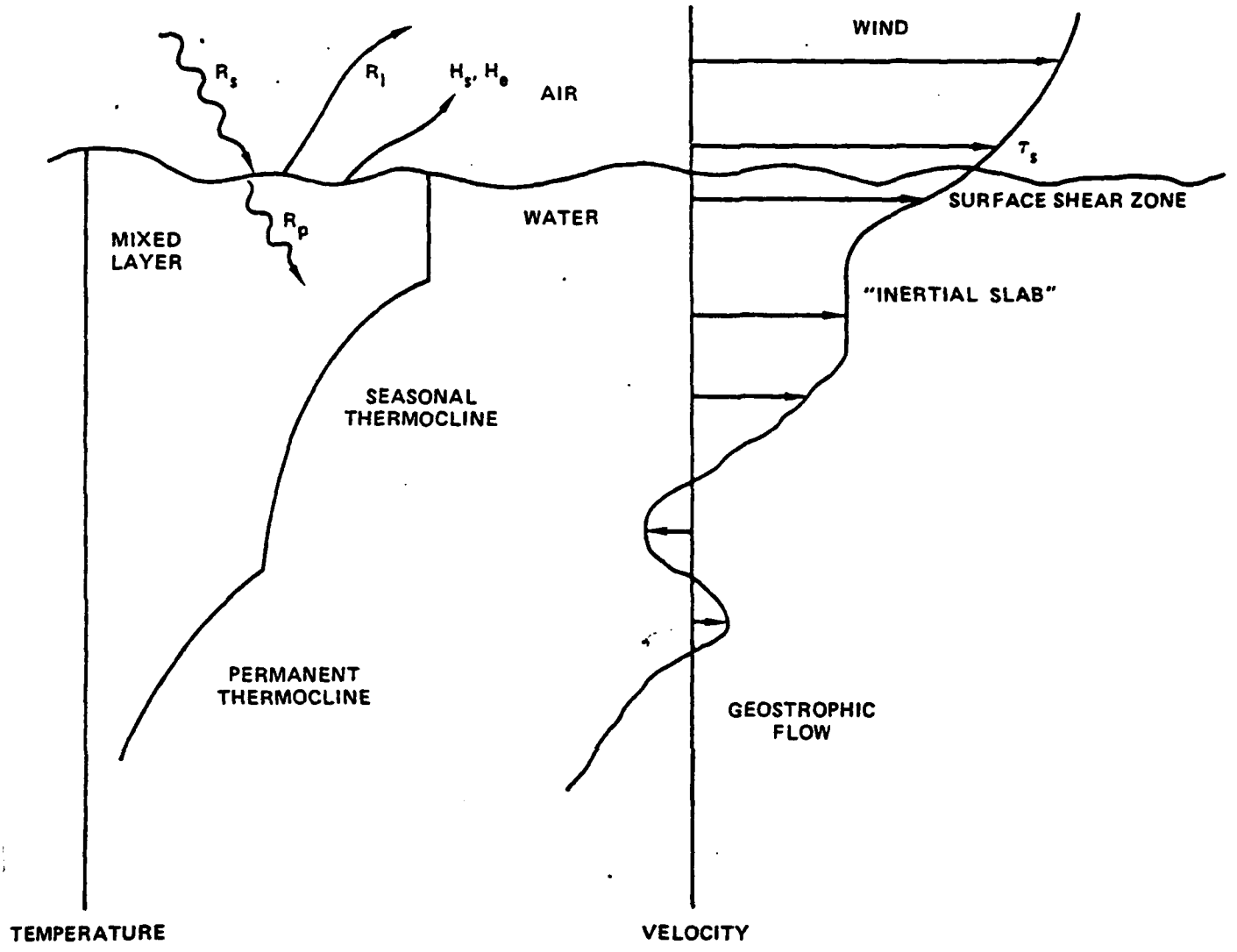

FIGURE 4-1: Schematic of major features of the temperature and velocity structure near the ocean's surface. The following flux components are indicated: R_s, short-wave radiation; R_l, long-wave radiation; R_p, the component of short-wave radiation absorbed below the surface; H_s, sensible heat transfer; H_e, evaporative heat transfer; τ_s, the surface wind stress (momentum flux). The reflected components of the short-wave radiation is not included.

tend to appear in the ST, and these patches are responsible for vertical transport of heat, salt and momentum. The patches may be induced by internal-wave instabilities and double diffusion phenomena. The ST internal-wave field may respond strongly in turn to meteorological forcing modulated by the existence of a mixed surface layer (Käse, 1979), and to forcing induced by mixed-layer turbulence (Bell, 1978).

One-dimensional upper-ocean models are based on the assumption that over an appropriate averaging time scale horizontal variations in averaged quantities (such as temperature, salinity and velocity) may be neglected compared with their vertical variation. Such models are useful because, in the absence of distinct fronts or eddies, quantities which have been averaged over time periods longer than those characteristic of the local internal-wave field tend to vary more over a vertical distance (from the surface) of a hundred meters than over horizontal distances of tens of kilometers. Under such conditions horizontal advection is likely to affect local conditions to a much lesser degree than vertical processes. In general the validity of the assumption must be considered on a case-by-case basis.

We can organize one-dimensional upper-ocean models into two broad classes:

- bulk mixed-layer or mixing-layer models;
- diffusion or grid-point models.

Bulk mixed or mixing-layer models, sometimes referred to as "slab" models, are based on the assumption that vertical variations in averaged values of temperature, and salinity and velocity when these quantities are included, may be neglected within a surface layer in which turbulent mixing is occurring. The partial differential equations for heat, salt and momentum conservation can then be reduced to ordinary differential equations. This uniformity assumption follows from many observations of vertical profiles of the sort presented earlier. In these models the upper-ocean response to surface forcing consists of changes in the depth of the active-mixing layer and in the temperature (and the salinity and velocity, if included) of the layer. As the layer deepens (due to wind mixing, say) it entrains water of different temperature (and salinity and velocity) and conditions within the layer are adjusted to satisfy conservation requirements. For example, as the layer deepens it may entrain cooler water and the net effect will be a slightly cooler, but still uniform, layer temperature. As the layer of active mixing recedes due to strong heating, it leaves behind non-turbulent water at each depth at the temperature (and salinity and velocity) of the layer when its base was at that depth.

In general, the treatment of the seasonal thermocline assumed in bulk upper-ocean models is trival: conditions at a fixed depth can vary only when that depth is within the mixed-layer. Some exceptions are the treatments proposed by Denman (1973) in which solar radiation is included and Niiler (1977) which includes some turbulent transport within the seasonal thermocline.

Diffusion models do not require a uniform mixed-layer assumption, and partial differential equations for temperature and velocity (and in at least one case, salinity) as a function of time and depth are solved numerically by a finite-difference grid-point approach. Turbulent transport is parameterized by a buoyancy-influenced eddy viscosity coefficient, and the distinction between the mixed-layer and seasonal thermocline is not required; that is, the existence of a mixed-layer is not imposed a priori but can be used to verify the model parameterization.

In the following sections we will examine models based on each of thse approaches and describe results obtained using them.

4.2 ONE-DIMENSIONAL CONSERVATION EQUATIONS

The equations for the conservation of heat, salt and momentum form the basis for all one-dimensional upper-ocean models. In this section we will present the equations. We will also present an equation of state, a buoyancy equation, a one-dimensional turbulence kinetic energy equation which we will use in our description of bulk and diffusion models, and ocean-surface flux boundary conditions.

4.2.1 One-Dimensional Heat, Salt and Momemtum Equations

To derive the one-dimensional upper-ocean equations we assume that:

- horizontal variations of quantities from their averaged (ensemble or Reynolds averaged*) values are negligible;

- the effects of density variations can be ignored except as they give rise to buoyancy forces;

- the effects of molecular diffusion of heat, salt and momentum on the local conservation of those quantities are negligible;

- the averaged vertical momentum equation is adequately represented by the hydrostatic balance equation.

Under these constraints the conservation of heat, salt and momentum are described by

$$\partial_t T + \partial_z q = -(\rho_r c)^{-1} \partial_z R_p \quad , \qquad (4.1a)$$

$$\partial_t S + \partial_z \gamma = 0 \quad , \qquad (4.1b)$$

and

$$\partial_t \underline{U} + \hat{k} \times f\underline{U} + \partial_z \underline{\tau} = 0 \quad . \qquad (4.1c)$$

---

* In experimental work Reynolds averaging is taken to mean time averaging over time scales which are long compared to the scales associated with small scale motion (an individual stirring/mixing event, say), but short compared to larger scale motion (inertial oscillations, for example). For the gross mixed-layer dynamics typical averaging times are on the order of an hour. The equivalency of the two forms of averaging is addressed by the ergodic hypothesis.

We define the variables in (4.1) as follows:

T the averaged water temperature;

S the averaged salinity;

$\underline{u}$ the averaged horizontal current vector with components (u,v) in the East and North directions respectively;

f the Coriolis parameter $2\Omega\sin\phi$ (where Ω is the earth's angular velocity and ϕ is latitude);

ρ_r a representative water density;

c the constant-volume specific heat of sea water;

R_p the component of solar (direct and diffuse) radiation which penetrates the ocean surface;

z the coordinate describing vertical distance (positive upward);

$\hat{k}$ a unit vector in the z direction;

t time.

We define the turbulent fluxes of heat, salt and momentum q, γ and $\underline{\tau}$ as

$$q = \overline{w'T'} \quad , \tag{4.2a}$$

$$\gamma = \overline{w'S'} \quad , \tag{4.2b}$$

and $$\underline{\tau} = \overline{w'\underline{v}'} \quad , \qquad (4.2c)$$

where primes represent the instantaneous deviation from the mean, and w is the vertical velocity. The notation $\overline{x}$ represents the average of the quantity x, and by definition

$$\overline{\underline{v}}' = \overline{w}' = \overline{S}' = \overline{T}' = 0 \quad .$$

For convenience we use the over-bar notation only as necessary, and we have defined our averaged variables such that

$$T \equiv \overline{T}, \text{ etc.}$$

Equations (4.1) form the basis for all one-dimensional upper-ocean models. In some formulations the penetrative radiation R_p is not included in the heat equation as a distributed source but is treated only as a surface flux. In some parts of the ocean this approximation may be reasonable; in certain areas, however, significant percentages of the total solar irradiance penetrate to depths of 10 - 20 m. As perhaps an extreme example, the irradiance at depths of 10 and 25 m in clear water (Sargasso or Caribbean Sea) can be as large at 20 and 13%, respectively, of the surface direct solar and diffuse radiation with the sun at 90° altitude (Jerlov, 1976). Energy deposited at these depths may significantly affect the near surface thermal structure.

In many problems the primary variable of interest is temperature and the assumption is often made that the

effects on water buoyancy of variations in salinity can be neglected. The mixed-layer model of Price et al. (1978), the diffusion model of Kondo et al. (1979), and an SAI-developed version of the Mellor and Durbin (1975) model, however include equations for the salinity.

In many instances the horizontal upper-ocean current field is of interest in its own right, however, there are many situations such as heat budget studies in which predictions of momentum may not be particularly desired. The necessity for the inclusion of an averaged momentum equation in this kind of study is directly related to fundamental questions about the nature of turbulent mixing and entrainment. There are two basic schools of thought on this issue. Kraus and Turner (1967) and Turner (1969) argued that wind-induced vertical mixing and entrainment may be related to mixed-layer turbulence somehow generated by the surface wind stress, and that the mean-momentum equation was irrelevant. The assumption implicit here is that near-surface shear can be adequately expressed in terms of the friction velocity ($|\underline{\tau}_s/\rho_o|^{\frac{1}{2}}$) divided by a surface shear layer length scale. This approach has been followed by Denman (1973), Kim (1976), and others, mostly on the basis of apparent predictive success, laboratory data, and convenience. On the other hand, Pollard, et al. (1973) and Price et al. (1978) argued that wind-induced mixed-layer deepening is dominated by the generation of turbulence at the base of the mixed layer. The large turbulence generation rates result from large vertical shears across the mixed-layer base. Price (1979) suggests that the laboratory experiments have actually been misinterpreted. Under this latter hypothesis the mixing-layer momentum equation is

crucial since it yields a prediction for the change in mean velocity across the layer base.

Diffusion models are not based on an assumption regarding the source of turbulence responsible for layer deepening except that turbulence resulting from surface wave breaking is not included. The simplest of these models parameterize vertical mixing in terms of local gradient Richardson number, while the more complex estimate fluxes from prediction of the turbulence kinetic energy or predict the fluxes directly. In all cases vertical shear is a major factor in the flux prediction.

4.2.2 One-Dimensional Buoyancy Equation

The temperature and salinity are related to the water density by an equation of state; formally,

$$\rho = \rho(S,T,p).$$

For most upper-ocean modeling purposes it is sufficient to ignore the rather weak pressure effect, and all models make use of a linearized equation of state:

$$\rho = \rho_r[1-\alpha(T-T_r) + \beta(S-S_r)] \qquad (4.3)$$

where T_r and S_r are the reference temperature and salinity corresponding to ρ_r. The coefficients α and β are defined by

$$\alpha = -\rho_r^{-1}(\partial_T \rho)_S$$

and

$$\beta = \rho_r^{-1}(\partial_S \rho)_T$$

and have positive values.

We define the "buoyancy" in the usual way (Phillips, 1977) as

$$b = -g(\rho-\rho_r)/\rho_r \tag{4.4a}$$

and from (4.3)

$$b = g[\alpha(T-T_r) - \beta(S-S_r)]. \tag{4.4b}$$

The linearized equation of state enables us to combine (4.1a) and (4.1b) for a single buoyancy conservation equation which can be used in place of one of those equations. The variation of buoyancy and not temperature and salinity individually is a key element in mixed-layer dynamics. We multiply (4.1a) by $g\alpha$ and (4.1b) by g and add to obtain

$$\partial_t b + \partial_z \eta = -\partial_z I_p \tag{4.5a}$$

where b is defined in (4.4b) and η is the turbulence flux of buoyancy given by

$$\eta = \overline{w'b'} = g(\alpha q - \beta\gamma). \tag{4.5b}$$

We have defined

$$I_p(z) = \frac{g\alpha}{\rho_r c} R_p(z) \tag{4.5c}$$

for convenience.

4.2.3 The One-Dimensional Turbulence Kinetic-Energy Equation

Nearly all upper-ocean models rely on the turbulence kinetic-energy (TKE) equation to provide a closure scheme. In bulk models the TKE budget is used to determine conditions under which sufficient mechanical energy is generated to keep the layer well-mixed. A good example of such an application is given by Niiler and Kraus (1977). The diffusion models of Mellor and Durbin (1975) and Marchuk et al. (1977) also make use of the turbulence kinetic energy equation to parameterize vertical mixing.

Under the horizontal homogeneity assumption described earlier, we can write the TKE (see Phillips, 1977) equation as

$$\partial_t k^2 = -\underline{\tau} \cdot \partial_z \underline{u} + \eta - \partial_z \left\{ \overline{w'(k^2 + \rho_r^{-1} p')} \right\} - \varepsilon \tag{4.6a}$$

where k^2 is the turbulence kinetic energy,

$$k^2 = \frac{1}{2} \overline{(u'^2 + v'^2 + w'^2)}. \tag{4.6b}$$

The first term on the right side of (4.6a) represents the production of TKE by the interaction of turbulence with the mean shear; the second, the conversion of potential energy to TKE; the third, vertical turbulent transport of TKE and work done by the turbulence against fluctuations in pressure about its hydrostatic value; and fourth the dissipation of TKE by viscosity.

4.2.4 The Parameterization of Surface Fluxes

The parameterizations of surface fluxes of heat, salt and momentum are essentially independent of the details of the particular mixed-layer or diffusion model which we might wish to apply. We let a subscript "o" represent the value of a flux or variable at the surface, and note that, in our coordinate system with z-positive upward, fluxes are positive out of the surface. Then

$$q_o = (\rho_o c)^{-1} [R_l + H_e + H_s] , \tag{4.7a}$$

$$\gamma_o = (P-E)\ S_o , \tag{4.7b}$$

and

$$\underline{\tau}_o = -\rho_r^{-1}\ \underline{\tau}_s \tag{4.7c}$$

where

τ_s is the stress applied by the wind on the surface (or the momentum flux into the surface),

R_l is the net infra-red heat flux out of the surface,

H_e is the evaporative heat flux,

H_s is the sensible heat flux,

E, P are evaporation and precipitation rates, respectively.

The surface buoyancy flux is just

$$\eta_o = g(\alpha q_o - \beta\gamma_o). \tag{4.7d}$$

The fluxes τ_s, H_e, H_s and E are usually parameterized adequately with bulk formulas. These have been studied by many investigators (e.g., Friehe and Schmitt, 1976). Essentially they all have forms similar to

$$H_s = C_s\rho_a|\underline{v}_a|c_p(T_o-T_a),$$

$$H_e = A_e E,$$

$$E = C_E\rho_a|\underline{v}_a|(r_a-r_o^*),$$

and

$$\underline{\tau}_s = C_D\rho_a\underline{v}_a|\underline{v}_a|$$

where subscript "a" refers to conditions in the air at some reference height (typically 10 meters), C_D, C_S and C_e are generalized flux coefficients, A_e is the latent heat

of evaporation of sea water, r is the specific humidity, and r_o^* is the saturation specific humidity at the sea-surface temperature. We will not describe these expressions further in this document.

The quantity R_l is the net flux of thermal infra-red radiation. It is comprised of energy emitted from the ocean surface and from the water vapor in the atmosphere (positive and negative energy fluxes in our coordinate system).

The penetrating short wave radiation, R_p, which includes both direct solar radiation as well as diffuse sky radiation, has been represented in (4.1) as a distributed source; it is absorbed to a very significant extent in the upper 0 to 20 meters. $R_p(z)$ is usually represented for most upper-ocean modeling purposes by a decaying exponential (e.g., Denman, 1973, Price, et al., 1978). A general formulation is

$$R_p(z) = \sum_i R_{pi} \exp(\kappa_i z) \tag{4.8}$$

in which we assume that the penetrating radiation may be represented in spectral bands with an exponential attenuation coefficient, κ_i, for each band. A convenient expression of this sort which includes water turbidity effects is given by Kondo, et al. (1979).

4.3 BULK MIXING-LAYER MODELS

One-dimensional bulk mixing-layer models are based on the assumption that a mixed-layer exists in which vertical variations in averaged values of temperature, and salinity and velocity when these quantities are included,

may be neglected. The archetype model is that due to Kraus and Turner (1967). Their work was refined and expanded upon by numerous investigators including Denman (1973), Pollard, Rhines and Thompson (1973), Kim (1976), Niiler (1975, 1977), Niiler and Kraus (1977), Garwood (1977), Price et al. (1978), and others.

4.3.1 Buoyancy, Salinity and Momentum Conservation in the Mixing-Layer

We assume a ML of depth h such that within it the average values T, S, b, and $\underline{\upsilon}$ do not vary vertically and have the values T_m, S_m b_m, and $\underline{\upsilon}_m$. We do not assume that the total instantaneous temperature, salinity, buoyancy and velocity are uniform, just their average values; as long as vertical transport is taking place there must be vertical variation. It is important to recognize that this assumption of uniform averaged ML values is not based directly on fundamental physical principles but strictly upon observation. In ML models the vertical structure is forced upon the solutions of the dynamic equations, and it places significant (and to some degree artificial) constraints on those solutions.

With the uniformity assumption described above we can integrate (2.1) and (2.5) across the ML to obtain the ML equations:

$$h\, d_t b_m = -(\eta + I_p) \Big|_{-h}^{0} \tag{4.9a}$$

$$h d_t S_m = -\gamma \Big|_{-h}^{0} \tag{4.9b}$$

and

$$h\,(d_t \underline{\upsilon}_m + \hat{k} \times f\underline{\upsilon}_m) = -\underline{\tau}\Big|_{-h}^{o}, \tag{4.9c}$$

and for reference

$$h\, d_t T_m = -[q+(\rho_r c)^{-1} R_p]\Big|_{-h}^{o} \tag{4.9d}$$

where

$$x\Big|_a^b \equiv x(b) - x(a).$$

Equations (4.9) relate the temporal rates of change of b, S, $\underline{\upsilon}$ and T in the layer to the fluxes of those quantities across the layer surface and base. There are a total of (10) unknowns (including h) in the above system. The penetrating solar radiation R_p is assumed known in terms of the solar flux at the surface and the water absorptivity.

The assumption of uniform b, S, and $\underline{\upsilon}$ across the ML places constraints on the behavior of η, γ and $\underline{\tau}$ in the layer which are worth noting. Equations (4.9) require that for b, S, and $\underline{\upsilon}$ to be independent of z; γ and $\underline{\tau}$ must be linear in z as must the combination $\eta + I_p$. These dependencies can be expressed

$$\eta(z) = \eta_o + I_p\Big|_z^o + \frac{z}{h}\,(\eta+I_p)\Big|_{-h}^{o}, \tag{4.10a}$$

$$\gamma(z) = \gamma_o + \frac{z}{h}\,\gamma\Big|_{-h}^{o}, \tag{4.10b}$$

and

$$\underline{\tau}(z) = \underline{\tau}_o + \frac{z}{h}\,\underline{\tau}\Big|_{-h}^{o}. \tag{4.10c}$$

4.3.2 Mixing-Layer Base Fluxes

While the mixing-layer deepens it entrains water of different buoyancy, salinity and momentum. This water must mix rapidly and uniformly throughout the layer through the action of turbulence in such a way that the buoyancy, salinity and momentum of the whole water column are conserved. This mixing requirement determines the values which the turbulence fluxes must have at the mixed-layer base to support a given rate of mixing-layer deepening. When the mixing-layer shallows there is no turbulence flux since no entrainment occurs and the fluid does not "unmix." The water is left behind with the temperature, salinity and velocity of the mixing layer at the time of recession. Since the mixing layer may subsequently deepen during a simulation these values are stored at a vertical array of grid points.

To obtain expressions for the turbulent fluxes at the mixing-layer base when the layer is deepening, we integrate (4.5a) and (4.1b-c) across the ML/ST interface. We assume that the interface is of thickness $\delta << h$; the integration does not require specification of b, S and $\underline{u}$ for a sufficiently thin interfacial layer. We also assume that turbulence fluxes of buoyancy and salt below the interface can be neglected. We define

$$\Delta b \equiv b_m - b(-h-\delta),$$

the jump in buoyancy across the interface and find

$$\eta_h \equiv \eta(-h) = -(d_t h)\Delta b, \qquad (4.11a)$$

$$\gamma_h = -(d_t h)\Delta S, \qquad (4.11b)$$

and

$$\underline{\tau}_h = -(d_t h)\Delta\underline{v}. \tag{4.11c}$$

We can generalize (4.11) to include the case of layer shallowing by writing

$$\eta_h = -\Lambda\ \Delta b\ d_t h, \tag{4.12a}$$

$$\gamma_h = -\Lambda\ \Delta S\ d_t h, \tag{4.12b}$$

and

$$\underline{\tau}_h = -\Lambda\ \Delta\underline{v}\ d_t h, \tag{4.12c}$$

where the Heaviside function is defined as

$$\Lambda = 1 \text{ for } d_t h > 0 \text{ (deepening)},$$

and

$$\Lambda = 0 \text{ for } d_t h < 0 \text{ (shallowing)}. \tag{4.12d}$$

4.3.3 The Turbulence Kinetic Energy Budget

Equations (4.7), (4.9) and (4.12) comprise a set of (9) equations for the ten problem variables

$$\underline{v}_m,\ b_m,\ S_m,\ \underline{\tau}_o,\ \eta_o,\ \gamma_o,\ \underline{\tau}_h,\ \eta_h,\ \gamma_h,\ h.$$

An additional constraint is required to close the system. Two basic approaches to closure have been proposed. These have been based on the mixing-layer turbulence kinetic energy budget, and on a mixed-layer mean energy budget. The

former approach has been incorporated in nearly all mixing-layer models, while the latter was proposed by Pollard, et al. (1973). Niiler (1975) argued that the mean energy budget approach was logically inconsistent, but he showed that the essence of the Pollard et al. closure scheme could be obtained through consideration of the turbulence kinetic energy budget. We will consider the turbulence kinetic energy budget approach only in this report.

The integral of the TKE equation across the mixing layer and ML/ST interface (that is, the region over which TKE can exist) may be written as

$$\int_{-h-\delta}^{0} \partial_t k^2 dz = G - D - CP \qquad (4.13a)$$

where

$$G = - \int_{-h-\delta}^{0} \underline{\tau} \cdot \partial_z \underline{v} \, dz - \overline{w'(k^2 + \rho_r^{-1} p')}\Big|_{-h-\delta}^{0} \qquad (4.13b)$$

represents the total rate of production of TKE by shear and the flux of TKE across the surface and ML/ST interface,

$$D = \int_{-h-\delta}^{0} \varepsilon \, dz \qquad (4.13c)$$

represents the total rate of viscous dissipation of TKE, and

$$CP = - \int_{-h-\delta}^{0} \eta \, dz$$

$$= - \frac{1}{2} h(\eta_o + \eta_h) - \int_{-h}^{0} (z + \tfrac{1}{2}h) \, \partial_z I_p \, dz \qquad (4.13d)$$

represents the rate at which kinetic energy is lost to potential energy. The first term on the right (in 4.13d) represents the rate at which turbulent motions perform work as they uniformly distribute the change in mixing-layer buoyancy caused by the surface and ML/ST interface fluxes. Since fluxes are defined positive upward η_0 appears with a negative sign to represent the flux into the layer. When $\eta_0>0$, buoyancy is lost from the layer and potential energy is converted to kinetic energy. The integral on the right of (4.13d) is the integro-differential counterpart of surface and ML/ST interface flux mixing for an internally distributed buoyancy source.

To conclude this section, we let

$$\langle k^2 \rangle \equiv \frac{1}{h} \int_{-h}^{0} k^2 \, dz$$

be the geometric mean of the turbulence kinetic energy. We can write

$$d_t(h \langle k^2 \rangle) = G - D + \frac{1}{2} h(\eta_o+\eta_h) + \int_{-h}^{0} (z+\tfrac{1}{2}h) \, \partial_z I_p \, dz, \quad (4.14)$$

which relates the rate of change of total mixed layer kinetic energy to the energy generation and dissipation rates, and to the rate of conversion to potential energy. We have assumed that $k^2(-h-\delta) = 0$, and have neglected the contribution to the mean TKE from the interval $-h \geq z \geq -h-\delta$.

4.3.4 Specific Bulk Models

In the previous sections we mentioned the application of the turbulence kinetic energy budget to the closure

of the bulk model equations. In this section specific models will be described. The essential difference between most of the models arise from their treatments of G, D and to a lesser extent $d_t(h\langle k^2\rangle)$. Nearly all of the models neglect $d_t(h\langle k^2\rangle)$, which is assumed to be small compared with $\frac{1}{2}h\Delta b d_t h$ and G-D. For these so-called "quasi-steady" models

$$\frac{1}{2}\, h\, \Delta b\, \Lambda\, d_t h = G - D + \int_{-h}^{0} (z+\tfrac{1}{2}h)\, \partial_z I_p dz + \frac{1}{2}\, h\, \eta_o, \qquad (4.15a)$$

and

$$\rho_r^{-1}\, d_t PE = G - D + \int_{-D}^{0} z\, \partial_z I_p\, dz. \qquad (4.15b)$$

This is, of course, a stratified flow approximation appropriate as long as

$$h\Delta b >> \langle k^2\rangle . \qquad (4.15c)$$

This strong stratification approximation fails in two regimes. During the very early stage of the response of an initially stratified ocean to wind, h will be small and $h\Delta b$ will be small compared with $\langle k^2\rangle$, which scales like u_*^2. Under typical conditions this stage has a time scale of about one minute and as a result is not significant in a description of overall response. The second regime may occur at the end of the annual ocean cooling period. In this case Δb can vanish; however, the mixing layer stops deepening, so that the TKE equation should become that for equilibrium turbulence in homogeneous fluid

$$G - D = 0 .$$

Parameterizations of G and D in terms of the applied wind stress and friction velocity have been used in many bulk models. As pointed out earlier, the mean momentum equation is irrelevant under these circumstances. Such parameterizations, however, do not predict equilibrium (that is G-D = 0). The value of G-D is independent of the mixing-layer depth in several of the models. This lack of an equilibrium state can have drastic implications. Equation (4.15a) requires non-zero η_h if G-D $\neq$ 0 in the absence of heating; if $\Delta b \to 0$ at the end of the cooling season $d_t \eta \to \infty$, and the mixing-layer can become infinitely deep. Also (4.15b) requires a non-zero rate of change of potential energy--an impossibility in a homogeneous fluid. Also (4.15a) does not predict a steady state solution to the case of wind deepening of a stratified ocean with no surface heat flux if G-D does not vanish. The layer will deepen as long as the wind stress is applied.

As will be described below, the singular behavior of quasi-steady models can be avoided if a so-called "background dissipation" is introduced. The background dissipation, D_b, provides a mechanism by which G-D can approach zero. Then D is written

$$D = D_\varepsilon + D_b$$

where D_ε is the dissipation of wind generated, ML/ST interface shear-generated, and/or convectively generated turbulence, and D_b is unrelated to any of these generation processes. In the gross parameterization models of Kim (1976) and Niiler (1977) D_b is simply set to $\varepsilon_m h$ where ε_m is an <u>imposed</u> background dissipation rate per unit volume.

The Kraus-Turner Model

Kraus and Turner (1967) proposed the first bulk model (henceforth referred to as KT) capable of addressing the time evolution of the mixing-layer/seasonal thermocline system. Their model did not include mean velocity since their interest was primarily thermal structure and their parameterizations of G and D did not require it. Nor did their model include TKE storage. They were first to propose use of the TKE budget to close the model system, and they assumed that the turbulence generation rate could be estimated as

$$\rho_r G = |\underline{\tau}_s| \, \upsilon_* = \rho_r \upsilon_*^3 \, , \qquad (4.16a)$$

when as before $\upsilon_* = |\underline{\tau}_o|^{\frac{1}{2}}$, the friction velocity.
Equation (4.16a) is a representation of the rate of working of the surface stress $\underline{\tau}_s$, which is constant across the interface on the water which has characteristic velocity $\underline{\upsilon}*$. This parameterization ignores the generation of TKE by the interaction of turbulence with shear across the mixing-layer base, and it does not account for the mean velocity of the layer, which can be much greater than $\underline{\upsilon}*$. Kraus and Turner simply set

$$D = 0. \qquad (4.16b)$$

Kraus and Turner demonstrated that the model could qualitatively reproduce major features of the seasonal mixing layer cycle including spring time shallowing to a minimum depth about the summer solstice, continued temperature increase but slow deepening after the solstice, and at first slow then rapid deepening and cooling with the approach of the winter solstice (see Figure 4-2).

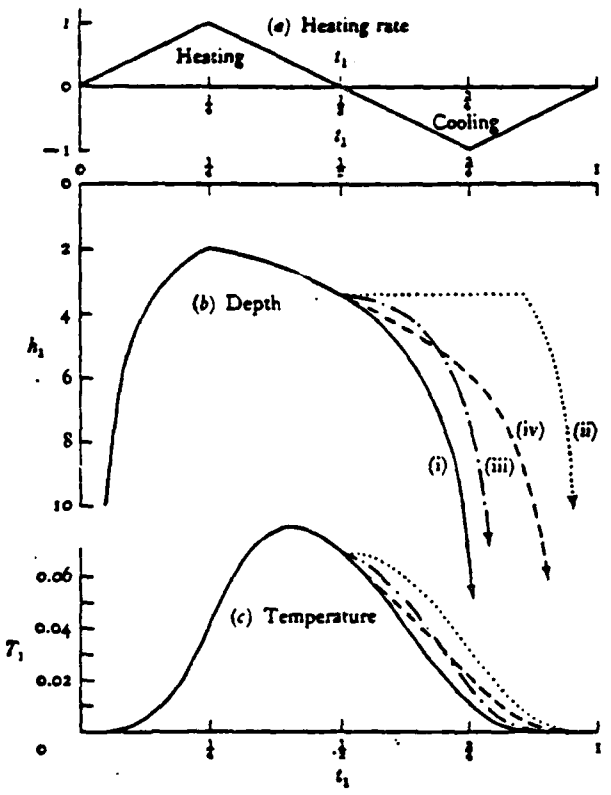

Figure 4-2: Non-dimensional plots of mixed-layer depth (b) and surface temperature (c) as functions of time calculated from a Kraus-Turner model for a sawtooth heating-cooling function (a) and a fixed rate of mechanical mixing. Curves (i) are based on the original energy conserving assumption of Kraus and Turner; (ii) on the assumption that no penetrative convection occurs; (iii) on the inclusion of entrainment due to convection alone (no wind mixing); (iv) on the inclusion of entrainment due to mechanical stirring alone (from Turner, 1973).

Denman included in his version of the KT model the absorption of solar radiation below the mixing layer.

Whereas Kraus and Turner developed the KT model with the intent of explaining seasonal-scale variations, Denman and Miyake (1973) applied Denman's (1973) version to the simulation of oceanographic conditions observed at Ocean Weather Station Papa in the North Pacific in June 1970. Meteorological observations performed at the station were used as the temperature (buoyancy) initial condition. Figures 4.3a and 4.3b present the surface meteorological conditions, measured oceanic response, and model predicted response. Predicted sea-surface temperatures and mixing layer depths are in reasonable agreement with the observations. An interesting feature of the observations and the predictions is the appearance of new shallow mixed layers superposed on deeper already existing mixed layers. The generation of new shallow layers effectively insulates the deeper thermal structure since most mixing activity occurs in the new layers. As the figure shows, each of the new layers eventually mixed down and replaced the existing structure. Differences between the observations and predictions in vertical profile details may result from internal-wave activity, the internal tide, horizontal advection, or, as likely, difficulties associated with the model parameterizations.

The Pollard - Rhines - Thompson Model

Pollard, Rhines and Thompson (1973) proposed a model (PRT) for the occurrence of deepening based on a very

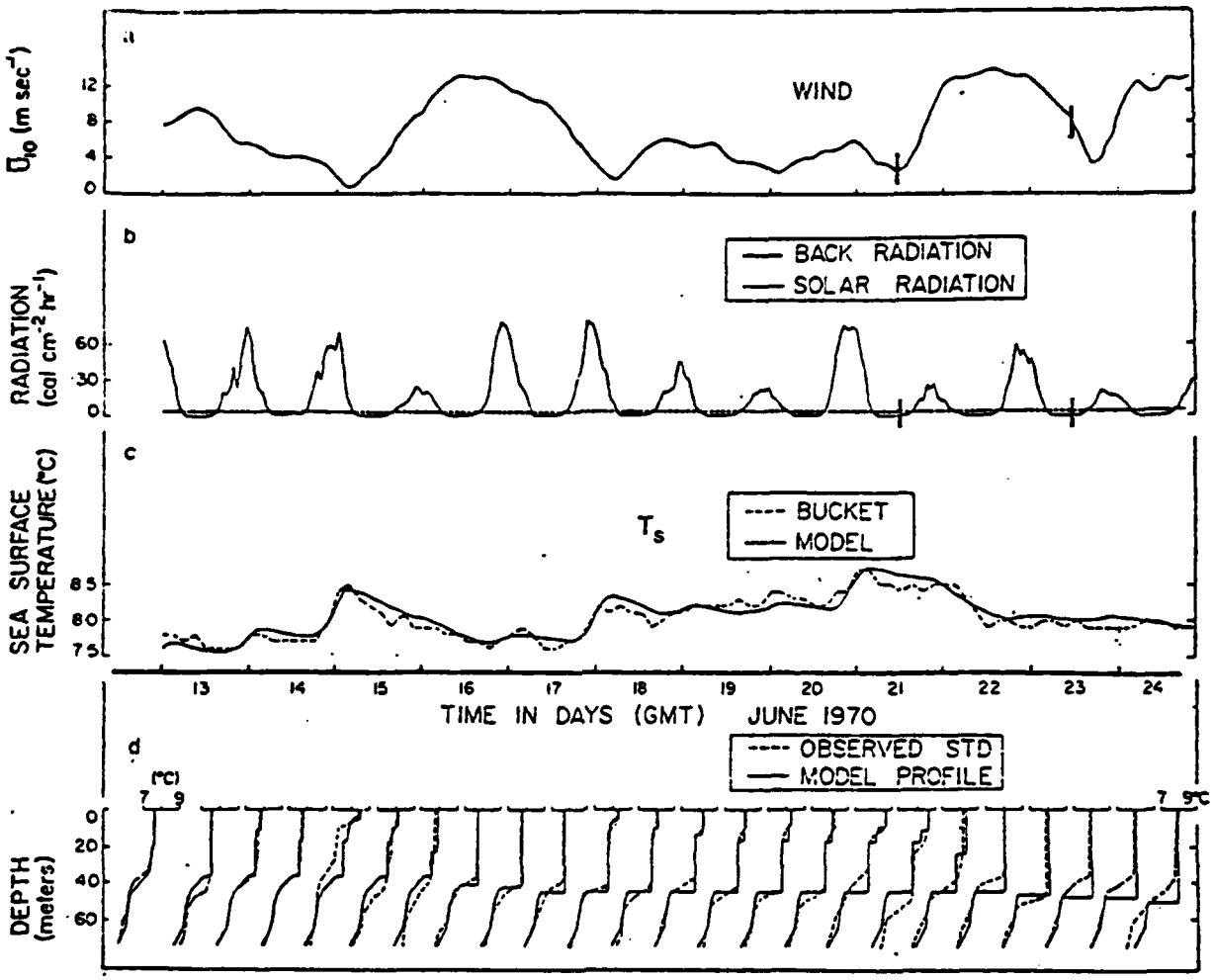

FIGURE 4-3a: Input and results from the Denman ML model for the period 13-24 June 1970 at OWS Papa U_{10} and Radiation components are observed inputs. Observed T_s and T(z) are indicated by dashed lines in the lower two plots; calculated T_s and T(z) indicated by solid lines.

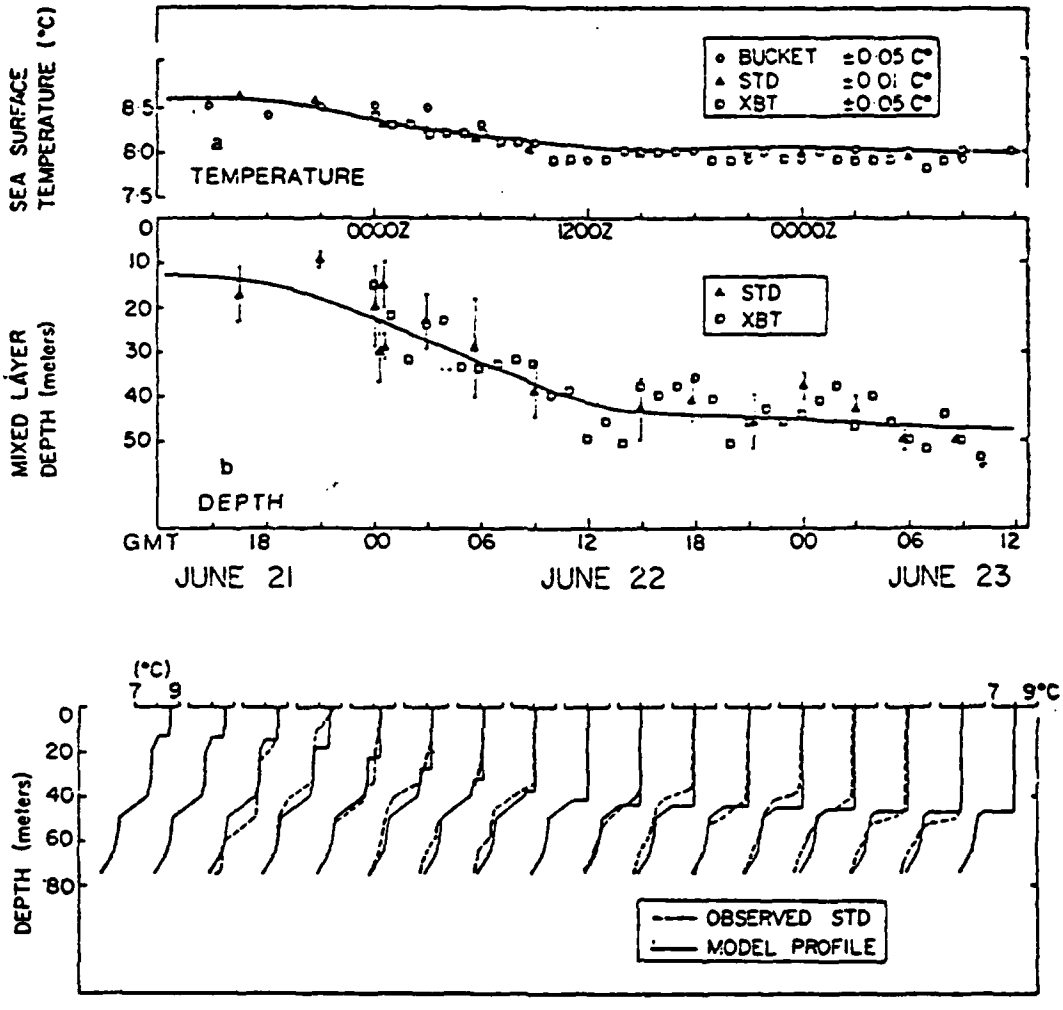

Figure 4-3b: Detail of results shown in Figure 4-3a for the period indicated by the vertical bars approximately 1200 June 21 to 1200 June 23.)

different approach. They defined a mixing-layer Froude number (originally a kind of bulk Richardson number F^{-1})

$$F = \Delta \underline{v} \cdot \Delta \underline{v} / h \Delta b$$

and they argued that while h is deepening

$$F = 1,$$

and that deepening would not occur if F<1. In this model the mean momentum of the mixing layer must be calculated as part of the solution, as distinct from the earlier KT models. This model yields, however, a simple analytic solution for the response of an initially linearly stratified ocean to the onset of a constant wind stress. The mixing layer should deepen for the first half inertial period as

$$h = v_* [4(1 - \cos ft)/f^2 N^2]^{1/4}. \qquad (4.20a)$$

At $t = \pi/f$ the layer should stop deepening and a maximum depth

$$h_{max} = 8^{\frac{1}{4}} v_* (fN)^{-\frac{1}{2}} \qquad (4.20b)$$

should be attained. No further deepening should occur since the Froude number will never again become greater than one. Pollard et al. generalized their results to the case of an arbitrary (stable) initial buoyancy profile $b_o(z)$. They found

$$h^2 \int_{-h}^{0} \left[b_o(z) - b_o(-h) \right] dz = 4 v_*^4 f^{-2}. \qquad (4.21)$$

For small times the PRT solution (4.30a) can be approximated as

$$h = 2^{1/4} u_* (t/N)^{1/2}.$$

Pollard et al. argued that the $t^{1/3}$ dependence proposed by Kato and Phillips (1969) could as easily be interpreted as a $t^{\frac{1}{2}}$ dependence.

Niiler's Synthesis

Niiler (1975) attempted to reconcile the KT and PRT approaches. He assumed that

$$G = G_s + G_i \tag{4.22}$$

where G_s and G_i represent the rate of TKE generation due to processes occurring at the surface and at the ML/ST interface respectively. We have

$$G_s = -\int_{-\zeta}^{0} \underline{\tau} \cdot \partial_z \underline{u}\, dz - \left[\overline{w'(k^2+\rho_r^{-1}p')}\right]_0 \tag{4.23a}$$

and

$$G_i = -\int_{-h-\delta}^{-h} \underline{\tau} \cdot \partial_z \underline{u}\, dz + \left[\overline{w'(k^2+\rho_r^{-1}p')}\right]_{-h-\delta}. \tag{4.23b}$$

These equations can, with suitable assumptions, be reduced to

$$G = m_o u_*^3 - \left[\overline{w'(k^2+\rho_r^{-1}p')}\right]_0 - \frac{1}{2}\, \underline{\tau}_h \cdot \Delta \underline{u}. \tag{4.24}$$

Niiler then applied the KT parameterization to the surface processes so that

$$G_s - D_s = m_o u_*^3,$$

where D_s refers to the dissipation of near-surface generated TKE. He assumed that none of the interface-generated TKE was dissipated so that

$$G-D = G_s + G_i - D_s,$$

or

$$G-D = m_o \upsilon_*^3 - \tfrac{1}{2}\underline{\tau}_h \cdot \Delta\underline{\upsilon}. \tag{4.25}$$

This can be used to obtain the entrainment rate equation

$$\tfrac{1}{2} \Lambda \, (h\Delta b - \Delta\underline{\upsilon}\cdot\Delta\underline{\upsilon}) \, d_t h = m_o \upsilon_*^3 + \int_{-h}^{0} (z + \tfrac{1}{2} h)\partial_z I_p dz + \tfrac{1}{2} h\eta_o, \tag{4.26}$$

If the surface generation rate $m_o\upsilon_*^3$ is ignored and if heat/cooling are neglected the right side of (4.24) becomes zero and h is determined from

$$\Delta\underline{\upsilon} \cdot \Delta\underline{\upsilon}/h\Delta b = 1,$$

precisely the criterion of PRT. Therefore, the PRT model may be considered as a limiting-case bulk model based on the TKE budget.

Niiler examined two classes of solutions to (4.26). He found that for the case of an initially linearly stratified ocean, the response to the onset of a constant wind stress in the absence of heating and cooling was given by

$$h \approx (12m_o)^{1/3} \, (\upsilon_*^2/N^2)^{1/2} \, (Nt)^{1/3} + O(Nt) \tag{4.27}$$

for an initial time period $0<t<N^{-1}<f^{-1}$ for arbitrarily small m_o. Therefore, the PRT solution which is valid for m_o equal zero is a singular special case inappropriate for $m_o \neq 0$, however small.

Niiler described mixing-layer deepening as a three phase process if $h_o<h^*$, where $h^* = 2\upsilon_*(Nf)^{-\frac{1}{2}}$ and h_o is the initial layer depth. Initially surface-produced turbulence is dominant as indicated by (4.27). After about a pendulum hour, however, ML/ST interface shear becomes important and the layer deepens to h^* within a half-pendulum day. Then, since the interface shear will never be as large as during the first half-pendulum day, surface generated turbulence once again becomes dominant. If $h_o>h^*$, on the other hand, G_s will be dominant and interfacially generated TKE can be neglected. Niiler then explained the rather slow thermocline erosion process observed by Denman and Miyake as a case in which $h_o>h^*$. He explained the rapid deepening observations of Stommel et al. (1969) as a case in which $h_o<h^*$, so that interfacially generated TKE was important. Surface processes could be responsible for the observed very rapid deepening rates only with an unreasonably large value of m_o.

A problem pointed out in passing by Niiler (1975) but well known previously with the KT-type model is that the parameterizations of G and D and the neglect of TKE storage lead to ever increasing potential energy since

$$\rho_r^{-1} d_t PE = G-D \qquad (4.28)$$

if solar radiation is treated as a surface flux. The KT model predicts, in fact, that the mixing layer becomes infinitely deep at the end of the cooling season (as long as $u_* \neq 0$) in the absence of an imposed deep thermocline. As was pointed out by Niiler this non-physical situation appears in cyclic simulations with an initially-imposed deep permanent thermocline as a slow cycle-to-cycle increase in the layer depth at any fixed phase.

Exponential Energy Decay

The infinite deepening problem was briefly addressed by Elsberry, Fraim and Trapnell (1976) in a model (EFT) for the response of the upper ocean to a hurricane. They proposed that

$$G-D = G_* \exp(-h/Z) \tag{4.29}$$

where $G_* = u_*^3$ and Z is a scale length on the order of 100 m. They argued that this would prevent the infinite deepening problem. No physical arguments were presented for the form. When h is small $G-D \approx G_*$ and G-D is equal to the downward transfer of turbulent energy by wind stress. As h becomes large, G-D approaches zero so that less energy is available for layer deepening as h becomes large. G-D goes to zero only as $h \to \infty$, however, and infinite deepening will still result. Gill and Trefethen (1977) proposed a similar formulation.

Gill and Turner Convective Dissipation

Gill and Turner (1976) addressed the simulation of oceanic seasonal cycles. They showed that the potential

energy, heat content and surface temperature would have a cyclic behavior if all or some portion of the potential energy which is released during cooling periods were dissipated, rather than converted to kinetic energy and used to deepen the layer. Potential energy is released when the net buoyancy flux becomes positive so that

$$B_o \equiv (\eta_o + I_{po}) > 0 \tag{4.30}$$

where the layer is assumed to be so deep that I_{ph} can be neglected. If we assume that the portion of this energy which is converted to TKE and remains, after dissipation, available to bring about further entrainment is a fraction n of the flux $\frac{1}{2}hB_o$, we must require a dissipation rate

$$D_c = \frac{1}{4} h(1-n) (B_o + |B_o|), \tag{4.31}$$

so that during warming periods $B_o<0$ and $D_c=0$, while during cooling periods $D_c = h(1-n)B_o$.

When n=0 all of the potential energy released during cooling periods is dissipated and no kinetic energy remains to deepen the layer. This is referred to as non-penetrative convection. If n=1 no energy is dissipated, and the mixing layer deepens sufficiently that all of the released potential energy is used in deepening the layer. If $0<n<1$ some portion of the energy is dissipated. This is referred to as partially penetrative convection. Gill and Turner (1976) were able to obtain agreement with the seasonal cycle potential energy, heat content and surface

temperature recorded at Ocean Weather Station Echo with n = 0.15, although the results with n = 0.0 were apparently little different. The observed cycle and model predictions are presented in Figure 4-4. In particular they showed that the combination of wind-induced mixing and dissipation of turbulence arising from convective events could reproduce the observed hysteresis of the water column energy budgets.

Kim's Energy Storage/Background Dissipation Model

Kim (1976) proposed a rather more complex version of the KT model (which we will refer to as KIM) which included a parameterization of TKE storage, and added a background dissipation rate. The latter of these features is sufficient to prevent infinite-deepening, although Kim did not address this issue.

Kim argued that the largest contribution to the rate of change of TKE would come from the first term in the chain rule expansion.

$$d_t(h\langle k^2\rangle) = d_t h\langle k^2\rangle + h d_t\langle k^2\rangle .$$

The first term represents the rate of increase in TKE due to layer deepening. Kim let $\frac{1}{2}c_m^2$ represent a typical value of $\langle k^2\rangle$.

Following KT-tradition, Kim proposed

$$G = m_o u_*^3, \qquad (4.32a)$$

but

$$D = m_d u_*^3 + \varepsilon_m h, \qquad (4.32b)$$

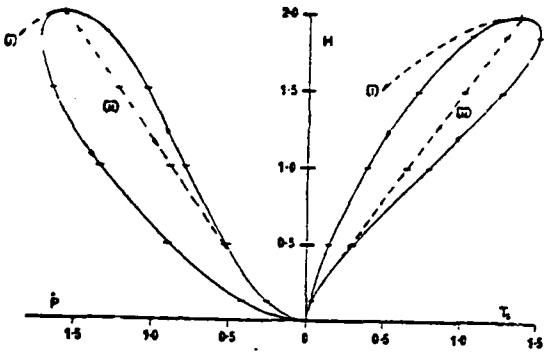

FIGURE 4-4: (a) Curves of H^* vs P^* and H^* vs T_s for the KT model and two variations. The solid lines with H^* increasing shows the identical results for all three versions. The original model produces (i) for decreasing H^*. The model with non-penetrative convection and no wind stirring produces (ii), while the model with both non-penetrative convection and wind stirring produces the solid line. Time marks are drawn at one month intervals. (b) H^* vs P^* and H^* vs T observed over the course of a year at OWS Echo (35°N, 48°W).

so that the KT dissipation is augmented by a contant background dissipation rate ε_m (per unit depth). The values m_o and m_d were chosen so that $m_o - m_d$ is in agreement with Kato-Phillips observations ($m_o - m_d = 1.25$).

The entrainment rate equation for Kim's model can be written as

$$\frac{1}{2} c_m^2 (1+\tilde{R}) d_t h = G-D + \int_{-h}^{0} (z+\tfrac{1}{2}h) \partial_z I_p \, dz + \frac{1}{2} h \eta_o , \tag{4.33a}$$

where

$$\tilde{R} = \Lambda h \Delta b / c_m^2 . \tag{4.33b}$$

We note here that (4.33b) can be written

$$\tilde{R} = R_\tau \upsilon_*^2 / \langle k^2 \rangle .$$

where R_τ was defined as $h\Delta b/\upsilon_*^2$. Then since υ_*^2 is of the same order of magnitude as $\langle k^2 \rangle$, the strong and weak stratification conditions can be written as $R_\tau >> 1$ and $R_\tau << 1$, respectively.

We can also derive

$$\rho_r^{-1} d_t PE = \frac{\tilde{R}}{1+\tilde{R}} (G-D) + \frac{CP+\frac{1}{2}h\eta_h}{1+\tilde{R}} + \int_D^o z \partial_z I_p dz. \tag{4.34}$$

Equation (4.34) states that the rate of increase of potential energy is equal to some fraction $\tilde{R}(1+\tilde{R})^{-1}$ of the conversion of kinetic energy to potential energy which results when the surface buoyancy flux and the internally absorbed buoyancy flux are mixed in the layer, plus the increase due to the increase in water column buoyancy due to internal solar absorption.

To obtain an estimate for c_m^2 Kim considered the case of no heating and no background dissipation so that (4.33a) be written in Kato-Phillips (1969) form as

$$d_t h/\upsilon_* = 2.5\ [(c_m/\upsilon_*)^2 + R_\tau]^{-1}\ . \qquad (4.35)$$

If $R_\tau << (c_m/\upsilon_*)^2$ as in a homogenous fluid, (4.35) yields

$$d_t h/\upsilon_* = 2.5(\upsilon_*/c_m)^2. \qquad (4.36)$$

Kim made use of homogeneous flow results of Lundgren and Wang (1973) who apparently found $d_t h/\upsilon_* \approx 0.25$ so that $(c_m/\upsilon_*)^2 = 9$. Kim argued that this result should be appropriate for all but very small values of υ_* (when $3\upsilon_*$ might be too small to be a reasonable scale.) He therefore set

$$c_m = \max\ (3\ \mathrm{cms}^{-1},\ 3\upsilon_*) \qquad (4.37)$$

with an arbitrarily chosen lower bound.

Kim compared predictions of this model with those of Denman and Miyake (1973) for the Ocean Weather Station Papa data. He reported good agreement with the earlier predictions, and suggested that this must be due to the fact that during periods of weak heating and cooling $\tilde{R}$ remained much larger than one so that the contribution to the TKE budget of $\frac{1}{2}c_m^2 d_t h$ is small, and that during periods of strong heating the meteorological data are too widely spaced in time to allow model differences to be observed (note that $\tilde{R}=0$ during shallowing).

The use of a background dissipation apparently independent of the physical mechanisms responsible for the turbulence is an ad hoc approach to improved predictions. As was subsequently shown by Garwood (1977) and Stevenson (1979), but apparently unknown to Kim, an imposed background dissipation can guarantee finite mixing layer depths under the quasi-steady approximation.

Garwood's Bulk Second-Order Closure

Garwood (1977) was first to show that background dissipation would produce a stable (no infinite deepening) model, under the quasi-steady approximation and his model is in some sense a logical step beyond Kim's. The outlines of Garwood's model were described earlier. He proposed that the mixing-layer base buoyancy flux should be explicitly related to the level of vertical velocity fluctuations, and he proposed that the ratio of the ML/ST interface buoyancy flux to the convergence of the TKE energy flux have a fixed value m_4. Then he derived the relationship

$$\eta_h = m_4 \langle \overline{w'^2} \rangle^{\frac{1}{2}} \langle k^2 \rangle / h. \qquad (4.38)$$

where $\langle w'^2 \rangle$ and $\langle k^2 \rangle$ are obtained by integrating parameterized differential equations for $\overline{u'^2}$, $\overline{v'^2}$, and $\overline{w'^2}$ across the mixed layer.

Garwood followed Niiler's earlier treatment of TKE generation, namely

$$G = m_o u_*^3 - \frac{1}{2} \underline{\tau}_h \cdot \Delta \underline{u}, \qquad (4.39)$$

and he derived a parameterization of the rate of TKE

dissipation from an argument (nearly always applied in second-order turbulence closure theory) that the per unit volume rate of energy transfer to smaller scales (and hence dissipation) can be estimated by $A\mu^2/\tau$ where A is an O(1) constant, μ^2 is the velocity scale of the largest eddies, and τ is the time scale of the largest eddies (see for discussion Tennekes and Lumley, 1972). The dissipation occurs at small scales at which the turbulence is assumed to be isotropic. Garwood suggested that there might be two important time scales in the oceanic boundary layer. Scale τ_1 is given by the mixing layer depth divided by the velocity scale $\langle k^2 \rangle^{\frac{1}{2}}$, and τ_2 is given by f^{-1}, the rotational time scale which Garwood argued could be important for deep mixing layers. He combined these scales on an ad hoc basis into a single time scale which was defined by

$$\tau^{-1} = \tau_1^{-1} + \tau_2^{-1} = \langle k^2 \rangle^{1/2} h^{-1} + f \qquad (4.40)$$

so that $\tau \to \tau_1$ for shallow layers. Then

$$\varepsilon \propto \langle k^2 \rangle \tau^{-1}$$

and from the definition of D (4.6c)

$$D = m_\varepsilon \langle k^2 \rangle^{3/2} + m_f fh \langle k^2 \rangle, \qquad (4.41)$$

so that the dissipation which would have been derived on the basis of a single time scale is enhanced by a contribution linearly proportional to h in a manner somewhat similar to that proposed by Kim. The dissipation rate is not assumed proportional to the rate of TKE generation. It may be worth noting that the estimation $A\mu^2/\tau$ for ε is appropriate only in the case of a single turbulence velocity scale and time scale.

Garwood's first paper (1977) did not include an example application of his model. It did include, however, an interesting analysis of his and several previous models. The analysis showed that the inclusion of the background dissipation is sufficient to prevent infinite mixed layer deepening under adiabatic conditions.

Niiler and Kraus' Synthesis

Niiler and Kraus (1977) published a review of one-dimensional bulk models. They propose a sort of canonical model with G given by (4.25) and

$$D = m_d u_*^3 - (1-s)^{\frac{1}{2}} \underline{I}_h \cdot \Delta\underline{u} + \tfrac{1}{4}h\,(1-n)\,(B_o+|B_o|) \qquad (4.42)$$

so that dissipation of surface generated, interface generated, and convectively generated turbulence is explicitly included. This model assumes that only a fraction s of the TKE generated by interface shear is available for mixing. The rest is dissipated. Then

$$\tfrac{1}{2}\Lambda\,(h\Delta b - s\Delta\underline{u}\cdot\Delta\underline{u})\,d_t h = (m_o-m_d)\,u_*^3 + \tfrac{1}{4}h\,[(1+n)\,B_o-(1-n)|B_o|]$$

$$+ \tfrac{1}{2}h\,I_{ph} - \int_{-h}^{0} I_p dz - C|\Delta\underline{u}|^3 \qquad (4.43)$$

where $C\,|\Delta\underline{u}|^3$ is a gross parameterization of the rate at which TKE is lost to internal waves. Equation (4.43) is slightly different than Niiler and Kraus' (10.29). They

define B_o as the sum of the surface buoyancy flux plus about 50% of the incoming solar radiation, which they treat as a surface flux.

For the case of a linearly stratified ocean to which a constant wind stress and heat flux are applied, the heat and momentum equations yield

$$h\Delta b = \tfrac{1}{2}N^2h^2 - B_o t,$$

and

$$\underline{\upsilon} = \frac{\upsilon_*^2}{nf}\,(\sin ft,\ \cos ft - 1).$$

Substituting these into (4.43) leads to

$$\underset{A}{\tfrac{1}{2}d_t h}\ [2\ \underset{B}{\langle k^2\rangle} + \underset{B'}{\tfrac{1}{2}N^2h^2} - \underset{C}{B_o t} - \underset{D}{2s\upsilon_*^4 f^{-2}h^{-2}(1-\cos ft)}]$$

$$= \underset{E}{m_o\upsilon_*^3 + \tfrac{1}{2}nhB_o}.$$

(4.44)

An analysis of this case revealed a sequence of phases in the development of the mixed layer:

- At the onset of the wind, terms A and D dominate and the depth of the ML is linearly dependent on t.

- By time t_1 (dependent on N and m_o) terms B and A become comparable.
- After this time, terms B and D dominate and the ML increases as $t^{1/3}$.
- The deepening process continues until term C becomes significant (at a time dependent on N^{-1}).
- As term B and C become comparable, deepening becomes rapid. Term C reaches its maximum at a time proportional to f^{-1}.
- Past this point, term C decreases, B and D again dominate and deepening occurs as $t^{1/3}$.
- Once depth becomes sufficiently large ($h \propto u_*^3/B_o$), convective deepening dominates the process and h is given by terms B, B', and E.

4.3.5 Bulk Model Predictions and Intercomparisons

In the previous section we described a number of bulk mixing layer models. The emphasis in this section will be on model predictions and intercomparison.

The application by Denman and Miyake (1973) of the Denman KT model (DKT) was described in the previous section. The model was able to predict the variation in sea-surface temperature, mixing-layer depth, and vertical thermal profile characteristics observed during an 11 day period at OWS Papa in June 1970. Tabata (1965) addressed the effects of advection on temperature and salinity at Papa, and Denman and Miyake argued that these were far smaller than the effects of synoptic scale meteorological events. Papa

therefore appeared to be an ideal site for the collection of data to support modeling of entrainment processes and mixed layer dynamics. It was later the site of the Mixed-Layer Experiment (MILE).

Thompson (1976) presented a rather detailed comparison of the predictions of a Kraus-Turner model (DKT), a Kraus-Turner model with Gill-Turner dissipation, and the Pollard et al. model (PRT) for a one-year time period at Ocean Weather Station N. The observed isotherm depths for the period are shown in Figure 4-5. Unfortunately, Thompson read the data tape incorrectly and the isotherm depths indicated in the figure, and used in the comparison should be multipled by 5/3. The PRT model agreed best with the misinterpreted data. Thompson (1977) published further comparisons using the corrected data. Figures 4-5b and 4-5c display simulations performed with the PRT and DKT models (but with a very small value of m with DKT model). Figure 4-6 displays simulation performed with the Elsberry and the Gill-Turner modifications of KT.

The summertime mixed layer predicted by PRT is substantially shallower than that observed in the data. For example, the PRT-predicted 1 October mixed-layer depth (actually the depth of the 23°C isotherm) is about 15 m versus 40-45 m. The depth predicted by the other models are: 30 m for DKT; 30 m for EKT; 25 m for GT. The KT-type models all predict overly large gradients at the layer base and below. Only the GT model predicts a final profile in near agreement to the initial profiles. The PRT model exhibits insufficient winter deepening, and the DKT and EKT models predict far too much deepening.

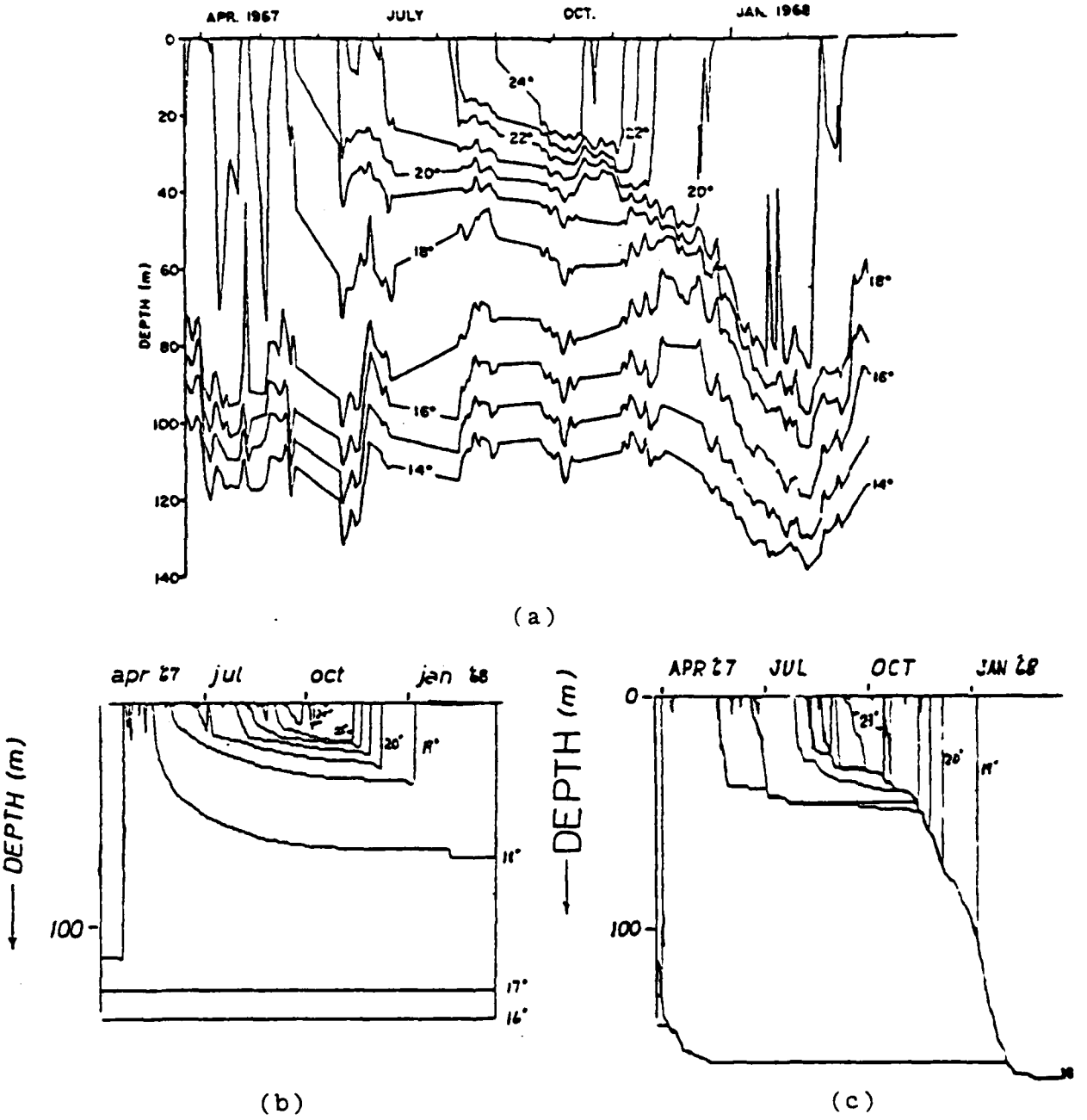

FIGURE 4-5: (a) Observed isotherm depths vs. time between 24 March 67 and 12 March 68 at OWS November (30°N, 140°W). Depths in this plot should be multiplied by 5/3 to obtain correct values. (b) Isotherm depths from KT model using stratification at OWS N on 24 March 67 as initial condition. (c) Same as (b), but with DKT model and the very small value m=0.0001.

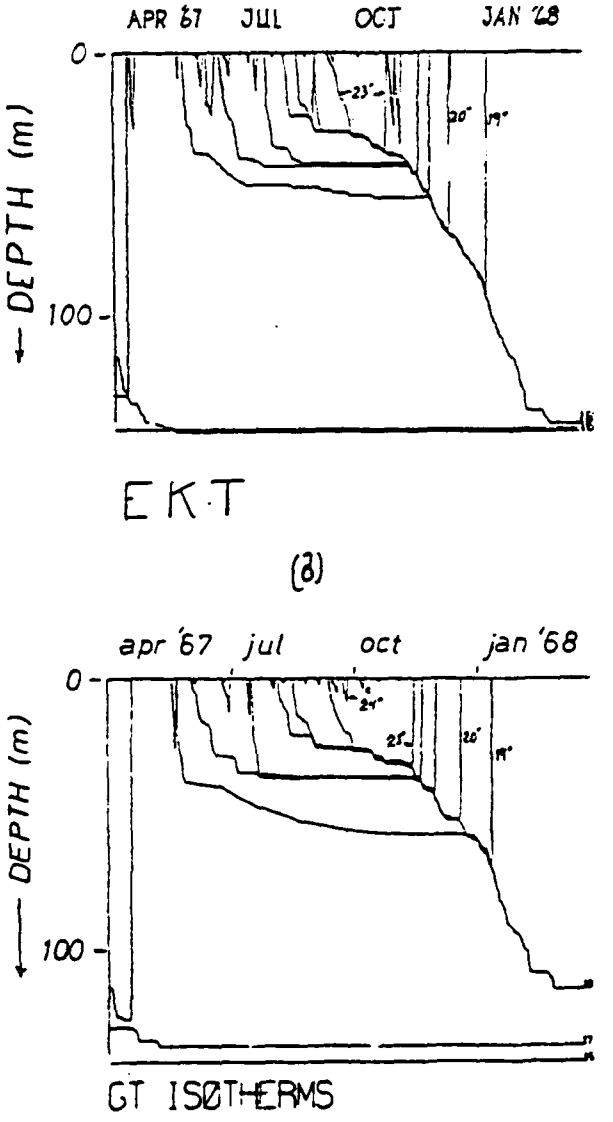

FIGURE 4-6: (a) Same as (4-5b) but with EKT exponential model with m=0.0012, z=100 m.
(b) Same as (4-5b) but with GT model using m=0.0012.

Price et al. (1978) performed an extensive analysis of two cases of storm-induced mixed-layer deepening. The emphasis in this work was on an assessment of the importance of ML/ST interface shear to mixed-layer deepening.

Temperature, salinity and currents were measured during February 1973 and June 1972 at nearby locations in the Gulf of Mexico. The cases were simulated using the Niiler-Kraus (1977) model (4.43) with the last three terms neglected. Two submodels were emphasized; both neglect the surface buoyancy effect. In the TEM model (turbulence erosion model), s = 0 and (4.43) becomes

$$\frac{1}{2}\,\Lambda(d_t h)\,h\Delta b = m u_*^3;$$

in the DIM (dynamic instability model) model $m_d = m_0$ and (4.43) reduces to

$$\frac{h\Delta b}{\Delta \underline{u}\cdot\Delta \underline{u}} = s,$$

a variant of the PRT model, but with a critical value of F equal to s^{-1}.

Figures 4-7 through 4-9 display the meteorological and oceanographic conditions observed in February and the DIM and TEM simulations. The constants m and s were set by requiring that the predicted mixed layer depths at the end of the simulations equal the observed layer depth of 46 m. Price et al. found s = 0.70 and m_o = 0.35. The required value of m_o found here is substantially smaller than unity as was used by Denman and Miyake (1973).

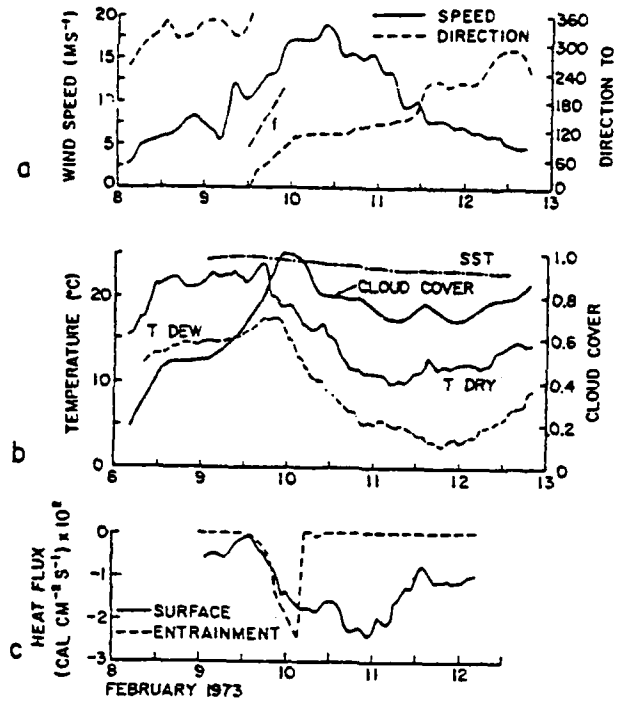

(4-7)

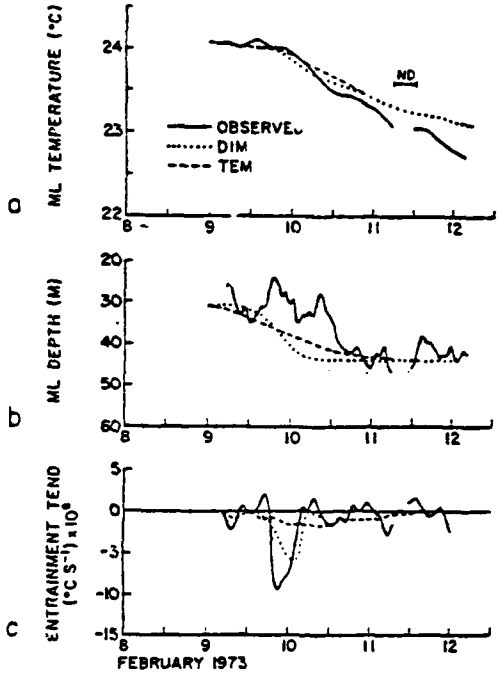

(4-8)

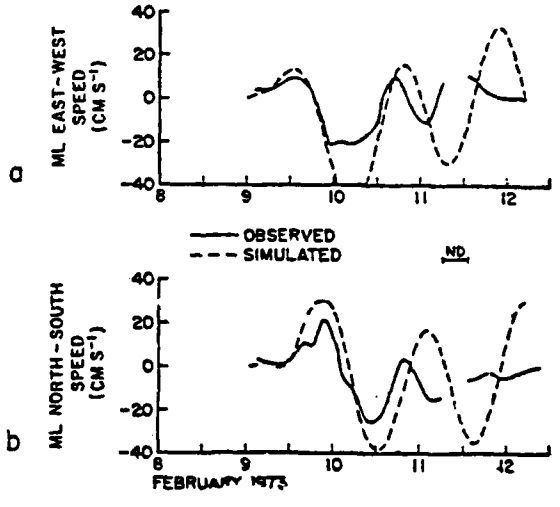

(4-9)

FIGURES 4-7 - 4-9 Meteorological forcing (4-8), mixed layer response (4-9), and velocity component response (4-10) predicted by Price et. al. DIM and TEM models simulated conditions in Gulf of Mexico in February 1973.

The entrainment heat flux in Figure 4-8c is that computed from DIM. A cold front passed over the observation site late on 9 February, and DIM predicts that nearly all entrainment occurs during a 12-hour period centered at about 2400 LT on 9 February. Price et al. argue that the differences between the predicted and observed ML temperatures shown in Figure 4-8a are due to horizontal advection. Mixed-layer depth is shown in Figure 4-8b. DIM predicts a very rapid deepening over about 12 hours and no further deepening; TEM predicts a much slower rate. Price et al. claim that the large variation in observed layer depth variations result from inertio-internal waves with O(5m) vertical displacement. The entrainment tendency displayed in Figure 4-8c is simply the rate of change of mixed-layer temperature due to entrainment. The observational data and DIM show large negative values of entrainment tendency late on the ninth. TEM is a gradual erosion model and does not exhibit the observed peak. TEM appears unable to describe the rapid entrainment process. The simulated and observed values of $\Delta \underline{v}$ are shown in Figure 4-9. Good agreement is realized only during acceleration on the ninth. After this $\Delta \underline{v}$-observed appears to rotate clockwise faster than $\Delta \underline{v}$-computed and becomes smaller. Price et al. suggest that these results indicate the vertical propagation in inertio-internal waves out of the mixed layer.

Price et al. provided additional evidence that mean shear, and not wind stress, per se, dominated ML deepening by showing that the observed entrainment tendency was well correlated with $\underline{\tau}_s \cdot \Delta \underline{v}$, a rate or work, not with $|\underline{\tau}_s| u_*$ as assumed by Kraus and Turner.

Price et al. performed similar analyses with predictions of DIM and TEM for the June observations. The observations and model predictions are displayed in Figures 4-10 through 4-12. The simulations were performed with values of s and m chosen so that the predicted layer depths were in agreement with the observed value, 26 m, at the end of the 5-1/2 day simulation. The value of s thus determined was 0.60, and the value of m was 0.9. These should be compared with the February values 0.70 and 0.35, respectively.

The central conclusion of this work is that under the circumstances observed mean momentum and shear across the ML/ST interface are the keys to parameterizing the entrainment process. Shear stress and u_* are not directly relevant, in contradiction with the usual assumption of KT models. These observations are in agreement with Price's (1979) later reevaluation of the Kato-Phillips and Kantha-Phillips-Azod observations. As described earlier, Price suggested that these observations indicate a critical bulk Richardson number (or inverse Froude number) of 0.6, in remarkable agreement with the field observation described above.

While the field observations and analysis of Price et al. are consistent with the revaluated laboratory observations, predictions with the PRT model, with $F_c = 1/0.6$, of the seasonal cycle as described earlier can only become less accurate. Mixing will be predicted to occur to shallower depths for larger F_c, as can be demonstrated by extending the PRT model to the general case of critical Froude number. Equation (4.20a) becomes

$$h = u_* F_c^{-\frac{1}{4}} [4(1-\cos ft)/f^2N^2]^{\frac{1}{4}}$$

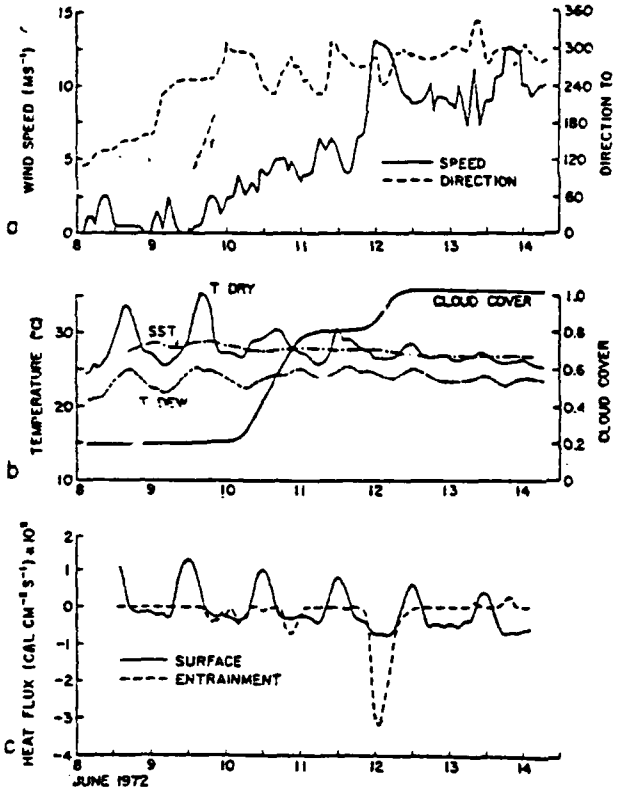

(4-10)

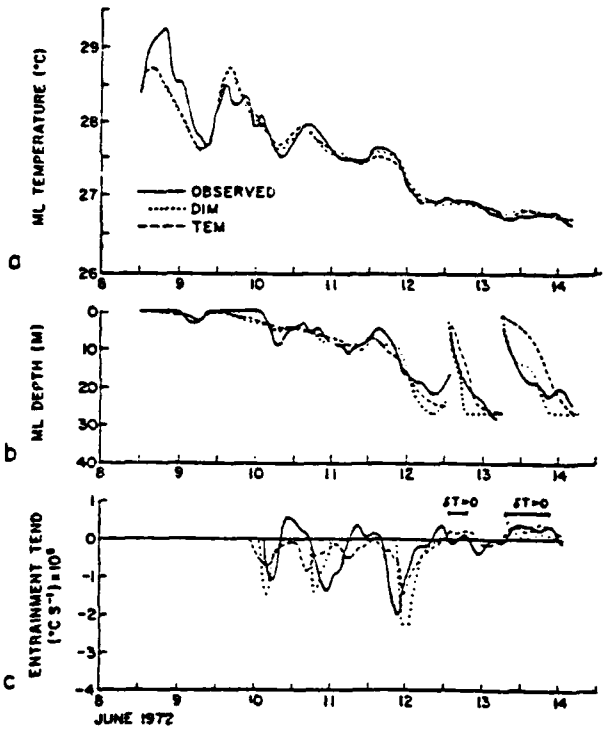

(4-11)

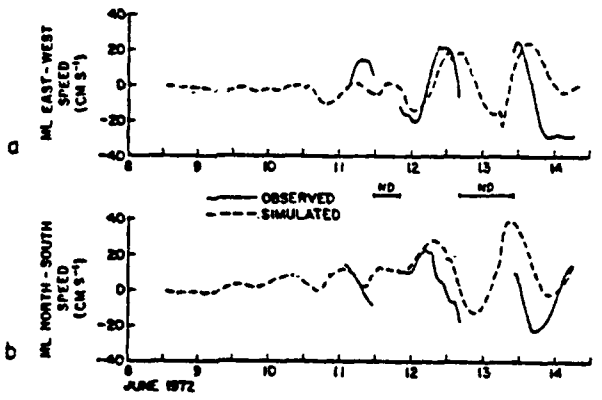

(4-12)

FIGURES 4-10 - 4-12 Same as Figures 4-7 - 4-9 but for June 1973.

4.4 DIFFUSION OR GRID-POINT MODELS

In the previous section we considered bulk mixing-layer models - models which assume the existence of a mixed surface layer. The partial differential equations for buoyancy, salt and momentum conservation reduce to ordinary differential equations for the mean values in the layer, and these models are analytically simple. They have the attractive feature that much of the physics involved in upper-ocean dynamics is explicitly treated, although in a parameterized fashion. They do not, however, treat the evolution of conditions below the mixed-layer base, and if such is desired an additional seasonal thermocline model must be appended. They also do not allow a detailed analysis of mixing processes within the layer.

Diffusion models, on the other hand, treat the mixed-layer/seasonal thermocline system in a uniform manner, and they do not require an *a priori* uniform mixed-layer assumption. The partial differential equations (in z and t) for b, s and $\underline{u}$ are solved numerically for the time evolution of b, s and $\underline{u}$ at a vertical array of grid points which are closely spaced compared with the mixing-layer thickness. The mixing-layer depth if required is determined *a posteriori* from an examination of turbulence flux predictions or from an examination of predicted temperature. The models are more complex to program and interpret and have not received nearly or much interest from the oceanographic community as bulk models.

Diffusion models require the explicit calculation of turbulence fluxes as a function of depth and time, and in many of the models the turbulence kinetic energy is predicted as well. At the expense of simplicity, diffusion models yield far more detailed predictions of mixing layer dynamics than are possible with bulk models.

4.4.1 Buoyancy, Salinity and Momentum Conservation

The basic conservation equations for buoyancy, salt and momentum were presented in Sections 4.2.1 and 4.2.2. Closure of these equations requires the computation of the turbulence fluxes.

4.4.2 Turbulence Flux Models

Turbulence flux models can be classified in terms of their complexity as "no equation" models, "one-equation" or "k" models, "two-equation" or "k-l" models and "many-equation" or "second-order closure" models. It may be useful to discuss what is meant by these terms before we describe specific models. "No-equation" models describe turbulence fluxes algebraically, in terms of mean variables (here b, S and $\underline{\nu}$), and perhaps an imposed length scale. An

"eddy diffusivity" is usually defined and the turbulence flux of a mean quantity, ϕ say, is related to the gradient of ϕ as

$$\overline{w'\phi'} = -K_\phi \partial_z \phi,$$

where K_ϕ is the "eddy diffusivity". Prandtl's (1925) mixing length hypothesis is a well-known example of this approach. Prandtl defined

$$K_\phi = l_m^2 |\partial_z \phi| \quad , \tag{4.45}$$

where l_m is an imposed mixing length. Equation (4.45) is usually explained in analogy with molecular diffusion in which case kinetic theory provides justification. Tennekes and Lumley (1972) should be reviewed for a critique of this approach.

"One-equation" or "k" models follow from Prandtl's (1945) suggestion that the eddy diffusivity be related to the local turbulence kinetic energy k^2. Prandtl argued that the eddy diffusivity should be a local property of the turbulence, which he characterized in terms of the kinetic energy and a length scale. Then

$$K_\phi = kl.$$

The energy k is determined from a parameterized version of the TKE equation, and l is imposed algebraically or empirically.

"Two-equations" or "k-l" models include a second transport differential equation for l or some quantity from which l can be computed. Then (4.45) is used to compute K_ϕ. The idea originated with Kolmogorov (1942). An equation for l or an l-like quantity such as $E = k^{3/2}l^{-1}$ must be derived from the Navier-Stokes equations, then parameterized to make it solvable.

"Many-equation" or "second-order closure" models are based on the transport equations for all of the Reynolds stresses $\overline{u_i'u_j'}$ (6 components) and turbulence heat fluxes $\overline{u_i'T'}$ (3 components) which are derived from the Navier-Stokes equation and from the heat or salt conservation equations. Usually geometric simplifications are possible and approximations can be made, both of which may significantly reduce the number of equations involved. The models are usually referred to as "second-order" closure models since closure is achieved by parameterizing higher-order statistics such as $\overline{u_i' u_j' u_k'}$. The first such model was proposed by Chou (1945), but real interest only arose in the late 1960's. The models are complex and computer-time consuming, and have only recently been applied to one-dimensional upper-ocean simulation (Warne-Varnas, private communication). The sequence of papers by Hanjalic and Launder (1972), Launder (1975) and Launder, Reece and Rodi (1975) provide detailed examples of this kind of model. They are in principle especially useful for complex flows which exhibit multiple length or time scales.

The Ekman Model

Probably the earliest upper-ocean diffusion model is that of Ekman (1905) which ignored buoyancy and salinity

effects and assumed K_m constant (a "no-equation" model). This classic work produced the "Ekman spiral" descriptions of the upper-ocean current response to steady wind stress. This model is not appropriate to buoyancy influenced upper-ocean studies and we will not address it further.

The MA Model

Munk and Anderson (1948) used dimensional considerations and proposed that the eddy diffusivity coefficients of a "no-equation" model for heat and momentum should be functions of the gradient Richardson number which, in the absence of salinity effects is

$$Ri = \alpha g \partial_z T / |\partial_z \underline{v}|^2 .$$

The Richardson number is a measure of the balance between the stabilizing effect of the averaged density gradient and the destabilizing effect of vertical shear. Munk and Anderson did not consider salinity; they proposed the following expressions (where K_h is the eddy diffusivity of heat):

$$K_h = K_o(1 + \beta_h Ri)^{-n_h} \qquad (4.46a)$$

and

$$K_m = K_o(1 + \beta_m Ri)^{-n_m} \qquad (4.46b)$$

where

$$n_h = 3/2,\ n_m = 1/2,\ \beta_h = 10/3,\ \beta_m = 10, \qquad (4.46c)$$

and K_o is a function (an unspecified function, in fact) of the surface wind stress. These coefficients were set by analysis of atmospheric boundary-layer data. Munk and Anderson proposed K_o = 150 cm^2/sec for a wind stress of one dyne-cm^{-2}.

The VZ Model

Vager and Zilitinkevich (1968) proposed a one-equation model for the eddy diffusion coefficients based on Prandtl's (1945) extension of classical mixing-length theory for homogeneous flows. They did not consider salinity effects, and they proposed

$$K_h = K_m = C_o \ell k, \tag{4.47a}$$

where C_o is a constant, ℓ is a turbulence mixing length, and k is the square root of the turbulence kinetic energy. The turbulence kinetic energy is computed from a parameterized form of the TKE equation for a buoyant fluid (4.6a):

$$\partial_t k^2 = K_m |\partial_z \underline{v}|^2 - K_h \alpha g \partial_z T + C_1 \partial_z (K_m \partial_z k^2) - C_2 k^3/\ell, \tag{4.47b}$$

where the first two terms on the right are the eddy diffusion parameterizations of the first two terms on the right of (4.6a), the third term is an eddy diffusivity treatment of the turbulence flux term, and the fourth term is a parameterization of turbulence energy dissipation rate.

The constants C_1 and C_2 are set to 0.73 and 0.099 respectively. The length scale ℓ is determined from a hypothesis regarding boundary-layer turbulence from which

$$\ell(z) = \kappa k \int_0^z k^{-1} dz.$$

The flux of TKE at the ocean surface is set to zero, and the TKE itself is set to zero at the model bottom (not the actual ocean bottom).

The MY Level 2 Model

Mellor and Yamada (1974) developed a series of four turbulence closure models for planetary boundary layers through a more or less systematic scaling of the terms in a second-order closure model. The MY Level 2 model is formally similar to, but simpler than, the VZ model. Mellor and Durbin (1975) applied it to the oceanic case. The MY Level 2 model can be expressed as

$$\overline{w'v'} = -\ell\sqrt{2}k\tilde{S}_M \partial_z \underline{v} \qquad (4.48a)$$

and

$$\overline{w'T'} = -\ell\sqrt{2}k\tilde{S}_H \partial_z T, \qquad (4.48b)$$

which suggest an eddy diffusivity formulation with $K_m=\sqrt{2}\ell k\ \tilde{S}_M$ and $K_h=\sqrt{2}\ell k\tilde{S}_H$. The turbulence kinetic energy, k^2, is determined from a parameterized, steady-state TKE equation,

$$0 = K_m|\partial_z \underline{v}|^2 - K_h \alpha g \partial_z T - (2^{\frac{1}{2}}k)^3/15\ell \qquad (4.48c)$$

which represents a balance between shear production, potential energy conversion, and dissipation.

The model neglects the turbulence flux of turbulence term. The mixing length ℓ is determined from a coarse measure of the vertical extent of the turbulence field given by the ratio of its first and zeroth moments:

$$\ell = \omega \int_{-\infty}^{z} k^2 z dz \Big/ \int_{-\infty}^{0} k^2 dz. \tag{4.48d}$$

The quantities $\tilde{S}_H$ and $\tilde{S}_M$ are stability functions which are given in terms of the flux Richardson number

$$R_f = \alpha g K_H \partial_z T / (\underline{\tau} \cdot \partial_z \underline{U}). \tag{4.48e}$$

The functions $\tilde{S}_M$ and $\tilde{S}_H$ are displayed in Figure 4-13 as a function of Richardson number. Note that $\tilde{S}_M$ and $\tilde{S}_H$ are zero for $R_f > 0.21$ or $R_i > 0.23$. This limiting Richardson number is a prediction of the model and is not an imposed constraint. It roughly agrees with the prediction of linear stability theory that a sufficient condition for stability in a stratified shear flow is $R_i > 1/4$.

Mellor and Durbin applied the model to the simulation of the Ocean Weather Station Papa data of Denman and Miyake (1973). They presented only a comparison of time-depth isotherm contours which is shown in Figure 4-14. The model predictions and the data agree very well. The data includes internal-tides and inertio-gravity wave displacements which are not relevant to this comparison.

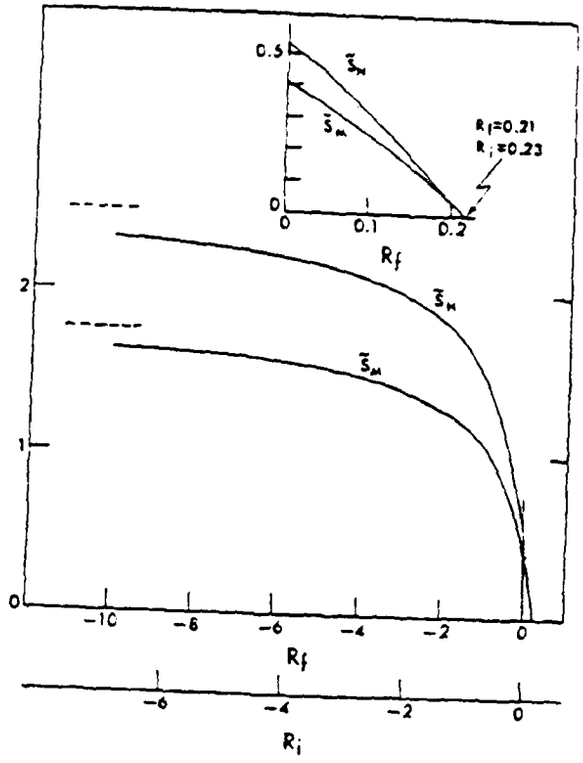

FIGURE 4-13: Functions S_M and S_H as functions of R_F according to (4.60^{H}f, g)

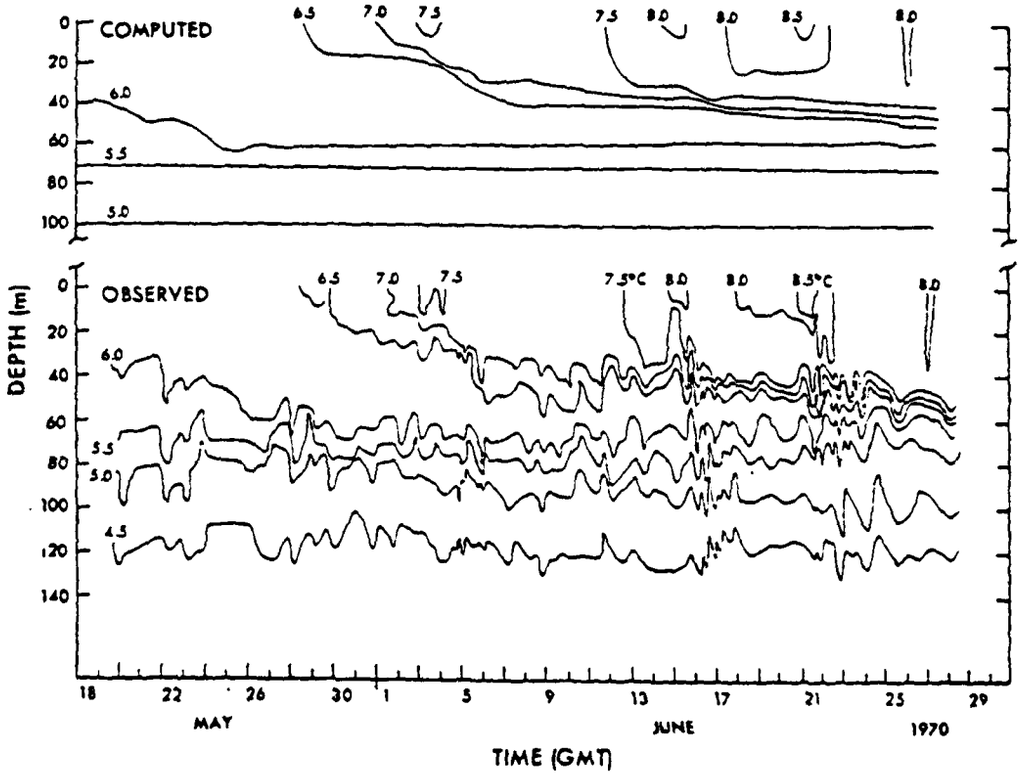

FIGURE 4-14: Mellor and Durbin computation of isotherm depths vs. time at OWS Papa using the data of Denman and Miyake.

The KKS Model

Kochergin, Klimok and Sukhorukov (1976) proposed a two-equation model for the turbulence fluxes which includes parameterized equations for the time rates of change of the TKE and turbulence dissipation rate. The model was applied to the oceanic case by Marchuk, et al. (1977), who argued that the model provides more details of the evolution of turbulent processes and the structure of the mixed-layer/seasonal-thermocline interface.

By the KKS model

$$K_m = 0.08k^2/\varepsilon \tag{4.49a}$$

and

$$K_h = K_m(1 + 10Ri)^{1/2}(1 + 10Ri/3)^{-3/2} \tag{4.49b}$$

The latter equation is based on the MA model.

The TKE is determined from a model equation very similar to that used in the VZ model:

$$\partial_t k^2 = K_m|\partial_z \underline{v}|^2 - K_h \alpha g \partial_z T + \partial_z(K_m \partial_z k^2) - \varepsilon. \tag{4.49c}$$

The dissipation rate is determined from

$$\partial_t \varepsilon = 1.38 \frac{\varepsilon}{k^2} K_m|\partial_z \underline{v}|^2 - 1.4 \frac{\varepsilon}{k^2} g\alpha K_h \partial_z T \tag{4.49d}$$
$$\frac{\varepsilon^2}{k^2} + \partial_z(K_m \partial_z \varepsilon).$$

The constants in (4.49d) were determined from an analysis of stationary duct flow. The fluxes of k^2 and ε are set to zero at the ocean surface, and the quantities themselves are set to zero at the model bottom.

Marchuk et al. applied the model to a rather qualitative simulation of a storm-induced mixed-layer deepening event reported by Halpern (1974). They presented no direct data/model comparisons, but pointed out that the layer did deepen approximately the correct amount. Figure 4-15 displays predicted temperature and dissipation rate profiles at 6-hour intervals. The model input wind speed increased linearly from a value of 4 ms^{-1} at the outset to 14 ms^{-1} at 36 hours. It then decreased linearly to 5 ms^{-1} at 60 hours. The predictions show a rather uniform mixed-layer deepening rate during the first 36 hours, followed by an increasing rate of deepening during the remaining 24 hours. The reason for this is not addressed. The turbulence energy dissipation rate (which is probably of the same order of magnitude as the production rate) is at first largest near the surface where shear is largest. As the simulation proceeds, however, shear at the layer base gives rise to equally large or larger production and, hence, dissipation rates. Turbulence generated at the layer base is most responsible for deepening.

The KSI Model

Kondo, Sasano and Ishi (1979) proposed an upper ocean model for the detailed analysis of diurnal period variations of current and temperature. The KSI model is substantially different from the other diffusion models discussed here in that the eddy diffusivities are based on

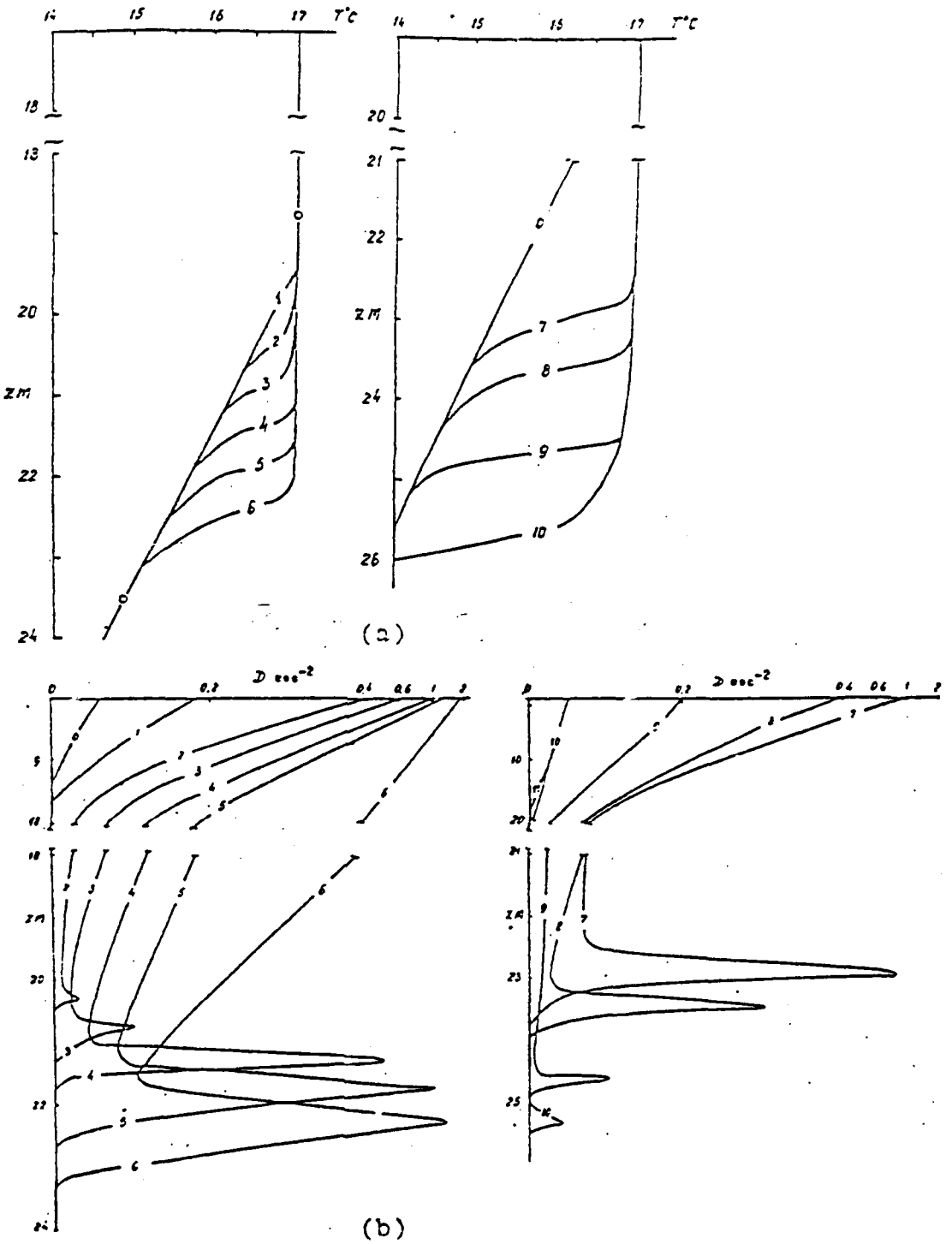

FIGURE 4-15: (a) T - Z profiles, and (b) TKE dissipation rate profiles at 6-hour intervals using the KKS model. (Marchuk, 1977). The quantity D is equal to $\frac{1}{2}\varepsilon\nu^{-1}$ where ν is the kinematic viscosity.

atmospheric boundary layer observations cast in the form of Monin-Obukhov theory. Monin-Obukhov theory was developed to describe the base region (first 30 meters, roughly) of the atmospheric boundary layer within which vertical variations of turbulence fluxes can often be neglected.

The KSI model extends Monin-Obukhov formalism to apply to cases in which the fluxes vary. It also incorporates the salinity equation with the assumption that the eddy diffusivity of salt and heat are equal.

Kondo et al. published the results of a series of computations. An example is presented in Figure 4-16 which shows predicted and observed surface temperature diurnal variations for four mean wind speeds. The data are averages over many observations performed in March, April and September. The model agrees well with the data and predicts diurnal temprature changes as large as 1°C under light winds of 2 - 3 ms^{-1} to about 0.2°C for winds of 7.3 ms^{-1}. Details of the observation and of the boundary condition applied to the model are not described.

4.4.3 Diffusion Model Intercomparisons

The diffusion models discussed in the previous section can be roughly divided into two classes: those based primarily on observation, dimensional analysis, and simple stability arguments, and those based on a treatment of some kind of the turbulence kinetic energy equation. The MA and KSI models fall into the former case while the VZ, MY

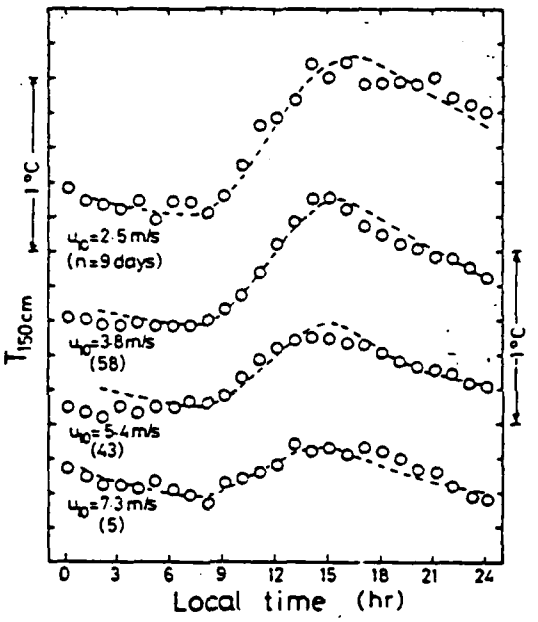

FIGURE 4-16: Diurnal changes in surface T vs time using KSI Model with four different surface wind speed. Circles indicate observations under similar wind conditions.

and KKS models fall into the latter. The numerical solution of the conservation equations is not made especially difficult by the use of any of these diffusion models, although the VZ and KKS models lead to substantially more complex computer codes. Perhaps it is a result of this complexity that very few comparisons between the models have been performed.

We are aware of only one attempt at a diffusion model intercomparison, and more comparisons are sorely needed. Martin (1976) compared the MA, MY and VZ models, and a first order result of the comparison is presented in Figure 4-17. The figure shows the ratios of K_m and K_H to their neutral unstratified values as a function of gradient Richardson number. The VZ model ratios are only approximate since they are based on a simplification of (4.59b). Clearly substantial differences exist between the models. The MA model predicts turbulent mixing even under very stable conditions (very large values of R_i). Under such conditions the diffusivity of momentum is far larger than that of heat and it could perhaps be argued that in this case the turbulence fluxes are parameterizations of momentum transport due to internal waves. The VZ and MY models, on the other hand, predict a Richardson number mixing cut-off of 1.0 and 0.23 respectively.

Martin also compared the predictions of the three models for two cases, wind deepening and wind deepening with heating. Figures 4-18 through 4-21 display predictions of the three models for a case in which a wind stress of 1 dyne/cm^2 was imposed at time zero on the surface of a body of water with an initial stratification corresponding to 0.1^{o}C/m. The surface heat flux was set to zero. Figure

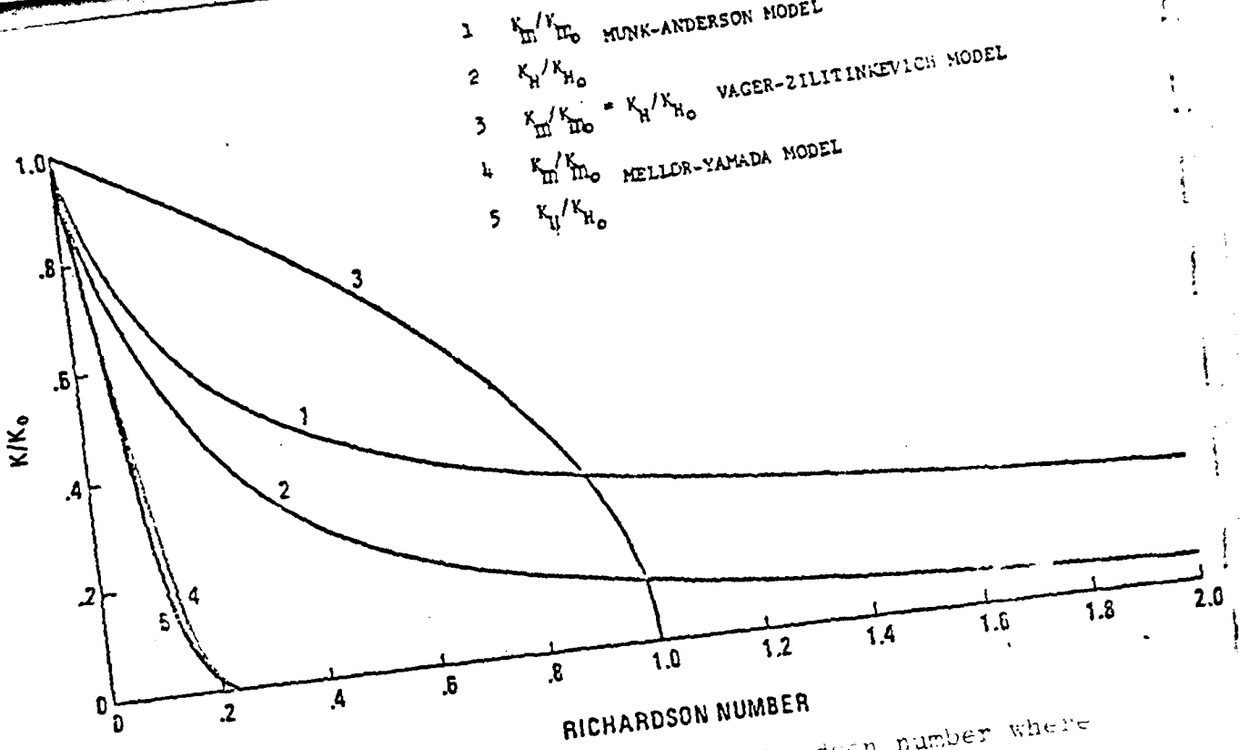

FIGURE 4-17: Dependence of K/K_o on Richardson number where K_o is the value under neutral conditions.

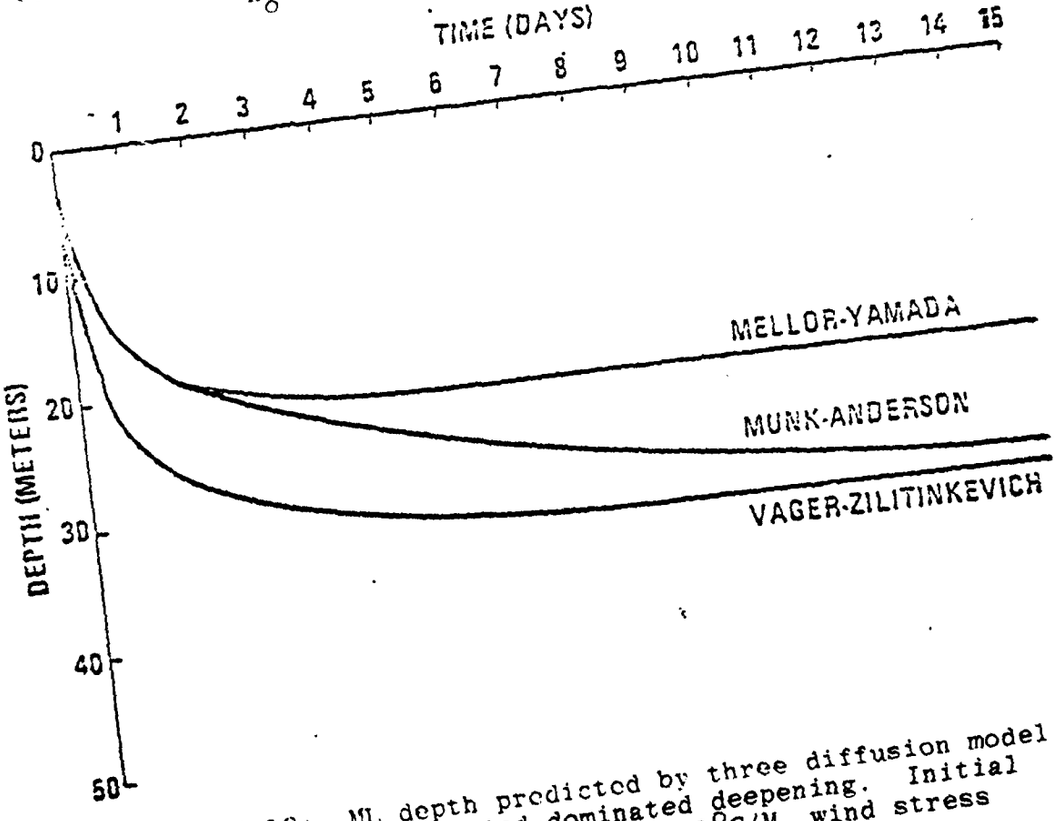

FIGURE 4-18: ML depth predicted by three diffusion model due to wind-dominated deepening. Initial stratification was $0.1^{o}C/M$, wind stress 1 dyne/cm^2, and zero heat flux.

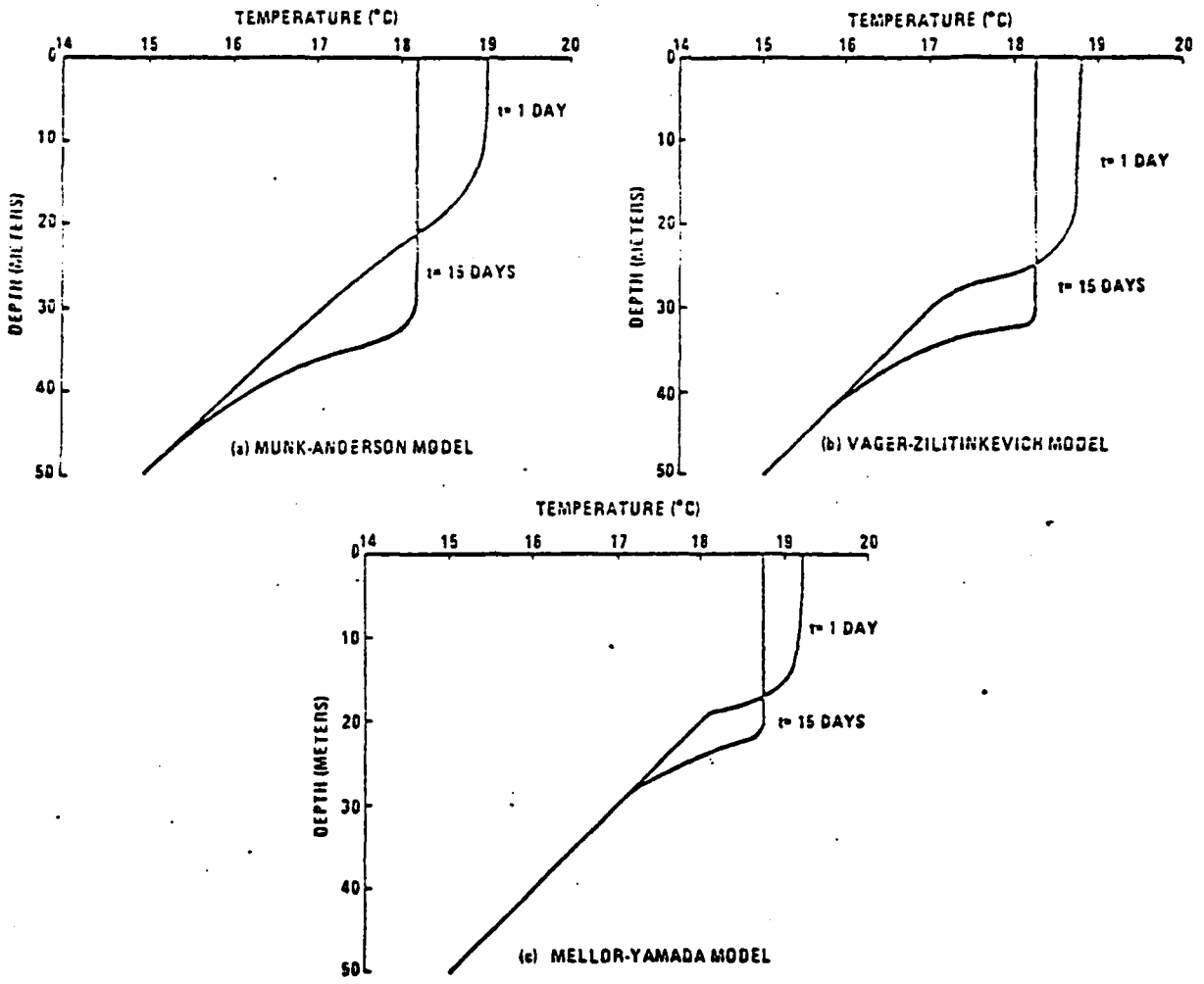

FIGURE 4-19: **Temperature profiles for three models one and 15 days after onset of wind stress.**

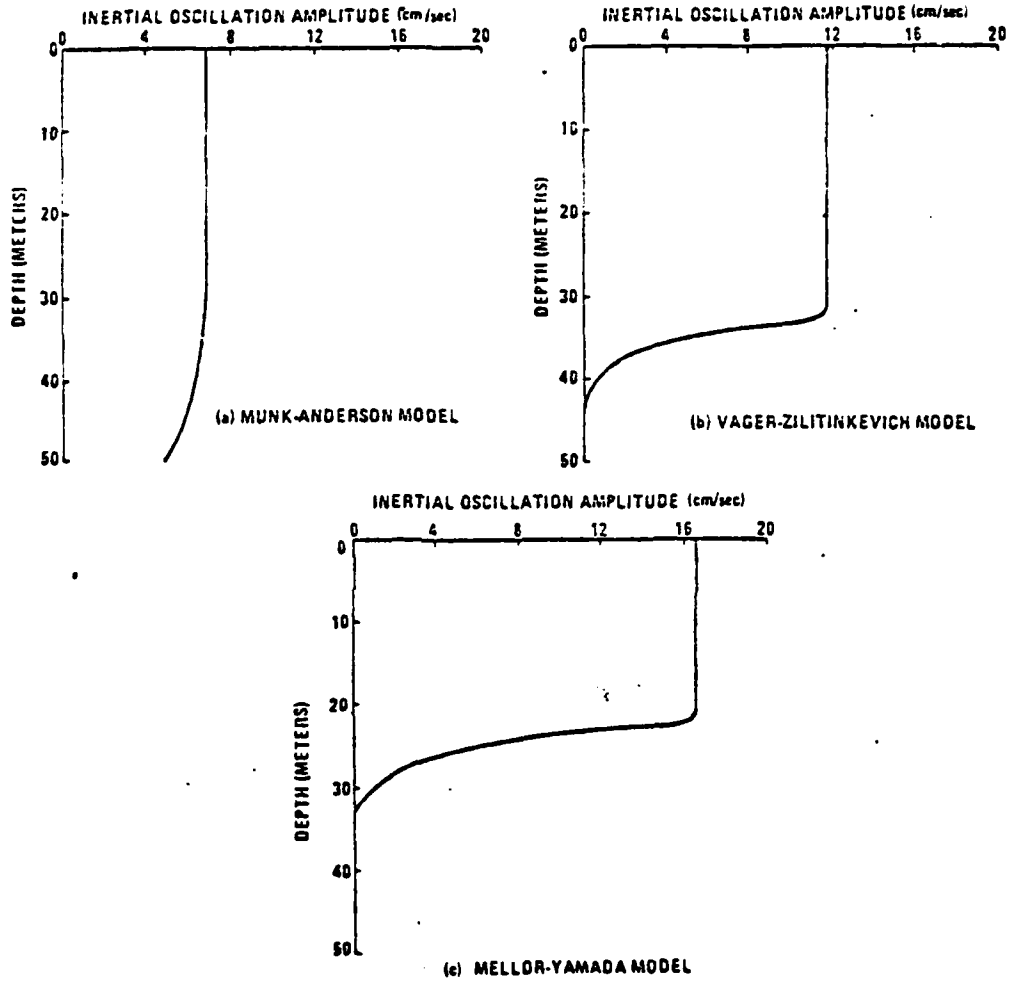

FIGURE 4-20: Inertial oscillation amplitudes for three models after 15 days.

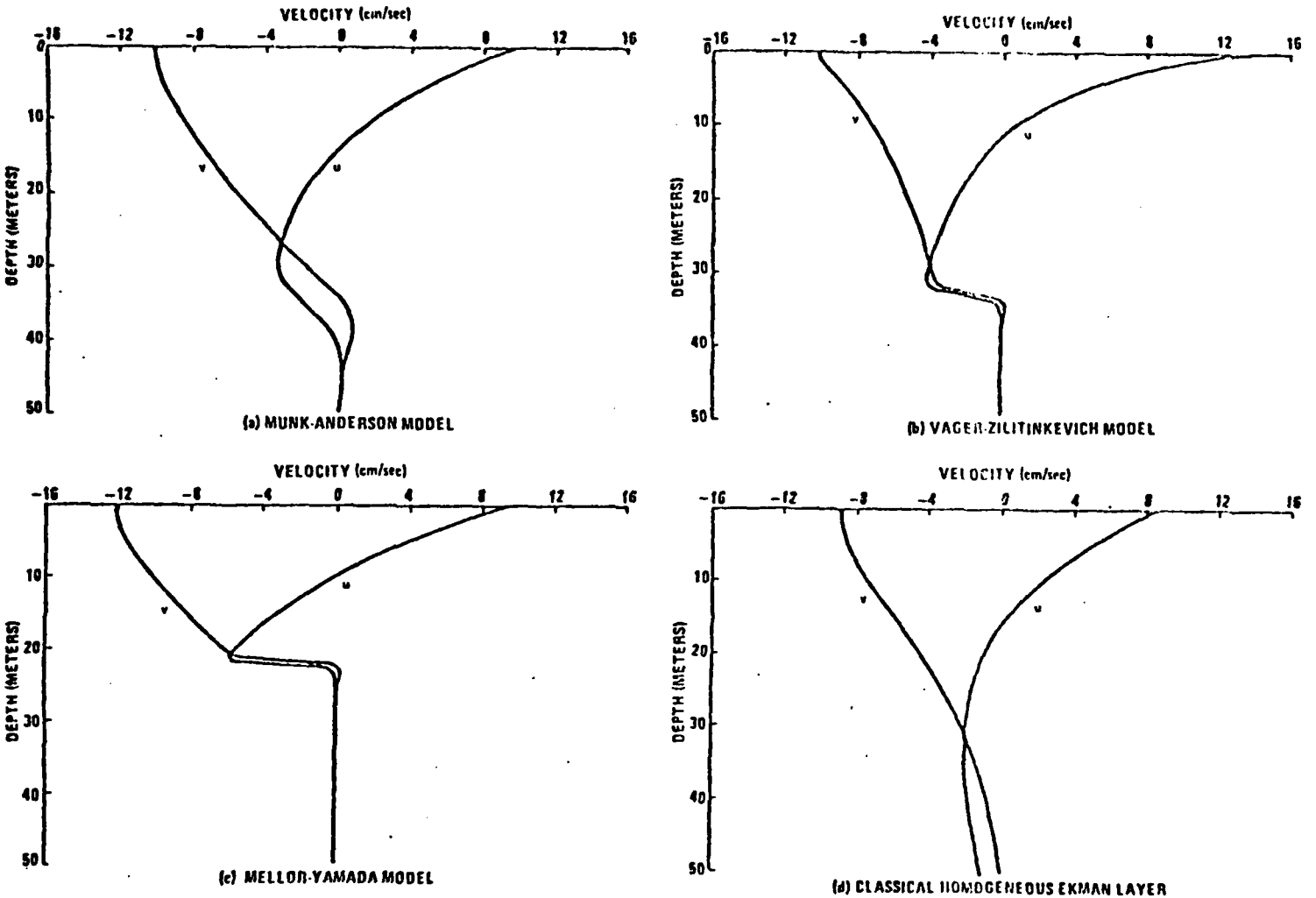

FIGURE 4-21: Mean velocity profiles in the mixed layer after 15 days.

4-18 presents the time evolution of mixed-layer depth and very substantial differences between the model predictions are apparent. Mixed layer depth is defined as the depth at which K_H was less than 1.0 cm^2/sec. Since there is no Richardson number cutoff, the MA Model predicts slow continued deepening. Eddy diffusivities predicted by the MY and VZ models do cutoff when the degree of stratification becomes sufficient. From that point no mixing can occur. Thus steady state solutions are possible with these models. Figure 4-19 presents the temperature profiles at t = 1 and 15 days after wind onset, and Figures 4-20 and 4-21 present the amplitudes of the inertial oscillation and the mean current after 15 days. The mean current is defined here as the current with oscillations of inertial period removed. The models all predict a slab-like inertial oscillation superposed on an Ekman-like spiral.

Predictions for Martin's second case, wind mixing and heating are shown in Figure 4-22. In this case the water is initially unstratified so that the response to the 1 $dyne/cm^2$ wind stress is rapid deepening. According to Martin, the MA predicted mixed-layer depth is not well defined until about day 10 and is shown as a dotted line. As the total amount of thermal energy input to the water increases, the water buoyancy impedes vertical mixing, the layer retreats to steady-state depth, and the layer continues to warm.

Martin also performed a similarity scaling analysis with the following results. First, for the case of wind mixing and no heating nearly all the differences

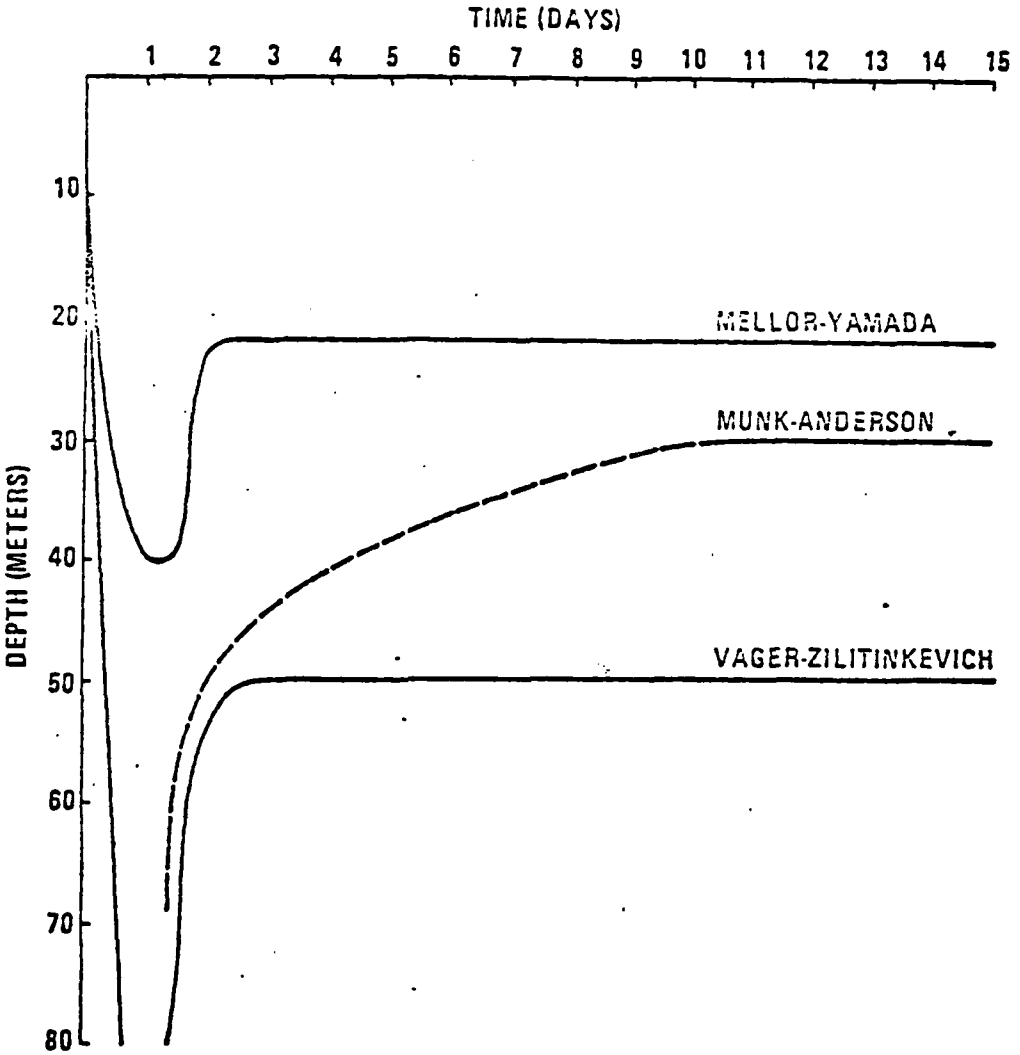

FIGURE 4-22: ML depth predicted by the three diffusion models for initially unstratified ocean, wind stress of 1 dyne/cm^2 and heat flux of 300 cal/cm^2 day.

between the VZ and MY models could be accounted for by the difference between the cutoff Richardson numbers. The predictions were not especially sensitive to the values of the vaious eddy coefficients. Second, for the case of wind stress and strong heating the differences in mixed-layer depth were greater than that which might be accounted for by the differences in cutoff Richardson number. Third, for the conditions simulated the steady state mixed-layer depth in the case of wind deepening and no heating is

$$h = 2.7\ Ri_c^{1/4} u_* (Nf)^{-1/2} \qquad (4.50)$$

where Ri_c is 0.23 for the MY model and 1.0 for the VZ model. This expression is identical in form to that derived by Pollard, et al. (1973). In fact, Pollard, et al. find in place of $2.7\ Ri_c^{1/4}$ in (4.50) the values 1.68, if we use Ri_c=0.23, then $2.7\ Ri_c^{1/4}$=1.86. This is very good agreement. The form of (4.50) results from the fact that for a constant surface stress, the fully developed inertial motion receives no net momentum over an inertial period. At the end of the first half-inertial period after the wind onset, the layer has as much momentum $((hu)^2+(hv)^2)^{1/2}$ as it ever will have and the layer has deepened to the depth at which the shear across the mixed-layer (seasonal thermocline) interface is small enough that mixing ceases. No further deepening can occur.

4.5 DISCUSSION

The one-dimensional upper-ocean models discused in this section represent attempts to understand the physics of

ocean processes on a small (tens of meters) scale at specific locations. The connection between these models and the types of models studied earlier (i.e.--large scale circulation and fronts) is not explicit, expecially since one-dimensional models neglect horizontal advection. And yet the larger scales of motion act in a sense to control ocean conditions at specific locations. The logical step seems to be twofold:

- modify one-dimensional upper-ocean models to include the influence of horizontal inhomogeneities in the temperature, salinity, and current fields of the regions modelled, and

- develop two- and three-dimensional models with sufficient horizontal resolution to include synoptic scale phenomena.

The first approach can be implemented by obtaining enough data to specify horizontal gradients as a function of time. Such comprehensive data is not always available, however.

The second approach seems to be more promising. Indeed, NORDA is developing a large-area upper-ocean model, based on the Mellor-Yamada Level 2 diffusion model, for FNOC. Specifics of the model and an evaluation of its success must await further testing.

The connection between the upper-ocean models and smaller scale processes is more readily apparent. The density structure above the seasonal thermocline strongly

influences the maintenance and propagation of internal wave energy. The turbulent region at the base of the mixed layer may contribute a good deal of energy to internal waves. And the motion of the mixed layer in response to atmospheric forcing may act to couple internal waves to atmospheric motions. On the other hand, the presence of internal waves in the upper ocean affects the observed thermal structure.

These types of questions are just now being addressed and very few attempts have been made to couple upper-ocean models with internal wave models. This is partially because the upper-ocean models are predictive, while most internal waves models are statistical, and partly because, although the existence of interactions between upper-ocean processes and smaller scale motions may be apparent, the physics of the interactions is not.

REFERENCES

Bell, T. H. (1978): Radiation Damping of Inertial Oscillations in the Upper Ocean, J. Fluid Mech., 88, 289-308.

Chou, P. Y. (1945): On Velocity Correlations and the Solutions of the Equations of Turbulent Fluctuations, Quant. Appl. Math., 3, p. 38.

Denman, K. L. (1973): A Time-Dependent Model of the Upper Ocean, J. Phys. Oceanogr., 3, 173-184.

_____ and M. Miyake (1973a): Upper Layer Modification Papa: Observations and Simulation, J. Phys. Oceanogr., 3, 185-196.

_____ and _____ (1973b): Behavior of the Mean Wind, the Drag Coefficient and the Wave Field in the Open Ocean, J. Geophys. Res., 78, 121, 1917-1931.

Ekman, V. W. (1905): On the Influence of the Earth's Rotation on Ocean Currents, Av. Kiv. Mat. Ashon. Fysik, 2, 1-53.

Elsberry, R.L., T. S. Fraim, and R. N. Trapnell, Jr. (1976): A Mixed Layer of the Oceanic Thermal Response to Hurricanes, J. Geophys. Res., 81, 1153-1162.

Friehe, C. A. and K. F. Schmitt (1976): Parameterization of Air-Sea Interface Fluxes of Sensible Heat and Moisture by the Bulk Aerodynamic Formula, J. Phys. Oceanogr., 6, 801-809.

Garwood, R. W. Jr. (1977): An Oceanic Mixed Layer Model Capable of Simulating Cyclic States, J. Phys. Oceanogr., 7, 455-468.

Gill, A. E. and L. N. Trefethen (1977): A Mixed Layer Model, Ocean Modelling, (Unpublished Manuscript).

_____ and J. S. Turner (1976): A Comparison of Seasonal Thermocline Models with Observation, Deep-Sea Res., 23, 391-401.

Halpern, D. (1974): Observations of Deepening of the Wind-Mixed Layer in the Northeast Pacific Ocean, J. Phys. Oceanogr., 4, 454-466.

Hanjalic, K., and B. E. Launder (1972): A Reynolds Stress Model of Turbulence and its Application to Thin Shear Flows, J. Fluid Mech., 52 (4), 609-638.

Kase, R. H. (1979): Calculations of the Energy Transfer by the Wind to Near-Inertial Internal Waves, Deep-Sea Research, 26, 227-232.

Kato, H. and O. M. Phillips (1969): On the Penetration of a Turbulent Layer into Stratified Fluid, J. Fluid Mech., 37, 643-655.

Kim, J. W. (1976): A Generalized Bulk Model of the Oceanic Mixed Layer, J. Phys. Oceanogr., 6, 686-695.

Kochergin, V. P., V. I. Klimok, and V. A. Sukhorukov (1976): A Turbulent Model of the Ocean Ekman Layer, Sb. Chisl. Metody Mekhan. Sploshnoi Sredy, 7, 72-81.

Kondo, J., Y. Sasano, and T. Ishii (1979): On Wind-Driven Current and Temperature Profiles with Diurnal Period in the Oceanic Planetary Boundary Layer, J. Phys. Oceanogr., 9, 360-372.

Kraus, E. B. and J. S. Turner (1967): A One-Dimensional Model of the Seasonal Thermocline: The General Theory and its Consequences, Tellus, 19 (1), 98-105.

Launder, B. E. (1975): On the Effects of a Gravitational Field on the Turbulent Transport of Heat and Momentum, J. Fluid Mech., 67 (3), 569-581.

_____ G. J. Reece and W. Rodi (1975): Progress in the Development of a Reynolds-Stress Turbulence Closure, J. Fluid Mech., 68 (3), 537-566.

Lundgren, T. S. and F. C. Wang (1973): Eddy Viscosity Models for Free Turbulent Flows, Phys. Fluids, 16, 174-178.

References (Continued)

Marchuk, G. I., V. P. Kochergin, V. I. Klimok, and V. A. Sukhorukov (1977): On the Dynamics of the Ocean Surface Mixed Layer, J. Phys. Oceanogr., 7, 865-875.

Martin, P. J. (1976): A Comparison of Three Diffusion Models of the Upper Mixed Layer of the Ocean, NRL Memorandum Rep. 3349, Naval Res. Lab., Washington, D. C.

Mellor, G. and P. Durbin (1975): The Structure and Dynamics of the Ocean Surface Mixed Layer, J. Phys. Oceanogr., 5, 718-728.

_____ and T. Yamada (1974): A Hierarcy of Turbulence Closure Models for Planetary Boundary Layers, J. Atmos. Sci., 31, 1791-1806.

Munk, W. H. and E. R. Anderson (1948): Notes on a Theory of the Thermocline, J. Mar. Res., 7 (3), 276-295.

Niiler, P. P. (1975): Deepening of the Wind-Mixed Layer, J. Mar. Res., 33, 405-422.

_____ and E. B. Kraus (1977): One-Dimensional Models of the Upper Ocean, Modelling and Prediction of the Upper Layers of the Ocean, E. B. Kraus Ed., Pergamon Press, 143-172.

_____ (1977): One-Dimensional Models of the Seasonal Thermocline, The Sea: Vol 6, Marine Modelling, E. D. Goldberg, J. N. McCave, J. J. O'Brien, and J. H. Steele, eds., Wiley, N. Y. 97-115.

Phillips, O. M. (1977): The Dynamics of the Upper Ocean, 2nd Edition, Cambridge, Univ. Press, London.

_____, P. B. Rhines, and R. O. R. Y. Thompson (1973): The Deepening of the Wind-Mixed Layer, Geophys. Fluid Dyn., 3, 381-404.

Prandtl, L. (1925): Berichte Uber Untersuchungen Zur Ausgebildeten Turbulenz, Z. Angew Math. Mech., 5, 136.

_____ (1945): Uber ein neues Favmelsystem fur die Ausgebildete Turbulenz,Nachrichten von der Akad, der Wissenschaft in Gottingen.

Price, James F. (1979): On the Scaling of Stress-Driven Entrainment Experiments, J. Fluid Mech, 90 (3), 509-529.

_____ , C. N. K. Mooers, and J. C. Van Leer (1978): Observation and Simulation of Storm-Induced Mixed Layer Deepening, J. Phys. Oceanogr., 8, 582-599.

Stevenson, J. W. (1979): On the Effect of Dissipation on Seasonal Thermocline Models, J. Phys. Oceanogr. 9, 57-64.

Stommel, H., K. Saunders, W. Simmons, and J. Cooper (1969): Observations of the Diurnal Thermocline, Deep-Sea Research, 16, (Suppl.), 269-284.

Tabata, S. (1965): Variability of Oceanographic Conditions at Ocean Station "P" in the Northeast Pacific Ocean, Trans., Roy. Soc. Canada, Series 4, 3, Sec. 3, 367-418.

Tennekes, H. and J. L. Lumley (1972): A First Course in Turbulence the MIT Press, Cambridge, Mass.

Thompson, R. O. R. Y. (1976): Climatological Numerical Models of the Surface Mixed Layer of the Ocean, J. Phys. Oceanogr., 6, 496-503.

_____ (1977): Reply to Garwood and Camp, J. Phys. Oceanogr. 7, 470-471.

_____ (1969): A Note on Wind Mixing at the Seasonal Thermocline, Deep-Sea Res., Suppl. 16, 297-300.

_____ (1973): Buoyancy Effects in Fluids, Cambridge University Press.

Vager, B. G. and S. S. Zilitinkevich (1968): A Theoretical Model of the Diurnal Variations of the Meteorological Fields, Meteorol. i Gidrol., 7.

Section 5

INTERNAL WAVE MODELS

Section 5
INTERNAL WAVE MODELS

5.1 INTRODUCTION

In this section we will discuss models which have been developed to describe the oceanic internal-wave field. To this point in this document we have addressed models of larger scale phenomena; these models are deterministic in the sense that they produce estimates of observables such as averaged current or temperature at specific locations and times from conservation principles. At smaller scales, such as those which describe internal waves (and turbulence), the models become far more empirical since the sources and sinks of the energy associated with small scale processes and their internal dynamics are not well understood.

5.2 INTERNAL-WAVE SPECTRAL MODELS

Garrett and Munk (1972) developed, or in their words "contrived," an internal-wave energy-density wave-number-frequency spectrum from which can be derived spectra and coherences of measurable quantities such as vertical displacement as a function of time or position. The model has provided a common framework for the analysis of data from fixed, towed, and dropped measurement systems, and has had a very significant impact on the way internal-wave observations are performed, on the manner in which data are analyzed, and on the interpretation of analyzed data.

In the following section we will describe the basic empirical internal-wave model of Garrett and Munk (1972) and its subsequent embellishments. The details of the construction process are important to an understanding of the model limitations. Then we will describe models which have been proposed to treat the effects of apparent fine structure in internal-wave measurements.

The essential components of the model are a horizontal wavenumber-frequency energy-density spectrum which describes the internal-wave energy content in wavenumber-frequency space, and vertical wave functions which describe the distribution of that energy in depth between horizontal and vertical currents and particle displacements. The energy density spectrum is not measured directly but may be inferred from measurements of what are, in effect, its projections. These include current and displacement frequency auto-spectra, horizontal and vertical wavenumber auto-spectra, and coherences.

5.2.1 Basic Assumptions of GM-Class Internal Wave Spectral Models

Internal wave spectral models attempt to describe the statistical characteristics of internal waves in terms of a wavenumber-frequency energy-density spectrum $E(k,\omega)$. From such a fundamental spectrum predictions of such quantities as current and displacement spectra and coherences can be made.

Garrett and Munk (1972) were first to derive an internal-wave energy-spectrum as part of what has become known as the GM72 model. Garrett and Munk (1975) subsequently produced a modified model, GM75, as did Cairns and Williams (1976), and Desaubies (1976). Müller, et al, (1978) performed a rigorous analysis of IWEX (Internal Wave Experiment) data and produced both a careful assessment of the GM-class of models and a much more complex energy-density spectrum model. The basic assumptions on which the models are based are the following (as characterized by Müller, et al.):

1. The observed fluctuations are a realization of a statistically stationary process.

2. The fluctuations are horizontally homogeneous.

3. The fluctuations are a superposition of linearly propagating internal waves.

4. The wave field scales according to WKB theory.

5. The wave field is horizontally isotropic.

6. The wave field is vertically symmetric.

The first, second and fifth of these assumptions reduce the complexity of the statistical fluctuation-field description. The third imposes a set of dynamic conditions which the fluctuations are assumed to follow and implies that the observed small-scale structure results from reversible internal-wave-caused distortion of otherwise smooth profiles rather than from persistent layering. The fourth allows the wave energy-density spectrum to be conveniently related to measureable wave field statistics such as correlation functions. The sixth assumption means that the averaged upward and downward wave-induced energy fluxes are equal.

5.2.2 Basic Formulation

In the analysis which follows, we will make use of the following quantities:

$u_m(\underline{x},z,t)$ the wave-induced velocity component in the m direction as a function of horizontal location $\underline{x}$, vertical location z, and time t;

$\underline{k}$ the horizontal wavenumber with components (k_1,k_2), magnitude k, and direction $\theta = \arctan(k_2/k_1)$;

ω the wave frequency, $f \leq \omega \leq N$;

σ the sign of the local vertical wavenumber which we take to be positive (negative) for downward (upward) propagating energy and upward (downward) propagating phase;

$A(\underline{k},\omega,\sigma)$ the random complex amplitude of the wave component with wavenumber $\underline{k}$, frequency ω, and vertical propagation direction σ.

Velocity components u_1 and u_2 refer to the horizontal directions x_1 and x_2, and u_3 refers to the vertical velocity (positive upward). For notational simplicity we will use the symbol u_0 to represent vertical displacement.

Linear Superposition of Waves

We follow Müller et al. (1978) and represent the mth velocity component at location $(\underline{x},z,t)$, which arises from both upward and downward propagating internal waves of all wavenumbers and frequencies, as the linear sum

$$u_m(\underline{x},z,t) = \sum_\sigma \int d\underline{k} \fint d\omega \Big\{ \exp[i(\underline{k}\cdot\underline{x}-\omega t)] U_m(\underline{k},\omega,z,\sigma) A(\underline{k},\omega,\sigma) + \exp[-i(\underline{k}\cdot\underline{x}-\omega t)] U_m^*(\underline{k},\omega,z,\sigma) A^*(\underline{k},\omega,\sigma) \Big\}, \quad (5.1)$$

where $U_m(\underline{k},\omega,z,\sigma)$ is an appropriate wave function. The sum over σ is taken with $\sigma=+1$ and -1. The integral over $\underline{k}$ is actually the double integral over k_1 and k_2 with $d\underline{k}=dk_1 dk_2$ and with limits of integration $-\infty$ to $+\infty$. Integral symbols without limits will represent integrals over these bounds. The frequency integral is taken over positive values only from zero to infinity. Slashed integral symbols will be used in this case. We can write

$$U_m(\underline{k},\omega,z,\sigma) = D_m(\underline{k},\omega)\ W(\underline{k},\omega.z,\sigma). \quad (5.2)$$

In (5.2) W is the suitably normalized solution to the linear equation for vertical velocity

$$d_z^2 W + k^2 p(z) W = 0, \quad p(z) = \frac{N^2-\omega^2}{\omega^2-f^2} \tag{5.3}$$

where N(z) is the local Brunt-Väisälä frequency which is assumed to vary only in the vertical, and f is the inertial frequency. The linear operators D_m relate the m velocity components to W through the linearized equations of motion which are assumed to describe the wave field.

These operators are:

$$\begin{aligned} D_0 &= i\omega^{-1} \\ D_1 &= k^{-2}(k_1^2+f^2k_2^2/\omega^2)^{\frac{1}{2}} \exp(ik_1\omega/k_2 f)d_z \\ D_2 &= k^{-2}(k_2^2+f^2k_1^2/\omega^2)^{\frac{1}{2}} \exp(ik_2\omega/k_1 f)d_z \\ D_3 &= 1 \end{aligned} \tag{5.4}$$

We note in passing that the integrand in (5.1) can be written more simply but less conveniently as

$$2\cos(\underline{k}\cdot\underline{x}-\omega t+\phi_m+\phi_a)|U_m||A| \tag{5.5}$$

where $\phi_m(\underline{k},\omega,z,\sigma)$ is a depth-dependent phase shift associated with the mth velocity component and depth and $\phi_a(\underline{k},\omega,\sigma)$ is a phase shift associated with the particular wave.

It may be of some help in understanding (5.1)-(5.5) to consider the simple special case of constant N. The basic

solutions to (5.3) are $C(\underline{k},\omega,\sigma)\exp(i\sigma\beta z)$ where $\beta=kp$ is the vertical wavenumber, and the coefficients $C(\underline{k},\omega,\sigma)$ are determined by a normalization requirement. Then from (5.4)

$$U_0 = C\omega^{-1}\exp[i(\tilde{\phi}_0+\sigma\beta z)] \quad ,$$

$$U_1 = C\sigma\beta k^{-2}(k_1^2+f^2k_2^2/\omega^2)^{\frac{1}{2}}\exp[i(\tilde{\phi}_1+\sigma\beta z)] \quad ,$$

$$U_2 = C\sigma\beta k^{-2}(k_2^2+f^2k_1^2/\omega^2)^{\frac{1}{2}}\exp[i(\tilde{\phi}_2+\sigma\beta z)] \quad , \qquad (5.6)$$

and

$$U_3 = C\exp(i\sigma\beta z) \quad ,$$

where the phases are given by

$$\tilde{\phi}_0 = \tfrac{1}{2}\pi, \quad \tilde{\phi}_1 = \tfrac{1}{2}\pi + k_1\omega/k_2f, \quad \tilde{\phi}_2 = \tfrac{1}{2}\pi - k_2\omega/k_1f. \qquad (5.7)$$

Equations (5.6) and (5.7) can be substituted into (5.1). The integrand becomes

$$\exp[i(\underline{k}\cdot\underline{x}+\sigma\beta z-\omega t)]\,U_mA + \exp[-i(\underline{k}\cdot\underline{x}+\sigma\beta z-\omega t)]\,U_m{}^*A^* \quad , \qquad (5.8)$$

or equivalently

$$2\cos(\underline{k}\cdot\underline{x}+\sigma\beta z-\omega t+\phi_m+\phi_a)|U_m||A| \quad ,$$

so that the wave field is the sum of simple plane waves with phase propagation angle $\tan^{-1}\left\{(k_1+k_2)^{\frac{1}{2}}/\sigma\right\}$ to the vertical.

The frequency integral in (5.1) is taken over the range zero to infinity primarily as a mathematical convenience. Strictly the integral should be taken over the range $f \leq \omega \leq N_{max}$ where N_{max} is the maximum Brunt-Väisälä frequency in the water column. In many situations it is taken effectively from f to the local value of N(z) with the assumption that motions induced by internal waves which exist in regions of higher N are negligible.

With the definition of negative frequencies (5.1) can be written in a more compact form. We define

$$A(\underline{k},-\omega,\sigma) = A^*(-\underline{k},\omega,-\sigma) \tag{5.9a}$$

and note that

$$U_m(\underline{k},-\omega,\sigma) = U_m{}^*(-\underline{k},\omega,-\sigma). \tag{5.9b}$$

Then (5.1) can be written as an integral over positive and negative frequencies:

$$u_m(\underline{x},z,t) = \sum_{\sigma}\int d\underline{k}\int d\omega\ \exp[i(\underline{k}\cdot\underline{x}-\omega t)]\,U_m(\underline{k},\omega,z,\sigma)\ A(\underline{k},\omega,\sigma). \tag{5.10}$$

We define the covariance R_{mn} between u_m at location $(\underline{x},z,t)$ and u_n at $(\underline{x}',z',t')$ as the ensemble-averaged inner product

$$R_{mn}(\underline{x},z,t;\underline{x}',z',t') = \langle u_m(\underline{x},z,t)\, u_n^*(\underline{x}',z',t')\rangle \qquad (5.11)$$

Since u_n is real $u_n^*=u_n$.

From (5.10), (5.11) can be expressed as

$$R_{mn}(\underline{x},z,t;\underline{x}',z',t') = \sum_{\sigma}\sum_{\sigma'}\iint d\underline{k}d\underline{k}'\iint d\omega d\omega' \exp[i(\underline{k}\cdot\underline{x}-\underline{k}'\cdot\underline{x}'-\omega t+\omega' t') \qquad (5.12)$$

$$\times \langle A(\underline{k},\omega,\sigma)A^*(\underline{k}',\omega',\sigma')\rangle\, U_m(\underline{k},\omega,z,\sigma)\; U_n^*(\underline{k}',\omega',z',\sigma').$$

Statistical Stationarity and Horizontal Homogeneity

The assumptions that the wave field be statistically stationary and horizontally homogeneous mean that

$$R_{mn}(\underline{x},z,t;\underline{x}',z',t') = R_{mn}(\underline{r},\tau,z,z'), \qquad (5.13)$$

where $\underline{r} = \underline{x}-\underline{x}'$ and $\tau = t-t'$. A necessary and sufficient condition for (5.13) is that amplitudes A be orthogonal with

respect to $\underline{k}$ and ω; that is

$$\langle A(\underline{k},\omega,\sigma)A^{*}(\underline{k}',\omega',\sigma')\rangle = \tfrac{1}{2}E(\underline{k},\omega,\sigma,\sigma')\,\delta(\underline{k}-\underline{k}')\delta(\omega-\omega')\dagger \tag{5.14a}$$

We note that our treatment of negative frequencies (5.9) implies through (5.14a) that

$$E(-\underline{k},-\omega,-\sigma,-\sigma') = E(\underline{k},\omega,\sigma,\sigma'). \tag{5.14b}$$

By (5.14) contributions to the covariance arise only from the products of wave components with identical $\underline{k}$ and ω. The contributions from other products vanish on average, and (5.13) becomes

$$R_{mn}(\underline{r},\tau,z,z') = \sum_{\sigma}\sum_{\sigma'}\int d\underline{k}\int d\omega\, \exp[i(\underline{k}\cdot\underline{r}-\omega\tau)]$$

$$\times\ \tfrac{1}{2}E(\underline{k},\omega,\sigma,\sigma')\, U_m(\underline{k},\omega,z,\sigma)\, U_n^{*}(\underline{k}',\omega',z',\sigma'). \tag{5.15}$$

The factor of $\frac{1}{2}$ has been inserted in (5.14) so that the variance of a variable u_m [i.e., $R_{mm}(0,0,z,z,)$] is obtained by integrating over positive frequencies. This will be clarified below.

---

†We note that if we ascribe units of length^3 to A as implied by (5.1), then E here has units of length^4/time.

AD-A098 189 SCIENCE APPLICATIONS INC MCLEAN VA F/G 8/3
A REVIEW OF OCEAN MODELS.(U)
JAN 81 W J GRABOWSKI, G T HEBENSTREIT N00014-78-C-0849
UNCLASSIFIED SAI-81-346-WA NL

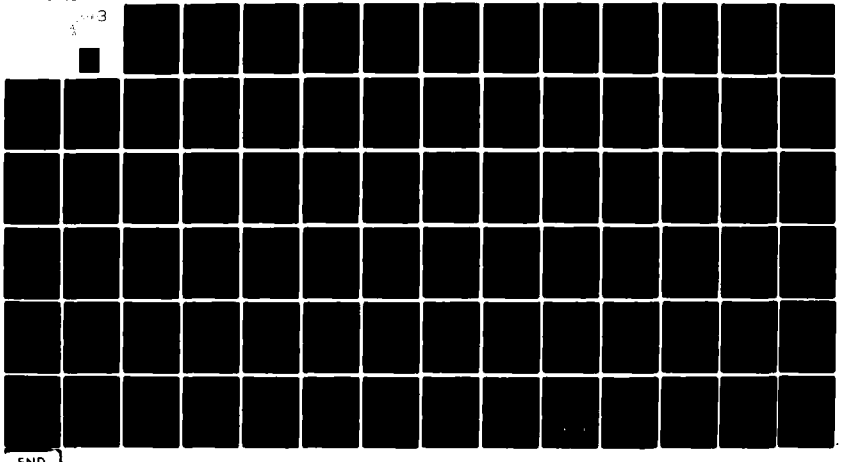

END
DATE FILMED
4-81
DTIC

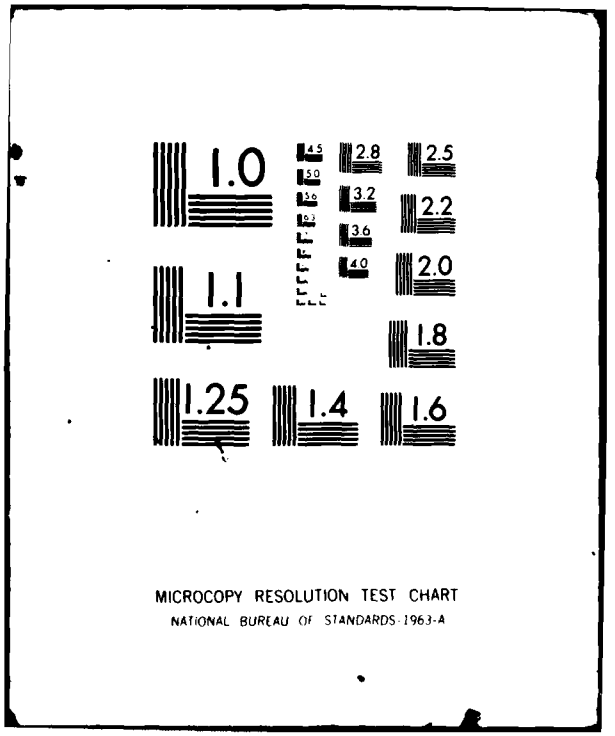
1.0
1.1
1.25
1.4
1.6
1.8
2.0
2.2
2.5
2.8
3.2
3.6
4.0
4.5
5.0
5.6
6.3
MICROCOPY RESOLUTION TEST CHART
NATIONAL BUREAU OF STANDARDS-1963-A

Normalization Condition

With a suitable normalization for U_m, $E(\underline{k},\omega,\sigma,\sigma')$ is the wavenumber-frequency energy-density (in $\underline{k}$- ω space) spectrum. We require

$$\tfrac{1}{2}\int_{-h}^{0} dz[U_1U_1^* + U_2U_2^* + (1+N^2/\omega^2)\, WW^*] = b \qquad (5.16)$$

where $z = -h$ represents the ocean bottom and b is a depth scale. The normalization determines $C(\underline{k},\omega,\sigma)$ such that the mean-square energy in each normalized elementary wave is identical. The quantity $N^2WW^*\omega^{-2}$ is the root-mean-square potential energy. With (5.16) the total root-mean-square energy per unit surface area, E_o, is given by

$$\tfrac{1}{2}\int_{-h}^{0} [R_{11}+R_{22}+(1+N^2/\omega^2)R_{33}]dz = \tfrac{1}{2}b\sum_{\sigma,\sigma'}\int d\underline{k}\int d\omega\; E(\underline{k},\omega,\sigma,\sigma') \qquad (5.17)$$

so that

$$\tfrac{1}{2}b\sum_{\sigma,\sigma'} E(\underline{k},\omega,\sigma,\sigma')$$

is the per-unit-area energy density associated with waves of wave number $\underline{k}$ and frequency ω.

Modal Wavefield Description

Two special cases of (5.15) corresponding to uncorrelated propagating waves and standing vertical modes are

of particular interest. The latter forms the basis of the GM models.

In the first case, if the complex amplitudes of upward and downward propagating waves are uncorrelated

$$E(\underline{k},\omega,\sigma,\sigma') = E(\underline{k},\omega,\sigma) \text{ if } \sigma = \sigma', \quad = 0 \text{ otherwise.} \tag{5.18}$$

Then (5.15) simplifies to

$$R_{mn}(\underline{r},\tau,z,z') = \int d\underline{k} \int d\omega \exp[i(\underline{k}\cdot\underline{r}-\omega\tau)] \times \tfrac{1}{2}\sum_{\sigma} E(\underline{k},\omega,\sigma)U_m(\underline{k},\omega,z,\sigma)\, U_n^*(\underline{k},\omega,z',\sigma). \tag{5.19}$$

Then, if we further assume that the wavefield is vertically symmetric so that on average the energy associated with upward and downward propagating waves is equal

$$E(\underline{k},\omega,\sigma) = E(\underline{k},\omega), \tag{5.20}$$

and

$$R_{mn}(\underline{r},\tau,z,z') = \int d\underline{k} \int d\omega \exp[i(\underline{k}\cdot\underline{r}-\omega\tau)] \times \tfrac{1}{2}E(\underline{k},\omega)\sum U_m(\underline{k},\omega,z,\sigma)\, U_n^*(\underline{k},\omega,z',\sigma). \tag{5.21}$$

Assumptions (5.18) and (5.20) imply a modal representation. Modes must satisfy vertical symmetry,

since upward and downward propagating waves are coupled through the surface and bottom boundary conditions. In this case (5.15) becomes

$$R_{mn}(\underline{r},\tau,z,z') = \int d\underline{k} \int d\omega \exp[i(\underline{k}\cdot\underline{r}-\omega\tau)]$$

$$\times \tfrac{1}{2} E_j(\underline{k},\omega) U_{mj}(\underline{k},\omega,z) U^*_{nj}(k,\omega,z') \quad (5.22)$$

where $E_j(\underline{k},\omega)=0$ except for discrete values of $\underline{k}$ or ω. The modal wavefunctions are given by the sum of two propagating components with appropriately related phases as

$$U_{mj}(\underline{k},\omega,z) = \sum_{\sigma} U_m(\underline{k},\omega,z,\sigma). \quad (5.23)$$

where U_{mj} is a solution to the boundary value problem (5.3) with $W = 0$ at top and bottom. We will take ω to be continuous and the solutions will be non-trivial only for a discrete set of values of $k = \kappa_j(\omega)$. Note that this dispersion relation involves the magnitude of k, not its direction. It then becomes convenient to express the integrals in (5.22) in terms of k and θ as

$$R_{mn}(\underline{r},\tau,z,z') = (2\pi)^{-1} \int d\omega \int dk \int_0^{2\pi} d\theta \exp[i(\underline{k}\cdot\underline{r}-\omega\tau)]$$

$$\times \tfrac{1}{2} \tilde{E}_j(k,\theta,\omega)\, U_{mj}(\theta,\omega,z)\, U^*_{nj}(\theta,\omega,z). \quad (5.24)$$

To obtain (5.24) we have defined the continuous wavenumber-magnitude/direction/frequency spectrum $\tilde{E}$ as

$$\tilde{E}(k,\theta,\omega) = 2\pi k E(\underline{k},\omega), \quad (5.25a)$$

where from (5.14b)

$$\tilde{E}(k,\theta+\pi,\omega) = 2\pi k E(\underline{k},-\omega) \qquad (5.25b)$$

We then introduce modes to obtain (5.24).

We can express $\tilde{E}_j(k,\omega,\theta)$ as $\tilde{E}_j(\omega,\theta)\,\delta(\kappa_j-k)$ using the dispersion relation so that (5.24) can be simplified to

$$R_{mn}(\underline{r},\tau,z,z') = (2\pi)^{-1}\int d\omega \int_0^{2\pi} d\theta \sum_j \exp[i\underline{\kappa}_j\cdot\underline{r}-\omega\tau)] \times \tfrac{1}{2}\tilde{E}_j(\theta,\omega)\, U_{mj}(\theta,\omega,z)\, U^*_{nj}(\theta,\omega,z') \qquad (5.26)$$

Equation (5.26) provides a complete description of the wave-field second-order statistics (i.e., covariances) with the stated assumptions. The wave functions $U_{mj}(\omega,\theta,z)$ can be obtained analytically (in cases of very simple N(z) profiles), numerically, or approximately with WKB methods. The specification of the spectrum $\tilde{E}_j(\omega,\theta)$ completes the description.

While it is not central to this section, the assertion that the wave field is a Gaussian random process is convenient in modeling certain aspects of the wavefield (for example, the influence of passive fine structure as described in a following section). In this case all moments and joint moments can be calulated in terms of the covariances. In addition, it can be shown that $\tilde{E}_j(\theta,\omega)$ is the variance of the amplitude of jth mode wave with

direction θ and frequency ω, and that these amplitudes themselves satisfy a Gaussian distribution. It is possible in fact to derive (5.26) from a multi-dimensional Karhunen-Loeve expansion of the process (Dozier and Tappert, 1978). This approach may be more rigorous than that described here. While intuitively appealing, (5.1) may not be formally appropriate since it implies that the Fourier integral of u_m exists. Strictly, such transforms do not exist for stationary random processes. The Karhunen-Loeve expansion circumvents this problem and allows (5.26) to be derived directly. The application of the expansion to a description in terms of propagating waves is less straightforward since the wave function used in the expansion must be orthogonal, which generally is not the case for the propagating wave functions.

Horizontal Isotropy

Garrett and Munk hypothesized that the internal wave field is horizontally isotropic, so that the covariance is a function of r, not $\underline{r}$. For this to be the case $\tilde{E}$ can not be a function of Θ. Then from (5.25)

$$\tilde{E}(k,\omega) = 2\pi k E(\underline{k},\omega), \tag{5.27a}$$

$$\tilde{E}(k,-\omega) = \tilde{E}(k,\omega), \tag{5.27b}$$

and clearly

$$\tilde{E}_j(\theta,\omega) = \tilde{E}_j(\omega) = \tilde{E}_j(-\omega). \tag{5.27c}$$

Equivalent Continuum

Garrett and Munk pointed out that a many-mode description of the wave field would be required so that they "preferred to blur the discrete lines into an 'equivalent continuum.'" In addition, the observational data which was available was cast in either frequency or horizontal wavenumber form so that a similar model formulation was appropriate. They obtained wave functions from a WKB-like analysis, and a WKB modal dispersion relation $\kappa_j(\omega)$. Then they introduced the equivalent continuum in which contributions to R_{mn} are assumed from all values of k and ω. In the equivalent continuum

$$\sum_{j=1} \tilde{E}_j(\omega)\, \exp(i\underline{\kappa}_j \cdot \underline{r})\, U_{mj}(\theta,\omega,z)\, U^*_{nj}(\theta,\theta,z') = \int dk\, \tilde{E}_c(k,\omega)\, \exp(i\,\underline{k}\cdot\underline{r})\, U_m(k,\theta,\omega,z)\, U_n^*(k,\theta,\omega,z') \tag{5.28}$$

where $\tilde{E}_c(k,\omega)$ is the equivalent continuum wavenumber-frequency spectrum and $U_m(k,\theta,\omega,z)$ is the WKB wave function with j replaced by k and ω using the inverse dispersion relation, $j(k,\omega)$, and with the integer constraint on j removed. Note that

$$\tilde{E}_c(k,\omega) = \tilde{E}_j(\omega)(\partial\kappa_j/\partial j) \tag{5.29}$$

where $\tilde{E}_j$ and κ_j are treated as continuous functions of j.

With (5.28), (5.26) becomes

$$R_{mn}(\underline{r},\tau,z,z') = (2\pi)^{-1}\int d\omega \int dk \int_0^{2\pi} d\theta\, \exp[i(\underline{k}\cdot\underline{r}-\omega\tau)] \times \tfrac{1}{2}\tilde{E}_c(k,\omega)\, U_m(k,\theta,\omega,z) U_n^*(k,\theta,\omega,z') \tag{5.30}$$

Alternatively, (5.30) can be written

$$R_{mn}(\underline{r},\tau,z,z') = \int d\omega \int d\underline{k}\ \exp[i(\underline{k}\cdot\underline{r}-\omega\tau)]$$

$$\times \tfrac{1}{2} E_c(\underline{k},\omega)\ U_m(\underline{k},\omega,z)\ U_n^*(\underline{k},\omega,z') \qquad (5.31)$$

where, following (5.25),

$$E_c(\underline{k},\omega) = (2\pi k)^{-1}\ \tilde{E}_c(k,\omega) \qquad (5.32)$$

Form (5.31) is sometimes convenient since it permits the direct evaluation of one-dimensional horizontal Fourier transforms. Equations (5.30) and (5.31) are the essential constituents of the model.

Frequency and Wavenumber Spectra

From (5.30) and (5.31) it is straightforward to obtain component frequency and horizontal wavenumber spectra. Such spectra are computed from experimental data. We define the frequency covariance or cross spectrum C_{mn} as the Fourier transform of R_{mn} by

$$C_{mn}(\underline{r},\omega,z,z') = \frac{1}{\pi}\int d\tau\ R_{mn}(\underline{r},\tau,z,z')\ \exp\ (i\omega\tau) \qquad (5.33)$$

so that the inverse transform is

$$R_{mn}(\underline{r},\tau,z,z') = \tfrac{1}{2}\int d\omega\ C_{mn}(\underline{r},\omega,z,z')\ \exp\ (-i\omega\tau). \qquad (5.34)$$

Since R_{mn} is real

$$C_{mn}(\underline{r},-\omega,z,z') = C^{*}_{mn}(\underline{r},\omega,z,z') \tag{5.35}$$

and since by stationarity and homogeneity

$$R_{mn}(\underline{r},\tau,z,z') = R_{nm}(-\underline{r},-\tau,z',z), \tag{5.36}$$

we have

$$C_{mn}(\underline{r},\omega,z,z') = C_{nm}(-\underline{r},-\omega,z',z). \tag{5.37}$$

The variance of component m then is

$$\begin{aligned} R_{mm}(o,o,z,z) &= \frac{1}{2}\int d\omega\ C_{mm}(o,\omega,z,z) \\ &= \oint d\omega\ C_{mm}(o,\omega,z,z) \end{aligned} \tag{5.38}$$

from (5.37). The variance of u_m is, therefore, equal to the integral of the autospectrum over positive frequencies.

The coincident spectrum $P_{mn}(\omega)$ (co-spectrum) and quadrature spectrum $Q_{mn}(\omega)$ are defined as the real and negative imaginary parts of $C_{mn}(\omega)$; that is

$$C_{mn}(\underline{r},\omega,z,z') = P_{mn}(\underline{r},\omega,z,z') - i\,Q_{mn}(\underline{r},\omega,z,z'). \tag{5.39}$$

Following Bendat and Piersol (1971) we can view the value of the cospectrum at frequency ω as representing the contribution of frequencies in a narrow band around ω to the average product $\langle u_m(t)u_n(t)\rangle$. The quadrature spectrum is the same except that either $u_m(t)$ or $u_n(t)$ is shifted in time sufficiently to produce a $\frac{1}{2}\pi$ change in phase at ω.

Often the covariance spectrum is presented in normalized form. Let

$$C_{mn}(\omega) = \left[P_{mn}^2(\omega) + Q_{mn}^2(\omega)\right]^{\frac{1}{2}} \exp\left[-i\phi_{mn}(\omega)\right]$$

where the phase is

$$\phi_{mn}(\omega) = \tan^{-1}\left(Q_{mn}/P_{mn}\right) \tag{5.40}$$

Then the coherence is defined as

$$Coh_{mn}(\omega) = \frac{|C_{mn}(\omega)|}{|C_{mm}(\omega)|^{\frac{1}{2}}|\ C_{nn}(\omega)|^{\frac{1}{2}}}, \tag{5.41}$$

the normalized squared amplitude of C_{mn}. If the coherence is zero at frequency ω, $C_{mn}=0$ at that frequency, and the contributions to u_m and u_n at that frequency are uncorrelated. The maximum possible value of Coh is unity, which is achieved only if the Fourier components of u_m and u_n at that frequency have proportional amplitudes throughout the ensemble. Lumley and Panofsky (1964) provide the

example of two time series u(t) and v(t) where v(t) is just u(t) shifted by some constant time interval τ. In this case the coherence is unity at all frequencies and the phase at frequency ω is $\omega\tau$. This suggests that we can use the phase to estimate a time lag τ by $\phi(\omega)/\omega$ at sufficiently large values of coherence.

An analogous set of relationships exists for horizontal wavenumber except that we consider both positive and negative values of k. We define

$$C_{mn}(\underline{k},\tau,z,z') = \frac{1}{2\pi}\int d\underline{r}\; R_{mn}(\underline{r},\tau,z,z')\exp(-i\underline{k}\cdot\underline{r}) \qquad (5.42)$$

so that

$$R_{mn}(\underline{r},\tau,z,z') = \int d\underline{k}\; C_{mn}(\underline{k},\tau,z,z')\exp(i\underline{k}\cdot\underline{r}). \qquad (5.43)$$

With definitions (5.33)-(5.43) the frequency and wavenumber spectra can be derived from (5.30) and (5.31). The frequency cross spectrum obtained from moored sensors at depths z and z' separated horizontally is, from (5.30) and (5.33),

$$C_{mn}(\underline{r},\omega,z,z') = \frac{1}{2\pi}\int dk \int_0^{2\pi} d\theta\; \exp(i\underline{k}\cdot\underline{r})\,\tilde{E}_c(k,\omega)U_m(k,\theta,\omega,z) \times U_n^*(k,\theta,\omega,z'). \qquad (5.44)$$

In the case of components at the same location, $\underline{r}=0$ and $z=z'$ so that

$$C_{mn}(\omega)\equiv C_{mn}(o,\omega,z,z) = \frac{1}{2\pi} \fint dk \int_o^{2\pi} d\theta \; \tilde{E}_c(k,\omega) U_m(k,\theta,\omega,z) \times U_n^*(k,\theta,\omega,z). \tag{5.45}$$

Horizontal wavenumber spectra are most easily obtained from (5.31). We imagine covariances $R_{mn}(\underline{r},0,z,z)$ which could be obtained from an instantaneous snapshot of $u_m(\underline{x},z,t)$ along a range in $\underline{x}$, perhaps from an acoustic sensor or a fast tow. If we take $\underline{r} = (r,0)$ so that the coordinate system is oriented along the separation, then from (5.31) and (5.42)

$$C_{mn}(k_1)\equiv C_{mn}(k_1,o,z,z) = \int d\omega \int dk_2 \; \tfrac{1}{2} E_c(\underline{k},\omega) \; U_m(k,\omega,z) \times U_n^*(\underline{k},\omega,z) \tag{5.46}$$

In the case m=n we make use of the isotropy condition that $E_c(-\underline{k},\omega) = E_c(\underline{k},\omega)$ so that

$$E_c(k_1,-k_2,\omega) \; U_m U_m^* \; (k_1,-k_2,\omega,z) = E_c(k_1,k_2,\omega) \; U_m U_m^*(k_1,k_2,\omega,z)$$

and then

$$C_{mm}(k_1) = \int d\omega \fint dk_2 \; E_c(\underline{k},\omega) \; U_m U_m^*(\underline{k},\omega,z)$$

This can be expressed in terms of $\tilde{E}_c(k,\omega)$ from (5.32) as

$$C_{mm}(k_1) = \frac{1}{\pi} \fint d\omega \int_{|k_1|}^{\infty} dk \; (k^2-k_1^2)^{-\frac{1}{2}} \; \tilde{E}_c \; (k,\omega) \; U_m U_m^*(k,\theta,\omega,z). \tag{5.47a}$$

In practice it is not possible to distinguish contributions to $C_{mm}(k_1)$ from positive and negative k_1. Therefore, it may be more appropriate to define the spectrum

$$C_{mm}(|k_1|) \equiv C_{mm}(k_1) + C_{mm}(-k_1) = 2\, C_{mm}(k_1) \qquad (5.47b)$$

since $C_{mm}(-k_1) = C_{mm}(k_1)$.

It is possible to perform ocean measurments and estimate various auto-spectra, co-spectra and coherence. These observations can be used to deduce $\tilde{E}_c(k, \omega)$ through expressions like (5.44)-(5.47) <u>if</u> the wave function can be specified.

5.2.3 Wave-Functions and the Dispersion Relation

Garrett and Munk obtained the wave function $W(k, \omega, z)$ from the exact solution of (5.3) with homogeneous boundary condition in the case of an exponential Brunt-Väisälä profile $N(z) = N_o e^{z/b}$.* An exact solution in the form of Bessel functions was derived which was simplified for two cases:

1. wave frequencies $\omega << N(-h)$ where $N(-h)$ is the minimum Brunt-Väisälä frequency of the water column;

2. wave frequencies $N(-h) << \omega << N(z)$ where $N(z)$ is the local Brunt-Väisälä Frequency;

*z is taken positive upwards.

The first case is distinguished by the absence of turning points where $\omega = N(z)$. The solutions of (5.3) change in character from oscillatory in z for $\omega < N(z)$ to exponential in z for $\omega > N(z)$. The second case corresponds to higher frequencies, which do have turning points, but it applies to locations z far from the turning point. The Bessel function solution is exact in both regimes.

An alternative approach was described by Desaubies (1973) using the WKB method, which was originally devised for boundary value problems in quantum mechanics. Asymptotic solutions for large k valid for all depths can be obtained from WKB theory for general N(z) profiles. In the case of frequencies less than the minimum BV frequency of the water column, N_{min}, the WKB solution is (Olver, 1974)

$$W(k,\omega,z) = F(k,\omega)\, p^{-\frac{1}{4}}(z) \sin\left[k \int_{-h}^{z} p^{\frac{1}{2}}(z')dz' \right] \qquad (5.48)$$

$$\text{for } \omega < N_{min},$$

where $F(k,\omega)$ is a constant determined by the imposed normalization condition. In the case of frequencies with one turning point z_o, and oscillatory behavior for $z>z_o$, the WKB solution is

$$W(k,\omega,z) = G(k,\omega)p^{-\frac{1}{4}}(z)\, (-\zeta)^{\frac{1}{4}}\, Ai\,(k^{2/3}\zeta) \qquad (5.49a)$$

$$\text{for } N_{min} < \omega < N(z)$$

where

$$\frac{2}{3}(-\zeta)^{3/2} = \int_{z_o}^{z} p^{\frac{1}{2}}(z')\, dz', \qquad (5.49b)$$

and Ai is the Airy function. The Airy functions Ai and Bi are sketched in Figure 5.1. At depths above the turning point ζ is negative and Ai is oscillatory; at depths below Ai decays. Strictly the solution should be written as (5.49a) with an additional term of identical form to (5.49a) but with Ai replaced by Bi. The contribution to the solution from this latter term is always very small and can be neglected. At large negative values of its argument

$$Ai(x) \simeq \pi^{-\frac{1}{2}} x^{-\frac{1}{4}} \cos\left[\frac{2}{3}(-x)^{3/2} - \tfrac{1}{4}\pi\right] \qquad (5.50)$$

which will be useful.

Low Frequencies

We will consider the low frequency case first. The bottom boundary condition (at z=-h) is satisfied by (5.48). The surface boundary condition is satisfied for

$$k = \kappa_j(\omega) = j\pi/\ell(\omega) \qquad (5.51a)$$

where

$$\ell(\omega) = \int_{-h}^{o} p^{\frac{1}{2}}(z')\, dz' \qquad (5.51b)$$

The eigenvalues computed from (5.51) are accurate to $0(k^{-1})$.

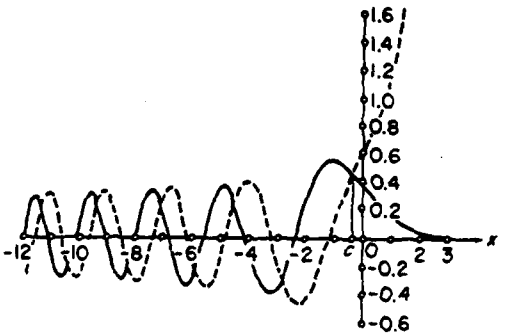

——— Ai

——— Bi

Figure 5.1: The Airy functions Ai(x) and Bi(x).

As mentioned earlier, Garrett and Munk normalized their wave functions so that the mean energy per unit surface area of each mode is identical. This means

$$\tfrac{1}{2}\int_{-h}^{0} dz\ [U_1U_1^* + U_2U_2^* + (1+N^2/\omega^2)WW^*] = b. \quad (5.52)$$

From (5.4)

$$U_1U_1^* + U_2U_2^* = k^{-2}\ (1+f^2/\omega^2)(d_zW)^2.$$

Equation (5.3) can be multiplied by W and integrated by parts to yield

$$\int_{-h}^{0}(d_zW)^2dz' = k^2\int_{-h}^{0}p(z')W^2dz'.$$

These two results can be combined with (5.52) to yield the normalization condition

$$\int_{-h}^{0}\frac{N^2-f^2}{\omega^2-f^2}\,W^2\,dz = b. \quad (5.53)$$

The coefficient $F(k,\omega)$ in (5.48) is obtained by substituting (5.48) into (5.53), replacing $\sin^2(\ )$ by $1/2[1-\cos2(\ )]$, and integrating the $\cos2(\ )$ integral using the method of stationary phase. The latter integral vanishes, and

$$F^2(k,\omega) = 2b(\omega^2-f^2)^{\frac{1}{2}}\left[\int_{-h}^{0}dz\ \frac{N^2-f^2}{(N^2-\omega^2)^{\frac{1}{2}}}\right]^{-1}, \quad (5.54)$$

or

$$F^2(k,\omega) = 2b\,(\omega^2-f^2)^{\frac{1}{2}}\,I^{-1}, \qquad (5.55)$$

which defines I.

For the case considered by Garrett and Munk $N(z) = N_0 e^{z/b}$ and

$$\int_{-h}^{z} p^{\frac{1}{2}}(z')dz' = \int_{-h}^{z}\left(\frac{N^2-\omega^2}{\omega^2-f^2}\right)^{\frac{1}{2}} dz$$

$$= b(\omega^2-f^2)^{-\frac{1}{2}}\left\{\left|N^2(z)-\omega^2\right|^{\frac{1}{2}} - \left|N^2(-h)-\omega^2\right|^{\frac{1}{2}}\right.$$

$$\left. - \left|\arccos\frac{\omega}{N(z)} - \arccos\frac{\omega}{N(-h)}\right|\right\}. \qquad (5.56)$$

If $\omega \ll N(-h)$ this becomes

$$b(\omega^2-f^2)^{-\frac{1}{2}}\,[N(z)-N(-h)]\quad,$$

and (5.48) can be approximated as

$$W(k,\omega,z) = F(k,\omega)\,\frac{(\omega^2-f^2)^{\frac{1}{2}}}{N^{\frac{1}{2}}(z)}\sin\left\{kb\,(\omega^2-f^2)^{-\frac{1}{2}}\,[N(z)-N(-h)]\right\}. \qquad (5.57)$$

The dispersion relation (5.51) becomes

$$\omega_j(\omega) = \frac{j\pi}{b}\,(\omega^2-f^2)^{\frac{1}{2}}\,[N_0-N(-h)]^{-1} \qquad (5.58)$$

and for a deep ocean

$$\omega_j = \frac{j\pi}{bN_o}(\omega^2-f^2)^{\frac{1}{2}}. \qquad (5.59)$$

The integral in (5.54) is easy to integrate and for $\omega << N$ has value bN_0. With $F(k,\omega)$ evaluated (5.48) is written finally as

$$W(k,\omega,z) = \left|\frac{2}{N_o N(z)}(\omega^2-f^2)\right|^{\frac{1}{2}} \sin\left\{kb(\omega^2-f^2)^{-\frac{1}{2}}\left[N(z)-N(-h)\right]\right\} \qquad (5.60)$$

for $\omega << N(-h) << N_o$
which is exactly the expression given by GM.

Higher Frequencies

In the case of frequencies with one turning point, the approximate dispersion relation is obtained from the surface boundary condition. If ζ_o is given by (5.49b) with z=0, the dispersion relation is given by

$$Ai(k^{2/3}\zeta_o) = 0$$

so that the eigenvalues of $k_j(\omega)$ are given in terms of the zeros of Ai. For large values of $k^{2/3}\zeta_o$, zeros of Ai are given by (Abramowitz and Stegen, 1965, p. 450).

$$k^{2/3}\zeta_o = -\left[\frac{3\pi}{8}(4j-1)\right]^{2/3}$$

or

$$\omega_j = \frac{3\pi}{2}(j-\tfrac{1}{4})(-\zeta_o)^{-3/2} \qquad (5.61)$$

The normalization condition is obtained by substituting (5.49) into (5.53) to obtain

$$G^2(k,\omega) = bk^{4/3} \left[\int_{\xi(o)}^{\xi(-h)} d\xi \, \frac{N^2-f^2}{\omega^2-N^2} \, \xi \, A_i^2(\xi) \right]^{-1}$$

where

$$\xi \equiv k^{2/3} z$$

Desaubies (1973) showed that this could be approximated

$$G^2(k,\omega) = 2\pi bk^{1/3} (\omega^2-f^2)^{\frac{1}{2}} \, I^{-1} \qquad (5.62)$$

where I was defined by (5.55) but with lower limit of integration z_0 instead of -h. With the assumption that $\omega \ll N(z)$, so that we are considering locations far from the turning point, $I = bN_0$ and we can make use of the asymptotic expression (5.50) to write

$$W(k,\omega,z) = \left[\frac{2}{N_o N(z)} \, (\omega^2-f^2) \right]^{\frac{1}{2}} \cos \left\{ \frac{kb}{(\omega^2-f^2)^{\frac{1}{2}}} \, \left[N(z) - \tfrac{1}{2}\pi\omega \right] - \tfrac{1}{4}\pi \right\} \qquad (5.63)$$

which is identical to GM's (2.9). The dispersion relation is obtained from (5.61) and (5.49b). We obtain

$$\kappa_j = (j-\tfrac{1}{4})\pi(\omega^2-f^2)^{\frac{1}{2}} \, (N_o - \tfrac{1}{2}\pi\omega)^{-1} b^{-1} \qquad (5.64)$$

which is consistent with (5.63), and since $\omega << N(z) \leq N_0$ we approximate this as

$$\kappa_j = (j-\tfrac{1}{2})\pi(\omega^2-f^2)^{\frac{1}{2}}(N_o b)^{-1}. \qquad (5.65)$$

Mean-Square Wave Functions

To simplify the induction of the form of the energy-density spectrum from various component spectra Garrett and Munk made use of a simplifying assumption. They proposed that the products of the wave functions $U_m U_m^*$ could be replaced by their mean-square values averaged over vertical phase (that is, between the zeroes of the function). The resulting mean-square functions are independent of horizontal wavenumber, and can be viewed as averaged over horizontal wavenumber or mode number (Desaubies, 1975).

When averaged this way, and with the assumption that N(z) in the coefficients of the sin and cos of (5.60) and (5.63) varies slowly over the phase, the mean square wave functions are identical in both the low and higher frequency cases. They are

$$\overline{U_o U_o^*}(\omega) = [N_o N(z)]^{-1} \omega^{-2} (\omega^2-f^2) , \qquad (5.66a)$$

$$\overline{U_1 U_1^*}(\theta,\omega) = N(z) N_o^{-1}\omega^{-2} (\omega^2\cos^2\theta + f^2\sin^2\theta) , \qquad (5.66b)$$

$$\overline{U_2 U_2^*}(\theta,\omega) = N(z) N_o^{-1} \omega^{-2}(\omega^2\sin^2\theta + f^2\cos^2\theta) , \qquad (5.66c)$$

$$\overline{U_3 U_3^*}(\theta,\omega) = [N_o N(z)^{-1}] (\omega^2-f^2) . \qquad (5.66d)$$

These apply when $w << N(z)$.

Note that the horizontal velocity squared

$$\overline{UU^*} \equiv \overline{U_1U_1^*} + \overline{U_2U_2^*} = N(z)\, N_o^{-1}\omega^{-2}(\omega^2 + f^2), \quad (5.66e)$$

The averaged value of $\overline{U_1U_2^*}$ is given by

$$\overline{U_1U_2^*} = \frac{N}{N_o}\left[\frac{k_1k_2}{k^2}\left(1-\frac{f^2}{\omega^2}\right)-if\omega\right] . \quad (5.66f)$$

Müller et al. (1978) argue that the combination of local vertical averaging and smearing of the mode structure associated with the equivalent continuum corresponds to a WKBJ approximation. This is not strictly correct. As an alternative we might view the vertical averaging as being consistent with ensemble averaging over a random vertical phase which is introduced with the "equivalent continuum". The Brunt-Väisälä frequency is assumed to vary slowly compared with the phase, consistent with a WKB approximation.

This wave-function model predicts several simple results. In particular, the ratio of the average potential energy E_p associated with waves of frequency ω to the average horizontal kinetic energy E_{kh} of those waves is given by

$$E_p/E_{kh} = N^2\, \overline{U_oU_o^*}/\overline{UU^*} \quad (5.67a)$$

or from (5.66)

$$E_p/E_{kh} = (\omega^2-f^2)/(\omega^2+f^2) . \qquad (5.67b)$$

The ratio of potential energy to the total kinetic energy is

$$E_p/E_k = \frac{N^2\,\omega^{-2}(\omega^2-f^2)}{N^2\omega^{-2}(\omega^2+f^2)+(\omega^2-f^2)} . \qquad (5.67c)$$

At the inertial frequency the vertical particle displacements are zero and $E_p=0$. At frequencies $f<<\omega<<N$

$$E_p/E_{kh} \approx E_p/E_k \approx 1 \qquad (5.67d)$$

so that in this frequency range most of the kinetic energy is associated with horizontal velocities, and there is approximate energy partition between potential and kinetic. Relations (5.67) are not appropriate near $\omega=N$. They were derived from wavefunctions which had been simplified with the assumption that $\omega<<N$. For $f<<\omega\leq N$ (5.67b) predicts that $E_p/E_{kh}=1$ and $E_p/E_k=1/2$ which means that half of the kinetic energy is associated with horizontal currents. At $\omega=N$, however, the wave motion should be strictly vertical so that E_{kh} should equal zero.

By vertically averaging (5.48) and (5.49) without the assumption $\omega \ll N$ Desaubies found

$$E_p/E_{kh} = \frac{N^2}{N^2-\omega^2} \cdot \frac{\omega^2 - f^2}{\omega^2 + f^2} \tag{5.68a}$$

and

$$E_p/E_k = \frac{N^2}{\omega^2} \cdot \frac{\omega^2(\omega^2-f^2)}{(\omega^2+f^2)(N^2-\omega^2) + \omega^2(\omega^2-f^2)} \tag{5.68b}$$

At $\omega=f$, $E_p=0$ and $E_k=E_{kh}$. At $\omega=N$, $E_{kh}=0$ and so $E_p/E_{kh} \to \infty$ and $E_p/E_k=1$. Note that there is energy equipartition between potential and kinetic energy only at $\omega=N$. The usual linear result $E_p=E_k$ is not true for inertio-internal waves. Relations (5.68a) and (5.68b) are appropriate away from the turning depth of the frequency in question. For depths closer to the turning point than the last zero of Ai (see Fig. 5.1) a modification is required (see Desaubies, 1973).

5.2.4 The Energy-Density Spectrum

Garrett and Munk (1972) proposed that $\tilde{E}_c(k,\omega)$ have the form

$$\tilde{E}_c(k,\omega) = c k_*^{-1}(\omega) A(\lambda)\, B(\omega) \tag{5.69a}$$

where $k_*(\omega)$ is a measure of the wavenumber bandwidth and $\lambda=k/k_*$. The wavenumber dependence is constrained such that $A(\lambda)=0$ for $\lambda < \lambda_1 = \kappa_1(\omega)/k_*(\omega)$ so that there is no energy associated with modes of horizontal wavenumber less than that of the greatest mode. In most cases λ_1, is sufficiently small that it can be taken as zero.

The wave number dependence is constrained such that

$$\int d\lambda\ A(\lambda) = 1 \qquad (5.69b)$$

and

$$\int dk\ \tilde{E}_c(k,\omega) = c\ B(\omega)\ . \qquad (5.69c)$$

From the normalization condition (5.52), the equivalent continuum counterpart to (5.17) is

$$E_o = b \int d\omega \int dk\ \tilde{E}_c(k,\omega) \qquad (5.69d)$$

or

$$E_o = cb \int_f^N d\omega\ \ B(\omega)$$

which relates c and the total energy per unit area E_0 (which has units $m^3 s^{-2}$).

GM72 required that the frequency dependence be such that $C_{00}(\omega)$, $C_{11}(\omega)$ and $C_{22}(\omega)$ (from 5.45) have an

ω^{-2} behavior for $\omega >> f$, and that $C_{11}(\omega)$ and $C_{22}(\omega)$ exhibit a cusp at $\omega = f$. The simple form

$$B(\omega) = \omega^{-1}(\omega^2 - f^2)^{-\frac{1}{2}} \quad \text{for} \quad f \leq \omega \leq N \qquad (5.70)$$

$$= 0 \text{ otherwise} \quad ,$$

which satisfies these rather gross constraints, was proposed. Then from (5.69d) $c = 2fE_0(\pi b)^{-1}$.

GM72 proposed a very simple "top hat" form for $A(\lambda)$:

$$A(\lambda) = 1 \quad \text{for} \quad 0 \leq \lambda \leq 1 \qquad (5.71a)$$

$$= 0 \text{ otherwise} \quad .$$

The bandwidth $k_*(\omega)$ is determined from the high mode, low frequency dispersion relation (5.59) as

$$k_*(\omega) = \frac{j_* \pi}{bN_o} (\omega^2 - f^2)^{\frac{1}{2}} \quad . \qquad (5.71b)$$

The quantity j_* may be viewed as the equivalent modal bandwidth since (5.71a) and (5.71b) imply that energy only exists at wavenumbers corresponding to mode numbers less than j_*. With (5.71), predicted towed wavenumber spectra

exhibit a k^{-2} dependence which is observed.

Equations (5.69)-(5.71) completely determine the energy density spectrum. Estimates of moored and towed spectra can be obtained from (5.45) and (5.47) and the phase average wavefunctions (5.66). The moored spectrum of isotherm displacement $MS_\zeta(\omega) \equiv C_{00}(0,\omega,z,z)$ can be obtained by substituting (5.66a) and (5.69)-(5.71) into (5.45) to yield

$$N\, MS_\zeta(\omega) = \frac{2}{\pi} \frac{E_o f}{bN_o} \frac{(\omega^2 - f^2)^{\frac{1}{2}}}{\omega^3}, \qquad (5.72a)$$

The moored spectrum of horizontal velocity $MS_u(\omega) \equiv C_{11}(0,\omega,z,z) + C_{22}(0,\omega,z,z)$ can be obtained by substituting (5.66b)-(5.66c) and (5.69)-(5.71) into (5.45) to yield

$$N^{-1} MS_u(\omega) = \frac{2}{\pi} \frac{E_o f}{bN_o} \frac{(\omega^2 + f^2)}{\omega^3 (\omega^2 - f^2)^{\frac{1}{2}}}, \qquad (5.72b)$$

From (5.47), (5.66a) and (5.70) GM derive the towed horizontal wavenumber spectrum $TS_\zeta(k_1) \equiv C_{00}(k_1,\omega,z,z)$ as

$$N\, TS_\zeta(k_1) = \frac{4}{\pi 3} E_o j_*^{-1} f \int_{\omega_*}^{N} d\omega\, \omega^{-3} \cosh^{-1}(k_*/k_1) \qquad (5.72c)$$

where ω_* is defined by

$$k_1 = \frac{j_* \pi}{bN_o} (\omega_*^2 - f^2)^{\frac{1}{2}} \quad ,$$

and it represents the lowest frequency which can be associated with wavenumber k_1. For $f << \omega_* << N$

$$NTS_\zeta (k_1) = \frac{2}{\pi} \frac{F_o f}{b^2 N_o^2} j_* k_1^{-2} \qquad (5.72d)$$

Figure 5.2 from GM72 shows horizontal kinetic energy frequency spectra and vertical displacement horizontal wavenumber spectra from several experiments. The figure also shows predicted spectral levels from equation (5.71b) and (5.71c). The model-predicted frequency spectra are in good agreement with the data over a substantial part of the spectra. Of the two low frequency peaks apparent in the data the lower is at the local inertial frequency of the experiments. The model predictions were for a slightly lower latitude (30° versus 39°N) and the model peak is slightly displaced. The higher frequency peak in the data is of semi-diurnal frequency and probably represents an internal-tide effect. The model prediction cut off at the specified level value of N. In the figure n=1/4 means a frequency 25% of 3 cph. The wavenumber spectra are in good agreement with the data for low wavenumbers (less than about 10 cpkm). The data does not show the model predicted roll-off at higher wavenumbers.

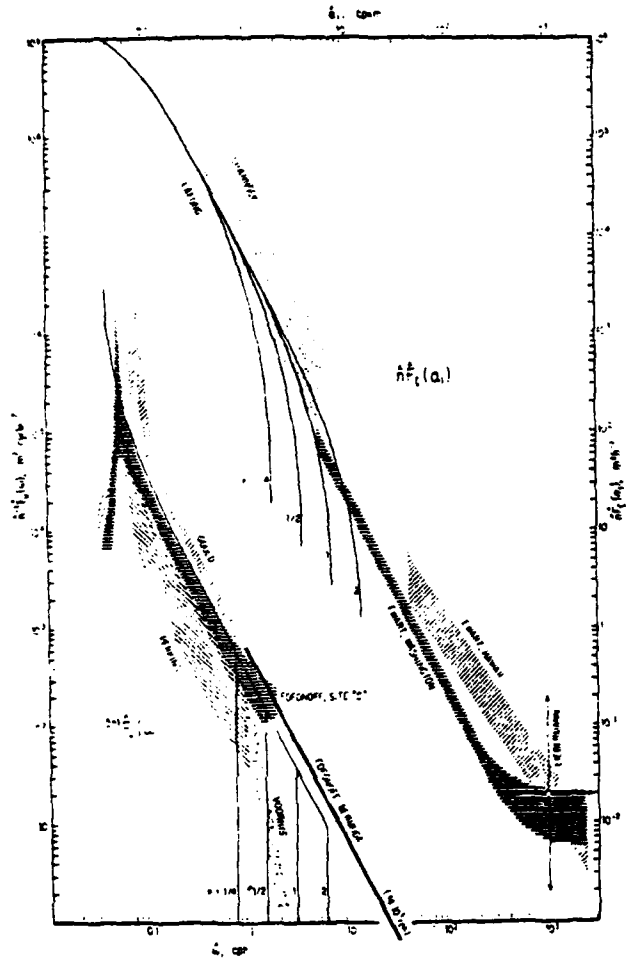

Figure 5.2: Spectra of horizontal kinetic energy vs. frequency and vertical displacement vs. horizontal wave number for various experiments.

Garrett and Munk argued that the continuation of Fofonoff's Bermuda spectra beyond the local Brunt-Väisälä frequency and the continuation of Ewart's wavenumber spectra beyond $k_*(\omega)$ were due to "fine-structure".

For the predictions above $\rho E_0 = 0.382$ Joules cm^{-2}, b=1300m and $N_0 = 3$ cph (6π hr^{-1}). This implies $E_0 = 3.7$ $m^3 s^{-2}$. If we write $E_0 = b^3 N_0 E'$, where E' is a dimensionless constant, then with these values of b and N_0, $E' = 2 \times 10^{-5}$, a value determined in GM72.

Garrett and Munk also found good agreement with the rather limited data which at that time was available to describe coherence. It is important to note that the frequency spectra (5.72a) and (5.72b) do not depend on the wavenumber or mode number bandwidths ($\mu(\omega)$ and j_*), so that their results could be obtained for essentially a single energetic mode. In addition, the horizontal wavenumber spectra (5.72d) could be obtained with a single mode of number $1/2j_*$. It is the lack of coherence in data which demands that the wave field be viewed as a many-mode superposition.

Garrett and Munk produced a revised model in 1975 based on the hypothesis that much of the observed fine-structure was actually the result of internal wave strain. In the model (GM75), they replaced the top-hat wavenumber function $A(\lambda)$ by

$$A(\lambda) = (t-1)\,(1+\lambda)^{-t} \qquad t = 2.5 \qquad (5.73a)$$

and reduced the bandwidth

$$k_*(\omega) = \frac{j_*\pi}{bN_o} (\omega^2 - f^2)^{\frac{1}{2}} \qquad (5.73b)$$

by reducing j* from 20 to 6. As defined in (5.72a)

$$\int d\lambda \; A(\lambda) = 1 \qquad (5.73c)$$

but most of the energy is contained in $\lambda < 1$. Figures 5.3 and 5.4 compare GM75 model predictions with isotherm displacement frequency and horizontal wavenumber spectra computed from observations by Cairns (1974) and Katz (1974). The frequency spectra (Figure 5.3) agree very well except near the local Brunt-Väisälä frequency where the observations show a peak. (We note that GM75 and GM72 frequency spectra are equivalent since they do not depend on the form of $A(\lambda)$). The wavenumber spectra (Figure 5.4) also agree very well. The range of agreement is now extended to wavenumbers of about 2×10^{-2} cpm, or wavelengths of 50 m. This is a major improvement over the GM72 model (Figure 5.2).

Figure 5.5 shows a comparison between a normalized spectrum of isotherm displacement in terms of vertical wavenumber from (Millard, 1972) and a GM75 model prediction. The vertical wavenumber spectrum, or "dropped spectrum (DS)", was computed from temperature spectra in vertical wavenumbers which were converted to displacement spectra

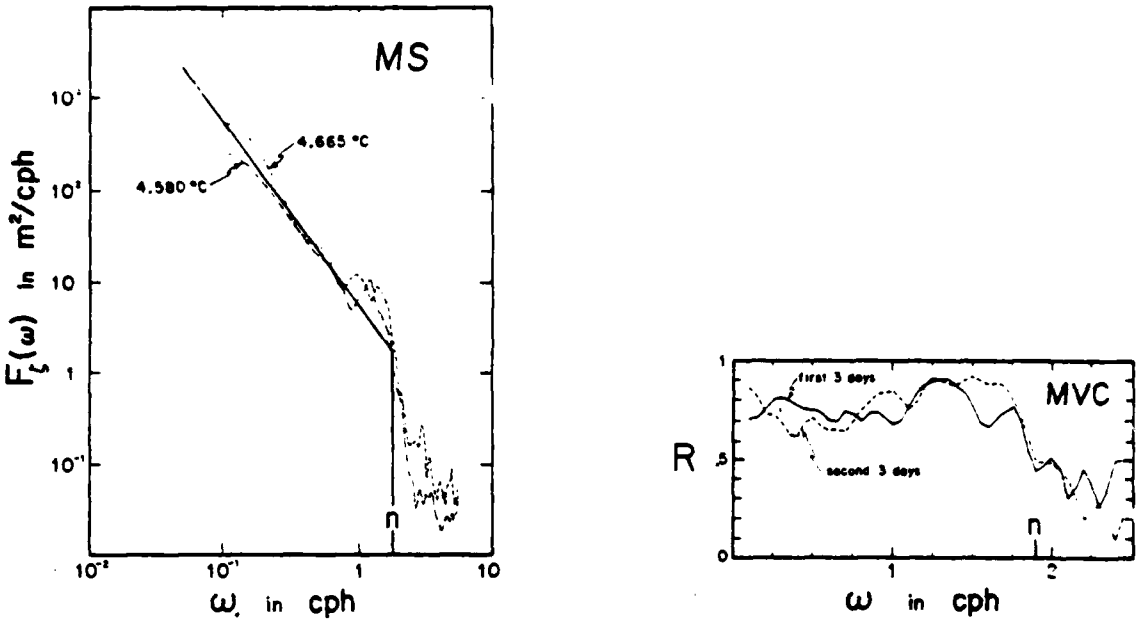

Figure 5.3: Vertical displacement spectrum vs. frequency and moored vertical coherence at 100 m separation. The solid spectrum line is based on GM75. Dashed lines are based on data from Cairns (1974).

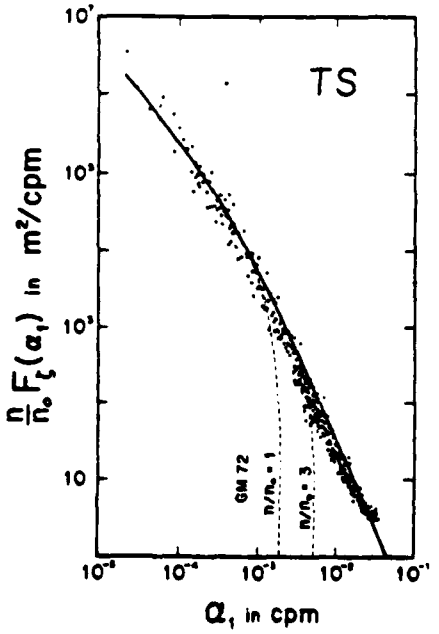

Figure 5.4: Normalized towed vertical displacement spectrum vs. horizontal wavenumber. Data from Katz (1974): solid line from GM75: dashed lines from GM72.

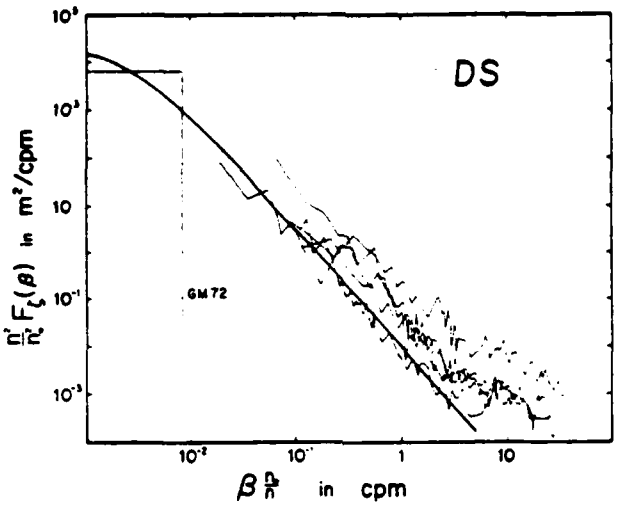

Figure 5.5: Normalized dropped vertical displacement spectrum vs. vertical wavenumber. Data are from Millard (1972): heavy solid curve from GM75: dotted curve from GM72.

using the mean temperature gradient. The local vertical wavenumber is defined in the model as

$$\beta^2 = k^2 \frac{N^2-\omega^2}{\omega^2-f^2} \approx \frac{j^2\pi^2N^2}{b^2N_o^2} \quad \text{for } \omega<<N \qquad (5.74a)$$

from the dispersion relation (5.59), and

$$\beta_*^2 = \frac{j^2*\pi^2N^2}{b^2N_o^2} \quad . \qquad (5.74b)$$

We see that $k/k*(\omega)=\beta/\beta*$. We define $\tilde{E}_c(k,\omega)$ and $\tilde{E}_c(\beta,\omega)$ such that

$$\iint dk d\omega\ \tilde{E}_c(k,\omega) = \iint dk d\beta\ \tilde{E}_c(k,\beta) = \iint d\beta d\omega\ \tilde{E}_c(\beta,\omega) \qquad (5.75a)$$

and

$$\tilde{E}_c(\beta,\omega) = \tilde{E}_c(k,\omega)\frac{dk}{d\beta} = \tilde{E}_c(k,\omega)\,(\omega^2-f^2)^{\frac{1}{2}}\,N^{-1} \qquad (5.75b)$$

or

$$\tilde{E}_c(\beta,\omega) = \frac{2}{\pi}\frac{E_o f}{b} A(\beta/\beta_*)\,B(\omega)\,\beta_*^{-1}(\omega) \quad .$$

Cairns and Williams (1976) described a model for the energy density in terms of discrete modes:

$$E_j(\omega) = \frac{2}{\pi} E_o f B(\omega)\, H(j) \qquad (5.76a)$$

where

$$H_j = (j^2+j_*^2)^{-p} / \sum_{j=1}^{\infty} (j^2+j_*^2)^{-p} . \qquad (5.76b)$$

Observations from a freely drifting midwater instrument package which supported a vertical array of thermistors were used to derive estimates of j_* and p. The model-predicted vertical coherences agree well with those derived from the observations for $j_*=3$ and p=1 (Figure 5.6). Then the isotherm displacement dropped spectrum $DS_\zeta(\omega)$ (where subscripts refers to isotherm displacement) is defined as

$$DS_\zeta(\beta) = \int_F^N d\omega\, \overline{U_o U_o^*}\, E_c(\beta,\omega) . \qquad (5.77)$$

The modeled and measured DS diverge at wavenumbers of about 10^{-1} cpm.

The value of t in (5.73a) was determined by matching the model-predicted and observed DS. The value of j_* was determined from a consideration of moored vertical and

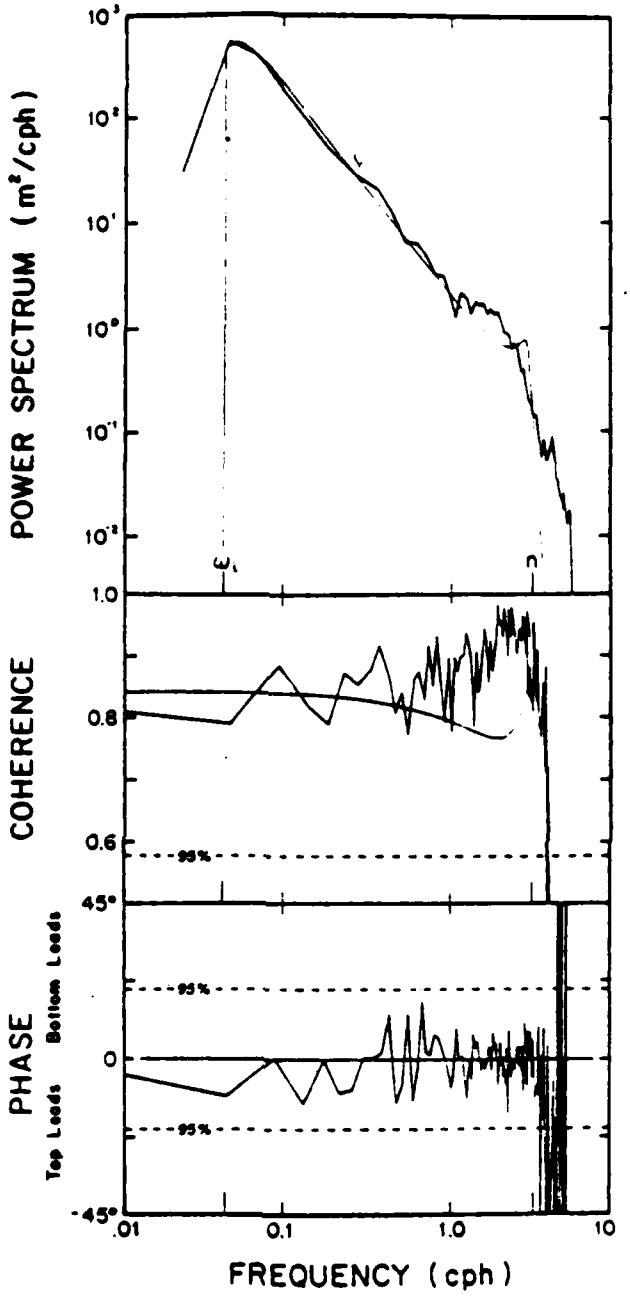

Figure 5.6: Vertical displacement spectrum, coherence, and phase vs. frequency. Data are from Cairns and Williams; smoothed curves are from the Cairns and Williams model.

moored horizontal coherences (MVC and MHC). The model MVC is not a function of frequency (consistent with the data in Figure 5.3), and it decreases as the bandwidth j_* decreases. The energy level E_0 is that derived in GM72.

5.2.5 Model Validation

The success of the internal wave spectrum models of Garrett and Munk and succeeding researchers can only be evaluated in the light of observational evidence. We have already discussed the work of Cairns (1975), who found good agreement throughout most of the frequency band between GM75 and observations of isotherm displacement. Discrepancies near the local B-V frequency led Cairns and Williams to modify the modal dependence of the model (see Section 5.2.4, Equation 5.77) to improve agreement with observations. *Figure 5-6 shows some of their results. Note* the localized peak in the power spectrum near N which was not present in Cairns' results.

Gregg (1977a) analyzed temperature records from several cruises in the North Pacific, one in the South Pacific, and records taken during MODE. All of the resulting temperature vertical wavenumber spectra showed an inflection point in the wavenumber range between 0.06 cpm and 0.1 cpm. At low wavenumbers the spectra decreased as k^{-3} (see Figure 5.7). GM75 indicated a $k^{-2.5}$ slope across the whole wavenumber band. As Gregg points out, the most striking fact in his study is not the discrepancies between GM75 and observations, but the striking similarities among the spectra, which were collected at widely

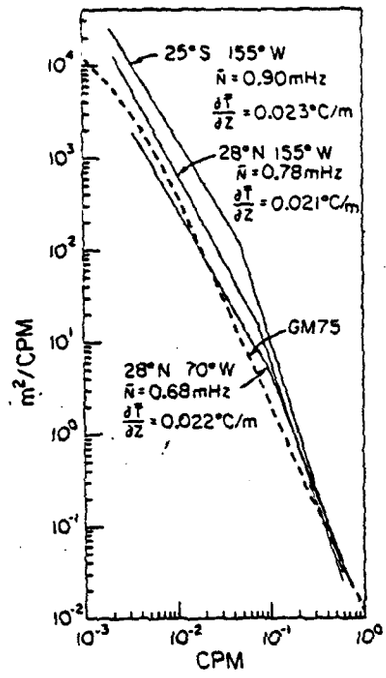

Figure 5.7: Isotherm displacement spectrum vs. wavenumber. Solid lines are based on data from Gregg (1977): dashed line from GM75.

separated locations. This fact lends credence to GM's assumption of a wide-spread uniformity (at least to a certain extent) in the internal wave field.

IWEX (Internal Wave Experiment; Briscoe, 1975) provided the first data set which contained sufficient horizontal, vertical, and temporal scales to allow an examination of the assumptions embodied in GM-class models. The IWEX array consisted of a trimooring of current meters, temperature sensors, and vertical temperature gradient sensors in a nearly perfect tetrahedral shape (including the base). Sensor depths ranged from 604 m to 2050 m in the Hatteras Abyssal Plain. Temperature gradients were measured over a vertical distance of 1.74 m. Horizontal and vertical temperature sensor separations ranged from 2 m to O(1500 m), while current meter separations ranged from 7 m to O(500 m). The array was in place for 42 days in late 1973.

Müller et al. (1978) performed a comprehensive analysis of the IWEX data. They calculated numerically all of the possible cross-spectra as a function of frequency (a total of 1444 auto- and cross-spectra!). They first analyzed spectra to determine the characteristics of the field. Autospectra showed peaks at the inertial and tidal (M_2) frequencies, and smaller peaks at the local B-V frequencies. Coherences between the same components of the wave motions showed that the high frequency portion of the data do not contain pure internal waves. Further examination revealed contamination by temperature and current finestructure, as well as current noise. Most of the low frequency motions,

on the other hand, can be ascribed to internal waves. The wave motions proved to be very nearly horizontally isotropic, except at low frequencies (especially near the M_2 tide) where southeastward propagation was evident. Some slight vertical asymetries were apparent also. The equivalent bandwidth of the power spectra varied from 20 to 10 with increasing frequency. At high wavenumbers the spectra dropped off as k^{-t}, where $2<t<3$, while the low wavenumber spectra contained peaks at mode numbers 0(1-2). At low frequencies the propagating wave interpretation was strongly supported by the data; at high frequencies the standing mode interpreation was favored; at intermediate frequencies either interpretation was adequate.

The results obtained by Müller et al. showed that most of the assumptions of GM-class models were valid for the small portion (5%) of the total IWEX data set examined. They developed a set of consistency relationships to show how well any model conformed to results obtained by using the complete data set. They determined that GM-class models (i.e., models based on the assumptions listed on page 5-3) cannot adequately characterize the IWEX spectra. Figure 5-8 shows plots of the consistency parameter, Δ^2, as a function of frequency for several simple models (5-8a), the full GM75 model (5-8b), each of the individual GM model assumptions (5-8c to 5-8g), and an IWEX-class model (see Müller et al. for details).* A model is consistent when Δ^2 values fall below the dashed line (95% confidence limit) and are randomly scattered about 1.0. In most cases the inconsistencies occur at the extreme ends of the band ($\omega \leq M_2$ or $\omega \rightarrow N_{max}$).

*Briscoe (1975) demonstrated the stationarity of the IWEX internal wave field. This assumption was not tested for consistency.

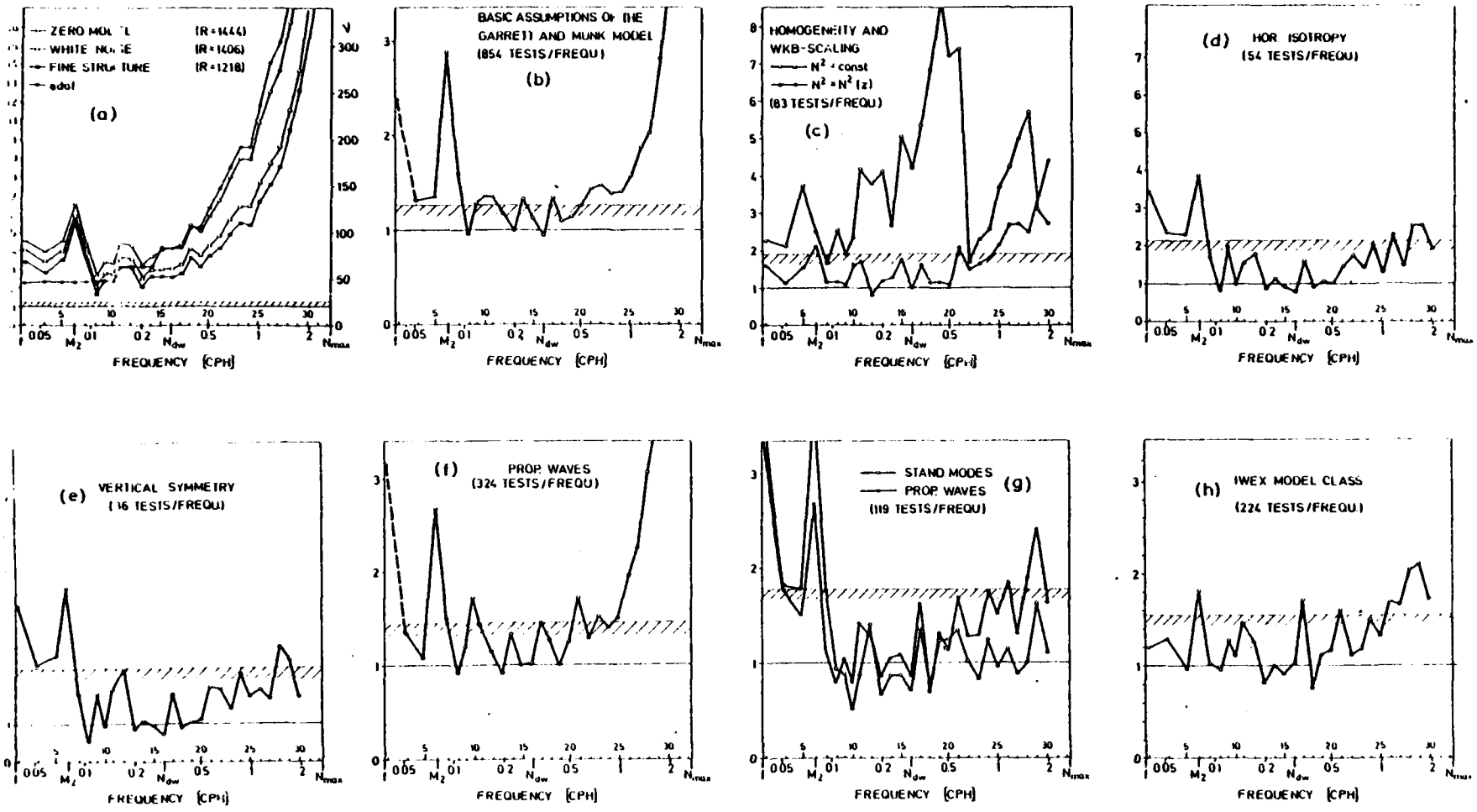

Figure 5.8: Consistency parameters vs. frequency for various configurations of GM-Type models.

Müller et. al. (1978)

Müller et al., following the path of Garrett and Munk, modified GM 75 to fit IWEX data. They factorized the internal wave energy spectrum in the form

$$E(k,\theta,\omega,\sigma) = E(\omega,\sigma)\, A(k;\omega)\, S(\theta;\omega) \tag{5.79}$$

where $E(\omega,\sigma)$ is the energy propagating upward or downward at frequency ω, $A(k;\omega)$ is the normalized wavenumber distribution, and $S(\theta;\omega)$ is the directional distribution. These last two are expressed as

$$A(k;\omega) = s\Gamma\left(\frac{t}{s}\right)\left\{\Gamma\left(\frac{1}{s}\right)\Gamma\left(\frac{t-1}{s}\right)\right\}^{-1}\left\{1+\left(\frac{k-k_p}{k_*}\right)^s\right\}^{-t/s} \qquad k \geq k_p \tag{5.80a}$$

and

$$S(\theta;\omega) = \frac{\Gamma^2(p+1)^{2p}}{2\pi\Gamma(2p+1)}\cos^{2p}\left(\frac{\theta-\theta_o}{2}\right). \tag{5.80b}$$

Equation (5.80a) provides for a sharp cutoff based on the low wavenumber cutoff k_p and the horizontal wave number scale k_*. The quantity t is the high wavenumber slope, and s is a shape parameter. The distribution always has a peak at k_p. Equation (5.80b) allows for horizontal anisotropy for a beam propagating in direction θ_o with beam width p. If p = 0 the distribution is isotropic. The inclusion of σ in (5.79) allows for vertical asymmetry. Figure (5.9) shows the frequency dependence of the various IWEX model parameters. Appropriate values from GM72, GM75, and Cairns and Williams are noted on the right hand vertical axes when they apply.

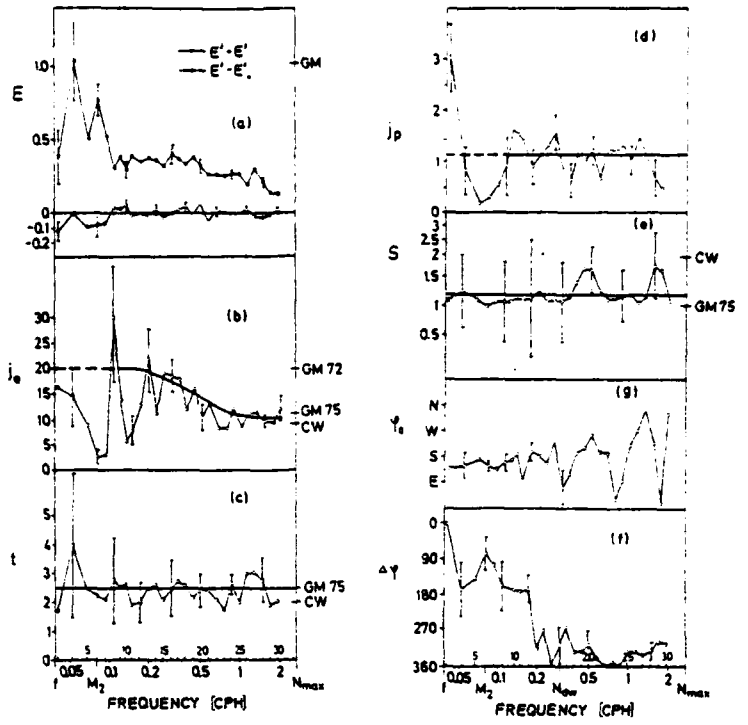

Figure 5.9: Parameters of the IWEX model (Müller et al., 1978) vs. frequency. Parameters are:

(a) total energy $E^+ + E^-$ and energy asymmetry $E^+ - E^-$
(b) equivalent bandwidth j_e
(c) high wave number slope t
(d) peak wave number j_p
(e) peak shape parameters s
(f) beam width parameter $\Delta\phi$
(g) propagation direction ϕ_o

Figure (5.8h) shows the consistency parameter for the IWEX model (after inclusion of functions to parameterize fine structure and current noise contamination). The model is everywhere consistent except at M_2 and near N_{max}.

Müller et al. reached the conclusion that, in general, GM-class models agree with IWEX data and that, after some admittedly complex modifications, better agreement can be obtained. It is important to recognize, however, that the representation by these models of the low frequency components of the wave field is not very good. The low frequency components tend to be highly non-stationary.

Wunsch (1976) tried to find circumstances under which deep ocean internal wave spectra differ significanty from the GM-class models. The level and shape of the spectra were quite constant except near topographic sources (where anisotropy was present), regions of strong shear, and the equator (where no inertial peak was present.)

Desaubies (1976) developed analytical expressions for various internal wave spectra (moored, dropped, and towed) and coherences (moored slant and vertical, towed horizontal and vertical, and dropped horizontal). He used Cairns and Williams' (1976) suggested modifications to GM75; however, he formulated his expressions in terms of continuous modal dependence, partly because of observational evidence and partly because integrals are more easily manipulated than summations. He found that his expressions depended on the local ratio $N(z)/f$ and on two model parameters: $r = E_o\ b^2 N_o$ and $t = j/2bN_o$. Thus his models do not depend on the exponential $N(z)$ which Garrett and Munk assumed. A survey of recent internal wave measurements

showed that estimated values of r, t, and rt were remarkably consistent despite varied measurement techniques. This seems to further underline the general applicability of the GM-type models.

In general, then, the GM approach to internal wave spectra has been verified as more than suitable for at least a first-order characterization of internal waves throughout the deep ocean. The model may founder on a detailed analysis, but it continues to serve as an excellent starting point from which to begin a study of specific observations.

5.3 FINE-STRUCTURE CONTAMINATION MODELS

5.3.1 The Fine-Structure Contamination Problem

In this section we will describe models which have been proposed to describe the effects of irreversible fine-structure on measurements of internal wave properties such as vertical displacement or current. Before the introduction about 15 years ago of electronic profiling systems, vertical profile data was generally of poor vertical resolution, and vertical profiles tended to appear quite smooth. As higher resolution systems were introduced a great deal of smaller scale (1 to 100m) vertical structure was observed. Figure 5-10 (from Gregg, 1977b) shows a good example of this fine structure. The fine structure has often been described in terms of low-gradient layers and thinner, high-gradient sheets. The visual observations made with dye by Woods (1968) and Woods and Fosberry (1966,1967) in the seasonal thermocline in the Mediterranean Sea suggest sheets as thin as a few centimeters and layers on the order of 4m.

Fine structure may result from a number of processes which may be thermodynamically reversible or irreversible. Internal waves may cause distortions of otherwise smooth profiles. No mixing is involved in this case and the process is essentially reversible. Mixing caused perhaps by instability mechanisms or double-diffusion processes represents an irreversible source of fine structure. At this time there appears to be a growing opinion that much of the apparent fine-structure is due in fact to internal-wave distortion. Important recent efforts in this direction

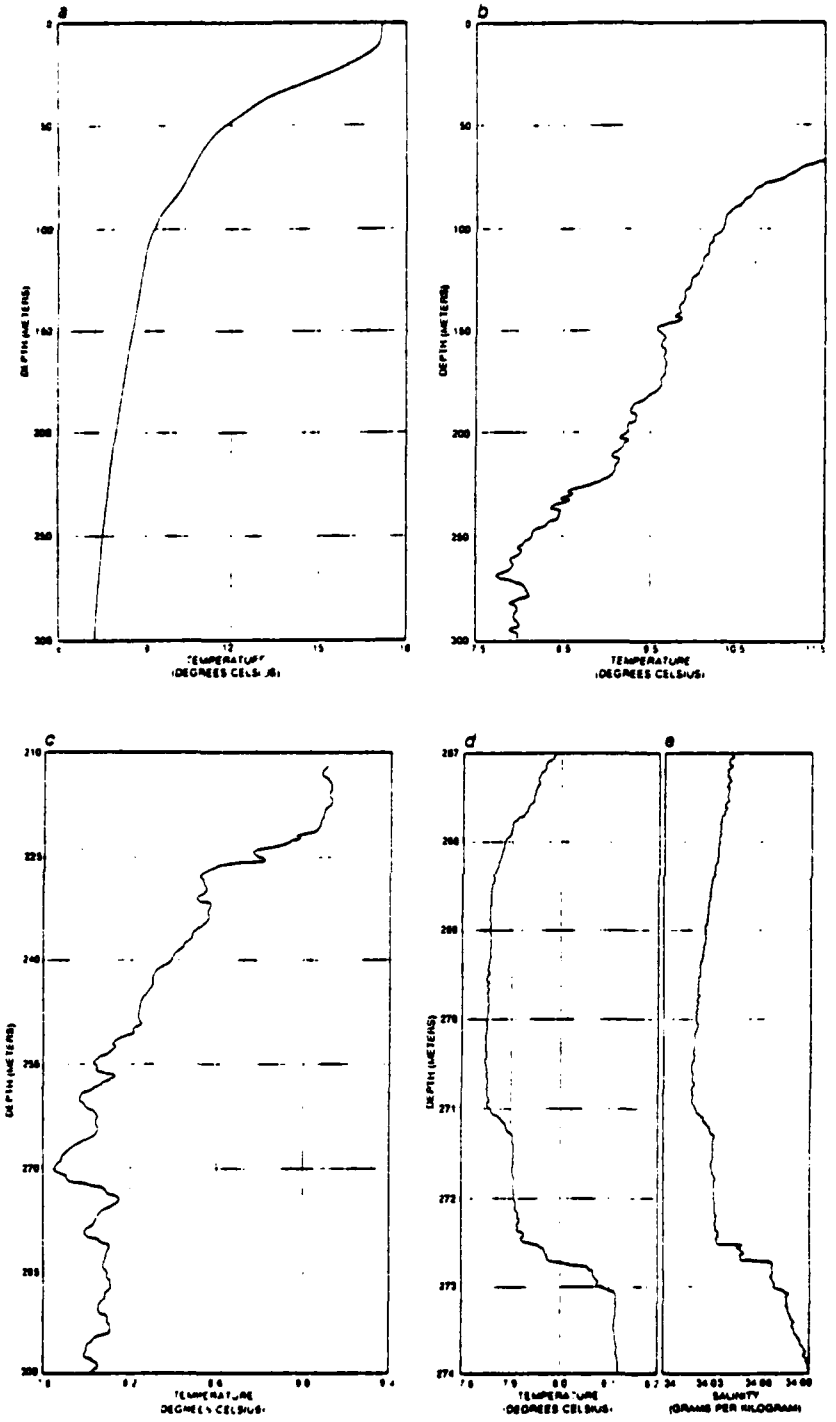

Figure 5-10: Vertical Temperature Profiles Obtained by Using Instruments of Increasing Sensitivity. (a) Record obtained by lowering a bulb thermometer to various depths. (b) Record obtained by using continuously recording electronic instrument with resolution of a few meters. (c) Record obtained by using continuously recording electronic instrument with resolution of roughly 1 cm. (d) Enlarged view of a 7 m portion of (c). (e) Salinity profile taken simultaneously with (c). (Gregg, 1977b).

have been described by Johnson, et al. (1978) and Desaubies and Gregg (1980). Irreversible fine structure does exist, however, and as the models described in this section make clear it may significantly affect the measurement of internal-wave properties.

The essence of the fine-structure contamination problem was apparently first described by Phillips (1971) and we recount his explanation before we discuss detailed modeling of fine-structure effects. The problem is illustrated most simply by considering the temperature spectrum measured at a fixed point in the oceanic thermocline which may be disturbed by internal gravity waves. The water column with the fine-structure variations may heave and subside past the observation point and the record obtained will reflect this. If the undisturbed temperature gradient were continuous and uniform the vertical displacement ζ of a fluid element would be proportional to the variation in temperature ΔT according to the simple relationship

$$\zeta = -\Delta T \; / \; \overline{\partial_z T} \quad , \tag{5.81}$$

where $\overline{\partial_z T}$ represents the mean, undisturbed temperature gradient. Equation (5.81) can be viewed as the first term in a Taylor series expansion for ΔT in terms of ζ, or it can be derived dynamically by considering the heat conservation equation in the limit of no horizontal advection, diffusion or sources. Then

$$\partial_t T = -w \partial_z T \quad , \tag{5.82}$$

where w is the vertical velocity associated with the internal wave field. Over a finite time interval

$$\Delta T = -\int w \partial_z T \, dt \qquad (5.83)$$

Now if over some depth interval we partition $\partial_z T$ into a stationary mean (locally independent of depth) and deviation as

$$\partial_z T = \overline{\partial_z T} + (\partial_z T)' \quad , \qquad (5.84)$$

then

$$\Delta T = -\overline{\partial_z T} \int w dt - \int w(\partial_z T)' \, dt. \qquad (5.85)$$

Equation (5.81) is recovered with the recognition that

$$\zeta = \int w dt \qquad (5.86)$$

and with the assumption that the integral in the second term on the right of (5.85) is small. It is this assumption which the occurrence of irreversible fine-structure calls into question.

In spectral terms, if $F_T(\omega)$ is the observed frequency spectrum of the temperature variation at a fixed depth (moored say), then (5.81) implies

$$F_\zeta(\omega) = F_T(\omega) / (\overline{\partial_z T})^2 \qquad (5.87)$$

where $F_\zeta(\omega)$ is the true displacement frequency spectrum. Since internal waves are described in essence by the displacement or velocities they induce, (5.87) plays an important role in the analysis of temperature time series data.* With the occurrence of significant irreversible fine-structure (5.87) is not appropriate and

$$F_\zeta(\omega) = \left[F_T(\omega) - F_T^f(\omega)\right] / (\overline{\partial_z T})^2 \qquad (5.88)$$

where $F_T^f(\omega)$ is the contribution to the temperature spectrum which arises from the passage of fine-structure past the instrument. It is the estimation of $F_T^f(\omega)$ which is of central interest in contamination estimation.

Similar comments apply to measurements of horizontal velocity fluctuations at a fixed point or measurement of either temperature or horizontal velocity along a horizontal traverse. If there is a non-internal wave shear

*The reliance on the measurement of advected scalar properties for the deduction of vertical displacement and velocity statistics results from the fact that direct vertical velocity measurements are extremely difficult.

concentrated in some sort of sheet-layer structure then the heaving of this structure may give rise to significant signals which may enhance the perceived internal-wave induced variations of the velocity field.

In the following subsections we will describe models which have been put forth by Phillips (1971), Garrett and Munk (1971) and McKean (1974) for the effects of fine-structure on the measurement and determination of internal-wave statistics.

5.3.2 Phillips' Analysis

Phillips (1971) derived expressions for the form of the fine-structure contribution to spectra under idealized conditions. The analysis was straightforward and drew attention to the problem. Suppose that in the undisturbed state (no internal waves) the temperature field is specified by $T_m(z)$, a function which on the large scale increases with height. On the small scale, however, $T_m(z)$ increases in some series of steps, being relatively constant in layers separated by thin sheets where the gradient is far larger. An internal wave motion results in the pattern of sheets and layers being displaced from equilibrium so that a fixed probe observes this pattern as it drifts slowly up and down. The pattern is of course strained so that the spacing of the sheets varies somewhat throughout the wave cycle. Phillips presumed the straining effect to be small.

To a first approximation then the pattern can be assumed to be carried rigidly up and down past the probe. Let $\zeta(t)$ be the vertical displacement from equilibrium of an

isothermal surface (which we assume to move with the isopycnal surface). Then

$$T(z,t) = T_m(z-\zeta(t)) \quad , \tag{5.89}$$

which means that the temperature at depth z and time t at which the vertical displacement is ζ is equal to the temperature of the isotherm at depth $z-\zeta$ in the undisturbed state.

We consider a record spanning a large but finite time period P of observation. We assume that the measured temperature is periodic with period P. Then

$$T(t) = \sum_{-\infty}^{\infty} C_j \exp(ij\omega_o t) \tag{5.90a}$$

where $\omega_o = 2\pi/P$ and the frequency of each component is $\omega = j\omega_o$. The inverse transform is

$$C_j = \frac{1}{P}\int_{-\frac{1}{2}P}^{\frac{1}{2}P} dt\, T(t) \exp(-ij\omega_o t) \quad . \tag{5.90b}$$

Equation (5.90b) can be integrated by parts to yield

$$C_j = \frac{-i}{2\pi j}\int_{-\frac{1}{2}P}^{\frac{1}{2}P} dt\, \partial_t T \exp(-ij\omega_o t) \quad . \tag{5.91}$$

If we treat the sheets as step functions we have

$$\partial_t T = \sum_r (\Delta T)_r \delta(t-t_r) \quad , \tag{5.92}$$

where $(\Delta T)_r$ is the change in T with the passage of the discontinuity at time t_r. Then

$$C_j = \frac{-i}{2\pi j} \sum_r (\Delta T)_r \exp(-ij\omega_o t_r) \quad , \tag{5.93}$$

and

$$C_j C_j^* = \frac{1}{4\pi^2 j^2} \sum_r \sum_s (\Delta T)_r (\Delta T)_s \exp\left[-ij\omega_o (t_r - t_s) \right] . \tag{5.94}$$

We require that the magnitude of the temperature change be uncorrelated with its occurrence and also that j be sufficiently large that

$$j\omega_o \tau_\ell >> 1 \quad ,$$

where τ_ℓ is the typical time interval between crossings. Then the ensemble average of the various terms in (5.94) vanishes except for r=s and

$$\langle C_j C_j^* \rangle = \frac{1}{4\pi^2 j^2} \sum_r \langle (\Delta T)_r^2 \rangle \quad , \tag{5.95a}$$

$$= \frac{\nu P}{4\pi^2 j^2} < (\Delta T)_r^2 > \quad . \qquad (5.95b)$$

where ν is the average number of crossings per unit time. The mean square value of the Fourier coefficients decreases as j^{-2} or ω^{-2}. This ω^{-2} behavior is similar to that of measured internal wave spectra. Therein lies the potential difficulty of distinguishing internal wave-induced and fine-structure-enhanced fluctuations.

Phillips also considered the case of finite thickness sheets in which case

$$\partial_t T = \sum_r (\Delta T)_r \, f_r(t-t_r) \qquad (5.96)$$

where $f_r(t-t_r)$ is a continuous function, non-zero only within a short time interval around zero. In this case (5.95a) applies but with the constraint

$$\tau_s^{-1} >> j\omega_o >> \tau_\ell^{-1} \quad , \qquad (5.97)$$

where τ_s is characteristic of the time a sheet takes to pass the instrument. Result (5.95) is thus appropriate for frequencies small compared with the sheet inverse time scale and large compared with the layer inverse time scale.

The spectral density function $\phi(\omega)$ of the ensemble of stationary random functions is given by

$$\phi(\omega)d\omega = \langle C_j C_j^* \rangle \tag{5.98}$$

in the limit $P \to \infty$. Therefore

$$\phi(\omega) = \frac{\nu}{2\pi} < (\Delta T)_r^2 > \omega^{-2} \quad , \tag{5.99a}$$

with

$$\tau_s^{-1} >> \omega >> \tau_\ell^{-1} \tag{5.99b}$$

If the thickness of the sheets is much less than that of the layers the frequency range over which the ω^{-2} behavior would exist would be quite large, perhaps masking the local Brunt-Väisälä frequency cut-off associated with internal wave motion.

This model for the effects of fine-structure is essentially qualitative. It draws attention to the potential problem, but it is not useful for the analysis of actual time series data.

5.3.3 Garrett and Munk's Analysis

Garrett and Munk (1971) performed a more general analysis of the fine-structure contamination problem which relates the fine-structure contribution to frequency spectra to fine-structure vertical wavenumber spectra. No sheets-layers assumption is required.

Define the covariance of temperature measurements at a fixed depth z as

$$R_T(\tau) = < T(t)T(t+\tau) > \qquad (5.100)$$

where the braces indicate ensemble averaging. Then at depth z_o

$$< T(t)T(t+\tau)> = \int_{-\infty}^{\infty}\int d\zeta_1 d\zeta_2 \; T_m(z_o-\zeta_1)T_m(z_o-\zeta_2)p(\zeta_1,\zeta_2;\tau) \qquad (5.101)$$

where $p(\zeta_1, \zeta_2; \tau)$ is the joint probability density function for displacement ζ_1, at time t and ζ_2 at time $t+\tau$.

For a single realization let the temperature profile referred to $T_m(z_o)$ be

$$T_m(z) = (z-z_o)T' + \theta(z) \quad , \qquad (5.102)$$

consisting of a vertically averaged mean gradient T' and a fine-structure component $\theta(z)$ which has zero vertical and ensemble mean values. Then at z_o

$$T(t) = -\zeta(t)T' + \theta(z_o-\zeta(t)) \qquad (5.103)$$

and

$$\langle T(t)\,T(t+\tau)\rangle = \langle \zeta_1 \zeta_2 \rangle\, T'^2$$

$$-T' \left\langle \left| \zeta_1 \theta(z_o - \zeta_2) + \zeta_2 \theta(z_o - \zeta_1) \right| \right\rangle$$

$$+ \langle \theta(z_o - \zeta_1)\,\theta(z_o - \zeta_2) \rangle \quad . \tag{5.104}$$

Since the displacement and fine-structure are statistically uncorrelated and since their individual means are zero the second term vanishes and

$$R_T(\tau) = R_T^g(\tau) + R_T^f(\tau) \quad , \tag{5.105}$$

where

$$R_T^g(\tau) = T'^2 R_\zeta(\tau) \tag{5.106}$$

is the "gradient covariance" with $R_\zeta(\tau) = \langle \zeta_1 \zeta_2 \rangle$ and

$$R_T^f(\tau) = \iint d\zeta_1 d\zeta_2 r(\zeta_1 - \zeta_2)\, p(\zeta_1, \zeta_2; \tau) \tag{5.107}$$

is the "fine-structure covariance" with

$$r(\zeta_1 - \zeta_2) = \langle \theta(z_o - \zeta_1)\,\theta(z_o - \zeta_2) \rangle \quad , \tag{5.108}$$

the fine-structure displacement correlation function. Note that $r(0) = \langle \theta^2 \rangle$.

To continue the analysis a form for the displacement joint probability density function is required. Garrett and Munk assumed that the displacement at any point arises from many different, independent wave components so

that the central limit theorem should apply and the displacements should be jointly normally distributed. Then

$$p(\zeta_1,\zeta_2;\tau) = (2\pi Z^2)^{-1}(1-\rho^2)^{-\frac{1}{2}} \exp\left[-\frac{\zeta_1^2-2\rho\zeta_1\zeta_2+\zeta_2^2}{2Z^2(1-\rho^2)}\right], \quad (5.109)$$

$$\rho(\tau) = R_\zeta(\tau)/Z^2$$

is the displacement autocorrelation and $Z^2=R_\zeta(0)$, the mean square displacement.

With (5.109), (5.107) becomes

$$R_T^f(\tau) = \tau^{-\frac{1}{2}} \int_{-\infty}^{\infty} dx\, r\left|2(1-\rho)^{-\frac{1}{2}}\, Zx\right| \exp(-x^2) \quad (5.110)$$

Formally $R_T^f(\tau)$ does not vanish as $\tau\to\infty$ and this is a deficiency in the model pointed out by Garrett and Munk. The fine-structure gives rise to temperature correlation at very large times when even the displacements become uncorrelated.

If r is specified then $R_T^f(\tau)$ can be determined from (5.110) and the fine-structure frequency spectrum $F_T^f(\omega)$ is simply its Fourier transform. To simplify the analysis expand $\rho(\tau)$ in a Taylor series as

$$\rho(\tau) = 1 - \frac{1}{2}S^2\tau^2 + 0(\tau^4) \quad (5.111)$$

where

$$S^2 = -\rho''(0)$$

Similarly

$$r(z) = \langle\theta^2\rangle \left[1 - \frac{1}{2} K^2 z^2 + 0(z^4)\right] \tag{5.112}$$

where

$$K^2 = -r''(0)/r(0)$$

With (5.110), (5.111) and (5.112) imply

$$R_T^f(\tau) = \langle\theta^2\rangle \left[1 - \frac{1}{2} K^2 Z^2 S^2 \tau^2 + \ldots\right] \tag{5.113}$$

If KZ>>1, (5.113) shows that the fine-structure correlation rolls off much more rapidly than the displacement correlation function so that the small time approximation (5.111) should be an adequate description of the internal wave field. Since K can be viewed as an inverse fine-structure length scale, the requirement KZ>>1 means that internal wave displacements must be large compared to the fine-structure scale. This approximation may not be appropriate since internal wave displacement and apparent fine-structure scales are often of this same order of magnitude. It will apply, however, to small-scale fine-structure, which may be most significant in that small scales contribute significantly to the high frequency measurement variance where direct internal wave-induced variance is smallest.

The Fourier transform of (5.110) with (5.111) yields after some manipulation

$$F_T^f(\omega) = \left(\frac{2}{\pi}\right)^{\frac{1}{2}} \frac{1}{SZ} \int_0^\infty dk \exp\left[-\left(\frac{\omega}{\sqrt{2}\, Szk}\right)^2\right] k^{-1} F_\vartheta(k), \tag{5.114}$$

where $F_\theta(k)$ is the fine-structure vertical wavenumber spectrum. Thus the fine-structure frequency spectrum is related to the vertical wavenumber spectrum. The only statistics of the internal wave field which enter this result are S and Z. The former can be shown to be equal to the wave-field root-mean square frequency. Equation (5.114) can also be expressed in terms of the fine-structure gradient spectrum $F_{\theta'}(k)=k^2F_\theta(k)$ as

$$F_T^f(\omega) = \left(\frac{2}{\pi}\right)^{\frac{1}{2}} SZ\omega^{-2}\int_0^\infty dq\, \exp(-q) F_{\theta'}\left(\frac{\omega}{\sqrt{2q}\, SZ}\right) . \qquad (5.115)$$

Equations (5.114) and (5.115) are the essential results of the analysis.

Estimation of the significance of the fine-structure to the observed spectrum requires the specification of $F_\theta(k)$ or $F_\theta'(k)$. The wavenumber spectrum

$$F_{\theta'}(k) = \overline{\theta'^2}\ /(k_s-k_\ell) \qquad (5.116)$$

roughly represents the case where the gradient θ' consists of a series of narrow spikes. Then from (5.115)

$$F_T^f(\omega) = \left(\frac{2}{\pi}\right)^{\frac{1}{2}} SZ\omega^{-2}(k_s-k_\ell)^{-1} \times \overline{\theta'^2}\left[\exp(-\omega^2\tau_s^2) - \exp(-\omega^2\tau_\ell^2)\right] \qquad (5.117)$$

where

$$\tau_{s,\ell} = (\sqrt{2}\ SZ\ k_{s,\ell})^{-1} .$$

The function in the brackets behaves as

$$\omega^2 \tau_\ell^2 \text{ for } \omega << \tau_\ell^{-1} \quad ,$$

$$1 \quad \text{for } \tau_\ell^{-1} << \omega << \tau_s^{-1} \quad ,$$

and

$$\exp(-\omega^2 \tau_s^2) \text{ for } \tau_s^{-1} << \omega \quad . \tag{5.118}$$

Over the frequency range $\tau_\ell^{-1} << \omega << \tau_s^{-1}$ (5.99b), $F_T^f(\omega) \sim \omega^{-2}$, which is consistent with Phillips' result.

The ratio

$$\gamma(\omega) = F_T^f(\omega)/F_T^g(\omega) \quad , \tag{5.119}$$

where $F_T^g(\omega)$ is the frequency transform of $R_T^g(\omega)$, is a measure of the significance of fine-structure to the overall temperature spectrum. For the simple gradient spectrum (5.116)

$$\gamma(\omega) = \frac{(2/\pi)^{\frac{1}{2}}}{k_\ell} \frac{ZS}{\omega^2 F_\zeta(\omega)} \quad . \tag{5.120}$$

Further analysis requires the specification of the internal wave displacement spectrum $F_\zeta(\omega)$. Consider two models (Figure 5-11)

$$F_\zeta(\omega) = \begin{cases} 0 & \text{for } \omega < \omega_o \\ A\omega^{-r} & \text{for } \omega_o \leq \omega \leq \omega_1 \end{cases} \quad , \tag{5.121}$$

and

$$F_\zeta(\omega) = \begin{cases} A\omega_o^{-r} & \text{for } \omega < \omega_o \\ A\omega^{-r} & \text{for } \omega_o \leq \omega \leq \omega_1 \end{cases} \quad . \tag{5.122}$$

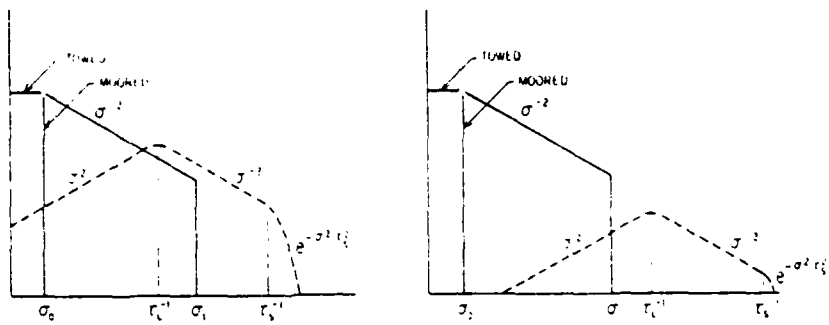

Figure 5-11: Solid lines show the assumed frequency spectrum from moored sensors (5.121) and wavenumber spectrum from towed sensors (5.122) in a log-log presentation. For either case, the dashed curves show the fine-structure spectrum when $\gamma>1$ (left) and $\gamma<1$ (right) (from Garrett and Munk, 1971).

The first model represents frequency spectra where ω_o is the local inertial frequency and ω_1 the local Brunt-Väisälä frequency. The second model represents towed horizontal wavenumber spectra, where ω is identified with horizontal wavenumber, since all of this analysis is formally appropriate to either fixed point frequency spectra or fixed depth horizontal wavenumber spectra. For r=2 and $\omega_o \ll 1$

$$\tau_\ell^{-1} = \frac{2\omega}{\pi\gamma} \quad , \quad \gamma = \left(1, \sqrt{2}\right) \left(\frac{2}{\pi}\right)^{\frac{1}{2}} \frac{\left(\omega_1/\omega_o\right)^{\frac{1}{2}}}{k_\ell Z} \tag{5.123}$$

for the two models respectively over the frequency range (5.99b). For the frequency spectra the ratio of ω_1/ω_o in the upper ocean is of $O(10^2)$. Take 10m for a typical layer thickness and vertical displacement. Then $k_\ell Z = 2\pi$ and $\gamma = O(1)$. For the wavenumber spectra take $\omega_o = 10^{-2}$ cpkm and $\omega_1 = 10$ cpkm following Garrett and Munk (1972). Then $\omega_1/\omega_o = 10^3$ and γ is a factor of ten larger.

Garrett and Munk included in their analysis estimates of vertical coherence. With the assumption that motions at all depths are coherent and in phase, they find

$$\mathrm{Coh}_T(\omega,H) = \left[1+\gamma(\omega)\ \mathrm{Coh}_T^f(\omega,H)\right]\left[1+\gamma(\omega)\right]^{-1} \quad , \tag{5.124}$$

where $\mathrm{Coh}_T^f(\omega,H)$ is the coherence obtained from the fine structure correlation function for points a distance H apart. In this case for $\tau_\ell^{-1} \ll \omega \ll \tau_s^{-1}$

$$\mathrm{Coh}_T(\omega,H) = 2\int_0^\infty dq\ \exp\left(-q^{-2}\right)\ q^{-3}\ \cos\lambda q \tag{5.125}$$

$$= \Lambda(\lambda) \quad ,$$

where

$$\lambda = \frac{\omega H}{\sqrt{2}\ SZ} \quad .$$

This result is plotted in Figure 5-12. The parameter λ involves only the characteristic vertical velocity SZ of the internal wave field and over the appropriate frequency range is not a function of the fine-structure. The fine-structure statistics affect the overall coherence through the factor $\gamma(\omega)$ in (5.124). If γ is independent of frequency, as in (5.123), then $\mathrm{Coh}_T(\omega,H)$ depends only on the product. ωH. In particular, $\mathrm{Coh}_T(\omega,H)=\frac{1}{2}$ for $\mathrm{Coh}_T^f(\omega,H)=\frac{1}{2}(\gamma-1)\gamma^{-1}$. For $\gamma>>1$ and $\gamma=1$ we have $\gamma=\frac{1}{2}$ and 0 respectively, or

$$(\omega H)_{\frac{1}{2}} = 0.95\ SZ,\ 1.8SZ \qquad (5.126)$$

For $S \approx (N(Z)f)^{\frac{1}{2}} \approx 0.4$ cph and $Z \approx 10$ m

$$(\omega Y)_{\frac{1}{2}} = 4,\ 7\ \text{m},$$

which are of the same order of magnitude as Webster's (1971) estimate

$$(\omega Y)_{\frac{1}{2}} = 13\ \text{m}.$$

Garrett and Munk, however, point out that Webster's data extend to far lower frequencies than might be expected to be strongly affected by fine-structure.

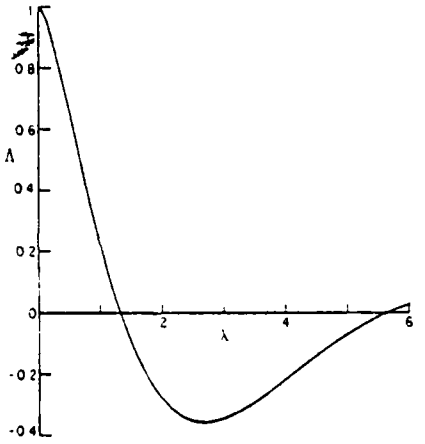

Figure 5-12: The "fine-structure coherence" $Coh_T(\omega,H) = \Lambda(\lambda)$ where $\lambda = \frac{\omega H}{2SZ}$.

5.3.4 McKean's Analysis

McKean (1974) modified the approach followed by Garrett and Munk by casting his analysis in the form of structure rather than correlation functions. The structure function formalism avoids the necessity of the fine-structure approximation. This analysis differs also from Garrett's and Munk's in that the fine-structure is described in terms of the Poisson statistics of the layers. McKean cast his analysis in terms of the contamination of internal-wave statistics of the sort which would be computed from data obtained from horizontally traversing measurement systems. These include horizontal wavenumber spectra and vertical coherence. The specific motivation of this work was the analysis of data obtained with the Self-Propelled Underwater Research Vehicle (SPURV) of the Applied Physics Laboratory of the University of Washington.

Assume a randomly layered temperature field $T_m(z)$ as before. Then the temperature record measured by a probe traversing the medium at some fixed depth z_o is

$$T(x) = T_m(z_o - \zeta(x)) \tag{5.127}$$

where $\zeta(x)$ is the internal wave induced displacement at location x. The structure function which describes the temperature field is defined as

$$D_T(\lambda) = \left\langle \left| T(x) - T(x+\lambda) \right|^2 \right\rangle \quad . \tag{5.128}$$

In terms of the more common correlation function $R_T(\lambda)$ and spectrum $F_T(k)$ (where k here refers to horizontal wavenumber)

$$D_T(\lambda) = 2\left[R_T(0)-R_T(\lambda)\right] \quad , \tag{5.129}$$

and

$$D_T(\lambda) = \pi^{-1}\int_{-\infty}^{\infty} dk\ F_T(k)\ (1-\cos k\lambda) \quad . \tag{5.130}$$

Clearly $D_T(\lambda)$ depends upon the statistics of both the medium and the internal wave field, and a key point of Garrett and Munk's analysis is the separation and definition of these statistics. With the assumption of horizontal homogeneity and vertical stationarity the medium can be described in terms of the structure function

$$D_m(\psi) = \left[T_m(z)-T_m(z+\psi)\right]^2 \quad . \tag{5.131}$$

The fraction of all points $x_1-x_2=\lambda$ having the specified difference $\zeta_1-\zeta_2=\psi$ depends on the joint distribution of internal wave denoted by $Q(\lambda,\psi)d\psi$. The total contribution is then

$$D_T(\lambda) = \int_{-\infty}^{\infty} d\psi\ D_m(\psi)Q(\lambda,\psi) \quad . \tag{5.132}$$

There are thus two parts to the estimation of $D_T(\lambda)$. First the structure function $D_m(\psi)$ of the medium must be

defined, and second the internal wave relative displacement distribution must be specified. Equation (5.132) is the structure function conterpart to (5.101). The structure function formalism combined with the Poisson fine-structure description, however, yields an integrable form which avoids the fine-structure approximation used in the earlier effort. Note that in the simple case of a medium with a uniform gradient, $T_m(z)= T'z$, $D_m(\psi)=T'^2\psi^2$. Then

$$\begin{aligned} D_T(\lambda) &= T'^2 \int_{-\infty}^{\infty} d\psi Q(\lambda,\psi)\psi^2 \quad , \\ &= T'^2 \langle \left|\zeta(x)-\zeta(x+\lambda)\right|^2 \rangle \quad , \\ &= T'^2 D_\zeta(\lambda) \quad , \end{aligned} \tag{5.133}$$

in analogy with (5.106). Then by virtue of 5.130, $F_\zeta(k)=F_T(k)/T'^2$.

Assume that in general the medium is described by a background temperature gradient T_b' and sheets of temperature change θ_n. Then

$$T_m(z)-T_m(z_o) = (z-z_o)T_b' + \sum_{n=1}^{N} \theta_n \quad , \tag{5.134}$$

where in this case the temperature internal $z-z_o$ contains N layers. Squaring and averaging over the steps yield

$$\left\langle \left| T_m(z)-T_m(z_o) \right|^2 \right\rangle = \left| (z-z_o)T_b' \right|^2 + 2N(z-z_o)T_b' \overline{\theta}_n + N^2 \overline{\theta}_n^2 + N\left(\overline{\theta_n^2} - \overline{\theta}_n^2 \right) . \qquad (5.135)$$

If the sheets are distributed randomly the probability of finding exactly N sheets in an interval (z_1-z_o) is given by the Poisson distribution

$$P(N,s) = e^{-s}(s^N/N!), \quad s = (z-z_o)h^{-1}, \qquad (5.136)$$

where h is the mean interval between layers. To obtain an average value for $\langle [T_m(z)-T_m(z_o)]^2 \rangle$ in the randomly layered medium (5.135) must be weighted by the Poisson probability distribution function. For a continuous process

$$\langle u \rangle = \int u \, dB(u) \qquad (5.137)$$

where dB(u) is the probability that any value of u, u_o say, lies between u and u + du. For the discrete Poisson process (5.136) the average value of any function f of N is given by

$$\bar{f} = \sum_{N=0}^{\infty} f(N) \, P(N,s). \qquad (5.138)$$

Relation (5.138) can be applied to (5.135) to obtain the average structure function for the randomly layered medium:

$$D_m(\psi) = (T_b' + \overline{\theta_n}\, h^{-1})^2 \psi^2 + \overline{\theta_n^2}\, \psi\, h^{-1}, \quad \psi>o \ , \qquad (5.139)$$

where $T_b' + \overline{\theta_n}\, h^{-1}$ is identified with the mean gradient T' and $\overline{\theta_n^2}\psi h^{-1}$ represents the fluctuations due to random layering.

With (5.139), (5.132) yields

$$D_T(\lambda) = T'^2 < \psi^2 > + \overline{\theta_n^2}\, h^{-1} <|\psi|> \ , \qquad (5.140)$$

$$= D_T^g(\lambda) + D_T^f(\lambda) \ , \qquad (5.141)$$

in analogy with (5.105). To actually carry out the averaging implied in (5.140) an explicit form for the internal-wave displacement distribution function is required. McKean proposed two centrally peaked forms:

$$\text{Gaussian:} \quad Q(\lambda,\psi) = (2\pi D_\zeta)^{-\frac{1}{2}} \exp\left[-\tfrac{1}{2}\psi^2 D_\zeta^{-1}\right] \ , \qquad (5.142)$$

$$\text{Rayleigh:} \quad Q(\lambda,\psi) = (2D_\zeta)^{-\frac{1}{2}} \exp\left[-\sqrt{2}\,|\psi|\, D_\zeta^{-\frac{1}{2}}\right] \qquad (5.143)$$

which depend only on the standard deviation, $D_\zeta(\lambda) = <(\zeta_1-\zeta_2)^2>$.

For these distributions:

$$D_T^f(\lambda) = \left(\frac{2}{\pi}\right) \overline{\theta_n^2}\ h^{-1} \left[D_\zeta(\lambda)\right]^{\frac{1}{2}}, \qquad (5.144)$$

$$D_T^f(\lambda) = 2^{-\frac{1}{2}} \overline{\theta_n^2}\ h^{-1} \left[D_\zeta(\lambda)\right]^{\frac{1}{2}} \qquad (5.145)$$

respectively. These results are very close.

The fine-structure spectrum due to layering depends in detail on the spectrum of the internal waves which displace the layer. McKean followed Garrett and Munk and proposed the model

$$F_\zeta(k) = \begin{cases} Ak^{-2}, & k_1 < k < k_n \\ 0, & \text{otherwise} \end{cases} . \qquad (5.146)$$

Then $D_\zeta(\lambda)$ can be obtained from the displacement counterpart to (5.130), $D_T^f(\lambda)$ from (5.144) or (5.145), and finally $F_T^f(k)$ from the inverse of (5.130):

$$F_T^f(k) = \int_{-\infty}^{\infty} d\lambda \cos(k\lambda) \left[D_T^f(0) - \tfrac{1}{2} D_T^f(\lambda) \right] , \qquad (5.147)$$

where we have made use of the fact that the correlation function R must go to zero as $\lambda \to \infty$ so that from (5.129) $D_T^f(\infty) = 2 R_T^f(o)$.

The resulting fine-structure spectrum for bandwidth $k_n k_1^{-1} = 100$ is shown in Figure 5-13 obtained with typical values from the GM72 model of $k_n = 2\pi$(3 cph) and $s = 15$ m hr^{-1}. The fine-structure falls into two distinct regimes separated

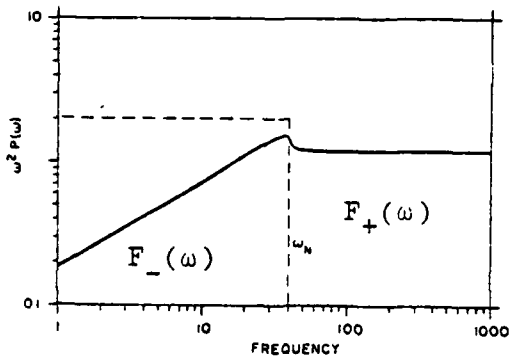

Figure 5-13: Fine-structure spectrum (solid line) generated by internal wave spectrum (broken line). Units are arbitrary.

by an inflection at k_n. Approximate results can be derived for these bands. For $k > k_n$ denote the spectrum by $F_+(k)$. Then for $k >> k_n$ McKean derived

$$F_+(k) = \left(\frac{2}{\pi}\right)^{\frac{1}{2}} \overline{\theta_n^2}\ h^{-1}\ S \quad , \tag{5.148}$$

where S is given by

$$S^2 = 2\int \frac{dk}{2\pi}\ k^2 P(k) \quad , \tag{5.149}$$

which can be interpreted as either the root-mean square slope for wavenumber spectra, or the root-mean vertical velocity for frequency spectra. (Thus, S is here equivalent to the product SZ in Garrett and Munk's analysis.) Equation (5.148) is basically identical to Phillips result.

For wavenumbers $k < k_n$

$$F_-(k) = \left(\frac{2}{\pi}\right)^{\frac{1}{2}} \eta\ \overline{\theta_n^2}\ h^{-1} A^{\frac{1}{2}} k^{-3/2} \quad , \tag{5.150}$$

with

$$\eta = \Gamma\left(\frac{3}{2}\right)\sin\left(\frac{1}{4}\pi\right)/\sin\left(\frac{1}{2}\pi\right)$$

This result is obtained by neglecting the bandwidth entirely; McKean did not discuss the error associated with

this assumption. Since $F_+(k)$ is in principle measureable, a relationship between $F_-(k)$ (which is the quantity required to estimate fine-structure contamination) and $F_+(k)$ is useful. McKean finds for r=2

$$F_+F_- = \tfrac{1}{2}\pi \frac{k}{k_n}^{\frac{1}{2}} \quad , \tag{5.151}$$

which depends only on the cut-off wavenumber k_n. The significance of (5.151) stems from the fact that if one assumes that a spectrum obtained from data at wavenumber $k >> k_n$ represents the effects of fine-structure alone then the spectrum thus measured is exactly $F_+(k)$. Then $F_-(k)$ at wavenumber k is immediately known given k_n. The value of $\overline{\vartheta_n^2} h^{-1} A^{\frac{1}{2}}$ is thus determined. Within the band $k_1 < k < k_n$

$$F_T(k) = F_\zeta(k)(\overline{\partial_z T})^2 + F_-(k)$$

so that if we assume $F_\zeta(k) = Ak^{-2}$ the value of A can be adjusted to fit the observed spectrum $F_T(k)$. Then $F_\zeta(k)$ and $F_-(k)$ are completely specified.

To estimate fine-structure effects on the measurement of internal-wave-induced temperature fluctuations at two vertically separated locations an extension of the above analysis is required. McKean extended Garrett and Munk's result (5.124) to

$$Coh_T(k,H) = \left[Coh(k,H) + \gamma(k)Coh_T^f(k,H)\right]\left[1+\gamma(k)\right]^{-1} \quad . \tag{5.152}$$

Here Coh(k,H) is the actual internal wave displacement coherence and

$$\gamma(k) = F_T^f(k)/F_T^g(k) \qquad \text{(as before)}, \tag{5.153}$$

and

$$\mathrm{Coh}_T^f(k,H) = \int d\lambda_1 D_f(\lambda,H)\cos(k\lambda) \Big/ \int d\lambda\ D_f(\lambda,0)\cos(k\lambda), \tag{5.154}$$

where

$$D_f(\lambda,H) = \int d\psi |H+\psi| Q(\psi,\lambda). \tag{5.155}$$

In general the fine-structure coherence is less than one (except at H=0 where it exactly equals one) so that the coherence observed in the presence of fine-structure is always less than the true coherence. Figure 5-14 shows the numerically obtained fine-structure coherence for a band limited displacement spectrum of the form Ak^{-2}. Like the fine-structure spectrum the results seem to fall into two bands.

For $k \ll k_n$

$$\mathrm{Coh}_T^f(k,H) = \Lambda_-(q) \tag{5.156a}$$

$$= \exp(-q^{\frac{1}{2}}) \left[\cos\sqrt{q} + \sin\sqrt{q}\right]$$

$$q = \frac{kH^2}{A} = \frac{k}{k_n} \frac{k_n^2 H^2}{\pi S^2}, \tag{5.156b}$$

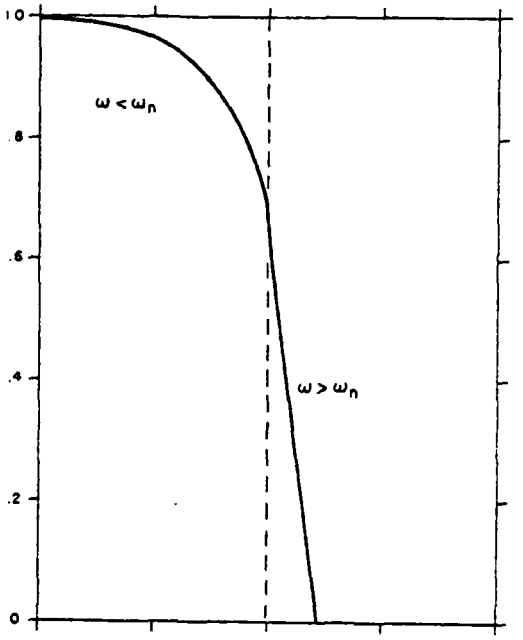

Figure 5-14: Fine-structure coherence form McKean (1974) for band-limited k^{-2} spectrum.

with $\Lambda_{-}(0.83)$= (the half-coherence point).

For $k>k_n$

$$\mathrm{Coh}_T^f(k,H) = \Lambda_+(p)$$

$$= \exp(-ap)\cos(bp) \quad , \tag{5.157a}$$

with

$$a = 0.44, \; b = 1.21,$$

$$p = \frac{k}{\sqrt{2}} \frac{H}{S} \quad , \tag{5.157b}$$

with $\Lambda_{+}(0.67) = \frac{1}{2}$ (the half-coherence point). The result (5.157) agrees closely with Garrett and Munk's prediction (5.126) for $\gamma >> 1$.

The observed coherence according to (5.152) depends on the true coherence Coh(k,H) and the fine-structure ratio γ, as well as the fine-structure coherence $\mathrm{Coh}_T(k,H) = \Lambda_{\pm}$. For wavenumbers or frequencies higher than the cut-off k_n the spectrum F_ζ approaches zero and $\gamma \to \infty$. Then the observed coherence is equal to the fine-structure coherence. Consider a moored vertical array in an internal wave field with parameters derived from GM72: $S = 15\mathrm{m\ hr}^{-1}$ and $k_n = \omega_n = 6\pi$ (cph). Then the half-coherence point p=0.67, with $\Lambda_{+}(0.67) = \frac{1}{2}$ satisfies the rule

$$(\omega H)_{\frac{1}{2}} = 4 \text{ cph m.}$$

The minimum frequency in this band corresponds then to a separation H = 1m. Therefore, the extension of "fine-structure coherence" into the forbidden band above the Vaisala frequency should be measureable only for sensor spacings on the order of 1m or smaller.

The more important case concerns the influence of "fine-structure coherence" in the overlap band ($k<k_n$). Taking the half-coherence point q = 0.83 with the GM72 parameters leads to

$$(\omega H^2)_{1/2} = 5 \text{ cph } m^2.$$

Now, to estimate the significance of the fine-structure coherence we consider a near-limiting case of low frequency, for instance $\omega = (12 \text{ hr})^{-1}$. The half coherence distance becomes smaller for higher frequencies. Then $H_{1/2} = 7.8$m. Coincidentally, this corresponds to the GM72 rms internal-wave amplitude Z = 7.9m. This suggests that the influence of the fine-structure coherence is generally not important for separations exceeding the mean-square amplitude.

McKean applied the decontamination model to a 7-km towed temperature data record. Vertical sensor separations were 2/3 and 1m so that the internal-wave displacement coherence Coh (k,H) was set to unity. The observed temperature spectrum is shown in Figure (5-15) where $k^2F_T(k)$ is plotted. The spectral density shows a sharp drop at 18 cpkm ($=k_n$). Similar breaks are seen in the two coherences shown in Figure (5-16). After some manipulation including the numerical modeling of the cross-correlation function

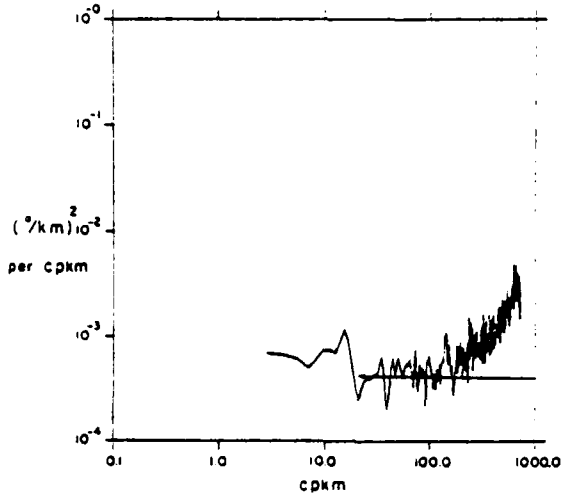

Figure 5-15. Plot of $k^2 F_T(k)$ vs. wavenumber with a cut-off wavenumber of 18 cpkm. (McKean, 1974).

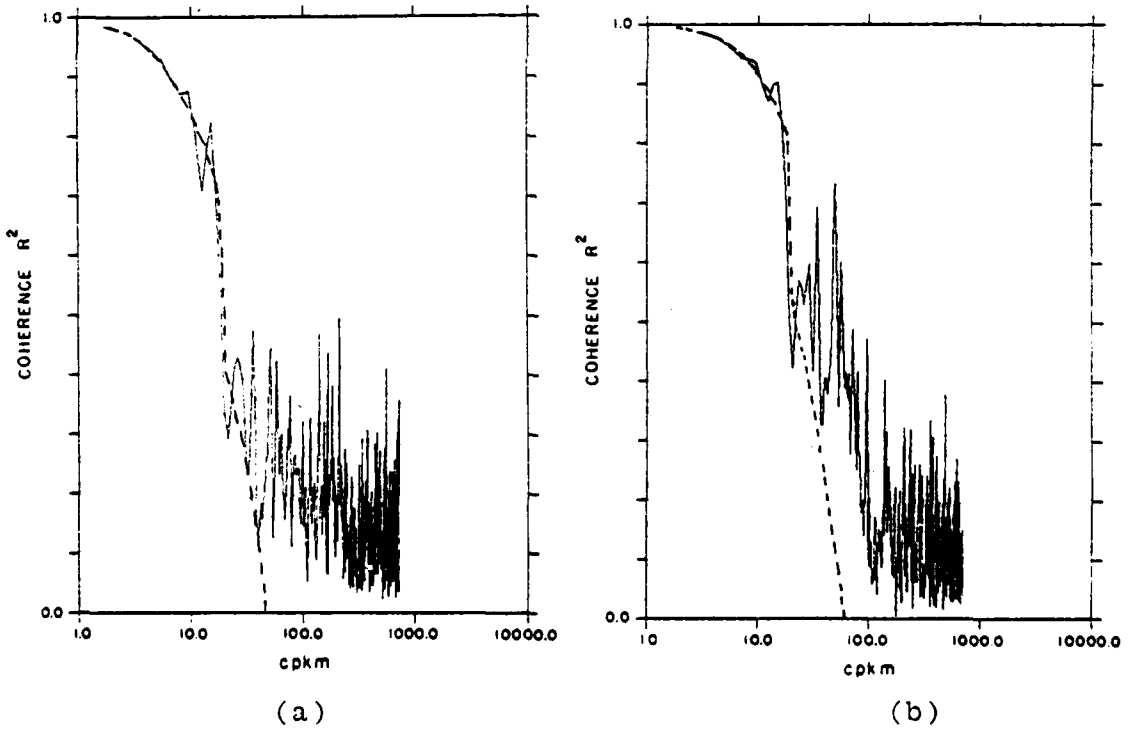

Figure 5-16. Coherence as a function of wavenumber (solid line) compared with McKean's random layer model with R=1, S=0.0016. (a) Vertical separation = 1 m. (b) Vertical separation = 2/3 m. (McKean, 1974).

associated with a band-limited power law spectrum from which $D\zeta(\lambda,H)$ and then $Q(\lambda,\chi,H)$ are determined, McKean produced the coherence estimates shown in Figure 5-16. The predicted coherences up to roughly k_n agree well with the observations. The wave slope S was adjusted for best fit with the data.

The model thus produces results consistent with the observations; such consistency should not, however, be viewed as a proof that fine structure is in fact irreversible. Desaubies and Gregg (1980) have demonstrated that fine structure observed in the main thermocline could be described solely as the result of reversible internal wave strain.

References

Abramowitz, M. and J. A. Stegun (1965): Handbook of Mathematical Functions, Dover Publications, New York.

Bendat, J. S. and A. G. Piersol (1971): Random Data: Analysis and Measurement Procedures, Wiley-Interscience, New York.

Briscoe, M. G. (1975): Preliminary Reports from the Trimyard World Internal Wave Experiment (IWEX), J. Geophys. Res., 80, 3872-3884.

Cairns, J. L. (1975): Internal Wave Observations from a Midwater Float, J. Geophys. Res., 80, 299-306.

_____ and G. O. Williams (1976): Internal Wave Observations from a Midwater Float, 2, J. Geophys, Res., 81, 1943-1950.

Desaubies, Y. F. (1973): Internal Waves Near the Turning Point, Geophys. Fluid Dyn., 5, 143-154.

_____ (1975): A Linear Theory of Internal Wave Specta and Coherences Near the Vaisala Frequency, J. Geophys. Res., 80, 895-899.

_____ (1976): Analytical Representation of Internal Wave Spectra, J. Phys. Oceanog., 6, 976-981.

_____ and M. C. Gregg (1980): Reversible and Irreversible Finestructure, Applied Physics Lab. and Dept. of Oceanogr., University of Washington, Seattle. (UNPUBLISHED MANUSCRIPT).

Dozier, L. B. and F. D. Tappert (1978): Statistics of Normal Mode Amplitudes in a Random Ocean, I. Theory, J. Acoust. Soc. Am., 63, 353-365.

_____ and _____ (1978): Statistics of Normal Mode Amplitudes in a Random Ocean, II. Computations, J. Acoust. Soc. Am., 64, 533-547.

Garrett, C. and W. Munk (1971): Internal Wave Spectra in the Presence of Finestructure, J. Phys. Oceanogr., 1, 196-202.

References (Continued)

Garrett, C. and W. Munk (1972): Space-Time Scales of Internal Waves, Geophys. Fluid Dynamics, 2, 225-264.

_____ and _____ (1975): Space-Time Scales of Internal Waves: A Progress Report, J. Geophys. Res., 80, 291-297.

Gregg, M. (1977a): A Comparison of Finestructure Spectra from the Main Thermocline, J. Phys. Oceanogr., 7, 33-40.

Gregg, M. (1977b): The Microstructure of the Ocean, Ocean Science: Readings from Scientific American, W. H. Freeman & Co., San Francisco, 157-169.

Johnson, C. L., C. S. Cox, and B. Gallagher (1978): The separation of Wave-Induced and Intrusive Oceanic Finestructure, J. Phys. Oceanogr., 8, 846-860.

Lumley, J. L. and H. A. Panofsky (1964): The Structure of Atmospheric Turbulence, Interscience Publishers, New York.

McKean, R. S. (1974): Interpretation of Internal Wave Measurements in the Presence of Finestructure, J. Phys. Oceanogr., 4, 200-213.

Millard, R. (1972): Further Comments on Vertical Temperature Spectra in the MODE Region, MODE Hot Line News, 18(1). (UNPUBLISHED MANUSCRIPT).

Muller, P. (1976): On the Diffusion of Momentum and Mass by Internal Gravity Waves, J. Fluid Mech., 77, 789-823.

_____, D. J. Olbers, and J. Willebrand (1978): The IWEX Spectrum, J. Geophys. Res., 83, 479-500.

Olver, F. W. J. (1964): Error Bound for Asymptotic Expansions in Turning Point Problems, Journal, Soc. Indust. and Appl. Math., 12, 200-214.

Phillips. O. M. (1971): On Spectra Measured in an Undulating Layered Medium, J. Phys. Oceanogr., 1, 1-16.

Woods, J. D. (1968): Wave-Induced Shear Instability in the Summer Thermocline, J. Fluid Mech., 32, 791-800.

References (Continued)

Woods, J. D. and G. G. Fosberry (1966): Observations of the Thermocline and Transient Stratifications Made Visible by Dye, Proceedings, 1965 Malta Sympt. Underwater Assn., London.

_____ and _____ (1967): The Structure of the Thermocline, Report 1966-1967, Underwater Assn., London.

Wunsch, C. (1976): Geographical Variability of the Internal Wave Field: A Search for Sources and Sinks, J. Phys. Oceanogr., 6, 471-485.

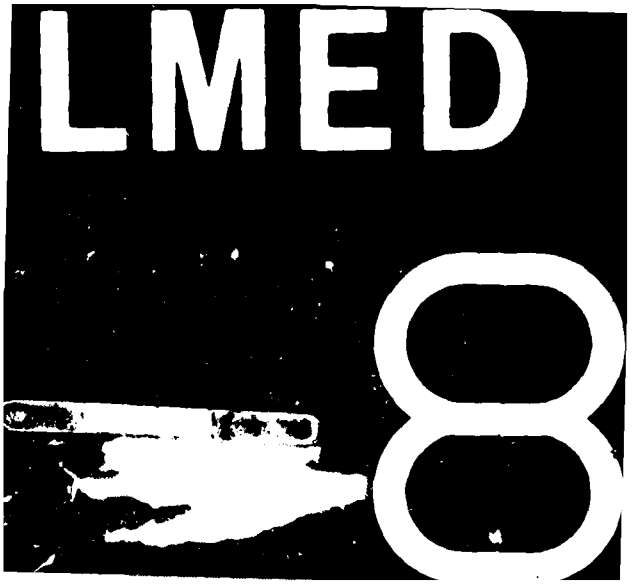
LMED
8